Exploring strategies for the production of ultracold RbYb molecules in conservative traps

Inaugural-Dissertation

zur

Erlangung des Doktorgrades der

Mathematisch-Naturwissenschaftlichen Fakultät

der Heinrich-Heine-Universität Düsseldorf

vorgelegt von

Cristian Bruni

aus Mesagne (Italien)

Düsseldorf, Juni 2015

Aus dem Institut für Experimentalphysik
der Heinrich-Heine-Universität Düsseldorf

Gedruckt mit der Genehmigung der
Mathematisch-Naturwissenschaftlichen Fakultät der
Heinrich-Heine-Universität Düsseldorf

Referent:	Prof. Dr. Axel Görlitz
Koreferent:	Prof. Dr. Georg Pretzler
Tag der mündlichen Prüfung:	14.07.2015

Summary

Within the scope of this thesis extensive experiments dealing with photoassociation spectroscopy and magnetic Feshbach resonances were performed with various isotopes of rubidium (Rb) and ytterbium (Yb) in the ultracold temperature regime of a few μK. It was possible to produce electronically excited molecules in a novel hybrid trap by means of 1-photon photoassociation spectroscopy in the $^2\Pi_{1/2}$ state and to characterize this state further extending previous works within the thesis of N. Nemitz [1]. The first experimental realization of photoassociation spectroscopy in a conservative trap is also a major step towards the ultimate project goal of producing ultracold RbYb molecules in the electronic ground state. Additionally, detailed attempts were undertaken to induce magnetic Feshbach resonances in ^{85}Rb and different Yb isotopes, especially ^{171}Yb in a crossed optical dipole trap at 1064 nm. Unfortunately, our efforts were without success. Furthermore, the molecular ground state $^2\Sigma_{1/2}$ could be modeled more precisely in collaboration with a theory group [2] that used our 2-photon photoassociation experimental results [3].

The presented experiments were basically carried out with the same apparatus that was already used for previous projects and theses treating experiments with ultracold Rb-Yb mixtures [4, 5, 1, 6, 3]. The newly implemented hybrid conservative trap, that was used within this thesis, combines a magnetic trap for Rb and a near-resonant optical dipole trap for Yb which is red-detuned by only 140 GHz with respect to the intercombination transition $^1S_0 \rightarrow {}^3P_1$. Here, a combined temperature of 1.7 μK could be reached where Rb served as a cold reservoir during sympathetic cooling of Yb. The achieved densities of $\rho_{\mathrm{Rb}} = 2.7 \cdot 10^{13}\,\mathrm{cm}^{-3}$ for Rb and $\rho_{\mathrm{Yb}} = 1.1 \cdot 10^{12}\,\mathrm{cm}^{-3}$ for Yb are several orders of magnitude larger than in previous photoassociation experiments in a combined magneto-optical trap [1, 3].

The 1-photon photoassociation produces electronically excited molecules from two colliding atoms with the help of a photon. Similar to previous theses in the group of Prof. Görlitz, photoassociation was performed close to the Rb D_1 line at 795 nm. Contrary to those experiments, which were performed in a MOT, here photoassociation was observed in the hybrid conservative trap. This conservative hybrid trap would in principle also allow to trap RbYb molecules which are produced by photoassociation. Since so far the molecules could not yet be directly detected, transitions to excited vibrational states were monitored by trap-loss spectroscopy of the atoms. Within this work, the binding energy of vibrational states in the electronically excited $^2\Pi_{1/2}$ state could be extended by a factor of three in a mixture of ^{87}Rb^{176}Yb reaching $E_b = -h \times 2.2\,\mathrm{THz}$ for the vibrational level $\Delta v' = -28$. Furthermore, the position of two resonances which were assigned in a previous work [1, 7] could be corrected in which artifacts were interpreted as weak lines.

An important experimental observation is the variation of the hyperfine splitting with increasing binding energy of a molecular state. In general, photoassociation produces weakly

bound molecules that hence show the properties of the constituent atoms. As a consequence, (almost) every detected vibrational state consists of two resonances, that could be assigned to the molecular analogue of the hyperfine structure of ^{87}Rb. In the case of atomic Rb, the splitting between the two resonances is 817 MHz. We observed, that the splitting decreases with increasing binding energy of the vibrational states of the excited RbYb molecule. For the deepest found vibrational state $\Delta v' = -28$ of the electronically excited $^2\Pi_{1/2}$ level the hyperfine splitting amounts only 70% of the atomic value. This variation is related to the hyperfine coupling constant of the Rb atom, that is influenced by the presence of the Yb atom and emphasizes a gradual passage from weakly to tightly bound molecules.

Within this work, the RbYb ground state $^2\Sigma_{1/2}$ was modelled precisely in collaboration with a theory group [2]. For this purpose, the data achieved by our 2-photon photoassociation experiments for various isotopic combinations of Rb and Yb [8], which precisely determines the interaction potential for large interatomic distances, was reevaluated more accurately. The theory group was therefore able to calculate the molecular interaction potential for small internuclear distances by ab-initio methods and to smoothly connect it to the experimental results for the long-range part of the potential. This resulted in a precise characterization of the ground state, that is composed of the potential depth $D_e = 787.4\,\mathrm{cm}^{-1}$, the number of vibrational bound states $N = 66$ and the van-der-Waals coefficient $C_6 = -2837.2\,E_h\,a_0^6$ that determines the long-range interaction. Furthermore, with the help of the 2-photon photoassociation results for ^{87}Rb and various Yb isotopes, the *s*-wave scattering length for all possible isotopic combinations in Rb-Yb could be deduced which dictates the interatomic interaction in the ultracold temperature regime. The obtained values agree well with previous experiments concerning thermalization in a mixture with different isotopic combinations of Rb-Yb [9] and the spatial separation in ^{87}Rb and ^{174}Yb [10].

The first attempt in this work to produce ultracold RbYb molecules was the search for magnetic Feshbach resonances. Until the year 2010, it was commonly believed that this type of resonances in a mixture of an alkali atom and an alkaline earth(-like) atom do not exist. But in recent publications [11, 12, 13] a small coupling between the hyperfine states was predicted theoretically, that would open the possibility for the observation and possibly exploitation of magnetic Feshbach resonances in this type of atomic mixture. This coupling has the same origin as the observed variation in hyperfine structure in the excited Rb*Yb molecule. Due to the exact knowledge of the ground state, the positions of possible Feshbach resonances could be predicted with a good accuracy. The most extensive examination was performed with ^{85}Rb and ^{171}Yb at temperatures of 10 µK in a crossed optical dipole trap. For this purpose, a homogeneous magnetic field was applied and scanned in small steps over the range of $\approx 495\,\mathrm{G} \ldots \approx 640\,\mathrm{G}$. Additionally, well known as well as not yet reported Rb_2 Feshbach resonances in ^{85}Rb and ^{87}Rb were detected. These resonances allowed for a detailed analysis of the typical behaviour of Feshbach resonances. However, in spite of an intensive study no unambiguous signals that could be related to RbYb Feshbach resonances could be identified.

The long-term goal of this experiment is the production of ultracold RbYb molecules in

the rovibronic ground state. Since the RbYb molecules provide a magnetic as well as an electric dipole moment, the novel hybrid trap constitutes already a possibility to spatially confine the created molecules. Within this thesis, RbYb molecules in the electronically excited $^2\Pi_{1/2}$ state have been produced and analyzed. The next step will be the production and detection of molecules in highly excited vibrational states of the $^2\Sigma_{1/2}$ electronic ground state in a conservative trap. In a previous work [3, 2] we have already determined the positions of the weakly bound vibrational states close to threshold in a combined MOT. The transfer of pairs of atoms into highly vibrating ground state molecules can be done using the method of „stimulated Raman adiabatic passage “ (STIRAP) which has been successfully achieved in the case of Sr_2 [14] but not yet in heteronuclear mixtures. In order to create deeply bound ground state molecules, eventually in the vibrational and rotational ground state, an additional transition step is needed which is most promisingly performed by a second STIRAP process. For this purpose, further knowledge on the positions of deeply bound vibrational states of the electronically excited and ground molecular state, respectively, will be required. The results achieved within this thesis point out the experimental feasibility of these processes.

Zusammenfassung

Im Rahmen dieser Arbeit wurden umfangreiche Experimente mit verschiedenen Isotopen von Rubidium (Rb) und Ytterbium (Yb) im ultrakalten Temperaturbereich von wenigen μK durchgeführt. Es war möglich, elektronisch angeregte Moleküle im $^2\Pi_{1/2}$ Zustand in einer neuartigen Hybridfalle mit Hilfe von 1-Photonen-Photoassoziation zu produzieren und diesen eingehender zu charakterisieren, wodurch vorausgehende Experimente in der Arbeit von N. Nemitz [1] erweitert wurden. Die erste experimentelle Realisation von Photoassoziationsspektroskopie in einer konservativen Falle ist zudem ein entscheidender Schritt in Richtung des endgültigen Zieles des Projektes, ultrakalte RbYb Moleküle im elektronischen Grundzustand zu erzeugen. Daneben wurden ausführliche Versuche unternommen, um magnetische Feshbach-Resonanzen in ^{85}Rb und verschiedenen Yb Isotopen, vor allem ^{171}Yb in einer gekreuzten Dipolfalle bei 1064 nm, zu induzieren. Unglücklicherweise blieben diese jedoch erfolglos. Zusätzlich, konnte der elektronische Grundzustand $^2\Sigma_{1/2}$ in Kollaboration mit einer theoretisch arbeitenden Gruppe [2] präziser modelliert werden, die unsere Ergebnisse der 2-Photonen Photoassoziation [3] als Grundlage nutzten.
Die präsentierten Experimente liefen an der Apparatur ab, an der bereits vorausgehende Projekte und Doktorarbeiten mit ultrakalten Rb-Yb Gemischen durchgeführt und vollendet wurden [4, 5, 1, 6, 3]. Die neu implementierte konservative Hybridfalle, die in dieser Arbeit verwendet wurde, kombiniert eine Magnetfalle für Rb mit einer nahresonanten optischen Dipolfalle für Yb, die nur 140 GHz gegenüber dem Interkombinationsübergang $^1S_0 \rightarrow {}^3P_1$ rotverstimmt ist. Dabei ist es möglich eine kombinierte Temperatur von 1.7 μK zu erreichen, wobei Rb als kaltes Reservoir während der sympathetischen Kühlung von Yb fungiert. Die erreichten Dichten sind mit $\rho_{\mathrm{Rb}} = 2.7 \cdot 10^{13}\,\mathrm{cm}^{-3}$ für Rb und $\rho_{\mathrm{Yb}} = 1.1 \cdot 10^{12}\,\mathrm{cm}^{-3}$ für Yb um einige Größenordnungen größer als in vorherigen Photoassoziationsexperimenten in der kombinierten magneto-optischen Falle [1, 3].
Die 1-Photonen-Photoassoziation bedient sich der Wechselwirkung zweier kollidierender Atome mit einem Photon, um Moleküle in einem elektronisch angeregten Zustand zu erzeugen. In dieser Arbeit, wie auch in vorherigen Arbeiten in der Gruppe von Prof. Görlitz, fand die Photoassoziation nahe der Rb D_1 Linie bei 795 nm statt. Im Gegensatz zu den vorherigen Experimenten, die in einer kombinierten MOT durchgeführt wurden, wurde hier Photoassoziation in einer konservativen Hybridfalle beobachtet. Diese Hybridfalle liefert prinzipiell die Möglichkeit die durch Photoassoziation erzeugten RbYb-Moleküle auch räumlich zu speichern. Da diese bisher jedoch nicht direkt detektiert werden konnten, wurden Übergänge in angeregte Vibrationszustände mittels Verlustspektroskopie der Atome nachgewiesen. In dieser Arbeit konnten in einem Gemisch aus ^{87}Rb^{176}Yb Vibrationslevel im elektronisch angeregten Zustand $^2\Pi_{1/2}$ bis zu einer Bindungsenergie von $E_b = -h \times 2.2\,\mathrm{THz}$ für den Vibrationszustand $\Delta v' = -28$ gefunden und damit die Bindungsenergie um einen Faktor drei erweitert werden. Außerdem wurde die Position

zweier Linien korrigiert, die in einer früheren Arbeit in schwache Signale hineininterpretiert wurden [1, 7].
Eine weitere interessante und experimentell wichtige Beobachtung ist die Änderung der Hyperfeinstrukturaufspaltung mit der Zunahme der Bindungsenergie eines Molekülzustands. Da mittels Photoassoziation in der Regel schwach gebundene Moleküle produziert werden, weisen diese noch atomare Eigenschaften auf. Darunter fällt das Auftreten zweier Resonanzen zu (nahezu) jedem Vibrationszustand, die als molekulares Analogon der Hyperfeinstruktur von Rb identifiziert werden konnten. Im atomaren Rb beträgt der Abstand der beiden Linien 817 MHz. Dieser Wert nimmt im RbYb-Molekül mit steigender Bindungsenergie stetig ab und beträgt für den Vibrationszustand $\Delta v' = -28$ nur noch knapp 70% des atomaren Wertes. Diese Änderung hängt mit der Hyperfein-Kopplungskonstante von Rb zusammen, die durch die Anwesenheit des Yb Atoms variiert wird. Dies weist auf einen allmählichen Übergang von schwach zu stärker gebundenen Molekülen hin.
Im Rahmen dieser Arbeit wurde in Kollaboration mit einer theoretisch arbeitenden Gruppe [2] der $^2\Sigma_{1/2}$ Grundzustand des RbYb Moleküls sehr präzise modelliert. Dazu wurden die Daten aus den Experimenten der 2-Photonen Photoassoziation mit diversen isotopischen Kombinationen von Rb und Yb [8] genauer ausgewertet, die das Wechselwirkungspotential für große interatomare Abstände sehr genau bestimmen. Die Theoretiker waren damit in der Lage, das Potential mittels ab-initio Berechnungen für kleine interatomare Abstände zu berechnen und das Modell für große Abstände an die experimentellen Daten anzupassen. Daraus folgten sehr genaue Charakterisierungen des molekularen $^2\Sigma_{1/2}$ Grundzustandes, die sich zusammensetzen aus der Potentialtiefe $D_e = 787.4\,\mathrm{cm}^{-1}$, der Anzahl gebundener Vibrationszustände $N = 66$ und dem van-der-Waals Koeffizienten $C_6 = -2837.2\,E_h\,a_0^6$, der die langreichweitige Wechselwirkung bestimmt. Außerdem wurden mit Hilfe der 2-Photonen Photoassoziationsdaten für ^{87}Rb und diversen Yb Isotopen die s-Wellen Streulängen für alle möglichen Isotopenverbindungen deduziert, die die interatomare Wechselwirkung der ultrakalten Atome festlegt. Diese Werte stimmen sehr gut mit früheren Experimenten zur Thermalisierung [9] und räumlicher Separation der atomaren Spezies [10] überein.
Der erste Versuch zur Erzeugung von ultrakalten RbYb Molekülen im Rahmen dieser Arbeit bestand in der Suche nach sogenannten magnetischen Feshbach Resonanzen. Bis zum Jahre 2010 war man allgemein der Meinung, dass diese Resonanzen in einem Gemisch aus einem Alkali und einem Erdalkali(-ähnlichem) Metall nicht existieren. Allerdings wurde in [11, 12, 13] eine schwache Kopplung zwischen den Hyperfeinzuständen theoretisch vorausgesagt, die die Möglichkeit zur Beobachtung und möglicher Ausnutzung von Feshbach Resonanzen eröffnete. Diese Kopplung im elektronischen Grundzustand hat denselben Ursprung, wie die beobachtete Änderung der Hyperfeinstrukturaufspaltung im angeregten Molekülzustand. Durch die genaue Kenntnis des molekularen Grundzustandes konnten die Positionen möglicher Feshbach Resonanzen mit hoher Genauigkeit eingegrenzt werden. Das ausgiebigste Experiment wurde mit ^{85}Rb und ^{171}Yb bei Temperaturen von 10 µK in einer gekreuzten optischen Dipolfalle durchgeführt. Dazu wurde ein homogenes Magnetfeld angelegt und kleinschrittig im Bereich von $\approx 495\,\mathrm{G}$ ... $\approx 640\,\mathrm{G}$ durchgefahren. Im Rahmen der Suche nach Feshbach Resonanzen in RbYb, wurden bekannte und unbekan-

nte Rb_2 Feshbach Resonanzen sowohl in ^{85}Rb als auch in ^{87}Rb gefunden. Anhand dieser Resonanzen konnte das typische Verhalten von Feshbach Resonanzen detailliert getestet und analysiert werden. Allerdings konnte trotz intensiver Suche kein eindeutiges Signal als RbYb Feshbach Resonanz identifiziert werden.
Das langfristige Ziel dieses Experiments ist die Erzeugung von ultrakalten RbYb Molekülen im absoluten rovibronischen Grundzustand. Da RbYb Moleküle sowohl ein magnetisches als auch ein elektrisches Dipolmoment besitzen, weist die neuartige konservative Hybridfalle bereits eine Möglichkeit auf, die produzierten Moleküle auch räumlich zu speichern. Innerhalb dieser Arbeit konnten RbYb Moleküle im elektronisch angeregten $^2\Pi_{1/2}$ Zustand produziert und analysiert werden. Der nächste Schritt bildet die Produktion und Detektion von Molekülen in hoch angeregte Vibrationszustände des elektronischen $^2\Sigma_{1/2}$ Grundzustandes in einer konservativen Falle. In einer früheren Arbeit [3, 2] haben wir bereits die Positionen von schwach gebundenen Vibrationszuständen nahe der Dissoziationsgrenze in einer kombinierten MOT bestimmt. Der Übergang von Atompaaren zu stark vibrierenden Grundzustandsmolekülen kann mit Hilfe eines sogenannten „stimulated Raman adiabatic passage “ (STIRAP) Prozesses absolviert werden, was bereits erfolgreich mit Sr_2 [14] jedoch noch nicht mit heteronuklearen Gemischen erreicht wurde. Um tief gebundene Grundzustandsmoleküle, und schlussendlich im absoluten Vibrations- und Rotationsgrundzustand, zu erzeugen, wird ein weiterer Übergangsschritt benötigt. Erfolgversprechend erscheint hier ein zweiter STIRAP Prozess, wofür allerdings weitere Kenntnis der stark gebundenen Zustände im elektronischen Grund- und angeregten Zustand unumgänglich ist. Die in dieser Arbeite erzielten Resultate weisen jedoch auf die experimentelle Realisierbarkeit dieser Prozesse hin.

Contents

1

Introduction

This thesis is part of a research project with the long term goal of creating ultracold rubidium-ytterbium (RbYb) molecules in the rotational, vibrational and electronic (short *rovibronic*) molecular ground state. Particularly, it focusses on the production of excited RbYb molecules in a novel hybrid conservative trap. This chapter gives a motivation for the work by briefly touching the fascinating field of ultracold atoms and molecules and their huge potential for exciting applications.

Ultracold atoms

The first experimental realization of slowing and laser cooling of neutral sodium atoms [15, 16, 17] in the 1980s has opened the door to a variety of experiments and novel discoveries with atomic gases in the ultracold temperature regime. The development of techniques of laser cooling and trapping was consequently rewarded with the Nobel Prize in Physics in 1997 for C. Cohen-Tannoudji, W. Phillips and S. Chu. With these cooling methods as a basis, that allowed for reaching temperatures below 1 mK, further techniques were developed [18] that expanded the ultracold temperature regime to a few nK.
All this opened the path to many fascinating investigations of quantum mechanical phenomena, that differ from the well-known behaviour in the macroscopic world. The most prominent of a variety of fascinating effects is the experimental realization of Bose-Einstein condensates (BEC) in 1995 [19, 20, 21]. This transition into a single macroscopic quantum state at suitable temperatures and densities was theoretically predicted by A. Einstein and S. Bose in the 1920s [22, 23] by taking only statistical considerations into account. In 2001, the Nobel Prize in Physics was awarded to E. Cornell, W. Ketterle and C. Wieman for the achievement of a BEC.
Since then, in addition to those milestones, many interesting quantum phenomena have been observed in ultracold atomic physics, such as superconductivity [24], Mott-insulator states [25] or entanglement of particles [26].

Ultracold molecules

After reaching the ultracold temperature regime with atoms, there has been great interest in transferring this knowledge to also create ultracold molecules which feature fascinating prospects due to their diverse interactions. The field of ultracold chemistry [27] benefits from ultracold temperatures, since then the spectral resolution of molecular spectroscopy

is only limited by the natural lifetime of the addressed molecular levels [28]. This gives the possibility to study the process of chemical reactions in a controlled way [29]. Additionally, this high-resolution spectroscopy of molecules leads the way to precision measurements that might provide new insight in fundamental physical laws. For instance, ultracold molecules have been proposed to measure possible variations in the electron-to-proton mass ratio with a high sensitivity [30, 31], possible changes of the fine structure constant [32] or even time-reversal symmetries [33].
Particularly, ultracold polar (heteronuclear) molecules, such as RbYb, are interesting in that respect due to their large internal electric fields. Thus they offer the possibility to perform experiments concerning the search for a permanent electronic dipole moment of the electron (eEDM) [34] which has also been proposed for the system RbYb [35]. Another interesting aspect is that heteronuclear molecules have an electric dipole moment which leads to a long-range dipole-dipole interaction between the molecules. This dipole interaction can be controlled using external electric fields making polar molecules to an attractive candidate for applications in quantum computation [36], as an experimental simulation of condensed matter systems [37] or the production of quantum matter with strong dipolar interactions [38]. If additionally paramagnetic heteronuclear molecules, such as RbYb, are confined in optical lattices this gives the possibility of realizing complex spin-lattice models [39, 40].
For these purposes, ultracold molecules preferably in the rovibronic ground state have to be produced efficiently and spatially confined in a trap for the following manipulation. Laser-cooling generally requires level structures with closed cycling transitions. While such structures can be found in many atomic species and have been used to cool them to temperatures in the mK regime, the complex internal structure of molecules compared to atoms complicates the application of laser-cooling techniques for molecules. Only in very special and exotic cases, such as SrF, it has been demonstrated that simple diatomic molecules are amenable to laser cooling [41, 42]. However compared to atoms, the experimental efforts are more challenging and the efficiency is reduced. Therefore, an alternative approach is given by producing ultracold molecules starting from mixtures of ultracold atoms. Among various routes to ground state molecules [43], the two most promising and common techniques are magnetically tunable Feshbach resonances [44, 45] or photoassociation [46].

A magnetic Feshbach resonance requires that a bound molecular state and the open channel of two free atoms can be shifted relative to each other by a homogeneous magnetic field. A resonance occurs when both channels are energetically degenerate and a coupling between them exists. Typically, Feshbach resonances are detected by atom loss caused by three-body recombination processes which are strongly enhanced close to a resonance. The first Feshbach resonances were observed in 1998 in ^{85}Rb [47] and ^{23}Na [48]. The first observation of Feshbach resonances in heteronuclear mixtures, was reported in 2004 in KRb [49] and LiNa [50]. Since then, Feshbach resonances have been found in various bialkali mixtures [44]. Consequently, Feshbach molecules, typically in a weakly bound vibrational level of the electronic ground state, can be efficiently created by adiabatically varying the magnetic field across the resonance and thus transferring the population from free atoms to weakly bound molecules [44, 45]. Recently, magnetic Feshbach resonances have also been

theoretically predicted in a mixture of an alkali and an alkaline earth(-like) metal [11, 12] which in principle should make it possible to reach the molecular ground state of RbYb by using magnetic Feshbach resonances.
The second route to ground state molecules is by means of photoassociation [51, 52] which is typically composed of two experimental steps. One approach uses 1-photon photoassociation where two colliding atoms absorb a photon and are transferred to a bound vibrational level in an electronically excited molecular state. This bound state can spontaneously decay either back in two free atoms or (more likely) into a vibrational level of the molecular ground state. The first observation of population of a highly excited vibrational level in the molecular ground state by spontaneous emission was reported in 1998 in Cs_2 [53]. Besides, molecules have been accumulated in the rovibronic ground state after excitation and subsequent spontaneous decay in LiCs using a single photoassociation step [54] or in Cs_2 with the help of an incoherent depopulation pumping method [55]. However, this method requires favourable Franck-Condon factors between the relevant states and the production will not be coherent.
Another approach employs a 2-photon photoassociation process where the atoms can be transferred into a well-defined vibrational level of the electronic ground state. Building on the 1-photon photoassociation process, the second photon addresses a bound-bound transition between the vibrational level of the excited state and vibrational level of the ground state. That way, heteronuclear RbCs molecules in their vibronic ground state have been produced by stimulated emission pumping [56].
A two-photon process which is intrinsically coherent is the so-called *stimulated Raman adiabatic passage* (STIRAP) [57, 58] which does not populate the excited molecular state. It has been shown with Sr_2 that this method can be used to convert pairs of atoms into weakly bound ground state molecules with an efficiency of 30% [14]. Rather commonly, STIRAP is used starting from weakly bound molecules in the molecular ground state and transferring the initial molecules coherently to a specific deeper bound vibrational level or even the absolute ground state. In a counter-intuitive pulse sequence two laser fields couple these states to a vibrational level in an electronically excited state. The final goal of reaching the rovibrational state of the molecular ground state was already achieved in several cases such as Rb_2 [59], KRb [60], Cs_2 [61], RbCs [62, 63] and very recently NaK [64]. Here, a combination of both presented techniques was used. First, weakly bound molecules in the ground state are produced by magnetic Feshbach resonances. Subsequently, a STIRAP process brings the created molecules to the rovibronic ground state.
All of these experiments are either performed with the atoms confined in a magneto-optical trap or a conservative trap. Although in a magneto-optical trap tightly bound ultracold molecules can be produced, the production rate is generally low and the created molecules are lost and elude the desired subsequent manipulation. Higher production rates can be achieved in conservative traps that are also able to trap the produced molecules. As was shown in an experiment dealing with ^{40}K and ^{87}Rb [65], an obstacle is present due to an exothermic chemical reaction between the molecules $2\,(^{40}K^{87}Rb) \rightarrow {}^{40}K_2 + {}^{87}Rb_2$. However, these reactive collisions can be suppressed in a careful adjusted 3D optical lattice and long lived molecules with a lifetime of up to 25 s have been produced [66]. Note that

the listed examples are only a tiny fraction of the countless experimental progresses in the research area of producing ultracold ground state molecules.

Previous work on Rb-Yb at the university of Düsseldorf

The experiment dealing with mixtures of ultracold Rb and Yb in the group of Prof. A. Görlitz was set up at the university of Düsseldorf in 2004. Since then, a variety of experiments with Rb and Yb have been carried out that provided comprehensive information on the interaction between the two elements. Thermalization experiments in a conservative trap gained first insights in the interspecies scattering cross section of several isotopic combinations [5, 6] and hence the interspecies s-wave scattering length. A striking behavior was measured in a mixture of ^{87}Rb and ^{170}Yb which was characterized by a very low interspecies interaction. This suggested an s-wave scattering length close to zero. The observation of an immediate thermalization between ^{87}Rb and ^{174}Yb with following spatial separation [10] indicated a large and positive scattering length. With that information the scattering lengths for any other isotopic combination could be approximated [67].
Furthermore, 1-photon [1] and 2-photon photoassociation experiments [8, 3] in a combined magneto-optical trap have paved the way for reaching the molecular rovibronic ground state in RbYb. These experiments provided spectroscopically the binding energy of weakly bound vibrational states in the molecular excited and ground state that consequently determined the long-range behaviour of the interaction potentials. The measurements were repeated for different isotopes, namely ^{87}Rb with ^{170}Yb, ^{172}Yb, ^{174}Yb and ^{176}Yb.

Outline of this thesis

In this thesis the next step aiming ultracold RbYb molecules and their subsequent manipulation was realized. Previous photoassociation experiments were performed in a combined magneto-optical trap and the produced molecules were simply lost after detection. Since RbYb molecules possess a magnetic as well as an electric dipole moment, they can be also trapped either magnetically or optically. In the course of this thesis work, photoassociation in a hybrid conservative trap was realized which in principle could also hold RbYb molecules. In addition, 1-photon photoassociation spectroscopy has been expanded reaching the vibrational level $\Delta v' = -28$ of the excited state in a hybrid conservative trap. Besides, a search for the theoretically predicted magnetic Feshbach resonances in RbYb was performed and previously obtained 2-photon photoassociation data was reanalyzed enabling a comprehensive theoretical modelling of interaction properties between various Yb and Rb isotopes.
In chapter 2 the theoretical background needed to understand the experiments and the experimental results is presented. After describing the basic ingredients of the hybrid conservative trap, a basic understanding of quantum scattering processes and their connection to molecular theory is given. The chapter ends by depicting the basic idea behind photoassociation spectroscopy and Feshbach resonances. Chapter 3 describes the experimental apparatus with a focus on the implemented laser systems. It is followed by a characterization of Rb and Yb in the different types of combined conservative traps used within this

work in chapter 4. Chapter 5 is dedicated to the experimental results achieved by means of 1-photon photoassociation in the hybrid conservative trap. The main results are composed of the photoassociation spectra and the hyperfine interaction in the excited molecular state. In chapter 6, I will briefly review the 2-photon photoassociation spectroscopy that served as a basis for precise modelling of the ground state potential. The search for magnetic Feshbach resonances in RbYb will be demonstrated in chapter 7, including also analysis of Rb_2 resonances. Finally, an outlook concerning future experiments will be given in chapter 8.

2

Theoretical background

This chapter describes the theoretical background needed to understand and characterize the experiments performed within this thesis. It begins by explaining the basic principles of trapping of ultracold rubidium and ytterbium atoms (sec. 2.1 and sec. 2.2). Section 2.3 will review the basics of a scattering process whose connection to molecular theory will be outlined in the following section sec. 2.4. Sections 2.6 and 2.7 put emphasis on the vibration and rotation of molecules. Main focus of attention is paid on the production of molecules by means of photoassociation (sec. 2.8 and sec. 2.9) together with the description of physical properties and experimental characterization in this context. Finally, the basic relations for magnetic Feshbach resonances will be repeated (sec. 2.10) that might be observable in RbYb due to the interesting hyperfine interaction which will be illustrated in sec. 2.11.

2.1 Optical dipole trap

This section will mainly follow the description of [68] which has already been summarized in [5, 6]. The ability of trapping atoms in an optical dipole potential (ODT) [69, 68] arises from their interaction with the intensity gradient of a far detuned light field $\vec{E}(\vec{r},t)$ known as the AC Stark effect [70, 71, 72]. If an atom is exposed to such an electric field usually created by laser light, it experiences an induced dipole moment

$$\vec{d}(\vec{r},t) = \alpha(\omega_{\mathrm{L}})\vec{E}(\vec{r},t) \tag{2.1}$$

with the complex atomic polarizability $\alpha(\omega_{\mathrm{L}})$, which in turn depends on the driving frequency ω_{L} of the laser light. The interaction between this dipole moment and the driving field leads on the one hand to the optical dipole potential [68]

$$U_{\mathrm{dip}}(\vec{r}) = -\frac{1}{2}\left\langle \vec{d}\cdot\vec{E}(\vec{r},t)\right\rangle = -\frac{1}{2\varepsilon_0 c}\mathrm{Re}\left(\alpha(\omega_{\mathrm{L}})\right) I(\vec{r}) \tag{2.2}$$

where the $\langle..\rangle$ brackets imply the time average over the fast oscillations. It depends on the real part of the atomic polarizability $\mathrm{Re}(\alpha(\omega_{\mathrm{L}}))$ and a spatially varying intensity of the light field $I(\vec{r}) = 2\varepsilon_0 c|\vec{E}(\vec{r})|^2$. On the other hand the laser light field induces photon scattering at a rate given by [68]

$$\Gamma_{\mathrm{sc}} = \frac{1}{\hbar\varepsilon_0 c}\mathrm{Im}(\alpha(\omega_{\mathrm{L}}))I(\vec{r}) \tag{2.3}$$

with the imaginary part $\mathrm{Im}(\alpha(\omega_\mathrm{L}))$ of the polarizability. The dipole force acting on atoms in such a laser field results from the gradient of the dipole potential

$$\vec{F}_\mathrm{dip}(\vec{r}) = -\nabla U_\mathrm{dip}(\vec{r}) = \frac{1}{2\varepsilon_0 c}\mathrm{Re}(\alpha(\omega_\mathrm{L}))\nabla I(\vec{r}) \tag{2.4}$$

and reveals to be a conservative force. Following [68] the complex polarizability can be calculated as a result of a Lorentz's model of a classical oscillator that can be transferred to the situation of a two-level system:

$$\alpha(\omega_\mathrm{L}) = 6\pi\varepsilon_0 c^3 \frac{\gamma/\omega_0^2}{\omega_0^2 - \omega_\mathrm{L}^2 - i\left(\omega_\mathrm{L}^3/\omega_0^2\right)\gamma}\,. \tag{2.5}$$

Here, ω_0 denotes the atomic transition frequency and γ the spontaneous decay rate of the excited state. It is worth noting that this classical derivation is a good approximation of the quantum-mechanical oscillator for large detunings $|\delta| = |\omega_\mathrm{L} - \omega_0|$ and small scattering rates $\Gamma_\mathrm{sc} \ll \gamma$. In a multi-level system, which is the case for real atoms, the total dipole potential and scattering rate is obtained by summing over all contributing transitions i

$$U_\mathrm{dip}(\vec{r}) = \sum_i -\frac{3\pi c^2}{2\omega_{0i}^3}\left(\frac{\gamma_i}{\omega_{0i} - \omega_\mathrm{L}} + \frac{\gamma_i}{\omega_{0i} + \omega_\mathrm{L}}\right) I(\vec{r}) \tag{2.6}$$

$$\Gamma_\mathrm{sc}(\vec{r}) = \sum_i \frac{3\pi c^2}{2\hbar\omega_{0i}^3}\left(\frac{\omega_\mathrm{L}}{\omega_{0i}}\right)^3 \left(\frac{\gamma_i}{\omega_{0i} - \omega_\mathrm{L}} + \frac{\gamma_i}{\omega_{0i} + \omega_\mathrm{L}}\right)^2 I(\vec{r})\,. \tag{2.7}$$

As a result, the sign of the dipole potential is basically defined by the detuning $\delta = \omega_\mathrm{L} - \omega_0$ with respect to the dominant transition. For red detunings ($\delta < 0$) the atoms can be trapped in intensity maxima. In the case of blue detunings ($\delta > 0$) the intensity maxima create repulsive potentials.

A helpful approximation that provides simplified equations is the *rotating-wave-approximation* [68]. It is valid for small detunings $|\delta| \ll \omega_0$ which makes the last term in eq. 2.6 and eq. 2.7 negligibly small. Consequently, the dipole potential is proportional to I/δ while the scattering rate scales as I/δ^2. Thus, optical dipole potentials are typically operated with large detunings and high intensities. However within this thesis, far-off resonance traps (ODT_{1064}, see sec. 3.2.5) as well as a near-resonant trap (still „far-off resonance“ as considered here) (ODT_{556}, see sec. 3.2.4) are utilized.

Optical dipole traps created by Gaussian laser beams

The simplest form of an optical dipole potential, which was and is also used in all of our experiments, is achieved by focussing a red-detuned Gaussian laser beam with a wavelength of λ to a waist w_0 [73]. This beam propagating in z-direction has consequently a shape according to

$$w(z) = w_0\sqrt{1 + \left(\frac{z}{z_\mathrm{R}}\right)^2}\,, \tag{2.8}$$

where $z_\mathrm{R} = \pi w_0^2/\lambda$ denotes the *Rayleigh range*. With the laser power P this leads to a spatially varying intensity

$$I(r,z) = \frac{2P}{\pi w^2(z)} \exp\left(-\frac{2r^2}{w^2(z)}\right) \tag{2.9}$$

along the radial r and axial z direction. The maximum intensity at the position of the waist is given by

$$I(r=0,z=0) = I_0 = \frac{2P}{\pi w_0^2}\,. \tag{2.10}$$

Summarizing equations 2.6, 2.8 and 2.9 this leads to a dipole potential of

$$U_\mathrm{dip}(r,z) = U_0 \frac{1}{1-\left(z/z_\mathrm{R}\right)^2} \exp\left(-\frac{2r^2}{w_0^2\left(1+\left(z/z_\mathrm{R}\right)^2\right)}\right)\,. \tag{2.11}$$

The magnitude

$$U_0 = U_\mathrm{dip}(0,0) = \sum_i -\frac{3\pi c^2}{2\omega_{0i}^3}\left(\frac{\gamma_i}{\omega_{0i}-\omega_\mathrm{L}} + \frac{\gamma_i}{\omega_{0i}+\omega_\mathrm{L}}\right) I_0 \tag{2.12}$$

defines the *trap depth* of the dipole potential. Figure 2.1 illustrates an example modeled potential for ytterbium using eq. 2.12.

A useful approximation that simplifies the characterization of the trapping potential is given by the harmonic approximation [5, 6]

$$U_\mathrm{ODT,harm}(r,z) = -U_0\left(1 - 2\left(\frac{r}{w_0}\right)^2 - \left(\frac{z}{z_\mathrm{R}}\right)^2\right)\,. \tag{2.13}$$

It is valid for small displacements inside the trap which is underlined in fig. 2.1 (b) and (c). The blue curves display the harmonic approximation to the optical dipole potential (red curves) in radial and axial directions. Consequently, the trapping frequencies are then given by

$$\omega_r = \sqrt{\frac{4U_0}{m w_0^2}} \qquad \text{and} \qquad \omega_z = \sqrt{\frac{2U_0}{m z_\mathrm{R}^2}}\,. \tag{2.14}$$

For an atomic cloud with a temperature $T \ll U_0/k_\mathrm{B}$ trapped in such a potential, the trapping frequencies determine the $1/e^2$-widths of the trapped atomic cloud given by [5, 6]

$$\sigma_r = \sqrt{\frac{w_0^2 k_\mathrm{B} T}{4U_0}} = \frac{1}{\omega_r}\sqrt{\frac{k_\mathrm{B}T}{m}} \qquad \text{and} \qquad \sigma_z = \sqrt{\frac{z_\mathrm{R}^2 k_\mathrm{B} T}{2U_0}} = \frac{1}{\omega_z}\sqrt{\frac{k_\mathrm{B}T}{m}}\,. \tag{2.15}$$

Assuming a Gaussian density distribution of the thermal atomic cloud

$$n_\mathrm{ODT}(\vec{r}) = n_0 \exp\left(-\frac{r^2}{2\sigma_r^2} - \frac{z^2}{2\sigma_z^2}\right)\,, \tag{2.16}$$

which holds for the harmonic approximation, this leads with the atom number N to the peak density

$$n_0 = \frac{N}{(2\pi)^{3/2}\,\sigma_r^2 \sigma_z}\,. \tag{2.17}$$

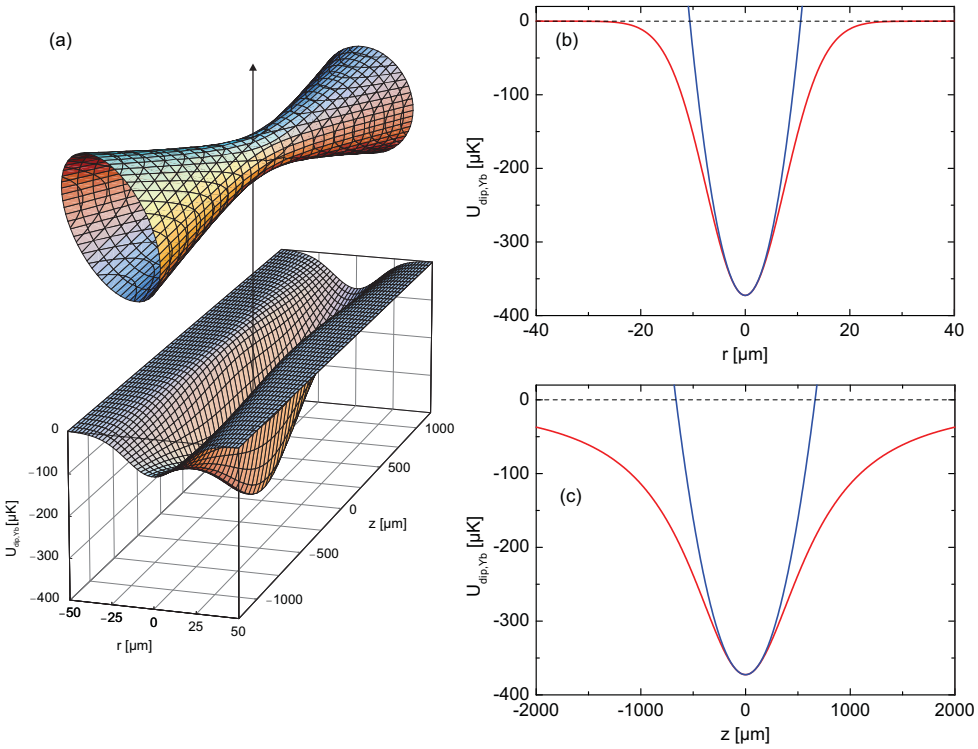

Figure 2.1: *Modeled optical dipole potential for ytterbium created by a red detuned focussed Gaussian laser beam with $\lambda = 1064\,\mathrm{nm}$, $P = 4\,W$ and $w_0 = 15\,\mu\mathrm{m}$. (a) 2D cross section of the 3-dimensional optical potential in radial and axial direction (bottom) and indication of the corresponding Gaussian laser beam (top) (from [6]). This potential is compared in radial (b) and axial (c) direction (red curves) with the harmonic approximation $U_{\mathrm{ODT,harm}}$ (blue curves) and emphasizes the validity for small displacements of the atomic cloud inside the trap.*

Heating in an optical dipole trap

The other important property of a dipole trap is heating of the atomic sample caused by scattered photons with a recoil energy of

$$E_{\mathrm{R}} = \frac{\hbar^2 k^2}{2m} \tag{2.18}$$

at a rate given by eq. 2.7. By summing over all contributions i, this leads to a heating rate in the focus of [68]

$$\begin{aligned} \dot{T}_{\mathrm{heat}} &= \frac{1}{3}\sum_i \frac{2\,E_{\mathrm{R}}}{k_{\mathrm{B}}} \langle \Gamma_{\mathrm{sc}} \rangle_i \\ &= \frac{1}{3}\sum_i \frac{\hbar^2 k^2}{k_{\mathrm{B}} m} \frac{3\pi c^2}{2\hbar\omega_{0i}^3} \left(\frac{\omega_{\mathrm{L}}}{\omega_{0i}}\right)^3 \left(\frac{\gamma_i}{\omega_{0i}-\omega_{\mathrm{L}}} + \frac{\gamma_i}{\omega_{0i}+\omega_{\mathrm{L}}}\right)^2 \frac{2P}{\pi w_0^2}\,, \end{aligned} \tag{2.19}$$

which is equivalent to an increase of temperature of the atomic sample with time.

2.2 Magnetic trap

Contrary to the optical dipole trap which can be applied in principle to every atomic species, only atoms with a magnetic moment can be magnetically trapped. Rubidium exhibits a magnetic moment and is therefore conveniently trapped magnetically while ytterbium can only be trapped optically due to a lack of magnetic moment in the ground state. The trapping potential arises from the interaction of the state-dependent magnetic dipole moment with an inhomogeneous external magnetic field [74, 75]. The magnetic trap (MT) in our experiment is a *Ioffe-Pritchard-trap* [76] with coils arranged in a clover-leaf configuration [77] (see sec. 3.1). It was already described in detail in [4, 5, 6] and therefore only the crucial properties that are necessary for basic understanding will be repeated here. An atom with a magnetic moment $\vec{\mu}$ in an external (weak) magnetic field $\vec{B}$ experiences the energetic shift

$$\Delta E = -\vec{\mu} \cdot \vec{B} = -\mu_\mathrm{z} B_\mathrm{z} = g_F \, m_F \, \mu_\mathrm{B} \, B_\mathrm{z} \,, \tag{2.20}$$

with the state dependent hyperfine Landé factor g_F and the Bohr magneton μ_B. The last equation holds, if the energetic shift is small with respect to the hyperfine splitting (see sec. 3.2.1 for the hyperfine splitting in rubidium). The orientation of $\vec{B}$ determines the z-axis with $|\vec{B}| = B_\mathrm{z}$ which in turn is the quantization axis of the magnetic projection m_F of the atom with the total angular momentum F. In order to magnetically trap the atoms one has to apply a magnetic field $\vec{B}(\vec{r})$ with a spatial potential minimum. Since magnetic field maxima are not allowed following Maxwell's equations [78] only atomic states with $g_F \, m_F > 0$ can be trapped. These states are called *low field seeker* and hence *high field seeker* with $g_F \, m_F < 0$ as well as states with $m_F = 0$ cannot be captured with a static magnetic field.

The simplest form of a magnetic field that is often used to confine atoms is a quadrupole field [79, 74]. One drawback of this configuration is the zero field in the center of the trap. If the magnitude of the magnetic field is close to zero the atomic quantization axis may be lost and *Majorana spin flips* [80] to untrappable states can be induced. Therefore in our experiment, a *Ioffe-Pritchard-trap* [76] is implemented. It was already used in our previous works and details on its experimental implementation and characterization can be found in [4, 5, 6]. In order to guarantee stable operation, the magnetic field is composed of a magnetic offset field B_0, a radial magnetic field gradient B' and an axial magnetic field curvature B'' [75]:

$$\vec{B}(\vec{r}) = B_0 \begin{pmatrix} 0 \\ 0 \\ 1 \end{pmatrix} + B' \begin{pmatrix} x \\ -y \\ 0 \end{pmatrix} + \frac{B''}{2} \begin{pmatrix} -xz \\ -yz \\ z^2 - \frac{1}{2}(x^2 + y^2) \end{pmatrix} . \tag{2.21}$$

This magnetic field is created by coils in a clover-leaf-configuration [77] (see fig. 3.2) leading to a potential of the following form [4]:

$$U_\mathrm{MT}(\vec{r}) = \mu |\vec{B}(\vec{r})| = \tag{2.22}$$

$$\mu \sqrt{\left(B_0 + \frac{B''}{4} \left(2z^2 - x^2 - y^2 \right) \right)^2 + \left(B' y + \frac{B''}{2} yz \right)^2 + \left(B' x - \frac{B''}{2} xz \right)^2} .$$

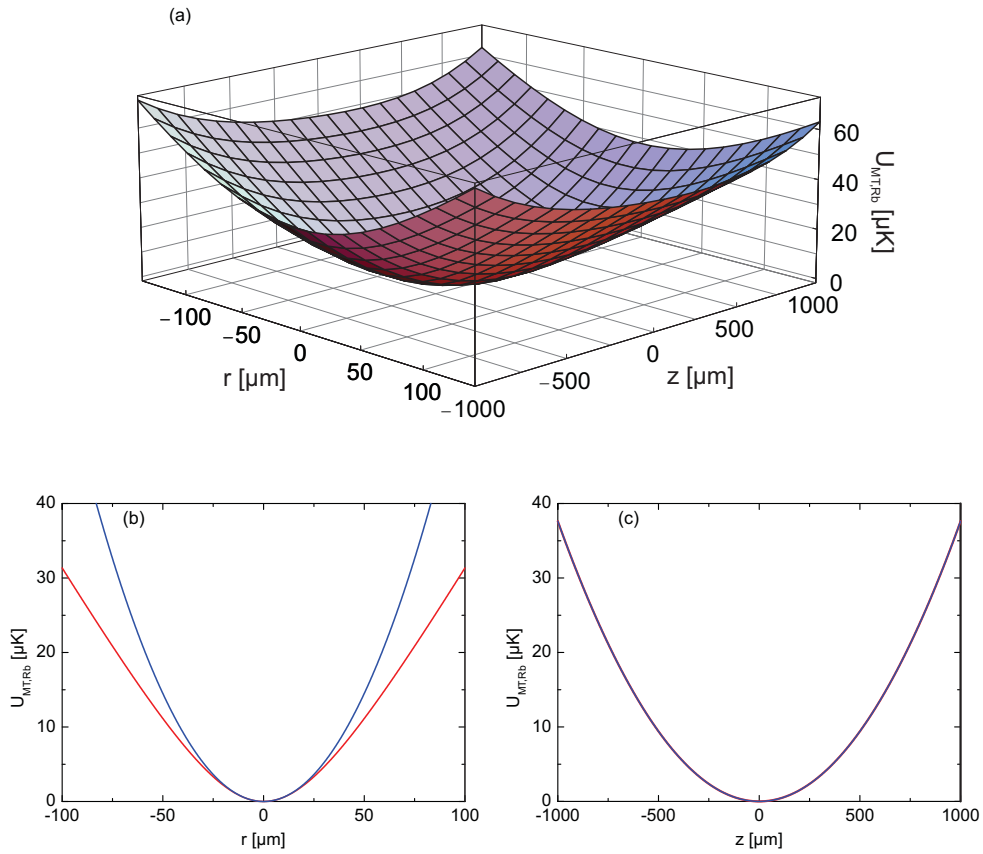

Figure 2.2: *Magnetic trapping potential for ^{87}Rb in the $|F = 1, m_F = -1\rangle$ state with $B_0 = 550\,\mathrm{mG}$, $B' = 133\,\mathrm{G/cm}$ and $B'' = 231\,\mathrm{G/cm^2}$. (a) 2D cross section of the 3D magnetic potential for Rb in radial and axial direction. The potential is compared in radial (b) and axial (c) direction (red curves) with the harmonic approximation $U_{\mathrm{MT,harm}}$ (blue curves). The potential in z-direction is already in its original form harmonic and the two curves overlap.*

Similar to the case of an ODT, the characterization of the trap is simplified by a harmonic approximation of the trapping potential:

$$U_{\mathrm{MT,harm}}(\vec{r}) = \frac{\mu}{2}\left[\left(\frac{B'^2}{B_0} - \frac{B''}{2}\right)(x^2 + y^2) + B'' z^2\right], \tag{2.23}$$

which is valid for small thermal energies of the atomic samples. The magnetic potential for ^{87}Rb in the $|F = 1, m_F = -1\rangle$ state, that is part of the hybrid conservative trap (see sec. 4.1.3), is depicted in fig. 2.2 and compared to the harmonic approximation. The radial (fig. 2.2 (b)) and axial (fig. 2.2 (c)) cuts through the magnetic potential (red curves) show the good agreement with the harmonic approximation (blue curves).
As a consequence, the potential can be characterized by the harmonic trapping frequencies

$$\omega_x = \omega_y = \sqrt{\frac{\mu}{m}\left(\frac{B'^2}{B_0} - \frac{B''}{2}\right)} \qquad \text{and} \qquad \omega_z = \sqrt{\frac{\mu}{m}B''}\,. \tag{2.24}$$

Assuming a Gaussian density distribution [81]

$$n_{\mathrm{MT,harm}}(\vec{r}) = n_0 \exp\left(-\frac{U_{\mathrm{harm}}(\vec{r})}{k_{\mathrm{B}}T}\right) = n_0 \exp\left(-\frac{x^2}{2\sigma_x^2} - \frac{y^2}{2\sigma_y^2} - \frac{z^2}{2\sigma_z^2}\right), \tag{2.25}$$

which is present in the basis of the harmonic approximation, the trap frequencies from eq. 2.24 are related to the $1/\sqrt{e}$-widths of an atomic cloud with a temperature T are given by

$$\sigma_x = \sigma_y = \sqrt{\frac{k_{\mathrm{B}}T}{\mu\left(\frac{B'^2}{B_0} - \frac{B''}{2}\right)}} = \frac{1}{\omega_x}\sqrt{\frac{k_{\mathrm{B}}T}{m}} \quad \text{and} \quad \sigma_z = \sqrt{\frac{k_{\mathrm{B}}T}{\mu B''}} = \frac{1}{\omega_z}\sqrt{\frac{k_{\mathrm{B}}T}{m}}. \tag{2.26}$$

This in turn yields with the atom number N a peak density of the atomic cloud of

$$n_{\mathrm{MT,harm}}(\vec{0}) = n_0 = \frac{N}{(2\pi)^{3/2}\,\sigma_x\sigma_y\sigma_z}. \tag{2.27}$$

2.3 Scattering theory

This section will briefly summarize the basic concepts behind a collision process between two quantum particles and highlight the main connections to ultracold molecular physics. Such a collision is the basis for molecule production by using photoassociation or Feshbach resonances and hence the description is needed for their understanding. It is written on the basis of [82, 83, 84, 85] in which further details can be found.
Two particles with masses m_1 and m_2 interact via the scalar potential $V(r_1, r_2)$. Moving into the center of mass frame this two-particle problem can be treated as a single-particle problem with the reduced mass $\mu = \frac{m_1 \cdot m_2}{m_1 + m_2}$ and the separation of both particles $r = r_2 - r_1$. The relative motion can then be described using the relative wavevector $\vec{k}$ which is equivalent to the relative velocity $\vec{v}$ or momentum $\vec{p} = \hbar\vec{k}$. A sketch of the scattering

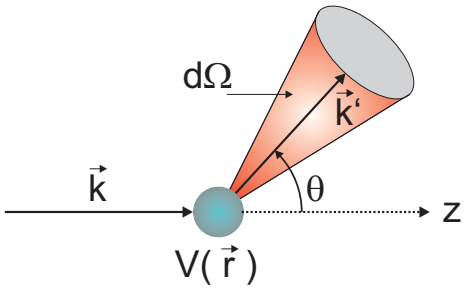

Figure 2.3: *Schematic illustration of a scattering process (following [86]). The relative wavevector $\vec{k}$ of the particle motion is scattered from the potential $V(\vec{r})$ into the solid angle $d\Omega$.*

process is shown in fig. 2.3. Treating the relative motion of the particles as an incoming wavefuntion $\psi(\vec{r})$, its scattering at the potential $V(\vec{r})$ is described by the time independent Schrödinger equation [87, 88]

$$\left(\frac{\hat{\vec{p}}^2}{2\mu} + V(\vec{r})\right)\psi(\vec{r}) = E\psi(\vec{r})\,. \tag{2.28}$$

$\psi(\vec{r})$ is composed of an incident plane wave ϕ_{in} and a scattered spherical wave ϕ_{out}

$$\psi(\vec{r}) \propto \phi_{\text{in}} + \phi_{\text{out}} = e^{-i\vec{k}\vec{r}} + f(k,\theta)\frac{e^{ikr}}{r}\,. \tag{2.29}$$

The angle dependent scattering amplitude $f(k,\theta)$ is connected to the differential scattering cross section via

$$\frac{d\sigma(k,\theta)}{d\Omega} = |f(k,\theta)|^2\,. \tag{2.30}$$

It describes the number of scattered particles dn per unit time and incident particle flux F_i into the solid angle $d\Omega$

$$\frac{d\sigma(k,\theta)}{d\Omega} = \frac{dn}{d\Omega \cdot F_i}\,. \tag{2.31}$$

Consequently, the total scattering cross section $\sigma(k)$ is obtained from

$$\sigma(k) = \int |f(k,\theta)|^2\, d\Omega\,, \tag{2.32}$$

which corresponds to an effective area of the particles in a collision process. In order to simplify calculations, $\psi(\vec{r})$ can be expanded in partial waves, each having an angular momentum ℓ

$$\psi(\vec{r}) = \sum_{\ell=0}^{\infty} \frac{u_\ell(r)}{r} P_\ell(\cos\theta)\,. \tag{2.33}$$

Here, $P_\ell(\cos\theta)$ are the Legendre polynomials and $u_\ell(r)$ the radial wavefunctions. This leads to a differential equation for the radial wave function of the following form:

$$-\frac{\hbar^2}{2\mu}\frac{d^2u_\ell(r)}{dr^2} + \left(-E + V(r) + \frac{\hbar^2\ell(\ell+1)}{2\mu r^2}\right)u_\ell(r) = 0\,. \tag{2.34}$$

A detailed discussion on the last term which denotes the centrifugal energy of a specific partial wave ℓ can be found in sec. 2.7. After some derivations (see e.g. [87]) the scattering amplitude can be approximated as

$$f(k,\theta) = \frac{1}{2ik}\sum_\ell (2\ell+1)\left(e^{2i\delta_\ell(k)} - 1\right)P_\ell(\cos\theta) \tag{2.35}$$

which yields the total cross section $\sigma(k)$ as a sum over each partial wave cross section $\sigma_\ell(k)$

$$\sigma(k) = \sum_\ell \sigma_\ell(k) = \frac{4\pi}{k^2}\sum_\ell (2\ell+1)\sin^2\delta_\ell(k)\,. \tag{2.36}$$

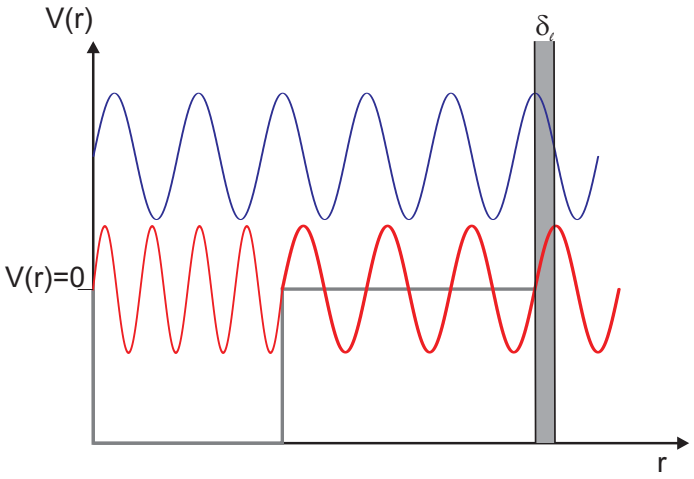

Figure 2.4: *Schematic demonstration of the scattering phase $\delta_\ell(k)$ using the example of a square-well potential. The wavefunctions of the unbound state (blue) and the bound state (red) differ in the region where $V(r) = 0$ only by the collisional phase shift δ_ℓ.*

The role of the collisional phase shift $\delta_\ell(k)$ [89] is depicted in fig. 2.4 using the example of a simple square well potential. It shows the phase shift between an unbound wavefunction and the bound wavefunction in the unbound region ($V(r) = 0$). This scattering phase $\delta_\ell(k)$ describes the collision process for each partial wave ℓ in the far field.
In the case of the so-called *unitarity limit*, in which $\sin^2(\delta_\ell) = 1$, the maximum contribution of the ℓ-th partial wave to the total cross section yields

$$\sigma_\ell = 4\pi(2\ell + 1)/k^2 \,. \tag{2.37}$$

If the collision energy E is small compared to the centrifugal energy (see sec. 2.7 and eq. 2.51), the sum can be truncated at a value $\ell_{\max}$. In the limit of very low energy collisions ($k_0 \to 0$) only the lowest partial wave contributes to the collision due to the rotational energy barrier (see fig. 2.9) and purely s-wave scattering with only $\ell = 0$ can be assumed. This yields a simplified scattering cross section of

$$\sigma_0(k) = \frac{4\pi}{k^2} \sin^2 \delta_0(k) \,. \tag{2.38}$$

Taking the Wigner threshold law into account [84], which holds in the case of $k \to 0$ [90], and defining the scattering length a as

$$a = -\lim_{k\to 0} \frac{\tan \delta_0(k)}{k} \tag{2.39}$$

the scattering phase reduces to

$$\delta_0(k) \approx -ka \,. \tag{2.40}$$

As a result the s-wave scattering cross section σ_0 for distinguishable particles is given by

$$\sigma_0 = 4\pi a^2 \tag{2.41}$$

and is to first order independent of the collision energy.
Therefore, the collision behaviour of an ultracold atomic or molecular ensemble can be summarized in the quantity of this crucial s-wave scattering length a. The elastic scattering cross section σ_0 is proportional to the square of the scattering length and characterizes the magnitude of „good“ collisions that are necessary for thermalization processes. The scattering length a can be positive or negative which determines the sign of the interaction potential which will be repulsive or attractive, respectively. This is relevant for the theory of an interacting Bose-gas [91]. The absolute value denotes accordingly the magnitude of this interaction. As a result, it determines the characteristic behaviour of ultracold quantum gases [92].

2.4 Basic molecular theory

As was already mentioned, the collisional properties of particles at low energies are determined by the scattering length a (sec. 2.3). The value of the scattering length is closely related to the interatomic interaction potential of the involved atoms. This section will give further details on this connection extending the explanation from [1, 3] and show how experimental techniques can be used to gain information on the scattering length and the interaction potential, respectively.
The interaction between two colliding atoms forming a molecule is very complex. Only the simplest form which consists of the H_2^+-molecule can be solved analytically [87]. The difficulty in calculating the interaction grows with increasing size of the molecule. In general, a Schrödinger equation of the form of equation 2.28 has to be solved, where the solutions with eigenenergies $E < 0$ are the molecular bound states. Several approximations can be done to simplify the solution. The Born Oppenheimer approximation [87, 93] consists in separating the electronic and nuclear part of the wavefunction. Since the electrons move much faster than the nuclei, it is assumed that the electronic wavefunction adapts instantaneously to the position of the nuclei. Further approximations and procedures can be performed according to the properties of the present system but will not be repeated here [93]. Nevertheless, the complexity of many interacting electrons and the atomic nuclei prevents the solution to be extracted analytically.
In the case of a rubidium-ytterbium molecule there are 37 electrons contributed by Rb and 70 electrons by Yb, respectively. This is already a complex molecule from a physicist's point of view. First ab initio calculations were performed by Sørensen et al. [94] and are shown in fig. 2.5. They used four-component coupled cluster calculations in order to model the molecular ground state potential and several excited molecular potentials. Although the results cannot give a full quantitative description, they give a good qualitative understanding of the interaction potential. The interaction region can roughly be divided into two parts separated around the internuclear distance for which the dominating interaction fluently switches from molecular to atom-atom behavior. At this internuclear distance the potential energy becomes comparable to the hyperfine interaction. In the case of alkali metal atoms, this distance is $\approx 20\,a_0$ [95]. On the one hand there is the inner region of the

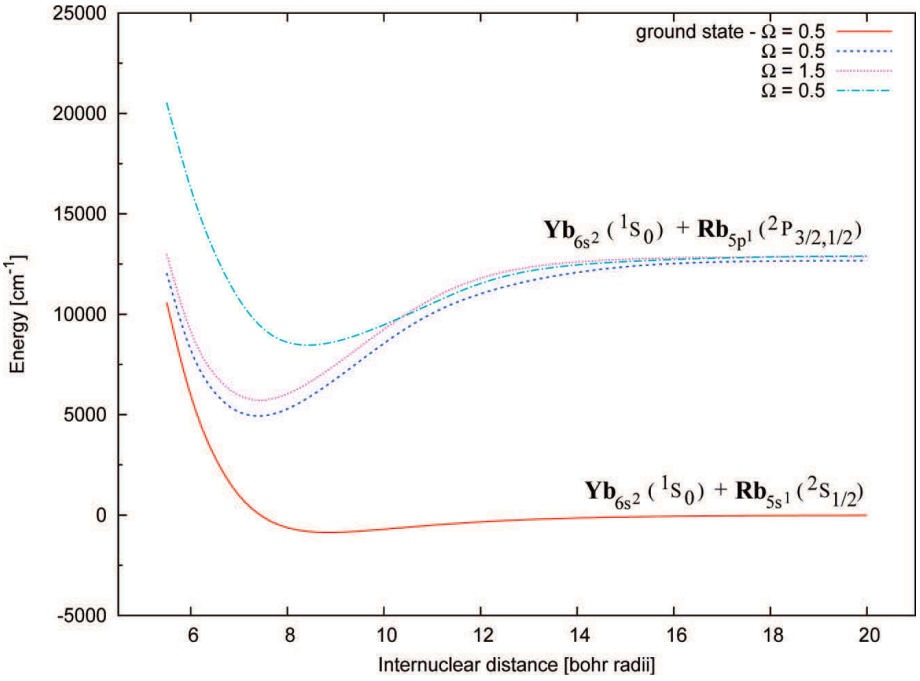

Figure 2.5: *Energy curves of the four lowest molecular electronic states of RbYb calculated by ab-initio methods by Sørensen et al. [94]. The atomic dissociation channels are labeled as well as the molecular potentials identified by* Ω.

potential in which the electron clouds of the atoms overlap and strong distortion results. Pauli's exclusion principle gives rise to a repulsion of the clouds if the valence electrons are in the same electronic and spin state. Otherwise it follows a strong attractive interaction potential except for very small distances where a strong electron-exchange repulsion and the repulsion of the nuclei dominates. As a consequence, a potential well is produced whose minimum is referred to as *potential depth* D_e and its internuclear separation as *equilibrium distance* R_e. As we will see later on, this potential depth is decisive for the sign and value of the scattering length a.

For large internuclear separations on the other hand the overlap of the electron clouds can be neglected and the attractive interaction arises from resonant or induced multipole moments. In general, ab-initio calculations are precise in the short-range but lose accuracy while approaching the long range part of the potential. A simple approximation of the long-range interaction potential is given by [96]

$$V(r) = E_D + \sum_n \frac{C_n}{r^n}\,, \tag{2.42}$$

with the dissociation limit E_D. Depending on the atoms and their states involved in the collision, the order n of the interaction and the dominant term of the dispersion coefficients C_n may take different values, while in general higher order terms are relatively small and can be neglected. The dominant term for RbYb in the electronic ground state $^2\Sigma_{1/2}$ as well as in the excited state $^2\Pi_{1/2}$ examined in this thesis is the *van der Waals* dispersion

coefficient C_6. The resonant dipole-dipole interaction in the homonuclear case found for instance in excited staes of Na_2 [97] or Rb_2 [98] is well described by a C_3-coefficient due to an allowed dipole-dipole interaction. A C_5-coefficient is dominating for identical atoms colliding in a P-state [99]. A C_4-coefficient appears for collisions between ions and neutral atoms.
Gribakin and Flambaum [100] derived simple analytical formulas to connect the long-range behaviour of the interaction potential characterized by the dispersion coefficient C_n to the scattering length a. For our case, in which the van der Waals term C_6/r^6 is the dominating one, the scattering length can be approximated by

$$a = \bar{a}\left(1 - \tan\left(\Phi - \frac{\pi}{8}\right)\right) , \tag{2.43}$$

where the characteristic mean scattering length

$$\bar{a} = 2^{-\frac{3}{2}} \frac{\Gamma\left(\frac{3}{4}\right)}{\Gamma\left(\frac{5}{4}\right)} \cdot \left(\frac{2\mu C_6}{\hbar^2}\right)^{\frac{1}{4}} \tag{2.44}$$

varies only slowly with the characteristic parameters of the interaction potential and takes the value $\bar{a} = 74.9 \cdot a_0$ for the system $^{87}Rb^{176}Yb$. Here, $\Gamma(x)$ is the Gamma-function and μ again the reduced mass. The semiclassical phase integral [101]

$$\Phi = \frac{\sqrt{2\mu}}{\hbar} \int_{r_{\mathrm{in}}}^{\infty} \sqrt{-V(r)}dr \tag{2.45}$$

is taken from the classical inner turning point r_{in} to infinity. The actual value of the phase integral classifies the number of bound states N supported by the interaction potential

$$N = \lfloor \Phi/\pi + 3/8 \rfloor , \tag{2.46}$$

where the brackets $\lfloor ... \rfloor$ imply to take the integer part of the expression.
Furthermore, there is an important direct link between the scattering length and the binding energy of the last bound vibrational state below the dissociation limit of the following form [102]:

$$E_{-1} = -\frac{\hbar^2}{2\mu a^2} . \tag{2.47}$$

The absolute value of a is the larger the closer the last bound state is located to the dissociation limit.
Due to the tangent function in equation 2.43 the scattering length may take values between $-\infty$ and $+\infty$ depending on the actual value of the phase Φ and if Φ is varied over a range of π as illustrated in fig. 2.6. Since Φ depends on the reduced mass μ of the considered system different isotopic combinations (see fig. 6.7) generally possess different scattering lengths, if the interaction potential is isotope-independent. With each phase shift of π (i.e. for each cycle of the scattering length values) an additional bound state appears in the interaction potential.
In the process of modeling the molecular ground state potential using our two-photon

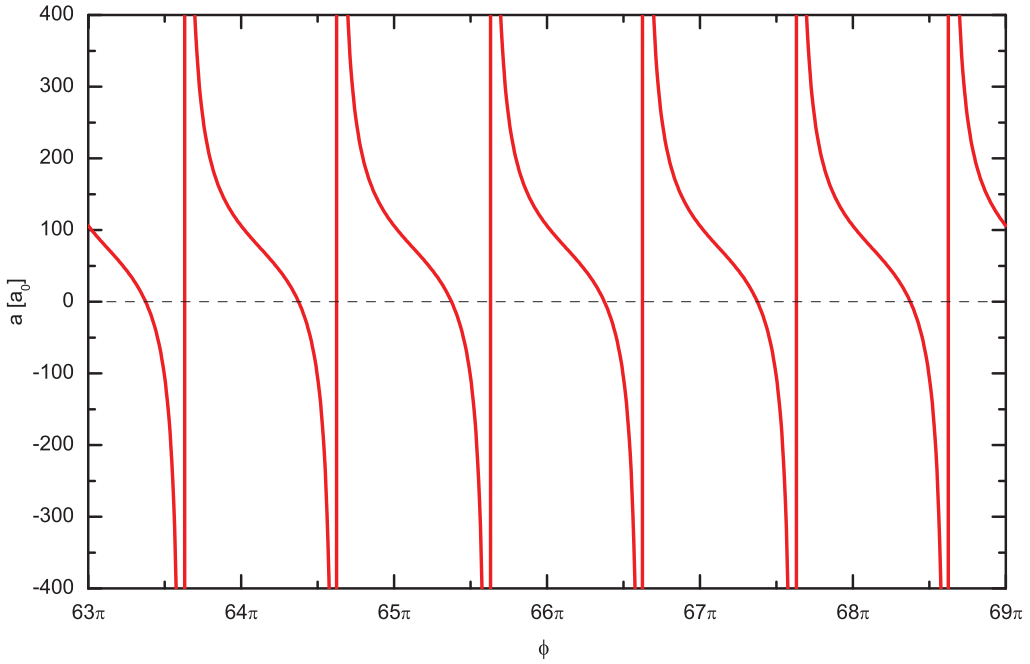

Figure 2.6: *Scattering length as a function of the phase integral* Φ *plotted with a* $C_6 = -2837.2 \cdot E_h a_0^6$ *from [2] for the combination of* $^{87}Rb^{176}Yb$*. A phase of* $\Phi = 65.625 \cdot \pi$ *corresponds to a number of bound states* $N = 66$*. Each augmentation of* Φ *modulo* π *adds an additional bound state to the interaction potential and hence enlarges the potential depth* D_e*.*

photoassociation data in collaboration with a theory group [2], we introduced a uniform, dimensionless scaling parameter λ in order to discuss the sensitivity of the scattering length on the potential for RbYb. The parameter λ scales either the interaction potential or the reduced mass of the system. Then one cycle of scattering length is spanned by [2]

$$\frac{\Delta\lambda}{\lambda} \approx \frac{2}{N}\,, \tag{2.48}$$

which is achieved by a change of only 3% in the depth of the interaction potential and shows a strong sensitivity of the last bound state to the potential well depth.
That is why ab initio calculations additionally to being utterly demanding can usually not predict the potential depth and hence the scattering length accurately enough. In order to achieve reliable results, experimental information on the molecular binding energies is needed that can be in turn used to correct the model potential. And this is the point where ultracold collision experiments and especially photoassociation experiments come into play [103, 104]. Photoassociation experiments probe due to its nature in general the vibrational states close to the dissociation limit and may yield information about the binding energy of the last bound state [46]. Chapter 6 presents the results that we achieved while performing 2-photon photoassociation spectroscopy in RbYb [3] and the information that we gained on the molecular potential of the electronic ground state. This data could be utilized by

our colleagues from a theory group [2] in order to model an accurate ground state potential and deduce crucial parameters characterizing the interatomic interaction. In a similar way, scattering lengths of a variety of ultracold atomic mixtures could be determined such as those for all isotopes of ^{x}Yb [105] or for ^{39}K [106].

2.5 Angular momenta and Hund's cases

Like an atom, a molecule exhibits different angular momenta but evidently with a higher complexity. Due to the presence of the second atom a diatomic molecule is cylindrically symmetric around the internuclear axis. Thus, projections of the angular momenta on the internuclear axis become important. The *Hund's cases* [107] describe in which way the occurring angular momenta can be coupled to each other. This section is written on the basis of [108, 88] and also covered in [1, 109, 3] in which the Hund's cases were already summarized.
Real molecules do not necessarily comply with one distinct Hund's case but may be described by a smooth transition between different cases according to the strengths of the couplings. Within one molecule the Hund's case may differ for different electronic states and it may even change from the weakly bound to more strongly bound vibrational levels. Each molecular angular momentum can be specified as following [108, 88]:

- $\vec{\boldsymbol{L}}$ is the electronic orbital angular momentum which is composed of the atomic electronic orbital angular momenta (atoms a and b): $\vec{L} = \vec{l}_a + \vec{l}_b$,
- $\vec{\boldsymbol{S}}$ is the electronic spin angular momentum which is, analogue to $\vec{L}$, composed of the two atomic electronic spin angular momenta: $\vec{S} = \vec{s}_a + \vec{s}_b$,
- $\vec{\boldsymbol{J_a}}$ is the electronic angular momentum that will be formed in the case of strong spin-orbit coupling: $\vec{J}_a = \vec{L} + \vec{S}$,
- $\vec{\boldsymbol{I}}$ is the angular momentum stemming from the nuclear spin,
- $\vec{\boldsymbol{R}}$ is the rotational angular momentum of the nuclei, and it is $\vec{R} = \vec{N} - \vec{L}$,
- $\vec{\boldsymbol{J}}$ is the total angular momentum and implies the electronic momenta as well as the rotational angular momentum: $\vec{J} = \vec{L} + \vec{S} + \vec{R}$,
- $\vec{\boldsymbol{F}}$ is the sum of the total electronic angular momentum and the nuclear spin: $\vec{F} = \vec{J} + \vec{I}$ and
- $\vec{\boldsymbol{N}}$ is defined as the total angular momentum without the electronic spin $\vec{N} = \vec{J} - \vec{S}$.

As already noted the projections of the angular momenta on the internuclear axis are pivotal and in general also good quantum numbers. The projection of $\vec{L}$ and $\vec{S}$ are labelled by the Greek analogue Λ and Σ, respectively. The projection of J_a is defined as Ω. This leads to the naming convention for molecular states

$$^{2S+1}\Lambda^{\pm}_{\Omega_{g/u}}\,.$$

The additional superscript $\pm$ indicates a reflection symmetry of the wavefunction through a plane which contains the internuclear axis. The gerade/ungerade (g/u) parity points out

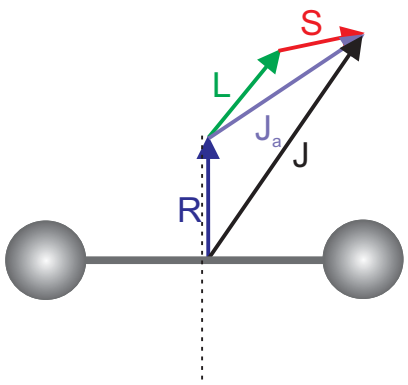

Figure 2.7: *Illustration of Hund's coupling case (e) (adapted from [109, 3]) predominating in the case of weakly bound RbYb molecules in the electronically excited state [1] (see also sec. 5.2).*

the inversion of the electronic wavefunction through the center of charge and is only defined for homonuclear molecules. There are five limiting coupling cases labelled by Hund's case (a)...(e). A description of all Hund's cases can be found in [108, 88, 1, 109, 3]. Figure 2.7 illustrates Hund's case (e) which is relevant for the excited molecular state of RbYb and is the only one that is treated here.

Hund's coupling case (e)

In Hund's coupling case (e) the momenta $\vec{L}$ and $\vec{S}$ couple to each other to form $\vec{J}_a$. Due to a weak coupling to the internuclear axis $\vec{J}_a$ is first coupled to the rotation $\vec{R}$ in order to create the total angular momentum $\vec{J}$. An indication for this situation is the splitting of the rotational levels in $2J_a + 1$ (if $|J_a| < |R|$) respective $2R + 1$ (if $|R| < |J_a|$) sublevels depending on the absolute values of $|J_a|$ and $|R|$. This is the coupling case assigned to be the predominant one for weakly bound RbYb molecules in the electronically excited state [1] as is evident by the appearing rotational substructure in the vibrational states (see also sec. 5.2).
Good quantum numbers: J_a, R, J.

2.6 Molecular vibration

Due to its complexity a molecule has more degrees of freedom compared to a single atom. A diatomic molecule can for example vibrate and rotate, which will be discussed in the following. Here, at first a rotationless molecule is considered. The rotation of the molecule is included in sec. 2.7.
An attractive molecular potential can have several bound states whose wave functions $\psi(r)$ are the solutions of the (numerically solved) Schrödinger equation 2.28. These bound states correspond to *vibrational states* of the molecule in which the nuclei of the atoms vibrate relative to each other around the mean internuclear separation r_{eff}. Figure 2.8 shows

schematically some wavefuntions for the vibrational states.
The number of bound states N is the entity of these vibrational levels of an electronic molecular state. Similar to the case of a harmonic oscillator the vibrational quantum number v describes the number of nodes of the wavefunction. In fact, for low vibrational quantum numbers the molecular potential resembles a harmonic oscillator and consequently the solutions, too. For higher v the vibrational frequencies and hence the vibrational energies deviate from the ones for the harmonic oscillator due the anharmonicity and asymmetry of the molecular potential (see for example [87]). The probability of finding the molecule in a position with the separation r is proportional to the square of the wavefunction $\propto |\psi(r)|^2$. Since the probability amplitude is larger at the classical turning points the lobes of the wavefunction at the outer turning points are emphasized.
The vibrational states accessible to photoassociation spectroscopy are typically the ones close to the dissociation threshold [46]. In order to assign the levels for which the binding energy has been measured, R. J. LeRoy and R. B. Bernstein [96] derived a semi-analytical

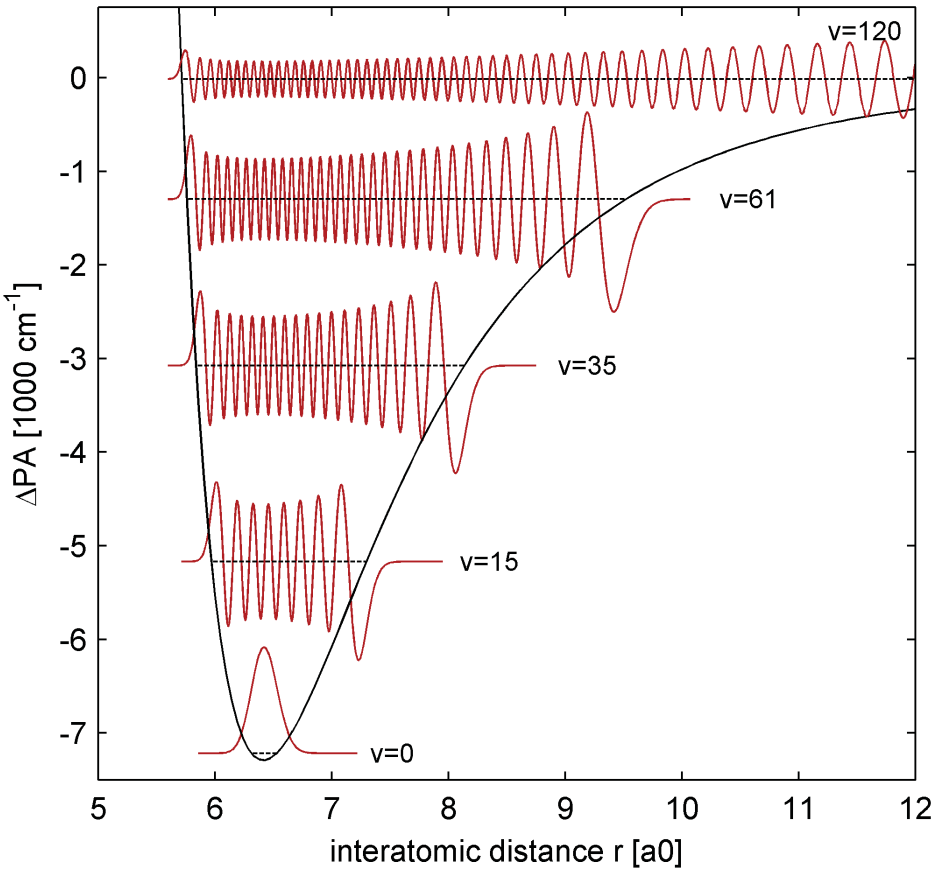

Figure 2.8: *Schematic nuclear wavefunctions in a model molecular potential (taken from [1]). The vibrational quantum number indicates the number of nodes of the wavefunction. A prominent feature are the enlarged lobes close to the classical outer turning points.*

approximation assuming a long range potential of the form $V(r) = E_D + C_n/r^n$ with the dissociation limit E_D and the leading term n analogue to eq. 2.42. It connects the (measured) binding energy E_v to the vibrational level v as follows:

$$E_\mathrm{v} = E_D - \left((\mathrm{v}_D - \mathrm{v}) \cdot \sqrt{\frac{\pi}{2\mu}} \cdot \frac{\Gamma(1+1/n)}{\Gamma(1/2+1/n)} \cdot \frac{\hbar(n-2)}{(-C_n)^{1/n}} \right)^{\frac{2n}{n-2}} . \tag{2.49}$$

Here, $\Gamma(x)$ is again the Gamma function and v_D the non-integer dissociation quantum number whose integer part indicates the maximum vibrational quantum number v_max (i.e. the vibrational quantum number of the last bound state). From the fractional part $\mathrm{v}_\mathrm{frac} = \mathrm{v}_D - \mathrm{v}_\mathrm{max}$ one can in principle qualitatively infer the energy difference of the last bound state to the dissociation threshold and hence the magnitude of the scattering length. The closer v_D gets to zero the closer the last bound state approaches the atomic threshold. In [110] the long-range potentials of heteronuclear molecules have been discussed in detail. Since photoassociation experiments probe the molecular levels starting from top of the interaction potential, it is convenient to define a relative vibrational quantum number $\Delta\mathrm{v} = \mathrm{v} - \mathrm{v}_\mathrm{max}$. Equivalently, the corresponding binding energy Δ_PA (in cm^{-1}) is expressed relative to the atomic threshold E_D (in our case the Rb D_1 line at 795 nm, see sec. 5.1). Following the references [1, 7], eq. 2.49 can be adopted to our situation of RbYb by inserting $n = 6$

$$\Delta_\mathrm{PA}(\Delta\mathrm{v}) \approx 0.163343 \, \frac{h^2}{c^*} \cdot \frac{1}{\sqrt{-C_6}} \cdot \left(\frac{\Delta\mathrm{v} - \mathrm{v}_\mathrm{frac}}{\sqrt{\mu}} \right)^3 , \tag{2.50}$$

where c^* is the speed of light in cm/s and all appearing numerical values have been summarized in the prefactor 0.163343. This equation allows for a deduction of the characteristic C_6-coefficient by fitting it to the experimental data. The approximation works quite well for bound states close to threshold as was already shown in our previous work [7]. However, it suffers from a larger error for states close to the dissociation limit with $E_D - E_v < 10\,\mathrm{GHz}$ [111] and even more for more tightly bound molecules as will be shown in sec. 5.3.3. Some attempts have been made to improve the approximation by including multipole expansion coefficients [111, 112]. This will not repeated here since it does not provide any deeper insight into the physical properties (see also sec. 5.3.3).

2.7 Rotation and centrifugal barrier

The rotation of a molecule adds another term to the potential in the Schrödinger equation (see eq. 2.34) coming from the molecular angular momentum $\vec{R}$ which results in an total potential of

$$V_\mathrm{eff}(r) = V(r) + \frac{\hbar^2 \, R \cdot (R+1)}{2\mu r^2} , \tag{2.51}$$

with the rotational quantum number R. This is the rotational energy of a fixed rotator as will be further described in sec. 5.2. In a collision of ultracold atoms with orbital angular

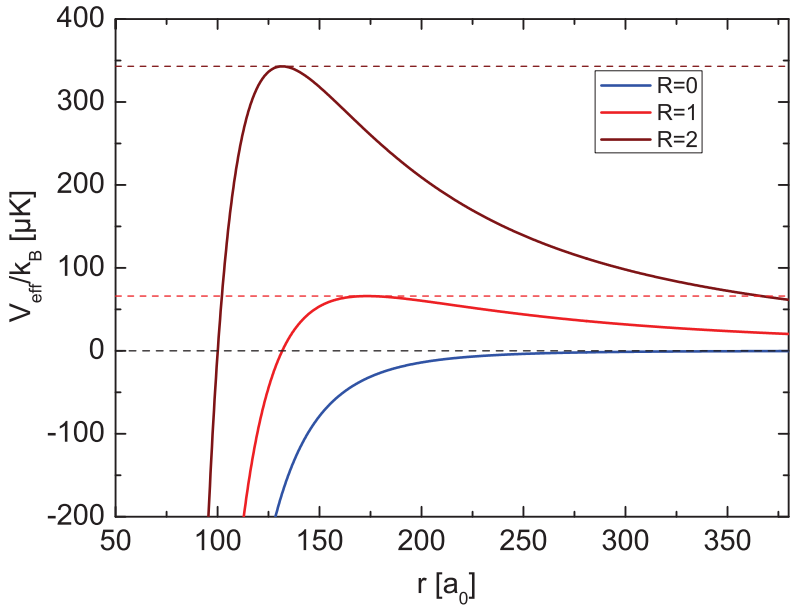

R	T_c [μK]
0	-
1	66
2	343
3	970

Figure 2.9: *Molecular potentials close to the dissociation threshold including the centrifugal potential of the lowest partial waves for collisions of ^{176}Yb and ^{87}Rb using a C_6 of $C_6 = -2837.2\, E_h a_0^6$ from [2]. The blue curve ($R = 0$) does not exhibit any rotational barrier. The height of the rotational barrier is given in μK according to $T_c(R) = E_c(R)/k_B$.*

momentum R this leads to a *centrifugal barrier* with an R-dependent height $E_c(R)$ (see fig. 2.9) given by [46, 5]

$$E_c(R) = \frac{1}{2}\left(\frac{R\cdot(R+1)}{3}\right)^{3/2} E_{\mathrm{vdW}}\,, \tag{2.52}$$

with

$$\begin{aligned} E_{\mathrm{vdW}} &= \frac{\hbar^2}{2\mu}\frac{1}{R_{\mathrm{vdW}}^2} \quad \text{and} \\ R_{\mathrm{vdW}} &= \frac{1}{2}\left(\frac{-2\mu C_6}{\hbar^2}\right)^{1/4}. \end{aligned} \tag{2.53}$$

Here, the values R_{vdW} and E_{vdW} are defined to give useful length and energy scales. R_{vdW} specifies the passage from short-range to long-range in the molecular potential.
In an ultracold collision, the centrifugal barrier has to be overcome in order for a collision to actually take place, i.e. the kinetic energy (characterized by the temperature) has to be larger than the potential barrier. Figure 2.9 outlines the potentials including the centrifugal barriers $E_c(R)$ for the lowest partial waves which are converted in units of temperature according to $T_c(R) = E_c(R)/k_B$. Therefore in photoassociation experiments, the partial wave of the collision determines which molecular rotational levels can be addressed. Only the partial wave for $R = 0$ (blue curve) does not show any rotational barrier and is therefore

always present. Thus, for low or vanishing collision energies $k \to 0$, which corresponds to low temperatures, the only partial wave contributing to the collision process is the so called *s-wave* and this highlighted situation is referred to as *s-wave scattering*. For the experiments in the conservative trap (see sec. 5.3) this can be assumed due to an occurring temperature of $T_{\mathrm{RbYb}} = 1.7\,\mu\mathrm{K}$ which is way below the rotational barrier for $R = 1$ with $T_c(R = 1) = 66\,\mu\mathrm{K}$. The consequences on the observed photoassociation spectrum in our experiment are illustrated in fig. 5.3. With an effective temperature of [5]

$$\bar{T} = \frac{m_{\mathrm{Rb}} T_{\mathrm{Yb}} + m_{\mathrm{Yb}} T_{\mathrm{Rb}}}{m_{\mathrm{Yb}} + m_{\mathrm{Rb}}} \approx 300\,\mu\mathrm{K} \tag{2.54}$$

for the operation in the combined MOT [1] rotational components up to $R' = 2$ can be observed (see sec. 5.2).

2.8 Line strengths and transition probabilities

When molecules are produced by photoassociation, the interaction with the light field changes the electronic wavefunction. Equal to the Born-Oppenheimer approximation (see sec. 2.3) this process does not modify the relative position of the nuclei and hence their internuclear separation r_{eff}. Therefore, the transition between two states is characterized by the overlap integral of their nuclear wavefunctions (see eq. 2.59). The relative position of possible molecule formation is called *Franck-Condon point* R_C and the transition probability is determined by the *Franck-Condon factor* f_{FC} [113] (see also sec. 2.9).
In general, it is difficult to model the exact wavefunctions of the involved molecular states due to a sensitive dependence on the interaction potential. Instead, it is possible to examine experimentally the line strength of transitions to different vibrational states, which is a measure for the transition probability [114]. If this is performed for a variety of vibrational states, the relative intensities of the vibrational states allow to infer knowledge of the overlap integral of the wavefunctions and hence the *s*-wave ground state wavefunction. Especially, if the ground state wavefunction has a node at the outer turning point of the excited state that is to be addressed the transition probability is zero.
According to [115] the position of a node in the scattering wave function is directly related to the *s*-wave scattering length a (see also [1])

$$a_{sc} = \frac{\sqrt[4]{\tilde{C}_6}}{2} \cdot \frac{J_{-1/4}(\tilde{r}_0)}{J_{1/4}(\tilde{r}_0)} \cdot \frac{\Gamma(3/4)}{\Gamma(5/4)} \tag{2.55}$$

$$\text{with} \qquad \tilde{r}_0 = \frac{\sqrt{2\,\mu\,C_6}}{2\,\hbar\,r_0^2} \qquad \text{and} \qquad \tilde{C}_6 = \frac{2\,\mu\,C_6}{\hbar^2}\,. \tag{2.56}$$

Here, the functions $J_{\pm 1/4}(\tilde{r}_0)$ are the Bessel functions and $\Gamma(x)$ the usual Gamma-function. The scattering length as a function of nodal position for $^{87}\mathrm{Rb}^{176}\mathrm{Yb}$ is illustrated in fig. 2.10 using a van-der-Waals coefficient of $C_6 = -2837.2\,E_h a_0^6$ [2] that was extracted from our two-color photoassociation experiments [3] (sec. 6.3). With the deduced scattering length of $a = +216.8\,a_0$ [2] for this system corresponding to the dashed line in fig. 2.10 the position

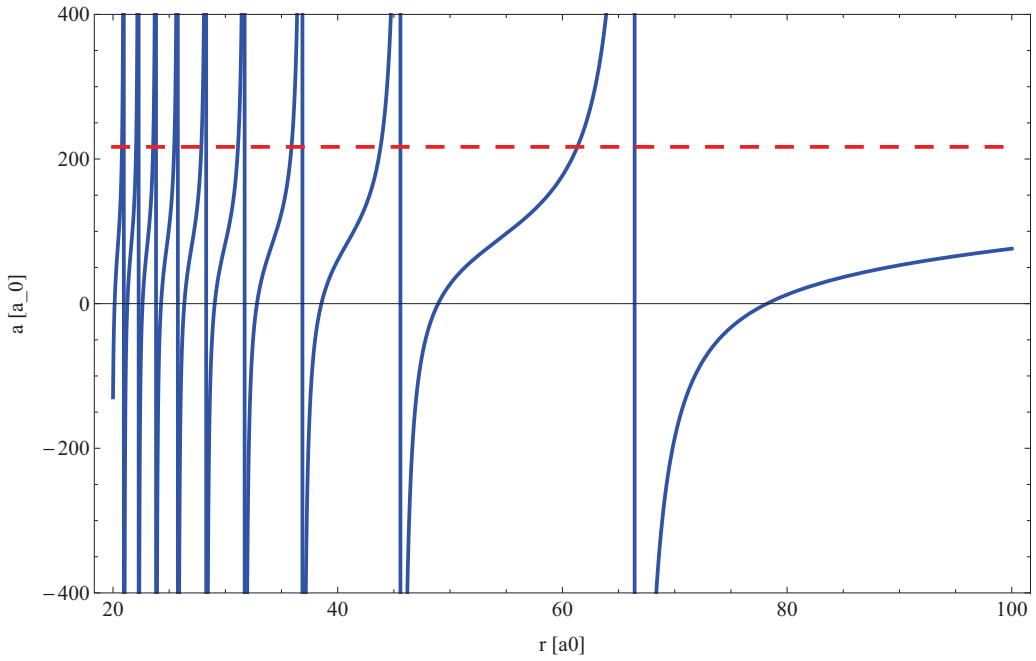

Figure 2.10: *Scattering length a as a function of nodal position of the s-wave ground state wavefunction for $^{87}Rb^{176}Yb$ with a C_6-coefficient of $-2837.2\,E_h a_0^6$ [2]. The dashed line corresponds to a scattering length of $a = +216.8\,a_0$ whose intersections with the graph denote the nodes in the wavefuntion. The position of the next node resides at $r = 218\,a_0$.*

of nodes should be precisely known. Within this thesis, the scattering wavefunction overlap was probed by 1-photon photoassociation spectroscopy. Several nodes were found and their positions will be compared in sec. 5.3.6 to the theoretical positions.

2.9 Photoassociation rate and lineshape

For the production and subsequent manipulation of rovibronic ground state molecules a high population in these states is desired. Using the approach of photoassociation as presented in this thesis, a large molecule production rate is achieved by suitable photoassociation rates. This section briefly reviews the theoretical approach for scattering event rates and line shapes for photoassociation processes following [46] that were already adopted to photoassociation in a MOT in our group [1].
The scattering probability $|S_p|^2$ for a one-color photoassociation resonance (see fig. 5.1) is given by the square of the S-Matrix [116, 117, 118]

$$|S_p\,(E,\ell)|^2 = \frac{\hbar\Gamma_\mathrm{d}\ \hbar\Gamma_\mathrm{b}(E,\ell)}{[E + h(\nu-\nu_0) - S_\mathrm{b}(E)]^2 + [\hbar\Gamma_\mathrm{tot}/2]^2}\,, \tag{2.57}$$

where $\Delta_1 = \nu - \nu_0$ is the detuning of the photoassociation laser frequency ν from the resonance frequency ν_0 of the bound molecular state. E is the collision energy of the

particles and ℓ the partial wave contributing to the collision. The linewidth of the transition to the bound state $\Gamma_{\mathrm{tot}} = \Gamma_{\mathrm{nat}} + \Gamma_{\mathrm{b}}(E,\ell) + \Gamma_{\mathrm{o}}$ is composed of the natural linewidth Γ_{nat} of the excited state determined by its lifetime, $\Gamma_{\mathrm{b}}(E,\ell)$ stemming from stimulated emission back to the entrance channel and other processes Γ_{o} that lead to decay of the bound state. The stimulated emission can be expressed with Fermi's golden rule as

$$\hbar\,\Gamma_{\mathrm{b}}(E,\ell) = 2\pi\,|V_{\mathrm{b}}(E,\ell)|^2\ . \tag{2.58}$$

Here, $V_{\mathrm{b}}(E,\ell)$ denotes the strength of the optical coupling between the collisional state $|E,\ell\rangle$ and the molecular bound state $|b\rangle$ given by the matrix element

$$V_{\mathrm{b}}(E,\ell) = \left(\frac{2\pi\,I}{c}\right)^{1/2} \langle b|\vec{d}(R)\cdot\vec{e}|E,\ell\rangle\,, \tag{2.59}$$

which is proportional to the square-root of the photoassociation laser intensity I. Here, $\vec{d}(R)$ is the dipole operator and $\vec{e}$ the polarization of the light field. Equation 2.59 can be further simplified by assuming a slowly varying dipole moment around the *Condon-point* R_C. Then one gets

$$\Gamma_{\mathrm{b}}(E,\ell) = \frac{2\pi V_{\mathrm{b}}^2\,|\langle E,\ell|b\rangle|^2}{\hbar} \tag{2.60}$$

with the *Franck-Condon factor* $|\langle E,\ell|b\rangle|^2$ for the free-bound transition.
The total event rate coefficient is then given by [46]

$$K_d(E) = \frac{\pi v_{\mathrm{rel}}}{k^2}\sum_{\ell}(2\ell+1)\cdot|S_p\,(E,\ell)|^2\ . \tag{2.61}$$

Here, $v_{\mathrm{rel}} = \hbar k/\mu$ is the relative velocity of the particles with the relative wave vector k. The effect on the event rate $K_d(E)$ for different energies following eq. 2.61 is depicted in fig. 2.11. Basically, higher temperatures shift the maximum of the line to lower frequencies since the thermal energy lifts the continuum energy and (slightly) reduces the transition energy. Besides, the maximum event rate is reduced.
In the experiment the collisions are not all at the same energy but the energies follow a Maxwell-Boltzmann distribution. Thus, the molecule production rate in the experiment at a temperature T is obtained by averaging over the thermal Boltzmann energy distribution [81]

$$K_{\mathrm{therm}} = \frac{2}{\sqrt{\pi}k_{\mathrm{B}}T}\int_0^\infty K_d(E)e^{-\frac{E}{k_{\mathrm{B}}T}}\sqrt{\frac{E}{k_{\mathrm{B}}T}}dE\,. \tag{2.62}$$

As can be seen in fig. 2.12, higher temperatures distort the lineshape and shift the center peak to the red side of the frequency. But these shifts are negligible for typical operating temperatures in a MOT ($\approx 300\,\mu\mathrm{K} \Rightarrow 3\,\mathrm{MHz}$) compared to our measurement accuracy or in a conservative trap ($\approx 2\,\mu\mathrm{K} \Rightarrow 50\,\mathrm{kHz}$). For the PA measurements in the conservative trap which are at the focus of this thesis they are even less relevant.

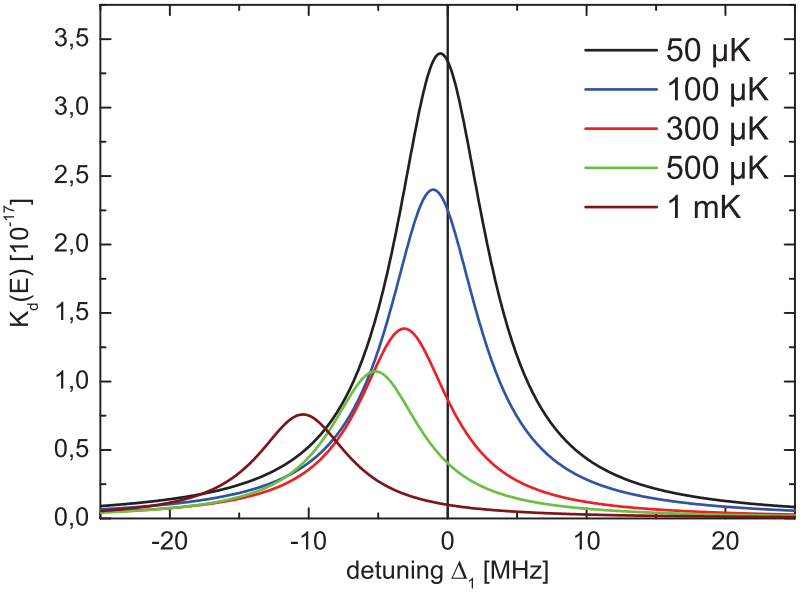

Figure 2.11: *Temperature effect for a large but not maximum event rate coefficients $K_d(E)$ from eq. 2.61 as a function of photoassociation laser detuning Δ_1. The energy is expressed in terms of a temperature using $E = k_\mathrm{B}\,T/2$ (for comparison with fig. 2.12).*

Application to our experiment

In the following, the presented relations will be applied to our specific experimental procedures and properties (see [1]).
In the relevant case for PA in a conservative trap, only s-wave scattering with $\ell = 0$ will be assumed. The intensity dependent light shift $S_\mathrm{b}(E)$ in equation 2.57 is small and will be neglected. For the case of trap-loss experiments, as was performed in our case, the detection rate Γ_d equals the natural linewidth Γ_nat. Other additional losses are assumed to be small, too, so $\Gamma_\mathrm{o} = 0$, and hence $\Gamma_\mathrm{tot} = \Gamma_\mathrm{nat} + \Gamma_\mathrm{b}$. For the on-resonance event rate ($\Delta_1 = 0$) eq. 2.61 reduces to

$$K_d^{res}(E) = \frac{\pi v_\mathrm{rel}}{k^2} \cdot \frac{4\Gamma_\mathrm{nat}\Gamma_\mathrm{b}(E,\ell)}{\left(\Gamma_\mathrm{nat} + \Gamma_\mathrm{b}(E,\ell)\right)^2}\,. \tag{2.63}$$

The stimulated emission rate into the ground state is then given by [1]

$$\Gamma_\mathrm{b}(E,\ell) = \frac{4\pi^2}{\hbar\, c} \cdot I \cdot V_\mathrm{b}^2\, |\langle E,\ell|b\rangle|^2 = \frac{4\pi^2}{\hbar\, c} \cdot I \cdot a_t^2\,, \tag{2.64}$$

and is intensity dependent. The specific transition properties are included in a_t. Equation 2.63 can then be further transformed into (see again [1])

$$K_d^{res}(E) = \frac{\pi v_\mathrm{rel}}{k^2} \cdot \frac{4I_\mathrm{opt} \cdot I}{\left(I_\mathrm{opt} + I\right)^2}\,, \tag{2.65}$$

with $I_\mathrm{opt} = (\hbar\Gamma_\mathrm{nat} c)/(4\pi^2 a_t^2)$. This final event rate coefficient as a function of photoassociation laser intensity is illustrated in fig. 2.13 (see also eq. 2.70). For low intensities it

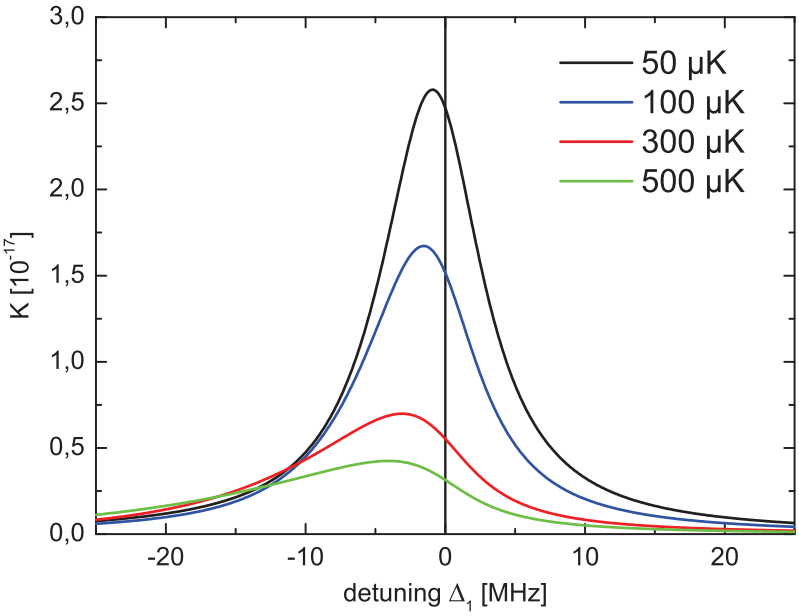

Figure 2.12: *Photoassociation line shape K_{therm} as a function of photoassociation laser detuning Δ_1 after integrating over the Boltzmann energy distribution. Higher temperatures slightly shift the resonance to the red side of the spectrum and additionally deform the lineshape. It is essential that the shift of the line occurs only to negative detunings since the kinetic energy of the atoms lifts the initial energy of the system and thus reduces the needed transition energy. These effects are nevertheless negligible small in our experiment.*

increases linearly. After reaching its maximum it turns over and decreases which is explained by saturation and broadening of the photoassociation line. The maximum rate is equal to the prefactor

$$K_{\mathrm{max}}^{res}(E) = \frac{\pi v_{\mathrm{rel}}}{k^2}, \tag{2.66}$$

which is achieved for $I = I_{\mathrm{opt}}$. This shows an interesting property. The maximum reachable event rate coefficient does not depend on the transition's Franck-Condon factor. While large Franck-Condon factors lead to easier addressable states, small transition probabilities can be compensated by increasing the photoassociation laser intensity. However, the typical temperatures in the MOT ($T_{\mathrm{MOT}} = 300\,\mu\mathrm{K}$, blue curve) and the hybrid conservative trap ($T_{\mathrm{RbYb}} = 1.7\,\mu\mathrm{K}$, red curve) set the course for the maximum achievable photoassociation rates.

Finally, the experimentally obtained maximum photoassociation rate depends on the peak density of the rubidium atomic cloud ρ_{Rb}, since PA is carried out close to the Rb D_1 line at 795 nm, and is hence given by

$$r_{\mathrm{PA}}^{\mathrm{max}}(E) = \frac{\pi v_{\mathrm{rel}}}{k^2} \cdot \rho_{\mathrm{Rb}}\,. \tag{2.67}$$

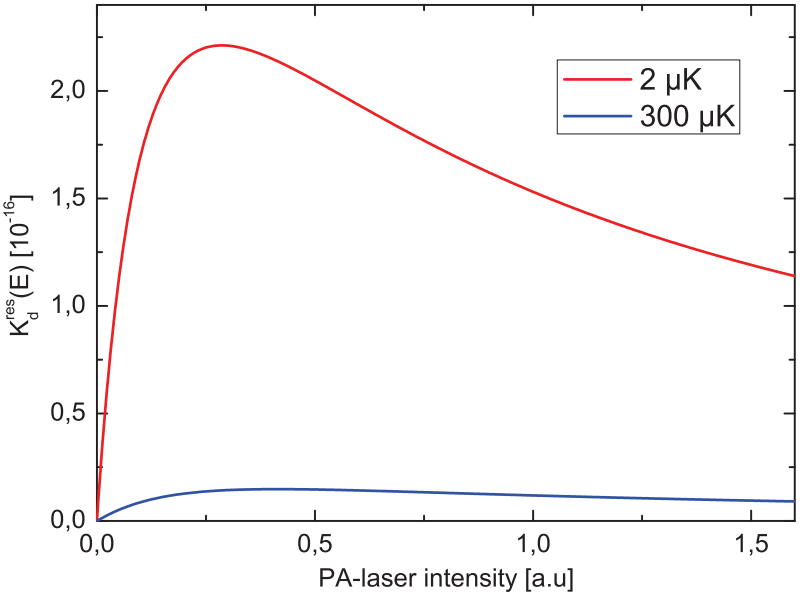

Figure 2.13: *Event rate coefficient $K_d^{res}(E)$ from eq. 2.65 as a function of photoassociation laser intensity. The maximum rate $K_{\max}^{res}(E)$ (eq. 2.66 and eq. 2.70) is reached for $I = I_{\text{opt}}$ and afterwards the rate decreases. Compared are the temperatures available in the MOT (blue curve) and the hybrid conservative trap (HT) (red curve) which lead to one order of magnitude different maximum rates.*

The parameters characterizing the relative motion of the particles are energy dependent according to

$$v_{\text{rel}} = \frac{\hbar k}{\mu} = \sqrt{\frac{2E}{\mu}} \qquad \text{and} \tag{2.68}$$

$$k = \frac{\sqrt{2E\mu}}{\hbar}\,. \tag{2.69}$$

Assuming the collision energy to be specified by an effective temperature, $E = k_{\text{B}}\,T_{\text{eff}}/2$, this leads to

$$r_{\text{PA}}^{\max} = \frac{\pi\,\hbar^2}{k_{\text{B}}\,T_{\text{eff}}\,\mu^3} \cdot \rho_{\text{Rb}}\,. \tag{2.70}$$

N. Nemitz et al. [1] performed photoassociation experiments in a combined MOT at temperatures of $T_{\text{MOT}} \approx 400\,\mu\text{K}$ and with a peak rubidium density of $\rho_{\text{Rb,MOT}} = 1.07 \cdot 10^{11}\,\text{cm}^{-3}$. This gave a maximum photoassociation rate of $r_{\text{PA}}^{\max} = 1.7\,\text{s}^{-3}$ per ytterbium ground state atom. The experiments in this thesis were carried out in the hybrid conservative trap presented in sec. 4.1.3. With a temperature of $T_{\text{RbYb}} = 1.7\,\mu\text{K}$ and $\rho_{\text{Rb,cons}} = 2.9 \cdot 10^{13}\,\text{cm}^{-1}$ this leads to considerably increased photoassociation rates of $r_{\text{PA}}^{\max} \approx 7000\,\text{s}^{-1}$ per ytterbium ground state atom.

2.10 Magnetic Feshbach resonances

A famous and well-established procedure for coherently producing ultracold ground state molecules is to use magnetically tunable *Feshbach resonances* [44, 45]. The concept of Feshbach resonances was developed independently by H. Feshbach [119, 120] and U. Fano [121] who basically describe the same situation, namely the existence of a bound state of a subsystem embedded in a continuum. That is why the physics of Fehsbach resonances and photoassociation are closely related. Photoassociation resonances can also be used to realize so-called *optical Feshbach resonances* [122, 123]. There have also been proposals to couple scattering channels by radio frequency [124] or static electric fields [125] which are also closely related to magentic Feshbach resonances but yet without a successful experimental implementation.
The basic principle of a magnetic Feshbach resonance is sketched in fig. 2.14. The molecular potential $V_{\mathrm{bg}}(r)$ with a collision energy E is called *open channel* or *entrance channel* [44, 45] which for the internuclear separation $r \to \infty$ and $E > 0$ results in two separated atoms. The other potential $V_{\mathrm{c}}(r)$ is crucial as it needs to possess a bound state with energy E_c close to the threshold of $V_{\mathrm{bg}}(r)$. If E_c is higher than the energy E of the scattering state then the corresponding channel is called *closed channel*. A Feshbach resonance, occurs if the bound molecular state in the closed channel is energetically degenerate with the scattering state in the open channel. Such a magnetic Feshbach resonance can be induced if

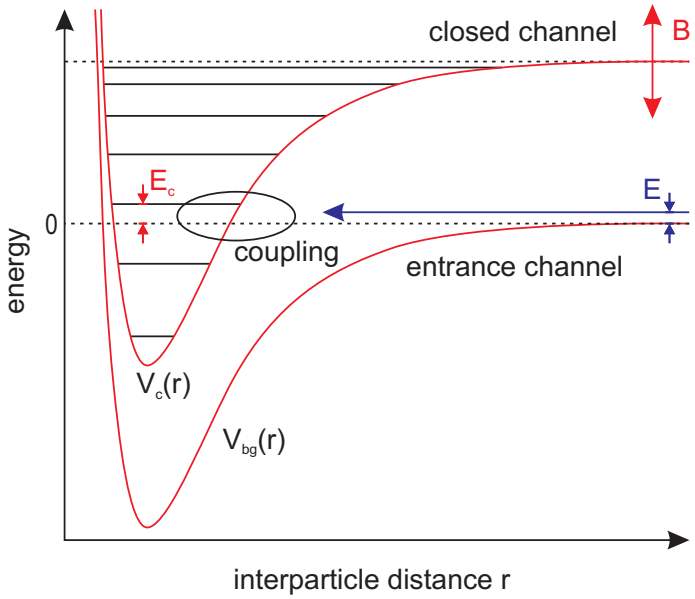

Figure 2.14: *Illustration of the basic principle of magnetic Feshbach resonances (taken from [6] and adapted from [45]). The closed channel potential $V_c(r)$ supporting a bound state with energy E_c is resonantly coupled to the entrance channel $V_{bg}(r)$ by shifting E_c close to the energy E of the colliding atoms. Magnetic tuning is possible if both potentials exhibit different magnetic moments.*

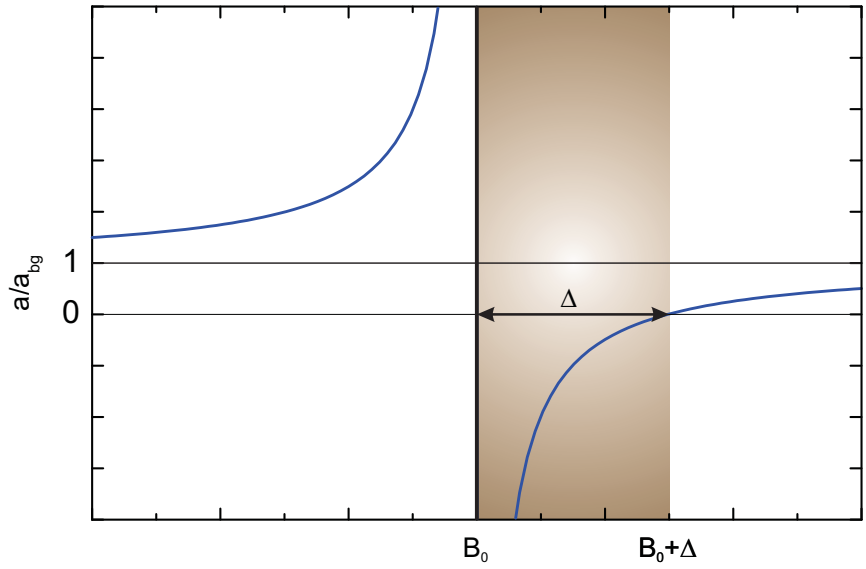

Figure 2.15: *Scattering length a as a function of external magnetic field B close to a Feshbach resonance following eq. 2.71. The background scattering length a_{bg} is the value of a far away from any resonance. The position B_0 of the resonance is marked by the pole in which a takes values close to $\pm\infty$. The width Δ of the resonance is defined by the difference between the position of the pole and the zero-crossing of a.*

the magnetic moments of the involved channels differ. As a consequence, both potentials $V_{\mathrm{c}}(r)$ and $V_{\mathrm{bg}}(r)$ can be shifted relative to each other which is generally possible for an alkali-alkali system. In this case a weak coupling might result in a strong mixing of the involved states.

An important feature of magnetic Feshbach resonances is that the scattering length characterizing the interaction of two (unbound) atoms can vary significantly in the vicinity of the resonance. Moerdijk et al. [126] developed a simple expression to characterize the s-wave scattering length a as a function of applied magnetic field B

$$a(B) = a_{\mathrm{bg}}\left(1 - \frac{\Delta}{B - B_0}\right) . \tag{2.71}$$

Figure 2.15 visualizes this expression where a_{bg} specifies the scattering length far away from any resonance and is therefore connected to V_{bg}. The position of the pole B_0 is equivalent to the position of the Feshbach resonance. The width of the resonance Δ is defined as the difference between the magnetic field position of the pole ($a \to \pm\infty$ at $B = B_0$) and its zero-crossing ($a = 0$ at $B = B_0 + \Delta$). According to this definition the sign of Δ can be positive or negative depending on the sign of a_{bg}. In ultracold atom experiments the collision energy is usually located near zero energy, $E \to 0$, and thus resonant coupling is achieved by tuning E_c close to 0. While the energy of the bound molecular state varies linearly with B far off the resonance, it varies quadratically near the resonance due to the coupling between the two channels that strongly bends the molecular state [44]. A bound molecular state close to threshold emerges in the case of a (large and) positive scattering

length a whose binding energy is given by eq. 2.47.
The ability to tune the parameter a, that determines ultracold collisions as presented in sec. 2.4, close to a magnetic Feshbach resonance already reveals the huge potential lying in these resonances. Besides the production of ground state molecules [45] it offers the possibility to manipulate the interatomic forces in ultracold collisions and enhance the elastic as well as the inelastic interparticle cross section (see sec. 2.10.1). To give some examples, Cornish et al. [127] were able to produce a Bose-Einstein-condensate close to a Feshbach resonance with ^{85}Rb and Weber et al. [128] with ^{133}Cs which was previously not possible due to their intrinsic negative scattering lengths.
The relation introduced by Köhler et. al [44] for the width Δ of the resonance

$$\Delta = \frac{2\mu(2\pi\hbar)^3}{4\pi\hbar^2 a_{\mathrm{bg}}\mu_{\mathrm{res}}} \left|\langle\phi_{\mathrm{res}}|W|\phi_0\rangle\right|^2 \tag{2.72}$$

states that Δ is essentially an indication for the coupling strength $\left|\langle\phi_{\mathrm{res}}|W|\phi_0\rangle\right|^2$ between the channels and is mainly applicable to alkali-alkali mixtures. Here, ϕ_{res} denotes the (molecular bound) Feshbach resonance state of the closed channel, ϕ_0 the background wavefunction in the limit of zero momentum and W the Hamiltonian responsible for the coupling. The difference between the magnetic moments of the states is μ_{res}.
An explicit form for the width of the resonance that is specifically applicable to mixtures of alkali atoms and spin-singlett atoms like RbYb was derived by Brue et al. [13] where the width is given by:

$$\Delta = \frac{\mu\bar{a}}{\hbar^2 a_{\mathrm{bg}}}\left[1+\left(1-\frac{a_{\mathrm{bg}}}{\bar{a}}\right)^2\right]\frac{[I_{m_{f,a}}(B)]^2}{N\mu_{\mathrm{res}}}\cdot\left[\int_{r_{\mathrm{in}}}^{\infty} k(r)^{-1}\Delta\zeta(r)dr\right]^2 . \tag{2.73}$$

Here, the coupling is induced by a separation dependent variation in the hyperfine coupling constant $\Delta\zeta(r)$ (see sec. 2.11), μ is the reduced mass of the system and $\bar{a}$ the mean scattering length from eq. 2.44. The normalization integral N is connected to the LeRoy-Bernstein relation from eq. 2.49. With the dominating C_6-coefficient it yields [13]

$$N = \frac{1}{2}\int_{r_{\mathrm{in}}}^{r_{\mathrm{out}}} k(r)^{-1}dr \approx \frac{1}{2}\left(\frac{\pi\hbar^2}{2\mu}\right)^{1/2}\frac{\Gamma(2/3)}{\Gamma(7/6)}\frac{C_6^{1/6}}{6}\left|E_n\right|^{-2/3} , \tag{2.74}$$

with the binding energy E_n. The expression $I_{m_{f,a}}(B)$ is an atomic property (see [13]) and is proportional to $\propto B$. As a result, it counts for the width of the resonance

$$\Delta \propto B^2\ \left|E_n\right|^{2/3} , \tag{2.75}$$

and therefore wider resonances can occur for deeper bound states and for resonances which reside at higher magnetic fields. Additionally, large widths are present if the absolute value of the background scattering length $|a_{\mathrm{bg}}|$ is either very large or very small.

2.10.1 Experimental detection schemes for Feshbach resonances

This subsection describes possible experimental methods and challenges to find magnetic Feshbach resonances. Generally, the width Δ of the resonance determines the magnetic

field resolution required for detection. Depending on the coupling responsible for the Feshbach resonance the occurring widths are on the order of G [127, 129], mG [130] or even μG as i.e. predicted for RbYb (see sec. 7.1). A stability of this magnitude turns out to be challenging since the resonances might occur at fields up to 1000 G or even higher. In order to detect Feshbach resonances it is possible to avail oneself of the magnetically tunable scattering length a close to the resonance and thereby connected physical effects as will be outlined in the following.

Inelastic collisions

The occurrence of a Feshbach resonance is (mostly) accompanied by inelastic losses resulting from two- or three-body processes [131]. In the case of a three-body collision, the molecular binding energy, which is generally much larger than the trap depth, can be transferred to the colliding atoms inducing losses from the trap. Furthermore, due to coupling to inelastic outgoing channels, the inelastic loss rate is enhanced close to a Feshbach resonance. Three-body recombination is in many experiments the leading cause for inelastic losses in which three atoms collide to form a diatomic molecule and a free atom. The density dependent three-body recombination rate can be expressed according to [132, 133, 134] as

$$\nu_{rec} = \alpha_{rec} n^3 \tag{2.76}$$

with

$$\alpha_{rec} = C \frac{\hbar a^4}{m}\,, \tag{2.77}$$

and the dimensionless factor C which may depend on the specific collision partners [135].

Elastic collisions

Another method for detecting Feshbach resonances utilizes the dependence of the elastic collision rate $\sigma_0(k)$ from eq. 2.41 on a [127]. Since the singularity of the scattering length near a Feshbach resonance allows a to take values between $\pm\infty$ a variation of the thermalization rate can be traced back to the existence of a Feshbach resonance. On the one hand Feshbach resonances can be monitored by measuring the enhancement of the elastic collision rate which could be for example achieved in experiments with ^{133}Cs [136] or ^{40}K [137]. On the other hand a decrease or lack of otherwise persisting thermalization rates can indicate a Feshbach resonance due the magnetic field dependent zero-crossing of a (see fig. 2.15) [127, 129].

2.11 Hyperfine interaction

This section describes the hyperfine interaction that might lead to observable Feshbach resonances in RbYb. The hyperfine interaction will be recapitulated following [11, 13] and using the example of rubidium and ytterbium atoms.

The magnetic properties of an atom are correlated to its angular momenta. Section 2.5 already presented the occurring angular momenta and their possible coupling in diatomic molecules. The electronic orbital angular momentum $\vec{\ell}$ of an atom creates a magnetic moment of [138]

$$\vec{\mu}_\ell = -(\mu_\mathrm{B}/\hbar) \cdot \vec{\ell}. \tag{2.78}$$

Similarly, the magnetic moment stemming from the electronic spin $\vec{s}$ is

$$\vec{\mu}_s = -(\mu_\mathrm{B} g_S/\hbar) \cdot \vec{s}. \tag{2.79}$$

These two momenta can couple to the total angular momentum $\vec{j} = \vec{\ell} + \vec{s}$. If a nuclear spin $\vec{i}$ is present it generates a magnetic moment of

$$\vec{\mu}_i = (\mu_\mathrm{N} g_I/\hbar) \cdot \vec{i}, \tag{2.80}$$

which is generally much smaller than magnetic contributions from the electrons due to the smaller value of the nuclear magneton μ_N. The corresponding Landé- g-factors are denoted g_S and g_I. These magnetic moments can now interact with each other. The interaction between $\vec{\mu}_\ell$ and $\vec{\mu}_s$ leads to a *fine-stucture* [138]. Here, the focus will be put on the *hyperfine structure* that originates from the interaction between the total angular momentum $\vec{j}$ and the nuclear momentum $\vec{i}$. The impact on the observable structure in the rubidium atom will be described in the following.

Origin of hyperfine interaction

The hyperfine interaction is composed of two different contributions. The anisotropic dipole-dipole interaction between the magnetic moment of the electron and the nucleus [139, 87] has an angular dependence and the hyperfine constant can be described as

$$A_\mathrm{dd} = \frac{\mu_0}{4\pi} g_I \, \mu_\mathrm{N} \, g_e \, \mu_\mathrm{B} \left\langle \frac{1}{r^3} \right\rangle \left\langle 3\cos^2\theta - 1 \right\rangle , \tag{2.81}$$

where the $\langle ... \rangle$-brackets indicate an average over the electronic wavefunction. This contribution depends on the relative orientation of the molecule and vanishes at the position of the nucleus. The main contribution in molecular physics results from the isotropic *Fermi-contact-interaction* [139, 87]

$$A_\mathrm{c} = \frac{2\mu_0}{3} g_I \mu_\mathrm{N} \, g_e \, \mu_\mathrm{B} \, |\Psi(0)|^2 . \tag{2.82}$$

It depends on the electronic probability density at the position of the nucleus $|\Psi(0)|^2$.

Hyperfine Structure of ^{87}Rb

Within this thesis, the molecular equivalent of the hyperfine splitting of the Rb D_1 line was analyzed further by means of photoassociation spectroscopy as will be presented in

sec. 5.3.5. We observed a variation in this hyperfine splitting Δ_{HFS} as a function of vibrational state of the molecule due to the distortion of the Rb electron cloud as will be explained there.
The fine and hyperfine levels of ^{87}Rb and ^{85}Rb are depicted in fig. 3.5. The fine structure in the electronically excited ^{5}P state of Rb is caused by a coupling between the angular momentum $\vec{\ell}_{\mathrm{Rb}}$ and the spin $\vec{s}_{\mathrm{Rb}}$. Consequently, the quantum numbers of the total electron angular momentum $\vec{j}_{\mathrm{Rb}} = \vec{\ell}_{\mathrm{Rb}} + \vec{s}_{\mathrm{Rb}}$ may take values between

$$|L - S| \leq |J| \leq |L + S| \,. \tag{2.83}$$

A much finer splitting can be observed known as the hyperfine structure, which results from the coupling between the magnetic fields originating from the nuclear spin i_{Rb} and the total angular momentum j_{Rb}. Without external magnetic field and neglecting higher order magnetic multipole terms, the Hamiltonian is (see also eq. 2.91)

$$\hat{H}_{Rb} = A_{\mathrm{Rb}} \hat{i}_{Rb} \cdot \hat{j}_{Rb} \,, \tag{2.84}$$

with a general state dependent hyperfine coupling constant A_{Rb}. The total atomic angular momentum $\vec{f}_{\mathrm{Rb}} = \vec{j}_{\mathrm{Rb}} + \vec{i}_{\mathrm{Rb}}$ may then take values between

$$|J - I| \leq |F| \leq |J + I| \,. \tag{2.85}$$

Consequently, the fine-structure components experience an additional state dependent energy shift of [138]

$$\Delta E_{HFS} = \frac{1}{2} A_{\mathrm{Rb}} \left[F(F+1) - I(I+1) - J(J+1) \right] . \tag{2.86}$$

Precise knowledge of the hyperfine coupling constant A_{Rb} can be gained by electron spin resonance (ESR) experiments [139]. In an intuitive view the magnetic field B_j created by the electronic angular momentum $\vec{j}$ at the position of the nucleus depends on the density probability of the electron cloud according to eq. 2.81 and eq. 2.82 [139, 87] and therefore the hyperfine constant is a measure for this density probability

$$A_{\mathrm{Rb}} \propto |\Psi(r)|^2 \,. \tag{2.87}$$

Table 2.1 lists the hyperfine constants for the relevant ^{87}Rb states [140] and derived values for B_j at the position of the nucleus according to [139]. However, B_j and hence the hyperfine splitting ΔE_{HFS} is the larger the closer the electrons are to the nucleus. While for s-electrons (Rb ground state) the Fermi-contact-interaction is decisive that leads to a large coupling, for electrons with $|\Psi(0)|^2 = 0$ such as p-electrons (Rb excited state) the dipole-dipole interaction is pivotal leading to a smaller coupling.
For two different hyperfine components F_2 and F_1 of the same electronic state the hyperfine splitting from eq. 2.86 reduces to

$$\Delta E_{\mathrm{HFS}} = \frac{1}{2} A_{\mathrm{Rb}} \left[F_2(F_2+1) - F_1(F_1+1) \right] . \tag{2.88}$$

More specifically, the hyperfine splitting of the Rb D_1 line (see again fig. 3.5) with $F_2 = 2$, $F_1 = 1$ and $A_{^2\mathrm{P}_{1/2}} = h \cdot 408.328\,\mathrm{MHz}$ can be calculated to be

$$\Delta E_{\mathrm{HFS}} = 2\, A_{^2\mathrm{P}_{1/2}} = h \cdot 817\,\mathrm{MHz} \,. \tag{2.89}$$

^{87}Rb state	denotation	Hyperine Constant/h [MHz]	B_j [T]
$5^2S_{1/2}$	$A_{^2S_{1/2}}$	3417.341305	130
$5^2P_{1/2}$	$A_{^2P_{1/2}}$	408.328(15)	16
$5^2P_{3/2}$	$A_{^2P_{3/2}}$	84.7185(20)	8,6

Table 2.1: *Hyperfine constants for ^{87}Rb from [140] and derived magnetic field at the position of the nucleus from [139].*

Hyperfine interaction and its connection to Feshbach resonances in Rb-Yb mixtures

The hyperfine interaction is the typical coupling that is responsible for Feshbach resonances. Here, the special case of a collision between an alkali (Rb) and a spin-singlett atom (Yb) is discussed following [11, 13]. If a scattering process between an alkali-metal atom a in a ^{2}S (Rb) and a closed-shell atom b in a ^{1}S state (Yb) is considered, then the Hamiltonian can be written as [13]

$$\hat{H} = \frac{\hbar^2}{2\mu}\left[-\frac{d^2}{dr^2}\right] + \hat{V}(r) + \hat{H}_a + \hat{H}_b \tag{2.90}$$

where the single atom Hamiltonians $\hat{H}_a$ and $\hat{H}_b$ can be expressed as

$$\hat{H}_a = \zeta_a \hat{i}_a \cdot \hat{s} + \left(g_a \mu_N \hat{i}_{a,z} + g_e \mu_B \hat{s}_z\right) B\,, \tag{2.91}$$

and

$$\hat{H}_b = g_b \mu_N \hat{i}_{b,z} B \tag{2.92}$$

with the spin operators stemming from the electron spin $\hat{s}$ and nuclear spins $\hat{i}_a$ and $\hat{i}_b$, the electronic and nuclear g-factors g_e, g_a and g_b and the Bohr and nuclear magnetons μ_B and μ_N. An external magnetic field B defines the quantization axis (z-axis). The parameter that leads to a coupling between the two atoms is the hyperfine coupling constant ζ_a of the alkali metal atom that can be affected due to the nearby presence of atom b and may exhibit a dependence on the separation r of the two atoms

$$\zeta_a(r) = \zeta_{a,0} + \Delta\zeta_a(r)\,. \tag{2.93}$$

This dependence results from the distortion of the electron cloud of atom a that effects the electronic density probability $|\Psi(0)|^2$ from eq. 2.82. Here we have adopted the notation of [13] for the hyperfine interaction in a molecule. However, in the case of Rb in its electronic ground state it is $\zeta_{a,0} = A_{^2S_{1/2}}$ (see table 2.1).
If the closed-shell atom has also a nuclear spin $i_b \neq 0$, which is for example the case for the fermionic Yb isotopes ^{171}Yb and ^{173}Yb, then there might be also a contribution to the coupling coming from the nucleus of atom b

$$\zeta_b(r) = \Delta\zeta_b(r)\,. \tag{2.94}$$

These two perturbations, although being small, are the most important ones that give rise to the predicted magnetically induced Feshbach resonances between an alkali-metal atom and a closed-shell atom. According to [11] there are also other interactions leading to even smaller couplings such as i.e. the interaction between the quadrupole nuclear moment of atom a and the above mentioned distortion of its electronic cloud due to atom b or the spin-rotation interaction between L and the Rb electron and nuclear spins. However, these contributions are even smaller and are thus neglected.
If Rb is in the $5^2\mathrm{P}_{1/2}$ excited state (as in our experiments presented in chap. 5) the atomic hyperfine constant is given by $\zeta_{a,0} = A_{^2\mathrm{P}_{1/2}}$. In that case, the electronic density probability at the position of the nucleus is zero $|\Psi(0)|^2 = 0$. Therefore, the Fermi-contact interaction from eq. 2.82 is replaced by the dipole-dipole interaction from eq. 2.81. However, the discussed coupling is caused by the same mechanism which is a distortion of the Rb electron cloud due to the presence of the Yb atom, that consequently leads to a variation in hyperfine splitting observed within this thesis (see sec. 5.3.5).

3

Experiment

This chapter describes the experimental apparatus that was used for the experiments performed within this thesis. The apparatus is composed of a vacuum chamber with attached coils for the required magnetic fields and several laser systems. While some parts of the setup have been left unchanged with respect to previous works [6, 8] most of the subsystems have been rebuilt, partly replaced and improved with the goal to allow for stable operation and production of excited RbYb molecules by photoassociation in the novel hybrid conservative trap as well as the search for magnetically induced Feshbach resonances in the crossed optical dipole trap. In particular, the photoassociation laser system was redesigned compared to [8] in order to carry out reliable experiments in the combined conservative trap. This also includes a new photoassociation laser covering a larger wavelength range.

3.1 Vacuum chamber and magnetic fields

The experiments presented in chap. 5, chap. 6 and chap. 7 were performed inside the main vacuum chamber depicted in fig. 3.1, just as in our previous experiments [4, 5, 1, 6, 3]. It provides optical access for Zeeman slower beams, magneto-optical trap (MOT) beams, optical dipole trap (ODT) beams, photoassociation (PA) laser beams and optical imaging beams needed for both, ytterbium and rubidium. To reduce collisions with hot background atoms, which would reduce the lifetime in the traps, the pressure is held at a level of $\approx 10^{-11}$ mbar by an attached titanium sublimation pump and ion getter pumps. In order to create a gaseous atomic beam the ovens are operated at 120°C and 470°C for Rb and Yb, respectively.

Figure 3.2 shows the arrangement of the water-cooled magnetic coils, whose mounting is foreshadowed in fig. 3.1 (a) but not visible in fig. 3.1 (b), and the current geometry for various purposes. Dipole and offset coils are used on only one side to create the magnetic field gradient needed for the MOT (fig. 3.2 (c)) while the second pair is switched on in addition together with the clover leafs to operate the magnetic trap (MT) for Rb (fig. 3.2 (b)). The arrows in the picture show the direction of current flow. Additionally, three pairs of compensation coils are implemented allowing for compensation for undesired magnetic stray fields (earth magnetic fields, ion pumps, etc.) and control the position of the MOTs for both atomic species and of the magnetic trap for Rb in all three dimensions.

While the general setup of the magnetic fields was adopted from our previous work, the

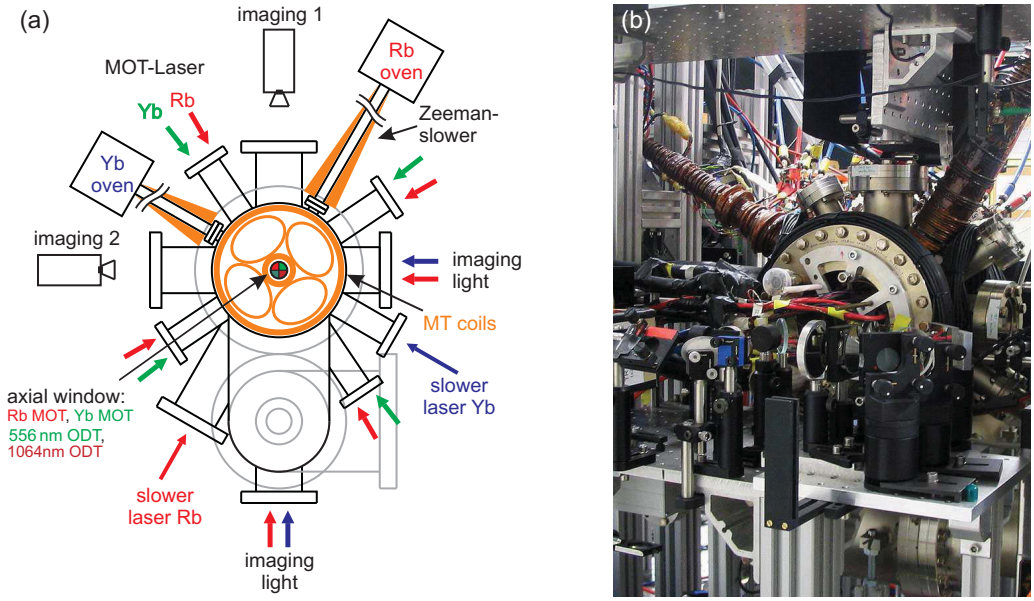

Figure 3.1: *Schematic illustration showing the optical access (a) and photograph (b) of the vacuum chamber (adapted from [5, 6]).*

search for magnetically induced Feshbach resonances in RbYb (chap. 7), required a homogeneous magnetic field at the position of the atoms. In order to create a nearly homogeneous magnetic field in the center of the vacuum chamber the current flux of dipole and offset coils has to be identical (fig. 3.2 (d)). Therefore, compared to MOT and MT operation, the polarity of the current through the dipole coils has to be reversed. This was achieved by the circuitry outlined in fig. 3.3. By controlling the configuration of the insulated gate bipolar transistors (IGBTs, labelled Q1...Q5) it is possible to choose the proper sequence of current flux through the coils (labelled LA...LD) and hence the magnetic field configuration as presented in table 3.1. Since the polarity of the current is partly reversed for the purpose of applying the Feshbach magnetic fields, dischargers in combination with varistors (fig. 3.3 (b)) were implemented on each coil to allow for fast switching in both current directions. These replaced the previously installed ring down circuits which were implemented to avoid large induction voltages resulting from fast switching of the magnetic fields for the clover-leaf magnetic trap and the MOT.
The calculated gradients for MOT operation are $(\partial B/\partial z)/I = 0.44\ {}^{\mathrm{G}}/_{(\mathrm{cm\,A})}$ in axial and $(\partial B/\partial r)/I = 0.22\ {}^{\mathrm{G}}/_{(\mathrm{cm\,A})}$ in radial direction [5] while the crucial parameters for the clover-leaf magnetic trap are a radial field gradient of $B' = 133\,\mathrm{G/cm}$ and an axial field curvature of $B'' = 231\,\mathrm{G/cm^2}$ [6]. The homogeneous magnetic field actually achieved and measured for Feshbach resonances is given by $B(I) = 2.72924\,\mathrm{G/A} \cdot I + 2.05729\,\mathrm{G}$ (see fig. 7.4).
According to eq. 2.24, the trap frequencies are determined by the magnetic trap parameters B_0, B' and B''. In [5] and [6] the trap frequencies of the MT were measured by deflecting the cloud and observing the resulting oscillations or by means of parametric heating [141, 142]. The gradient $B' = 133\,\mathrm{G/cm}$ and the curvature $B'' = 231\,\mathrm{G/cm^2}$ of the mag-

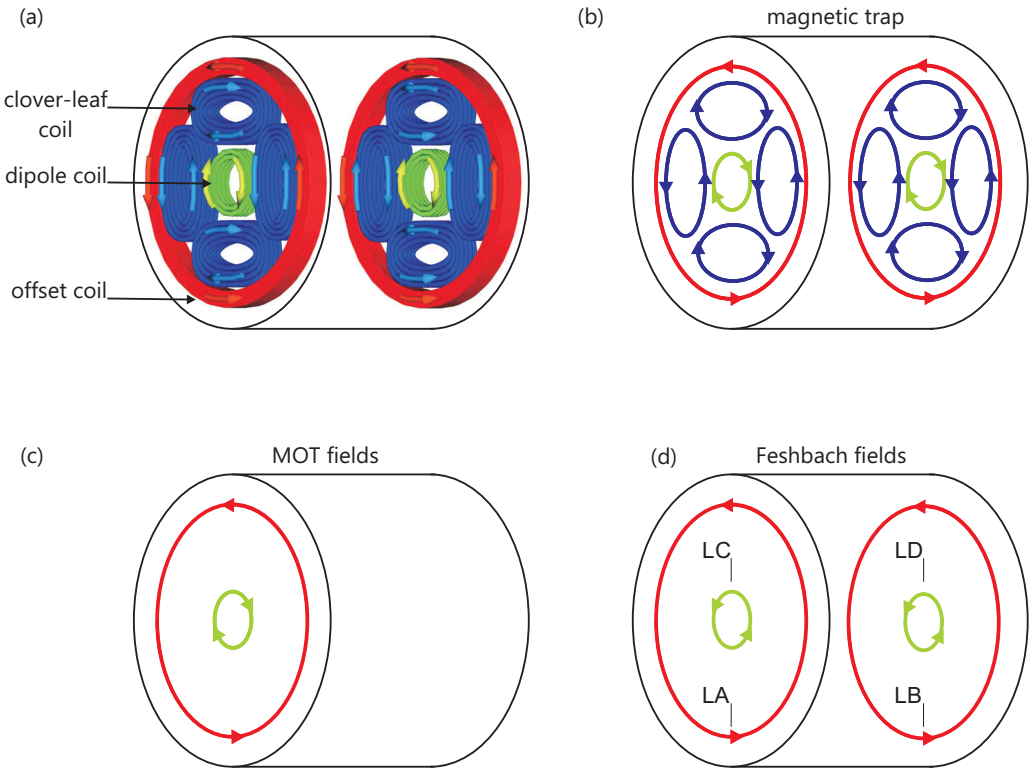

Figure 3.2: *Coil setup and current geometry implemented in the experiment. (a) Illustration of the coil design (from [4]). (b)-(d) Current geometry for different experimental situations. The arrows indicate the direction of current in the different configurations. These were the same as in our previous experiments for (b) the magnetic trap and (c) the MOT magnetic fields. (d) In order to create a homogenous field in the vacuum chamber the direction of current in the dipole coils has to be reversed using the electronic circuitry shown in fig. 3.3.*

configuration	current direction	IGBT outputs on	IGBT outputs off
magnetic trap	LA-LC-LD-LB	Q1, Q5	Q2, Q3, Q4
MOT fields	LA-LC	Q1, Q4	Q2, Q3, Q5
Feshbach fields	LA-LD-LC-LB	Q2, Q3	Q1, Q4, Q5

Table 3.1: *Magnetic field configuration achieved by controlling the outputs of the IGBTs and hence the current direction through the coils. The labelled coils can be found in fig. 3.2 (d).*

netic fields applied in the MT do not change in the present trap and hence a measurement of the magnetic field offset B_0 of the MT, also called *trap bottom*, directly gives the trap frequencies and densities.

The trap bottom B_0 can be determined by keeping the Rb atoms (^{87}Rb atoms spin polar-

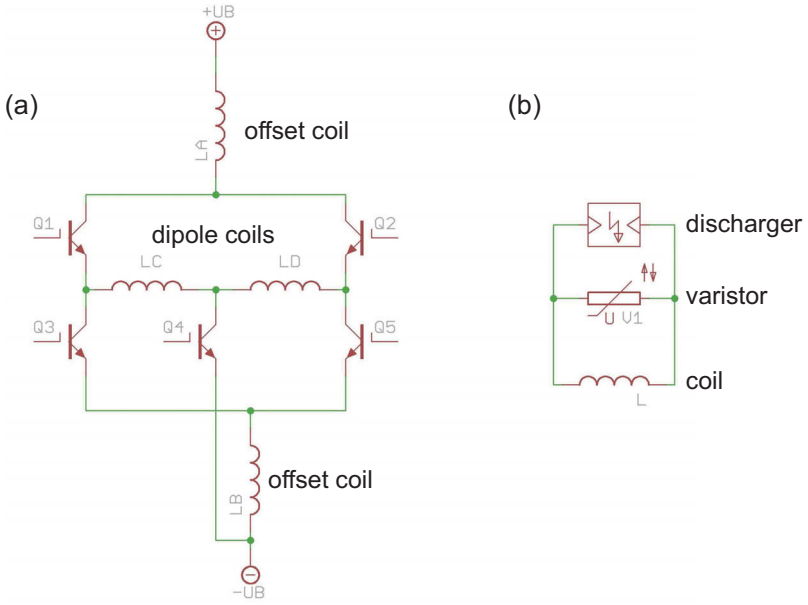

Figure 3.3: *(a) Circuit diagram used for obtaining the desired magnetic fields in the vacuum chamber (see fig. 3.1). By controlling the output of the IGBTs Q1...Q5 the required current direction through the coils LA...LD and hence the magnetic field configuration can be chosen. (b) Electronic circuit that replaced the former ring-down circuits [4] used to get rid of the high induction currents appearing while fast switching the magnetic fields.*

ized in the $|F = 1, m_F = -1\rangle$ state) in the magnetic trap and measuring the number of atoms as a function of irradiated radio-frequency with successively varying frequency, as is shown in fig. 3.4. If the frequency is lower than the energetic difference to the next m_F-state no transitions can be induced. As soon as the frequency exceeds this difference, the atoms are transferred to untrappable spin states and a loss channel is introduced (see also fig. 7.3). The red bar in fig. 3.4 indicates a cut-off frequency of 390 kHz that corresponds to $B_0 = 550\,\mathrm{mG}$ according to the Breit-Rabi relation in eq. 7.1. This results in harmonically approximated trap frequencies of

$$\omega_x = \omega_y = \sqrt{\frac{\mu}{m}\left(\frac{B'^2}{B_0} - \frac{B''}{2}\right)} = 1.01\,\mathrm{kHz} \qquad \text{and} \tag{3.1a}$$

$$\omega_z = \sqrt{\frac{\mu}{m}B''} = 86\,\mathrm{Hz}\,. \tag{3.1b}$$

3.2 Laser systems

This section reviews the laser systems used for the experimental investigations presented in this thesis but mainly emphasizes the changes that were carried out during the course of this work. Additional information can be found in [5, 1, 6, 3].

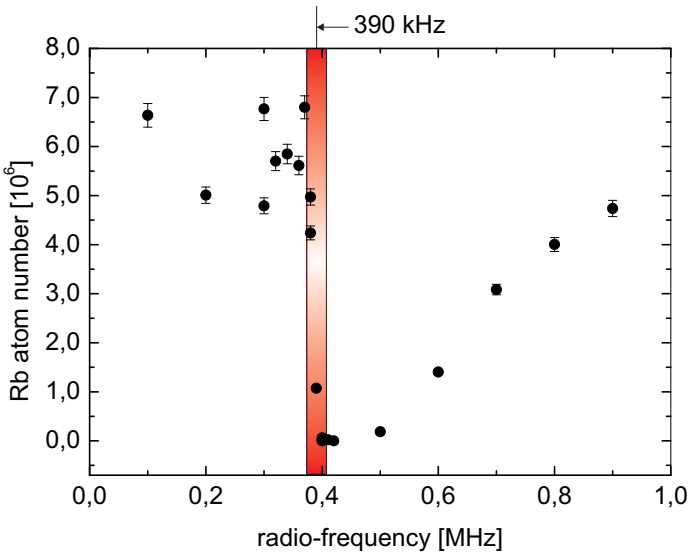

Figure 3.4: *Measurement of the magnetic field offset B_0 in the magnetic trap which represents the trap bottom. Plotted is the Rb atom number in the magnetic trap over applied radio-frequency. As soon as the radio-frequency matches the energy difference to the next m_F state depending on the offset field B_0 (see also fig. 7.3), the atoms can be transferred to untrappable states and hence a loss channel is introduced. Here, the cut-off frequency is 390 kHz corresponding to $B_0 = 550\,\mathrm{mG}$.*

The Rb laser system was essentially left unchanged apart from the fact that in addition to the usually prepared isotope ^{87}Rb in our previous experiments, the laser system was slightly modified to be able to trap ^{85}Rb which was required for the search for magnetic Feshbach resonances (see chap. 7). The Yb laser system was improved insofar as the installation of a new frequency doubling PPLN waveguide crystal with higher efficiency generates a higher output power for the green light at 556 nm. The photoassociation laser system was modified in order to extend the characterization of the excited molecular RbYb state in a combined conservative trap (see chap. 5) beyond the results obtained in [1, 7]. Finally, the laser systems for the optical dipole traps are described consisting of the infrared ODT_{1064}, $\mathrm{ODT}_{1064,2}$ and the crossed ODT at 1064 nm, as well as the green ODT_{556} at 556 nm. This includes the implementation of a motorized translation stage that is used to move the focussing lens during the experiment.

3.2.1 Rb laser system

Cooling and trapping Rb

As was already mentioned, the Rb laser system is basically the same as in our previous experiments [6, 109, 3]. The Rb MOT is operated on the D_2 transition $5^2S_{1/2} \rightarrow 5^2P_{3/2}$ at 780 nm whose detailed hyperfine substates are illustrated in fig. 3.5. This transition has a linewidth of $\gamma_{780} = 2\pi \times 6.06\,\mathrm{MHz}$ [140] and the limiting Doppler temperature is 146 µK [91]. The difference between the two isotopes ^{87}Rb and ^{85}Rb becomes noticeable in the

exact values for the hyperfine structure due to a different nuclear spin of $I = 3/2$ and $I = 1/2$, respectively. In the following, I will therefore treat both isotopes in parallel and give the values for ^{85}Rb in brackets (...).
The main transition for cooling, trapping and imaging is the $|F = 2\rangle \rightarrow |F' = 3\rangle$ ($|F = 3\rangle \rightarrow |F' = 4\rangle$) transition addressed by the so-called *MOT Master* laser (see fig. 3.5 and fig. 3.6). The MOT Master is operated with a variable detuning $\delta = 0... - 60\,\mathrm{MHz}$ from resonance. But due to a small hyperfine splitting there is a small possibility to excite the atoms into the $|F' = 2\rangle$ ($|F' = 3\rangle$) state by off-resonant excitation which then decays to the $|F = 1\rangle$ ($|F = 2\rangle$) state. As a result, the atoms are lost from the cycling transition crucial for MOT operation and a *Repumper* laser is needed to pump them back and produce a closed cycle. This addresses the $|F = 1\rangle \rightarrow |F' = 2\rangle$ ($|F = 2\rangle \rightarrow |F' = 3\rangle$) transition. In order to selectively enhance the population of the $|F = 1\rangle$ ($|F = 2\rangle$) Rb ground state a *Depumper* is utilized that drives the $|F = 2\rangle \rightarrow |F' = 2\rangle$ ($|F = 3\rangle \rightarrow |F' = 3\rangle$) transition. This occurs only in the case of photoassociation experiments in the continously loaded combined Dark Spot MOT [1, 145] (in this thesis only as reference) or shortly before loading the Rb magnetic trap.

Laser system

The complete laser system for Rb is depicted in fig. 3.6 and is based on four laser diodes (Sharp GH0781JA2C, specified as 120 mW, 784 nm). The MOT Master is an external cavity diode laser (ECDL) in Littrow-configuration [146] and the Repumper laser is a narrow band interference filter based laser system [147]. Both produce an output power of $\approx 20\,\mathrm{mW}$. While this is enough in the case of the Repumper, the main cycling transition requires a higher intensity. In order to generate sufficient optical power for MOT operation

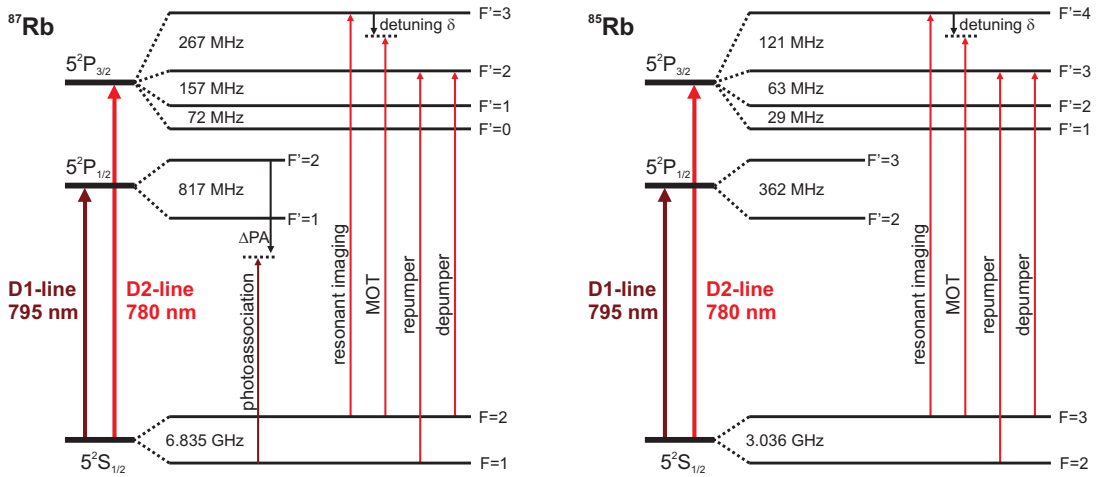

Figure 3.5: *Level diagram of ^{87}Rb and ^{85}Rb belonging to the Rb D_1 and D_2 line (adapted from [3, 143]). Due to a different nuclear spin of the isotopes the quantum number of the hyperfine structure and the hyperfine splitting differs. The energetic splitting is taken from [140, 144].*

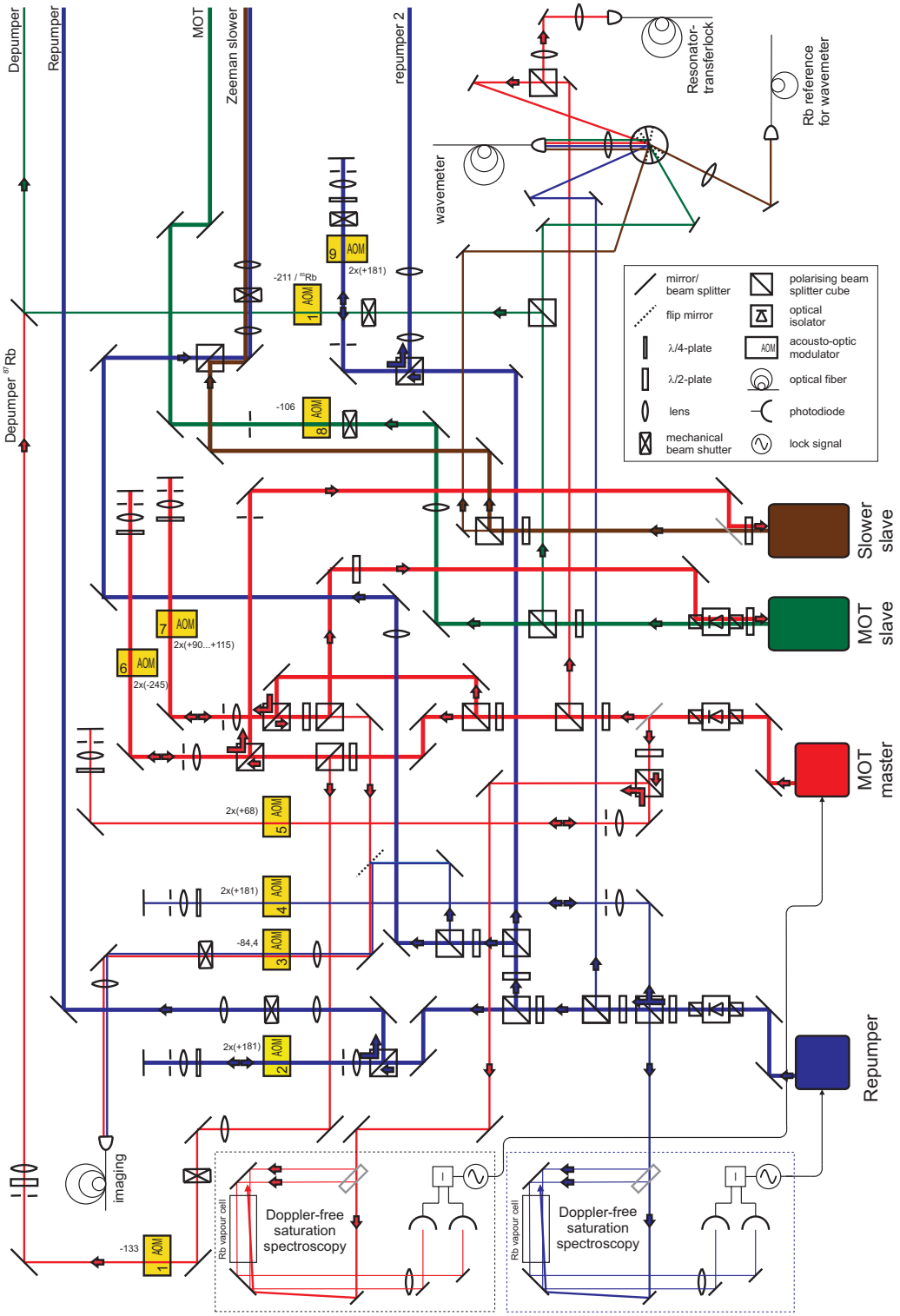

Figure 3.6: *Rubidium laser system (adapted from [109]). It is essentially the same as was used in our previous works [6, 109, 3]. The only modification is the Depumper beam for* ^{85}*Rb that was taken from the MOT slave beam.*

and Zeeman slower, the Master laser injects two slave lasers (*MOT slave* and *Slower slave*) that produce a usable output power of $\approx 60..70\,\mathrm{mW}$. The MOT laser beam is split into 6 independently adjustable branches with the axial MOT beams containing only half of the radial MOT beams' intensity.
The exact frequencies that are needed are achieved by fine tuning them using acousto optic modulators (AOMs) which are also used for fast switching. Both, the Repumper and the Master laser, are frequency stabilized to the respective atomic transition by Doppler-free saturation spectroscopy in Rb vapor cells [148] that provide the absorptions signals (see fig. 3.7). Frequency modulation of these AOMs and subsequent demodulation using lock-in techniques provide the dispersive signals for locking the lasers on the desired frequency. The imaging light ($\approx$ 500 µW) is provided by splitting off a part of the master laser. The Depumper beam ($\approx$ 20 µW) was taken from the MOT slave in order to be able to adjust the frequencies for the different Rb isotopes. For the photoassociation experiments in the conservative trap with ^{87}Rb it was not needed anymore to improve the transfer into the magnetic trap in contrast to previous works [6]. For this purpose, the effect of the Depumper could also be achieved by ramping down the intensity of the Repumper shortly before loading the MT out of the MOT. However, the Depumper was used for ^{85}Rb and for photoassociation experiments in the combined MOT. Additionally, the mechanical beam shutters were replaced by speaker shutters due to a lower disturbance for the lasers and better experimental feasibility.

3.2.2 Yb laser system

Cooling and trapping Yb

Yb has two closed cycling transitions with different properties that are used to cool and trap Yb in our setup (see fig. 3.8). The first transition $^1\mathrm{S}_0 \rightarrow {}^1\mathrm{P}_1$ at 398.9 nm has a relatively large linewidth of $\gamma_{399} = 2\pi \times 28\,\mathrm{MHz}$ [149] with a Doppler-limit of 672 µK and is thus used for fast deceleration in the Zeeman slower and for imaging of the atomic clouds. The second one is the intercombination transition $^1\mathrm{S}_0 \rightarrow {}^3\mathrm{P}_1$ at 555.8 nm with a narrow linewidth of $\gamma_{556} = 2\pi \times 181\,\mathrm{kHz}$ [149] which is utilized as MOT transition leading to a Doppler limit of 4.4 µK. Since the vapor pressure for Yb is pretty low a Doppler-free saturation spectroscopy cannot be arranged as easy as for Rb and hence fluorescence spectroscopy on a collimated Yb beam in a separate vacuum chamber is performed creating a spectroscopy signal displayed in fig. 3.9.

Blue laser system

The blue laser system was left practically unchanged as compared to [6, 3]. It is composed of two laser diodes in master/slave configuration (master diode: Nichia NDHV310ACAEI, rated 30 mW at 399 nm; slave diode: Nichia NDHV310APC, rated 60 mW at 401 nm) which produce a useable output power of $\approx$ 18 mW for the Zeeman slower. The master diode is a self-made ECDL which generates the light for the spectroscopy, imaging and injection of the slave laser. Figure 3.10 illustrates the setup including the adjusted power

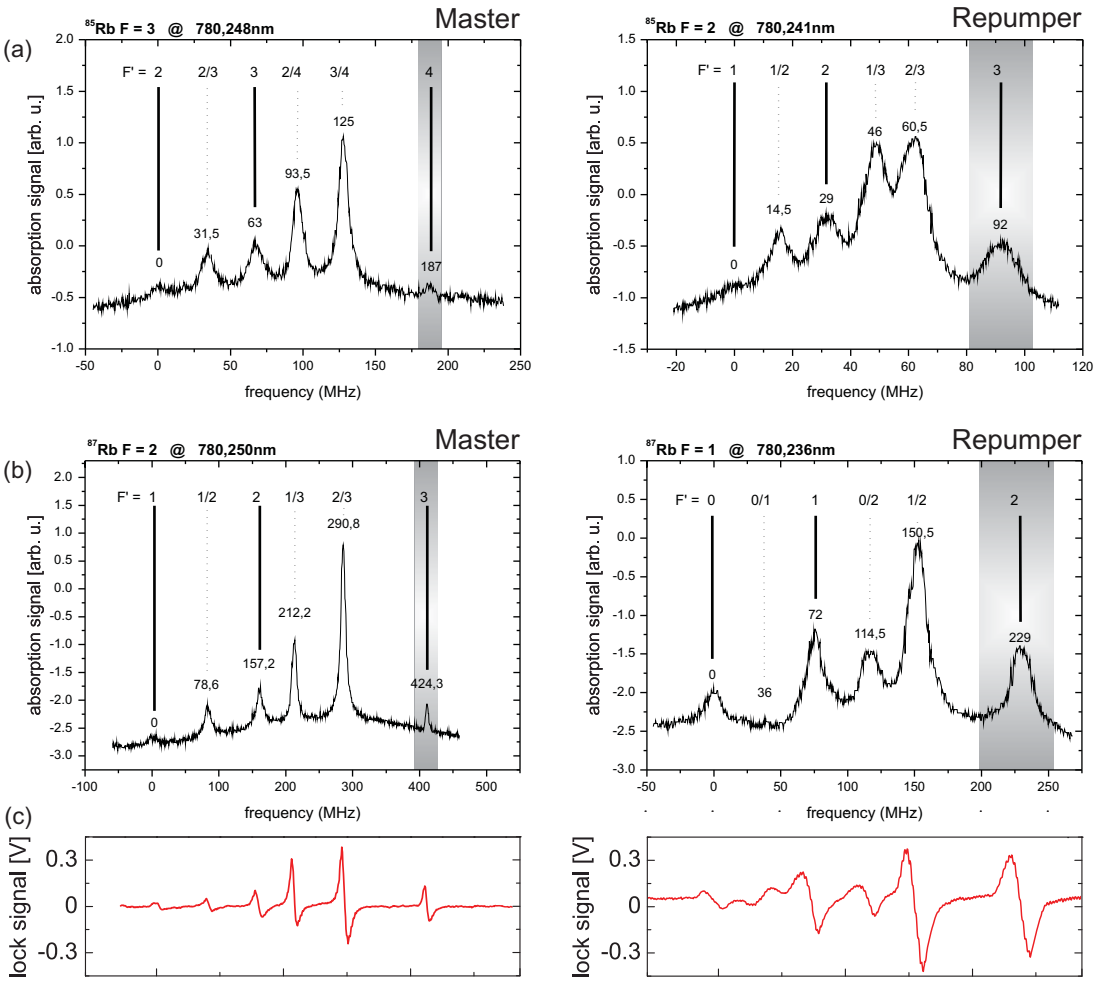

Figure 3.7: *Doppler-free saturation spectroscopy for (a) ^{85}Rb and (b) ^{87}Rb (adapted from [6, 143]). The peaks used for stabilization are marked. (c) Dispersive signal for ^{87}Rb created by lock-in techniques used for frequency stabilization.*

distributions. The only innovation is the implementation of a cavity with a higher finesse for an improved control of single mode operation of the slave laser. Similar to the Rb setup, the exact frequencies are adjusted by means of AOMs and the dispersive signal for frequency stabilization is achieved by lock-in-techniques (see fig. 3.9). By stabilizing the laser on the proper line it is easily possible to trap any Yb isotope.

Green laser system

Contrary to the blue laser system, the green laser system was modified in several respects compared to the previous works [1, 6, 3]. The green light is still provided by frequency doubling the infrared light at 1112 nm (Koheras Boostik BoY10PztS) with an output power of $P = 1\,\mathrm{W}$ and a linewidth of $\gamma_{1112} < 10\,\mathrm{kHz}$. But the previously employed frequency doubling PPLN crystal with an output power of 30 mW at a temperature of 180°C was

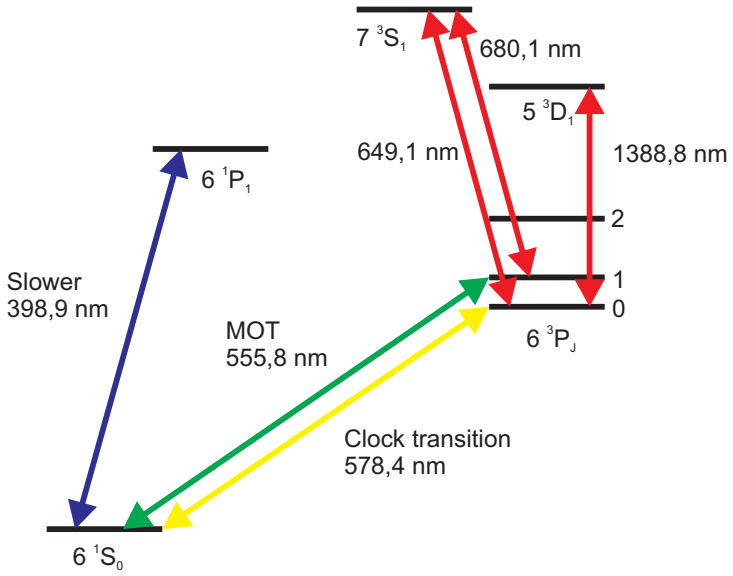

Figure 3.8: *Reduced schematic level diagram for Yb displaying the most important transitions [150]. In this experiment, only the transitions for slower (blue arrow) and MOT (green arrow) are used. Yb also exhibits a narrow transition that can be used for optical clock operation [151] (yellow arrow) and other possible repumping transitions (red arrows).*

replaced by a novel PPLN waveguide crystal (MenloSystems GmbH, WH-0556-000-A-B-C) yielding typically 200 mW output power at a temperature of $\approx$ 52.5°C. Figure 3.12 (a) shows the output power at 556 nm as a function of crystal temperature around the absolute maximum. It introduces a sharp maximum with a sensitive dependence on the temperature at the level of a few mK.

The light at 1112 nm needs to be coupled into a fiber which guides the light to the crystal. The achieved green output power is plotted in fig. 3.12 (b) against the utilized infrared power directly in front of the fiber. Residual infrared light which simply passes the crystal without being frequency doubled is absorbed at the output facet of the crystal by an IR filter. Therefore, fig. 3.12 (b) gives only an idea of the conversion efficiency of the crystal because the exact light at 1112 nm inside the crystal is not known. Assuming a coupling efficiency of $\approx$60% for $P_{1112} = 700$ mW and an output power of $P_{556} = 200$ mW the conversion efficiency yields $\eta = 163\,\%/\mathrm{W}$.

A sketch of the green laser setup is shown in fig. 3.11. The minimum reflected light ($\approx$ 3 mW) of the first PBS cube is used for the spectroscopy signal. The dispersive signal used to stabilize the frequency of the laser is produced by modulating the center frequency of +97 MHz of AOM1. AOM2 is placed in the beam when stabilizing the laser frequency in order to trap the fermionic Yb isotopes (for details see [6]). Here, the frequency is set to +78 MHz to trap ^{171}Yb (fig. 3.9 (c)). The linewidth of the resulting spectroscopy signal was estimated to be $\approx$ 8 MHz which is caused by residual Doppler broadening, but is nevertheless good enough to ensure stabilization of the laser at the level of the atomic

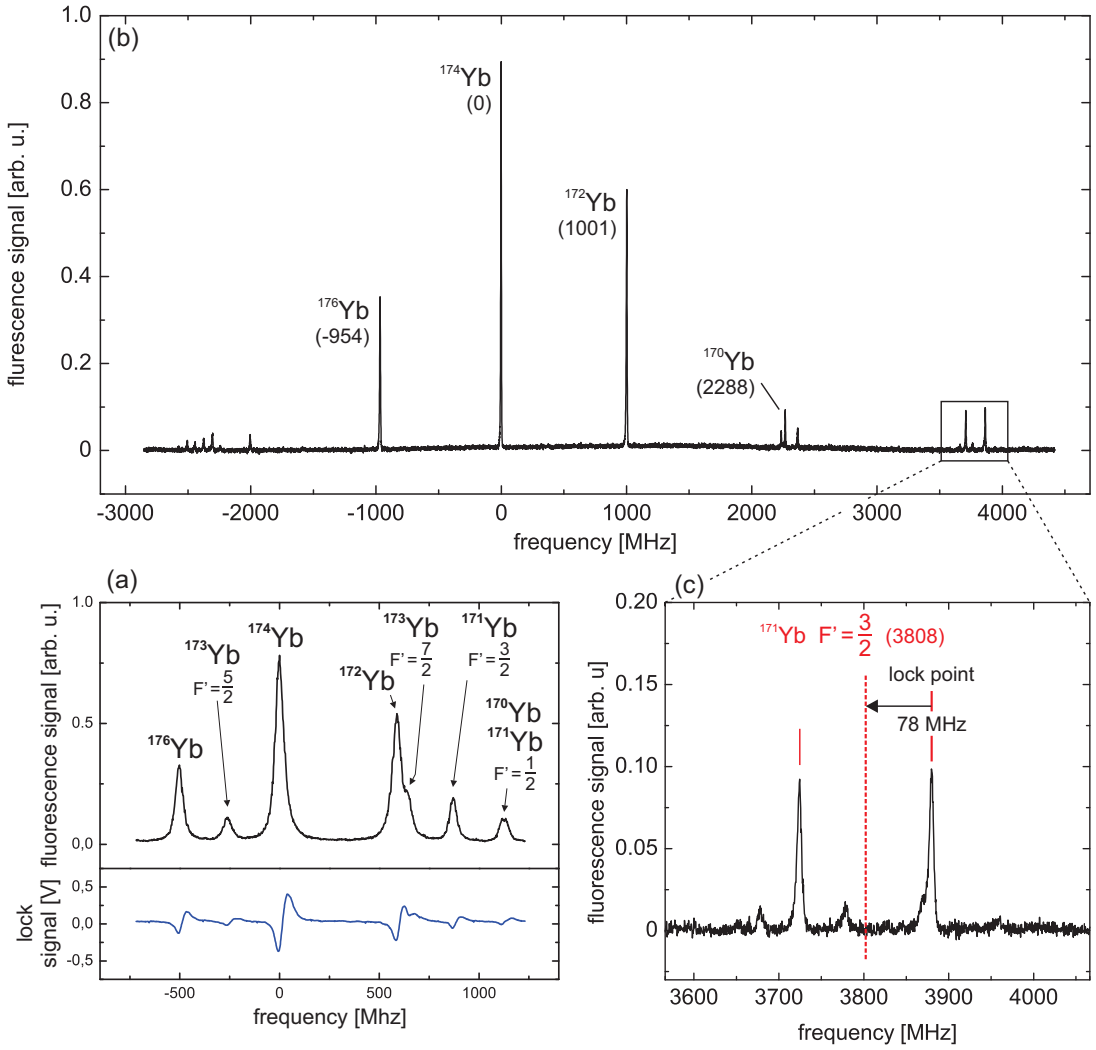

Figure 3.9: *Ytterbium spectroscopy signal (from [6]). (a) Spectroscopy at 399 nm with dispersive signal used for frequency stabilization. (b) Spectroscopy at 556 nm. (c) Enlarged signal for stabilizing the green laser on the frequency needed for ^{171}Yb. A defined magnetic field in the spectroscopy vacuum chamber shifts the right peak 78 MHz from the needed lock point.*

linewidth (180 kHz) and allow for stable MOT-operation and transfer into the optical dipole trap (sec. 4.1.1).

AOM3 is used for fast switching and controlling the frequency as well as the intensity during the experimental cycle. It has an adjustable center frequency of +88...+100 MHz which results in a detuning of $\delta = -9... + 3$ MHz from the atomic resonance. As was already mentioned above, the small linewidth of $\gamma_{556} = 2\pi \times 181$ kHz of the $^1S_0 \rightarrow {}^3P_1$ transition results in a low Doppler-limit but also in low loading rates. Within the work described here, sidebands with a spacing of 120 kHz over a range of 2 MHz were added to the center frequency of AOM3. This corresponds to an artificial broadening of the

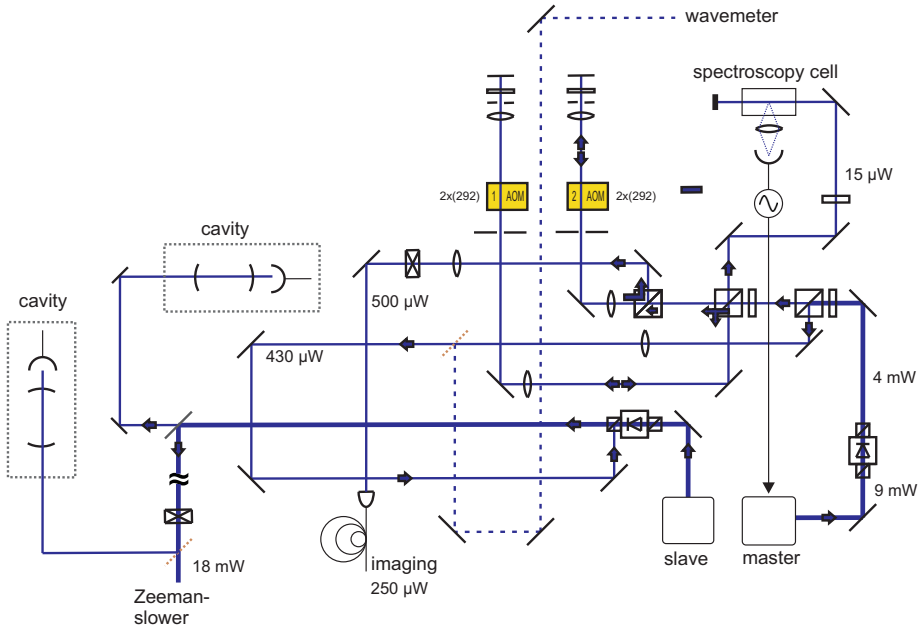

Figure 3.10: *Laser system at 399 nm that generates the light for the Yb Zeeman slower showing crucial power distributions (adapted from [109, 6]).*

transition which has the impact of an increased loading rate in the green MOT . These sidebands are switched off before transferring the atoms into the ODT so that low MOT temperatures can be achieved.
After AOM3 there are 150 mW of green light available for the experiment that are divided into three branches for the three backreflected arms of the MOT. This increased usable power allows for an increased capture volume of the green MOT by enlarging the MOT beams by a factor of 2 to a diameter of ≈ 2 cm. The relative power distribution of the three branches was left unchanged with the intensity of the axial beam containing only half of the radial beams' intensity. Together with the implemented sidebands this leads to a faster loading of the Yb MOT with a larger atom number simplifying the experiment.

3.2.3 Photoassociation laser system

The photoassociation laser system, which is illustrated in fig. 3.14, was modified compared to previous experiments [1, 109, 3] with the objective of investigating the excited molecular state further and in more detail in the hybrid conservative trap. The previously used commercial laser (Toptica DL pro) could only reach a maximum wavelength of ≈ 796 nm with a reasonable output power. In order to find deeper bound vibrational levels close to the Rb D_1-line at 795 nm a new laser diode (from now on called *PA-laser*) (eagleyard Photonics, EYP-RWE-0810-03010-1300-SOT02-0000, rated 80 mW) was installed which can be tuned over a larger wavelength range from 770...810 nm. The mechanical setup is our usual self made ECDL-setup [146]. This laser with an output power of $14 - 30$ mW, according to the laser settings (operated conservatively), injects the same tapered amplifier (TA) (m2k

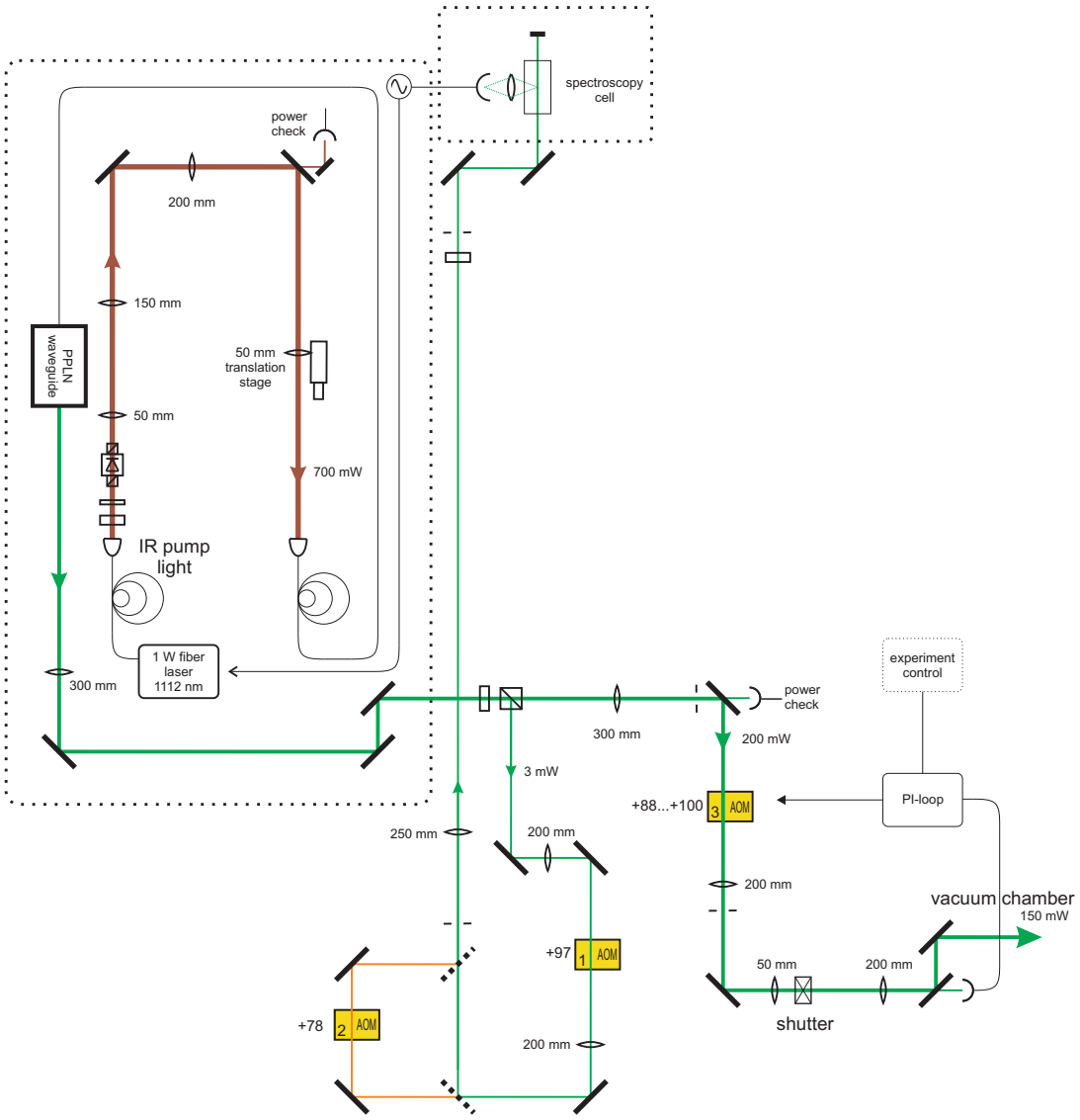

Figure 3.11: *Laser system for the green light used for the Yb MOT. The crucial modification is the PPLN waveguide crystal with a higher conversion efficiency of* $\eta = 163\,\%/\mathrm{W}$ *as displayed in fig. 3.12 that produces a typical output power of 200 mW. For more information see text.*

TA-0800-0500, rated 500 mW at 790-810 nm) from [109, 3] which yields an output power of $\approx 400\,\mathrm{mW}$. After optical isolation, adjustment through an AOM to create well-defined pulses and fiber coupling to increase the position stability there are $\approx 100\,\mathrm{mW}$ with a beam waist of 230 µm (fig. 3.13) available for the experiment leading to a maximum intensity of $\approx 120\,\mathrm{mW/cm^2}$ at the estimated position of the atoms.

One crucial drawback of the tapered amplifier is that it suffers from a large amplified spontaneous emission (ASE) background. If the experiment is performed in a MOT where the Rb atoms are continuously exposed to near-resonant light, this background has no effect.

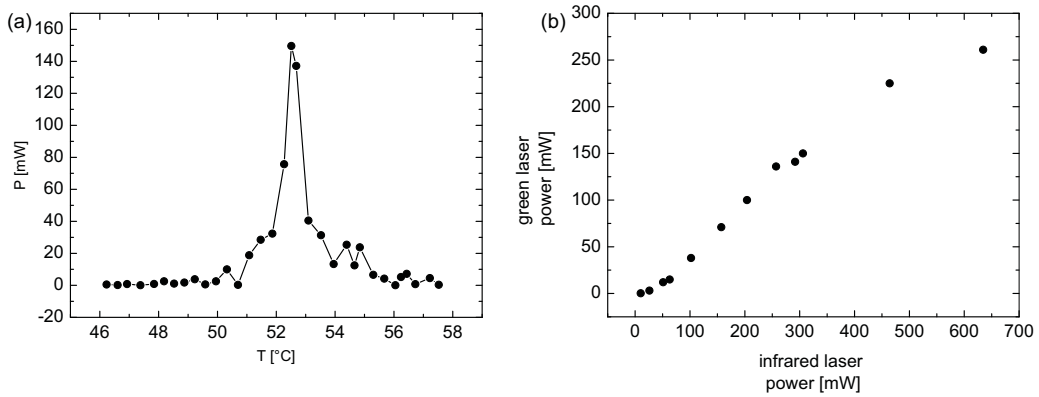

Figure 3.12: *Characterization of the novel implemented frequency doubling waveguide at 556 nm used for the Yb MOT. (a) Frequency doubled output power at 556 nm as a function of crystal temperature around the maximum. There is one single pronounced maximum which sensitively depends on the applied temperature. The lines connecting adjacent points are only a guide-to-the-eye. (b) Output power at 556 nm of the frequency doubling PPLN waveguide as a function of input power at 1112 nm. The input power was measured directly in front of the input fiber. For low input power a quadratic increase of output power is expected and for high power (i.e. when the complete fundamental is converted) saturation is expected. In a typical experiment, 200 mW of green light were used.*

However, due to the state dependent conservative trapping of Rb in the magnetic trap already a small amount of resonant radiation suffices to remove the atoms from the trap resulting in a reduced $1/e$-lifetime of $\tau = 9\,\mathrm{ms}$ as depicted in fig. 3.15 for a wavelength of 800.10 nm and a power of $\approx 90\,\mathrm{mW}$. By inserting a narrowband interference filter with a FWHM linewidth of 0.4 nm this lifetime is extended to $\tau_{IF} = 3.2\,\mathrm{s}$ allowing for a suitable interrogation time. However, since the interference filter does not have a spectrally sharp edge, the exposure times aiming the production of excited molecules have to be chosen according to the detuning with respect to the D_1-line (see chap. 5).
For the scans for the vibrational levels in the excited state the unstabilized frequency of the PA-laser was shifted by applying a voltage to the piezo element which was controlled by the experimental control program [1]. Here, a 16 bit channel was chosen with an output voltage of -10 V...+10 V with subsequent high voltage amplification connected to the piezo. This enables a minimum scanning step of 0.3 mV which corresponds to 0.69 MHz. The conversion coefficient of 2.25 GHz/V was obtained from calibration to a reference cavity.
Several measurements of the PA-laser drift result in values ranging from 100 kHz/min to 3 MHz/min that depend on the pressure and temperature stability in the laboratory. Figure 3.16 (a) depicts an exemplary drift of the free running PA-laser recorded with our data logger (see sec. 3.2.6) for 30 minutes relative to our wavemeter reference. The red line in fig. 3.16 (a) and (b) is a 20-point average that linear fitted (blue line) yields a drift of 3 MHz/min. The reliably working resonator transfer lock (for elaborate details see [152, 109]) was not utilized in its destined purpose as was done during our measurements

for the 2-photon photoassociation spectroscopy (chap. 6 and [3]), but still really helpful for adjustment and as absolute frequency reference. The result of the laser drift was hence cross-checked with a difference signal stemming from our resonator transferlock (fig. 3.16 (c)) that was calibrated to be $\approx 1.5\,\mathrm{MHz/mV}$. Both measurements provide the same drift of 3 MHz/min which again emphasizes the much better relative accuracy of our self-built wavemeter if averaged over long times.
The experimental cycle for the production of excited molecules takes $\approx 45\,\mathrm{s}$ (see chap. 4). This leads to a drift of $75\,\mathrm{kHz} \ldots 2.25\,\mathrm{MHz}$ between two adjacent data points. The expected linewidth of a molecular level is on the order of the Rb linewidth of $2\pi \times 6.06\,\mathrm{MHz}$. When searching for unobserved vibrational levels with a fast scan rate of $> 40\,\mathrm{MHz}$ per cycle this drift was unremarkable (see sec. 5.3.2). On the other hand, when studying the vibrational level in detail with a slow scan rate of 2...10 MHz per cycle (see again sec. 5.3.2) the laser drift might influence the experimental result. Depending on the sign of the drift relative to the scanning direction the measured linewidth of the resonance is either broader or shallower than the natural linewidth. For example, if scanning over the resonance in frequency steps of 2 MHz and assuming a laser drift of -1 MHz the measured linewidth appears to be twice the natural linewidth.
Furthermore, we have ruled out non-linear effects in the fiber, which might lead to broadening of the laser linewidth, by measuring the power dependence of the rubidium loss in the magnetic trap. Figure 3.17 shows a linear behaviour of the Rb loss rate as a function of irradiated PA-laser power. Non-linear effects would show up in the figure as a quadratic

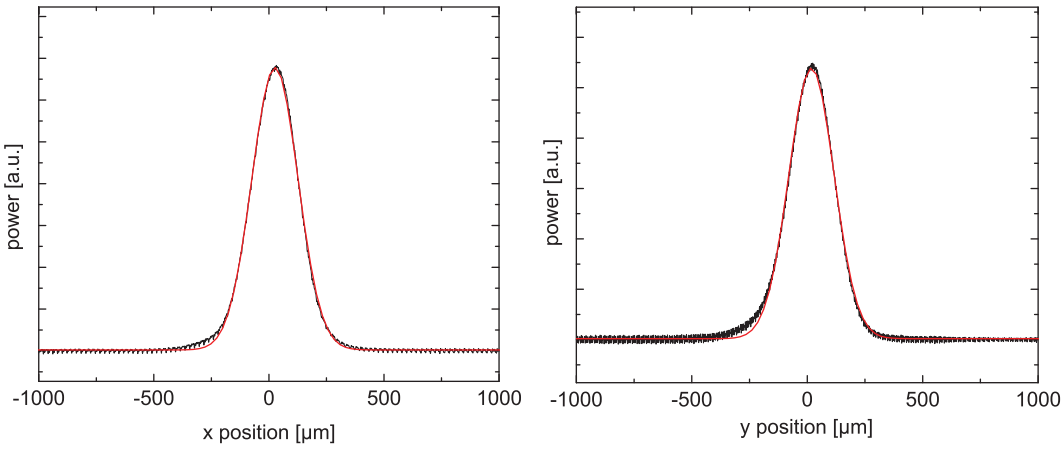

Figure 3.13: *Measured cross sections of the PA-laser beam in x- and y-direction at the position of the conservative trap (black lines). This position was determined by reflecting the ODT_{556} beam (see sec. 3.2.4) with a mirror in front of the vacuum chamber and placing the beam profiler with a micro positioning stage in the focus. This focus position represents the position of the confined atoms in the ODT. However, the effect of the bucket window was not taken into account. Thus, the actual persisting beam shape at the position of the atoms might be different. The red curves are simple Gaussian fits in order to extract the FWHM-linewidths of the beam. These are $r_{\mathrm{x,PA}} = r_{\mathrm{y,PA}} = 230\,\mu\mathrm{m}$ for both axes.*

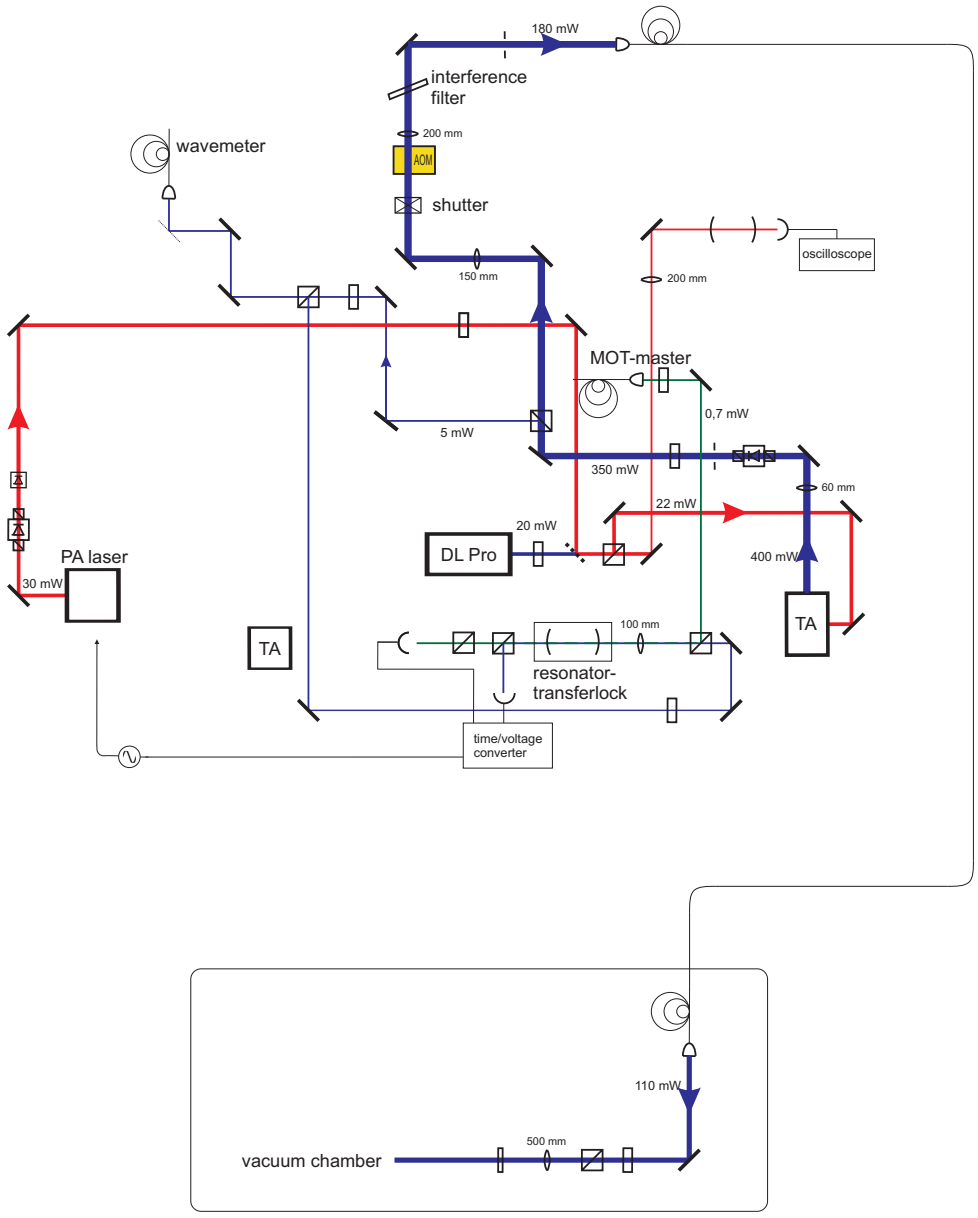

Figure 3.14: *Photoassociation laser system. Several modifications and improvements compared to [109, 3] have been carried out in order to allow for a more detailed examination of the electronically excited state of RbYb. For detailed information see text.*

dependence of the loss on the power coupled into the fiber.

3.2.4 Optical dipole trap at 556 nm

The trapping potential for Yb (complementary to the magnetic trap for Rb) is created by a near-resonant ODT_{556} at 555.95 nm. The light for the ODT_{556} is generated by frequency

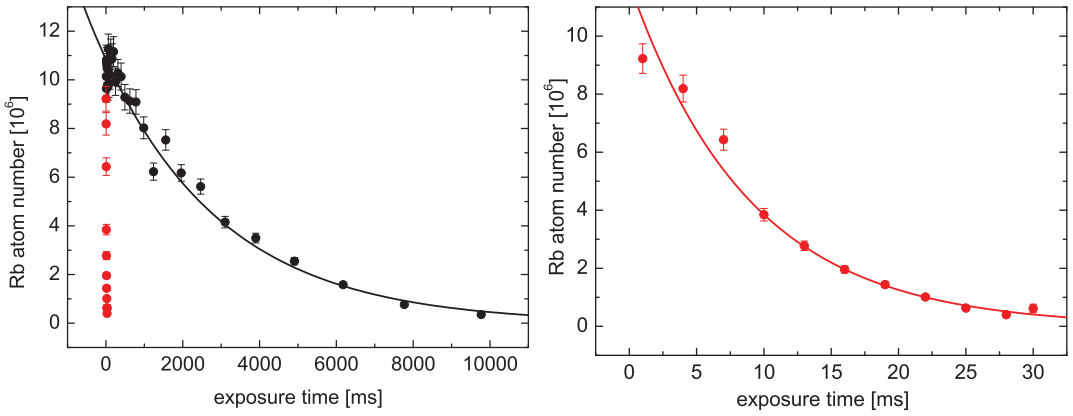

Figure 3.15: *Lifetime of the Rb atomic sample in the magnetic trap as a function of exposure time by the PA-laser with* $\approx 90\,mW$ *at a wavelength of* 800.10 nm *with (black dots) and without (red dots) interference filter. Note the difference in time scale in the figures. The right figure shows a zoom on the short timescale relevant for the Rb loss rate without interference filter. The ASE background of the tapered amplifier excites the atoms completely within 40 ms out of the trap (*$1/e$*-lifetime* $\tau = 9$ ms*, red curve, right). By implementing the interference filter the* $1/e$*-lifetime can be extended to* $\tau_{IF} = 3.2$ s *(black curve, left).*

doubling laser light at 1111.909 nm with a PPLN waveguide crystal similar to the one used for the green MOT. Figure 3.18 outlines the setup for this ODT. Frequency-stable infrared light is provided by a fiber laser (NKT Photonics). It has a fiber coupled output power of 10 mW and an intrinsic linewidth of < 10 kHz. This laser light is used to inject a slave laser diode (Toptica LD-1120-0300-1) that produces an output power of 120 mW. As usual, a cavity serves for surveying single-mode operation. By coupling the infrared light into the fiber belonging to the frequency doubling crystal, 18 mW green light are generated.
Due to the low potential depth of the ODT_{556} (see sec. 4.1.3) for Yb, it is not loaded directly out of the Yb MOT but the atoms are first captured by the ODT_{1064} (see sec. 3.2.5). The setup was therefore built in order to match the required experimental parameters.
Both ODTs are superimposed by a dichroic mirror which is highly transmitting at 556 nm (actually 532 nm) and highly reflecting at 1064 nm [5, 6]. After overlapping both beams they are focussed by the same achromatic lens ($f = 500$ mm) in order to reduce chromatic aberration which is built on a motorized translation stage (Thorlabs DDSM100 Direct Drive Translation stage). This stage, which is depicted in fig. 3.19, is driven by a Thorlabs TBD001 Brushless DC Motor T-Cube. The controller needs an external trigger which is provided by the main control program during the experimental sequence. On the right hand side of fig. 3.19 the graphic interface of the control program is illustrated that determines the target position, velocity and acceleration of the translation stage [143]. In the simplest operation mode the stage alternates between two preset positions. The maximum translation distance is 10 cm but only 1.6 cm were needed in the experiment.
The overlap of the atomic clouds is not as critical as for the BIODT and thus the position stabilization using the 4-quadrant photodiodes is not used any more [5, 6]. In order to be

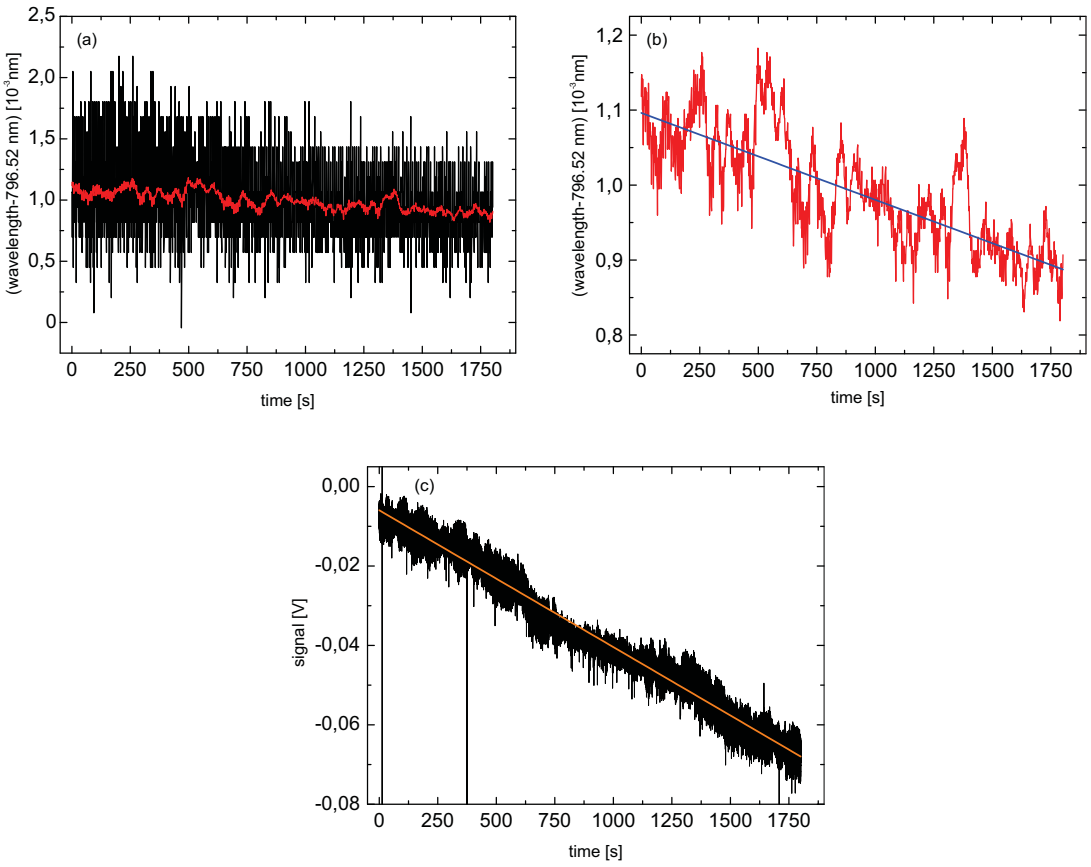

Figure 3.16: *Exemplary measurement of the drift of the not frequency stabilized PA-laser for 30 minutes. (a) Measurement with our self-built wavemeter. The black line is the raw data from the data-logging system (see sec. 3.2.6) whose fluctuations are reduced by the 20-point average displayed by the red line. (b) Zoom on the 20-point average from (a). The blue line is a linear fit to the 20-point averaged data. (c) Difference signal from our resonator transferlock system [152] (black line) with higher accuracy ($\approx 1.5\,MHz/mV$) and linear fitted (orange line). Both measurement techniques yield a drift of 3 MHz/min, which was the worst appearing drift, allowing for the investigation of vibrational levels in the excited molecular state.*

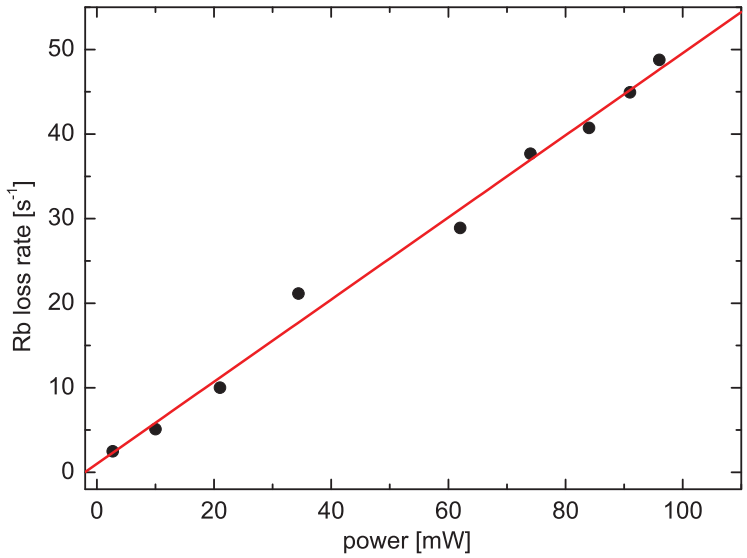

Figure 3.17: *Rb loss rate in the magnetic trap as a function PA-laser power coupled into the fiber. The linear dependence shows that broadening of the laser linewidth due to nonlinear effects in the fiber is not relevant for our experimental investigations.*

able to match the positions of the foci of the two trap laser beams at 556 nm and 1064 nm, one lens of a beam expanding telescope for the 556 nm laser is placed on a micro positioning stage. The $1/e^2$ waist of the 556 nm laser beam is $w_{556} = 11\,\mu$m (see fig. 3.20) as measured with a beam profiler with a resolution of 1 µm. One of the lenses in the beam expanding telescope of the 556 nm laser ($f = 750$ nm achromat) is mounted on a mirror mount and can thus be tilted in order to eliminate residual astigmatism.

3.2.5 Crossed optical dipole trap at 1064 nm

This subsection outlines the experimental setup for the optical dipole traps at 1064 nm used within this thesis. Those are the two single beam ODTs ODT_{1064} and $\mathrm{ODT}_{1064,2}$ which create the crossed optical dipole (CODT) if combined. The laser radiation is derived from a single ytterbium doped fiber laser (IPG PYL-20M-LP, rated 20 W) with 12 W usable power and the optical setup for both beams is illustrated in fig. 3.21.

Single beam ODT_{1064} The ODT_{1064} realizes the intermediate trapping and storage of Yb during the preparation of ultracold Rb (see chap. 4). The optical setup for this beam (solid lines in fig. 3.21) was almost left unchanged compared to [5] except for the achromatic lens ($f = 500$ mm) which focusses the ODT_{1064} and the ODT_{556} into the vacuum chamber. It was placed on a motorized translation stage (see sec. 3.2.4) to be able to shift the atomic sample during the experimental cycle.
After optical alignment for the ODT_{1064}, $P = 4$ W of infrared light are focussed to a measured waist of $w_{1064} = 15\,\mu$m in a typical experiment. The 4-quadrant photodiodes that were previously used for position stabilization were here used as a reference.

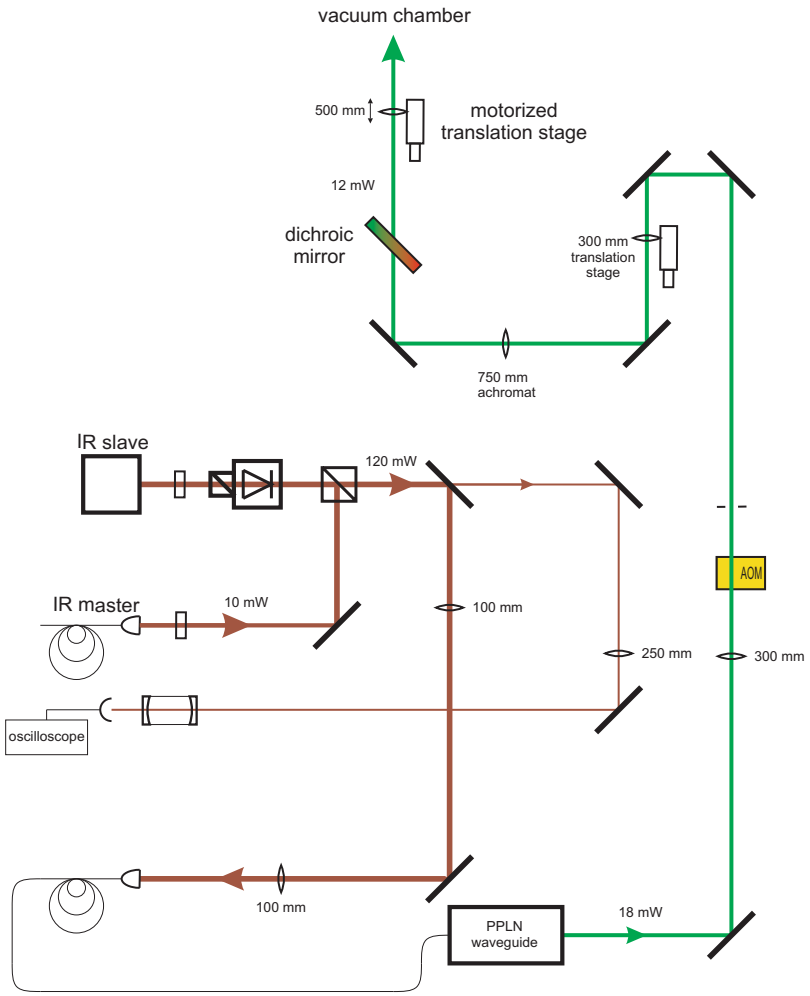

Figure 3.18: *Setup for the ODT_{556}. The green light at 555.95 nm is generated by frequency doubling the light at 1111.909 nm using a PPLN waveguide crystal. 120 mW infrared light is converted into 18 mW green light. The ODT_{556} and the ODT_{1064} are superimposed at the dichroic mirror and focussed by the $f = 500$ mm achromatic lens on the motorized translation stage (see also sec. 3.2.5). For more information see text.*

Crossed optical dipole trap (CODT) An additional optical path for the $ODT_{1064,2}$ (dashed lines in fig. 3.21) was implemented during the search for magnetic Feshbach resonances (see chap. 7) in order to increase the Rb density by means of a crossed optical dipole trap. With the help of a polarizing beam splitter (PBS) a part of the infrared light is split from the main beam. The optical setup for the $ODT_{1064,2}$ is essentially a copy of the setup for the ODT_{1064} with the difference that the design focus is a factor of ≈ 1.5 larger. After passing an AOM, which is as usual used for fast switching and power stabilization, the beam is focussed by a $f = 750$ mm-lens to a waist of $w_{1064,2} = 25\,\mu$m. While the $ODT_{1064,2}$ was occasionally also used as a single optical dipole trap (see fig. 7.8) its main purpose is to create a crossed dipole trap together with the ODT_{1064}. The crossing

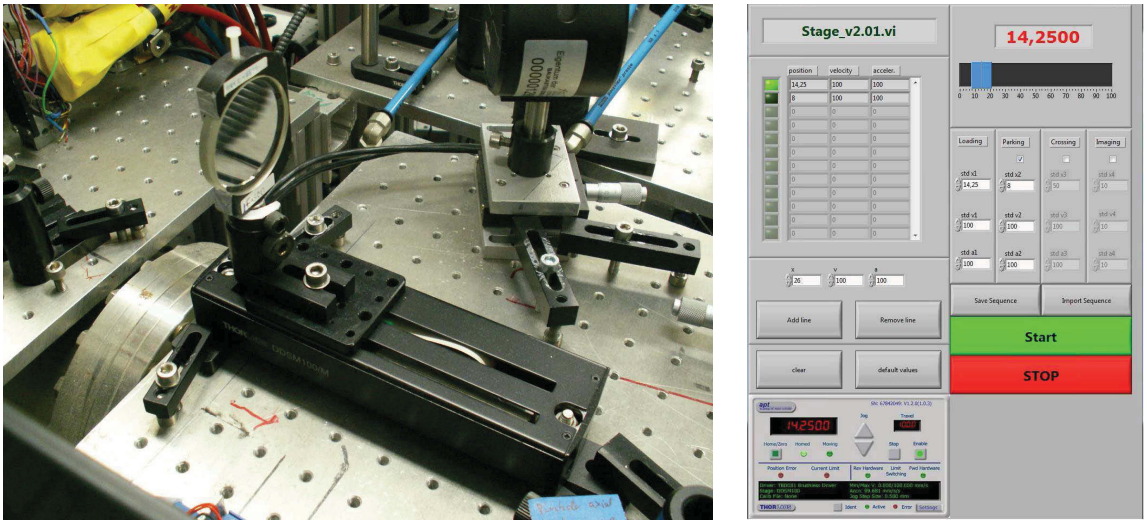

Figure 3.19: *(Left) Picture of the newly implemented motorized translation stage (Thorlabs DDSM100 Direct Drive Translation stage) which carries the lens ($f = 500\,\mathrm{mm}$ achromat) that focusses the ODT_{556} and the ODT_{1064} into the vacuum chamber. The maximum translation distance is 10 cm. In the experiment the stage was used to move the optically trapped Yb atoms by only 1.6 cm. (Right) Graphical control interface that controls position, velocity and acceleration of the translation stage.*

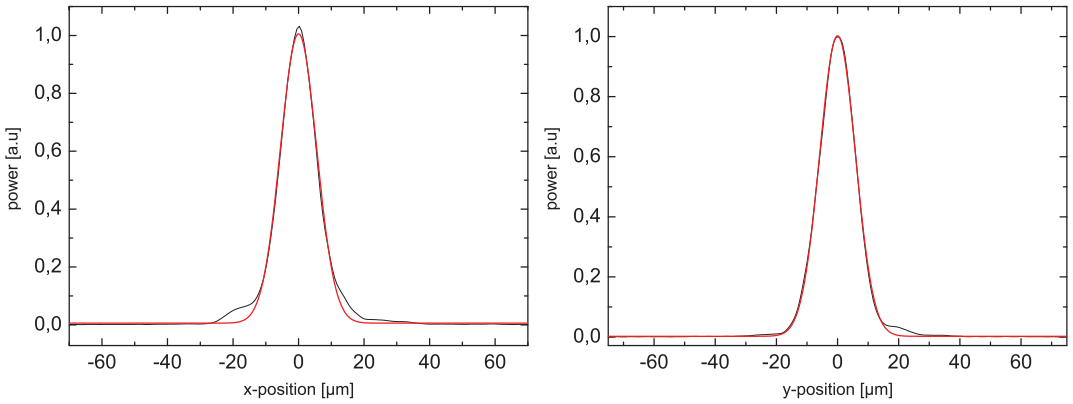

Figure 3.20: *Measured radial beam profile of the ODT_{556} in x- and y-direction (black lines) using a beam profiler with a resolution of 1 µm. It was measured by reflecting the beam in front of the vacuum chamber with a mirror and placing the beam profiler with a micro positioning stage in the focus of the ODT_{556}. Again, the effect of the bucket window was not taken into account. Thus, the actual persisting beam shape at the position of the atoms might be different. The Gaussian-fits (red curves) yield a $1/e^2$-radius of $w_{556} = 11\,\mu\mathrm{m}$ in both axes.*

angle of the two beams is $\approx 10.5°$ as can be seen by means of absorption images with Rb in fig. 3.22. Details on each ODT potential and on the combined conservative trap can be found in chap. 4.
Knowledge of the beam waists is required in order to model the occurring potentials properly. The available beam profiler demands low intensities and hence the power was reduced to a minimum when measuring the beam waists. Due to thermal lensing effects in the AOMs the resulting beam waists vary slightly while operating the ODTs with the usual power. Additional to the neglected deforming effect stemming from the bucket window, the beam sizes in the vacuum chamber might vary from the measured values but give nevertheless a good approximation for the actual arising sizes.

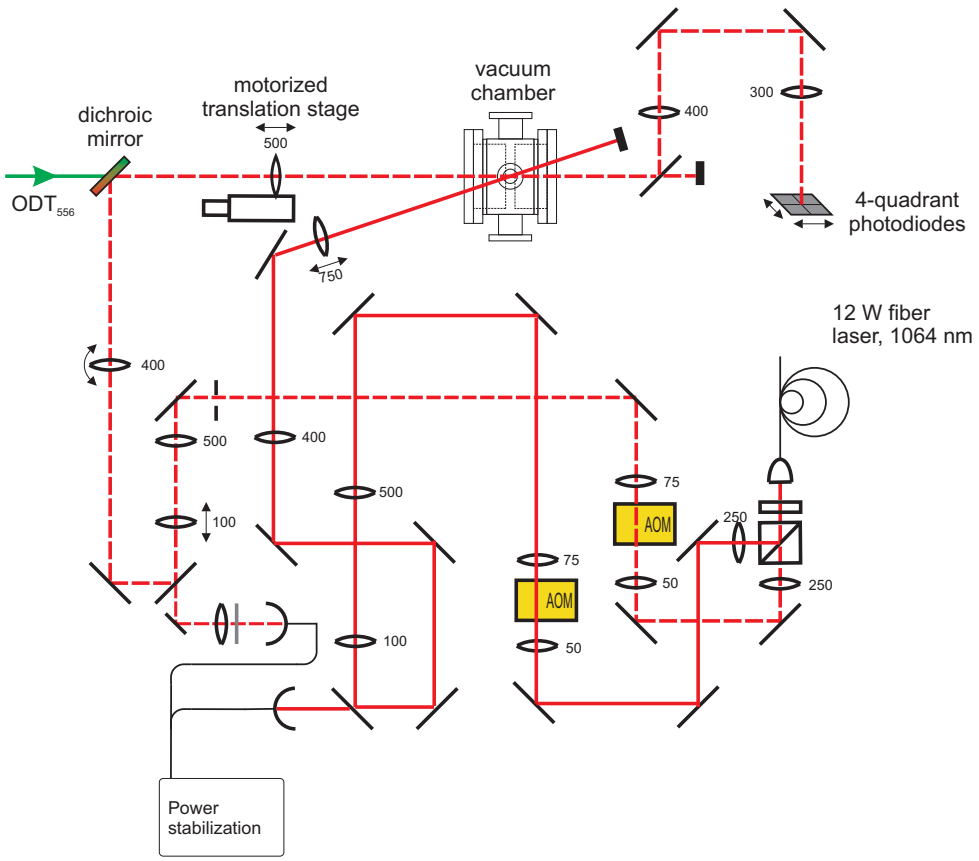

Figure 3.21: *Lasersystem of the infrared laser at 1064 nm (adapted from [143]). The output power of 12 W is split in two branches by a polarizing beam splitter. The setup for the ODT_{1064} (solid lines) was essentially left unchanged except from the newly implemented motorized translation stage (see fig. 3.19). Overlap of the ODT_{556} and ODT_{1064} takes place at the dichroic mirror. The path for the $ODT_{1064,2}$ (dashed lines) was built within this thesis in order to create the crossed optical dipole trap.*

3.2.6 Atom detection and data evaluation

The most important information of our ultracold experiments is obtained by false color absorption images of the atomic clouds of Rb and Yb. These provide the density distribution of the atomic clouds and after evaluation of the data one can gain information about the crucial physical properties. This section briefly recapitulates the way how properties like atom number, cloud size, density and temperature of the atomic samples are extracted from the absorption images.

Imaging system

Figure 3.23 displays the complete imaging setup which is practically unchanged with respect to our previous experiments [6, 3]. The installed webcams were used for adjustment purposes such as adjustment of both MOTs or PA-laser position. The CCD cameras could be utilized for adjustments as well and were additionally needed to take fluorescence images or the typically required absorption images. We used two CCD cameras of the same type (ABS Jena UK1117) variably positioned at three places providing different magnifications to image the atomic clouds. While CCD camera 2 was fixed and in general used to image the Yb cloud from the side, CCD camera 1 and 3 was the same camera built on a magnetic mount that could be switched in position when needed. Typically, camera 3 was used when imaging larger sections of the Rb atomic cloud and camera 1 when imaging the conservative trap. Calibration values for the magnification of the three imaging systems are given in table 3.2.

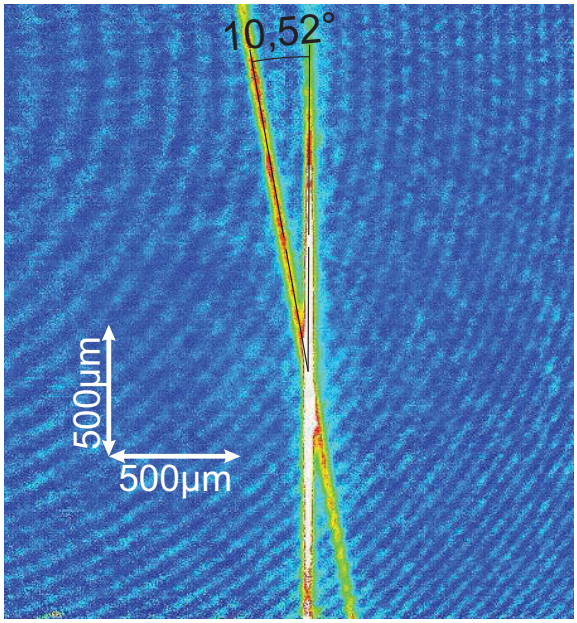

Figure 3.22: *Absorption image of Rb trapped contemporaneously in the ODT_{1064} and the $ODT_{1064,2}$. The crossing angle is 10.5°.*

CCD camera	atom	resolution [pixel × pixel]	calibration [µm/pixel]
1	Rb	768 × 567	4.05
2	Yb	768 × 567	5.83
3	Rb/Yb	768 × 567	20.3

Table 3.2: *CCD camera positions and calibrations used in the experiments.*

Principle of absorption imaging

The principle of absorption imaging relies on the attenuation of a resonant probe light with the wavelength λ_{img} when propagating through the atomic sample. With an incident intensity $I_0(y,z)$ and propagation along the x-direction, the measurable intensity distribution according to the Lambert-Beer law after passing through the atomic sample yields [5, 6]:

$$I_{\text{trans}}(y,z) = I_0(y,z) \cdot e^{-OD(y,z)} \,. \tag{3.2}$$

The optical density $OD(y,z)$ of an atomic sample is related to the column density $\tilde{n}(y,z) = \int n(x,y,z)dx$ and the resonant cross section $\sigma_0 = 3\lambda_{\text{img}}^2/2\pi$ according to

$$OD(y,z) = \tilde{n}(y,z) \cdot \sigma_0 \,. \tag{3.3}$$

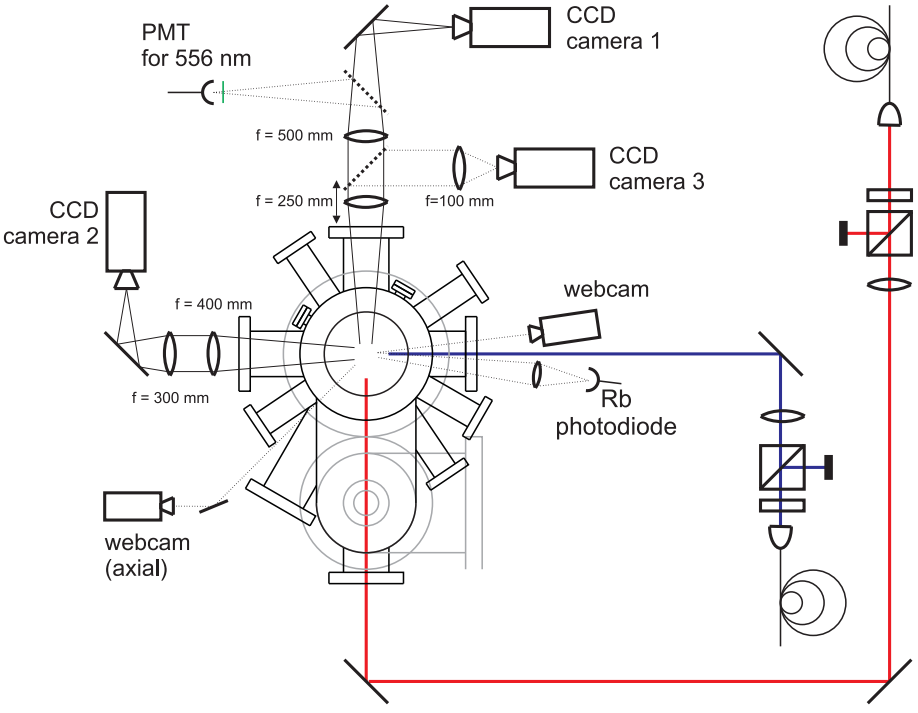

Figure 3.23: *Imaging system for Rb and Yb in our experiment from [6, 3].*

In order to reduce disturbances stemming from background noise, an absorption image measurement is composed of three pictures that image the transmitted intensity with atoms $I_{\mathrm{trans}}(y,z)$, the intensity without atoms $I_0(y,z)$ and only the background signal $I_{\mathrm{bg}}(y,z)$. The column density is consequently obtained from

$$\tilde{n}(y,z) \;= \frac{1}{\sigma_0}\, OD(x,y) = -\frac{1}{\sigma_0}\, \ln \frac{I_{\mathrm{trans}}(y,z) - I_{\mathrm{bg}}(y,z)}{I_0(y,z) - I_{\mathrm{bg}}(y,z)} \tag{3.4}$$

which leads to the atom number N after summing over all camera pixels

$$N = \frac{M}{\sigma_0} \sum_{pixels} \ln \frac{I_{\mathrm{trans}}(y,z) - I_{\mathrm{bg}}(y,z)}{I_0(y,z) - I_{\mathrm{bg}}(y,z)} \tag{3.5}$$

where M is the pixel size multiplied by the magnification of the camera.
Assuming a Gaussian density distribution, which is approximately valid for optical as well as magnetic trapping (see fig. 2.1 and fig. 2.2), the column density yields

$$\tilde{n}(y,z) = n_0 \sqrt{2\pi}\sigma_x \exp\left(-\frac{y^2}{2\sigma_y^2} - \frac{z^2}{2\sigma_z^2}\right) . \tag{3.6}$$

By fitting a 2-dimensional Gaussian shape the values that can hence be extracted out of each absorption image, additional to the atom number N, are the cloud sizes in radial direction σ_{y} and in axial direction σ_{z}. Since the atomic clouds in the trapping potentials show a cylindrical symmetry, the third dimension that cannot be directly measured is deduced from the radial width $\sigma_{\mathrm{x}} = \sigma_{\mathrm{y}}$.
In a typical experiment, both atomic clouds, Rb and Yb, are exposed to $\approx$ 300 µW resonant light for 100 µs. The three images are taken consecutively with a waiting period of 1.5 s between the images in order to download the data from the camera.

Temperature measurement

The experimental procedure used to determine the temperature of an atomic sample is a time-of-flight (TOF) method. The atoms, either captured in a magnetic trap or an optical dipole trap, are released at a well defined instant of time. The following ballistic expansion time t_{TOF} before an absorption image is taken can be varied in each step. As was described above, after taking absorption images of the atomic clouds the Gaussian cloud widths in radial and axial direction, σ_{y} and σ_{z}, respectively, are fitted. Recording these as a function of ballistic expansion time t_{TOF} and fitting the time evolution according to [153]

$$\sigma_i(t_{\mathrm{TOF}}) = \sqrt{\sigma_i(0)^2 + \frac{k_{\mathrm{B}}T}{m}\cdot t_{\mathrm{TOF}}^2} = \sqrt{\frac{k_{\mathrm{B}}T}{m\omega_i^2} + \frac{k_{\mathrm{B}}T}{m}\cdot t_{\mathrm{TOF}}^2}\,, \qquad i = x,y,z \tag{3.7}$$

gives the temperature T of the atomic sample. In combination with the trap frequencies ω_i the initial cloud size $\sigma_i(0)$ and hence the initial peak density can be deduced. On the other hand, approximate trap frequencies can be calculated from the temperature fit that provides also fitted values for the initial cloud sizes exemplary shown in fig. 3.24 following

$$\omega_i = \frac{1}{\sigma_i(0)}\sqrt{\frac{k_{\mathrm{B}}T}{m}} \qquad i = r,z\,. \tag{3.8}$$

Recording of molecular spectra

This section explains the analysis of the recorded data obtained from photoassociation experiments. Chapter 4 describes the preparation of Rb and Yb in the novel combined hybrid conservative trap. The experimental cycle to produce this ultracold mixture takes $\approx 45\,\mathrm{s}$ as will be shown in fig. 4.1. With both atomic species captured in the hybrid conservative trap, the PA-laser can be irradiated and produces excited molecules if it is resonant to a vibrational level in the excited molecular state (sec. 5.1). In order to find the vibrational levels the PA-laser is scanned over a well-defined frequency range during exposure of the atoms (see sec. 5.3.2). This results in a stair-like devolution of the PA-laser frequency over the consecutive experimental cycles as depicted in fig. 3.25. After exposure of the atoms by the PA-laser the number of remaining atoms for both atomic species are recorded via false-colour absorption images (see above). An experimental sequence consists of several consecutive experimental cycles and typically takes 20...30 minutes.
The wavelength of the PA-laser during the complete experimental sequence was measured with our self-built wavemeter [1] and recorded by the attached datalogging system. It is the same datalogger used for 1- and 2-photon photoassociation spectroscopy in [7] and [8] and is able to record 5 more analog input channels and creates an independent data file. One channel of the datalogger is connected to a TTL signal. This TTL signal marks the start and end position of the PA-laser exposure time (see again fig. 3.25). The absolute accuracy of the wavemeter is $\approx 5 \cdot 10^{-3}\,\mathrm{cm}^{-1}$ when applying a frequency stabilized laser light stemming from the Slower slave as reference. Nevertheless, the relative accuracy is much better and can estimated to be $\approx 1 \cdot 10^{-3}\,\mathrm{cm}^{-1}$. Thus, the raw data present after completion of the experimental sequence is composed of absorption images of Rb and Yb

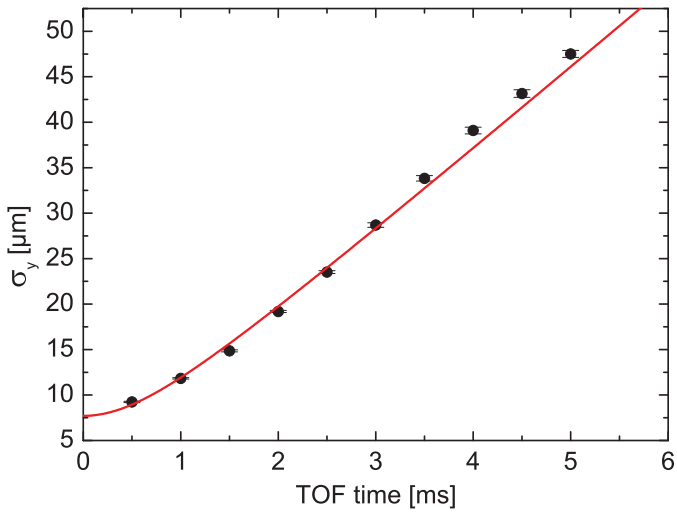

Figure 3.24: *Example of a temperature determination of an atomic sample using ^{176}Yb in the ODT_{556} in y-direction. Shown is the Gaussian fitted width of the cloud as a function of ballistic expansion time t_{TOF}. Here, the fit according to eq. 3.7 provides the temperature $T_{\mathrm{Yb}} = 1.75 \pm 0.06\,\mu\mathrm{K}$ and the initial size of the cloud $\sigma_{\mathrm{y}}(0) = 7.7 \pm 0.3\,\mu\mathrm{m}$.*

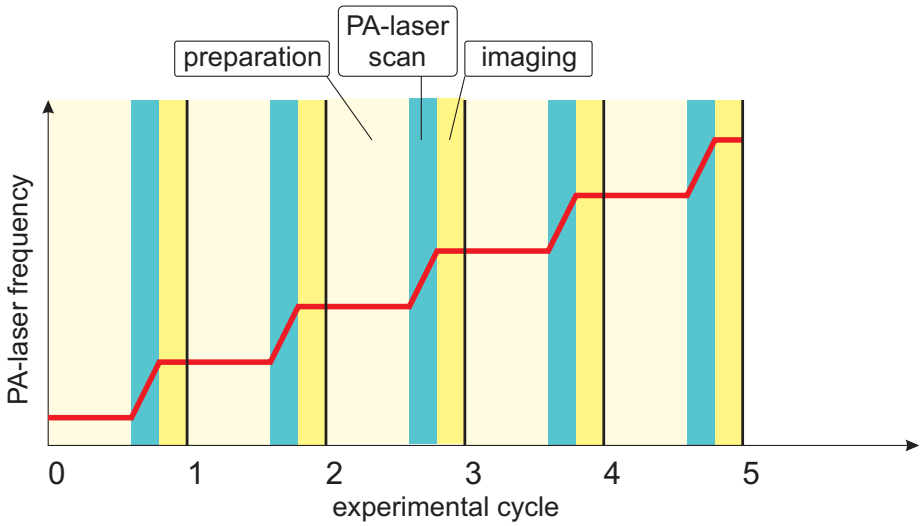

Figure 3.25: *Schematic illustration of the devolution of the PA-laser frequency during an experimental sequence. An experimental sequence is composed of several consecutive experimental cycles. While preparing the Yb and Rb atoms in the combined conservative trap the PA-laser frequency is constant. During exposure of the atoms by the PA-laser radiation the frequency is ramped for a well defined time and frequency range (see sec. 5.3.2). At the end of an experimental cycle the number of remaining atoms is measured by absorption images while the PA-laser frequency is again kept constant. This results in a stair-like progression of the PA-laser frequency during the experimental sequence.*

specifying the atom numbers and a data file containing the PA-laser wavelength as a function of time. In order to obtain a photoassociation spectrum (atom number as a function of frequency), this data has to be combined. Figure 3.26 illustrates the process of this combination, which was executed by means of an OriginPro script, that consequently yields the photoassociation spectrum and hence the precise binding energies of the vibrational levels in the excited molecular state (table 5.1).
First, the wavemeter data is edited in order to increase the accuracy of the recorded PA-laser wavelength (fig. 3.26 (a)). An imperfect wavemeter adjustment leads occasionally to wavelength values with a huge deviation from the real value. These outliers are eliminated by removing wavelength values that exceed a deviation of $> 0.001\,\mathrm{cm}^{-1}$ from the median wavenumber and are not visible in fig. 3.26 (a). The fluctuations between two adjacent points of the wavemeter data ($\approx 700\,\mathrm{MHz}$, sampling rate of $\approx 1\,\mathrm{s}^{-1}$) are in general much larger than the frequency range scanned by the PA-laser in an experimental cycle. Thus, the stair-like progression depicted in fig. 3.25 is not visible in the wavemeter data. A linear fit (red line) averages these fluctuations out.
The second step of evaluation consists in determining the exact PA-laser frequency during the exposure to the atoms in each experimental cycle. For this purpose, the above mentioned TTL signal (fig. 3.26 (b)) is differentiated which provides the instant of time of the PA-laser scanning. The wanted PA-laser frequency (blue dots in fig. 3.26 (b)) is

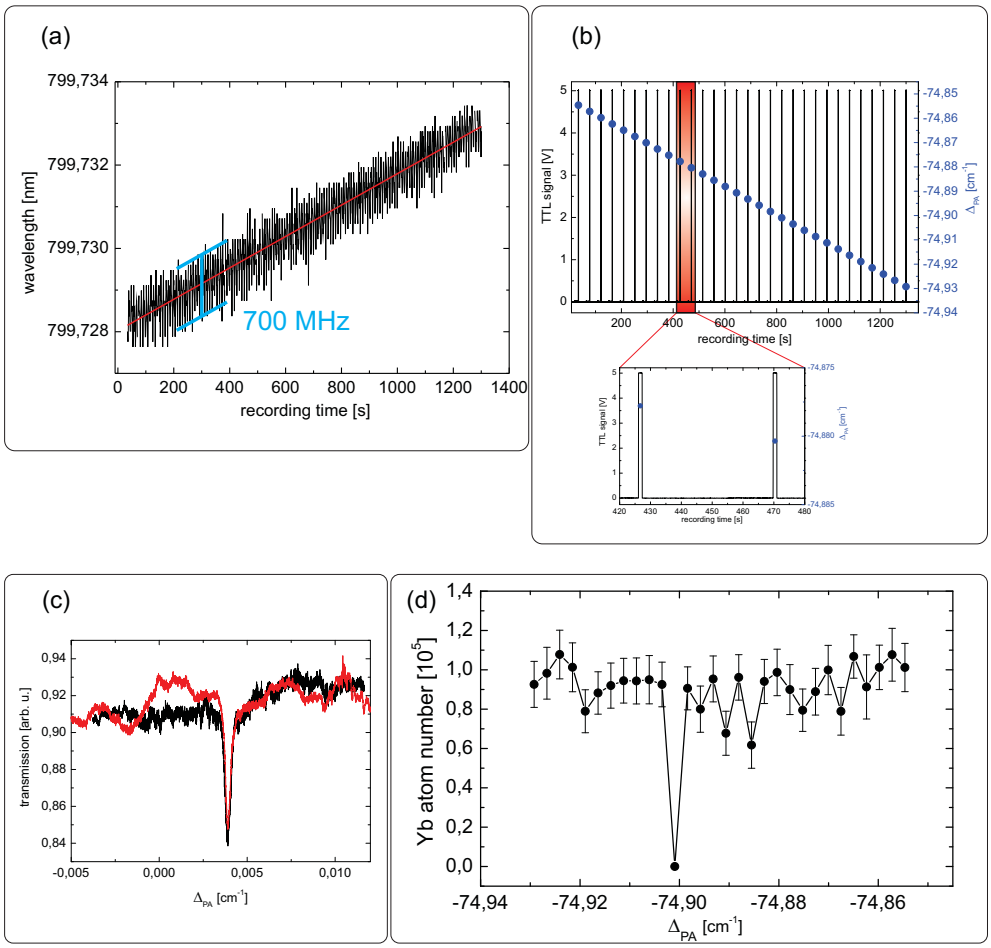

Figure 3.26: *Example of our data evaluation procedure. (a) Wavelength of the PA-laser in the course of an experimental sequence measured by our self-built wavemeter (black curve). Huge outliers are removed and the large fluctuations of up to 700 MHz in the data are averaged out by a linear fit (red line). (b) TTL signals (black lines) marking the process of PA-laser scanning in each experimental cycle. After determination of the instant of time of the TTL signals the PA-laser wavelength and hence the wavenumber* Δ_{PA} *(blue dots) at that instant is found by means of the linear fit in (a). (c) Absolute reference for calibrating our wavemeter. Shown is the absorption of the PA-laser radiation through a Rb MOT as a function of frequency. The PA-laser is continuously scanned back and forth (black and red curve) over the* $|F = 2\rangle \rightarrow |F' = 3\rangle$ *transition at* $\tilde{\nu}_{\mathrm{D1}} = 12579.1037\,\mathrm{cm}^{-1}$ *and recorded by a simple photodiode. This scan yields an offset of* $+0.0038\,\mathrm{cm}^{-1}$ *which is needed to correct* Δ_{PA} *and precisely determine the binding energy of the vibrational levels. (d) Example of a resulting photoassociation spectrum after combination of the datasets belonging to each experimental cycle. Here, the vibrational level* $\Delta v' = -28$ *was detected by trap-loss spectroscopy after plotting the remaining Yb atom number as a function of PA-laser frequency.*

obtained from the linearly fitted wavemeter data (red line in fig. 3.26 (a)) at that instant of time. Here, the PA-laser frequency is already given in wavenumbers Δ_{PA} relative to the $|F = 2\rangle \rightarrow |F' = 3\rangle$ transition of the Rb D_1 line with $\tilde{\nu}_{\mathrm{D1}} = 12579.1037\,\mathrm{cm}^{-1}$ (see sec. 5.1). Again, imperfect wavemeter adjustment might lead to an offset in the absolute wavemeter values. This offset can be precisely determined by continuously scanning the PA-laser over the Rb D_1 line and monitoring the absorption through a Rb MOT by a photodiode as is illustrated in fig. 3.26 (c). This measurement is repeated when large deviations in the absolute value of the wavelength are encountered.
Finally, the datasets belonging to each experimental cycle are combined and the atom numbers obtained from absorption imaging are plotted as a function of PA-laser frequency Δ_{PA}. This leads to a photoassociation spectrum of the type shown in fig. 3.26 (d) using the example of the vibrational level $\Delta\mathrm{v}' = -28$ (see sec. 5.3.2).

4

Preparation of Rb and Yb in combined conservative traps

This chapter describes and characterizes the preparation of ultracold rubidium and ytterbium atoms in combined conservative potentials at a temperature of a few μK that serve as experimental basis for the production of ultracold molecules. Two different types of traps were built and used within this thesis. The most promising one for future experiments is the newly implemented hybrid conservative trap (HT) which is composed of a Ioffe-Pritchard-type magnetic trap (MT) for Rb and an optical dipole trap at 555.95 nm (ODT_{556}) for Yb. The idea behind this HT is an independent trapping and manipulation of the two atomic species. It is based on the combined trap from previous experiments [5, 6] that used a MT for Rb and a bichromatic optical dipole trap (BIODT) for Yb. The BIODT was composed of a sensitive superposition of two ODTs at 1064 nm and 532 nm, respectively, and was designed to minimize the effect on Rb. However, the HT shows considerably simplified experimental considerations.
Additionally, the density enhancing crossed optical dipole trap (CODT) at 1064 nm that was implemented for the search for magnetically induced Feshbach resonances in RbYb will be discussed here.

4.1 Hybrid conservative trap

The description for the preparation in the hybrid trap (HT) will follow the experimental cycle, which is displayed in fig. 4.1, starting from an Yb MOT over the intermediate ODT_{1064} into the final ODT_{556}. Rb is transferred from a MOT into the Ioffe-Pritchard-type magnetic trap (MT). Main focus of attention is placed on the combination of optical and magnetic potentials in which both atomic species are brought into contact. Each potential is modeled and characterized by the experimentally achieved temperature, atom number (also summarized in fig. 4.1) and hence resulting densities. In the following sections, details for the consecutive experimental steps can be found.

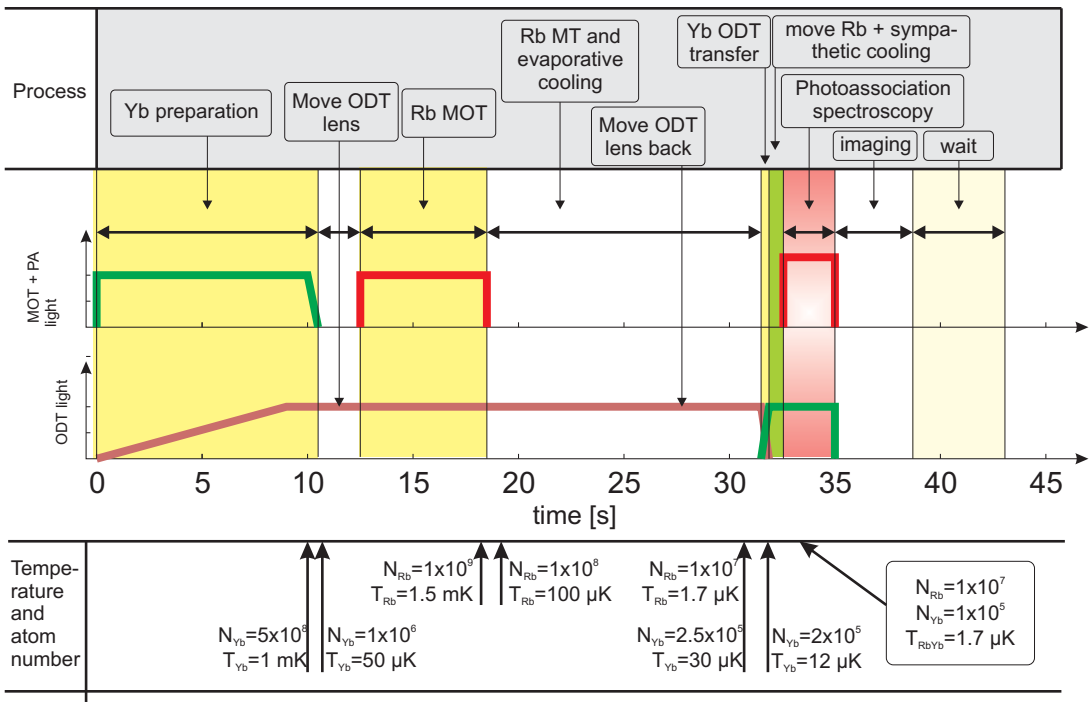

Figure 4.1: *Experimental cycle (duration ca. 45 s) for producing excited molecules in the combined hybrid conservative trap. Shown is each step together with the achieved atom number and temperature. For more details see the text.*

4.1.1 Preparation of ultracold Yb atoms

4.1.1.1 Yb MOT

As already mentioned, an experimental cycle (fig. 4.1) starts by loading an Yb MOT using the $^1S_0 \rightarrow {}^3P_1$ intercombination line at 555.8 nm which is able to capture $5 \cdot 10^8$ atoms. It is typically loaded for 10 s in order to saturate the captured atom number. The setup for the light generation is depicted in fig. 3.11. With the new frequency doubling crystal implemented in the course of this work the usable output power was increased from 30 mW to 200 mW (fig. 3.12) compared to our previous experiments [6, 3] which allows for faster loading of the Yb MOT. The MOT beams could therefore be enlarged to a diameter of 2 cm in order to guarantee a similar intensity as before with the same power distribution in the MOT beams. The narrow linewidth of $\gamma_{556} = 2\pi \times 180$ kHz leads to a low Doppler limit of 4.4 µK but also to a low loading rate.

The MOT is loaded from a Zeeman slower operated on the $^1S_0 \rightarrow {}^1P_1$ at 398.9 nm with a linewidth of $\gamma_{399} = 2\pi \times 28$ MHz and a Doppler limit of 672 µK. In order to increase the loading rate of the Yb MOT further, sidebands on the frequency modulating AOM3 (see again fig. 3.11) were added with a spacing of 120 kHz over a frequency range of 2 MHz. This has a similar effect to a broadening of the transition. The applied detuning with respect to the atomic resonance has then to be increased from $\delta = -3.5$ MHz to $\delta = -5$ MHz with

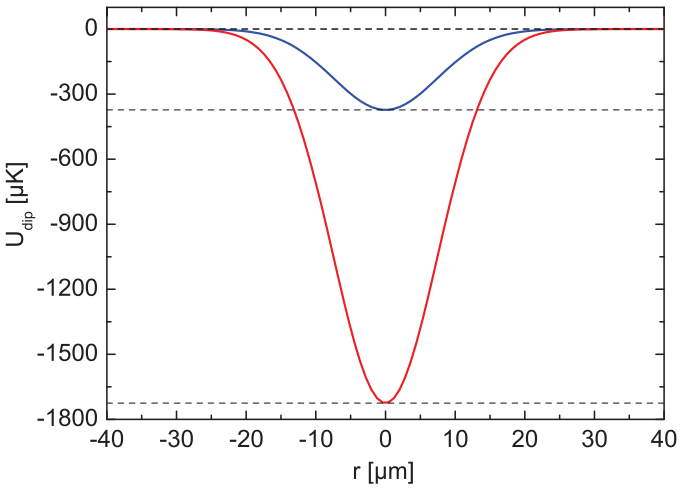

Figure 4.2: *Modeled potentials created by the ODT$_{1064}$ for Rb (red curve) and Yb (blue curve), respectively. For this calculation, the measured values of $P = 4\,\mathrm{W}$ and $w_{1064} = 15\,\mu\mathrm{m}$ were used producing potential depths of $U_{1064,\mathrm{Rb}} = -k_B \times 1720\,\mu\mathrm{K}$ and $U_{1064,\mathrm{Yb}} = -k_B \times 370\,\mu\mathrm{K}$ and hence a 4.6-times deeper potential for Rb.*

and without sidebands, respectively. The magnetic field gradient used is on the order of 4 G/cm by applying 10 A to the MOT coils (fig. 3.2). Final properties of the loaded MOT are temperatures of 1 mK and $5 \cdot 10^8$ captured Yb atoms.

4.1.1.2 Transfer of Yb atoms to the ODT$_{1064}$ at 1064 nm

After loading the Yb MOT, the atoms have to be transferred to the first stage conservative trap, the ODT$_{1064}$. The latter is produced by focussing a laser beam with $P = 4\,\mathrm{W}$ at 1064 nm to a waist of $w_{1064} \approx 15\,\mu\mathrm{m}$ (see sec. 3.2.5). According to eq. 2.12 this results in a potential depth of $U_{1064,\mathrm{Yb}} \approx -k_B \times 370\,\mu\mathrm{K}$ (see fig. 4.2) for Yb and is hence not deep enough to trap atoms out of the loading MOT efficiently. The parameters of the Yb MOT are thus varied in a way that its temperature is decreased and its density is increased in order to effectively load the ODT. Particularly, that means that the detuning as well as the intensity of the laser beams is decreased and the magnetic field gradient is increased. The sidebands modulated on the green light that are needed for faster loading are preventing efficient cooling and are thus turned off together with the slowing magnetic fields and light. The detuning needs to be ramped close to resonance ($\delta \lesssim 0\,\mathrm{MHz}$) while the power is ramped to the lowest technically possible value ($\approx 1\,\mathrm{mW}$) and the magnetic field gradient to $\approx 35\,\mathrm{G/cm}$. A characterization of the green MOT can be found in [154] together with exact settings for the transfer in the ODT$_{1064}$ that are optimized experimentally. The optimized final MOT values are $T_{\mathrm{Yb}} = 30\ \mu\mathrm{K}$ and $N_{\mathrm{Yb}} = 10^7$. The reason for the deviation from the theoretically predicted Doppler limit lies in residual heating mechanisms such as imperfect MOT adjustment. However, the achieved MOT temperatures are similar to other experiments using the transition at 556 nm for MOT operation [155, 156].
While the Yb MOT is loaded, the power of the ODT$_{1064}$ is ramped to its maximum value

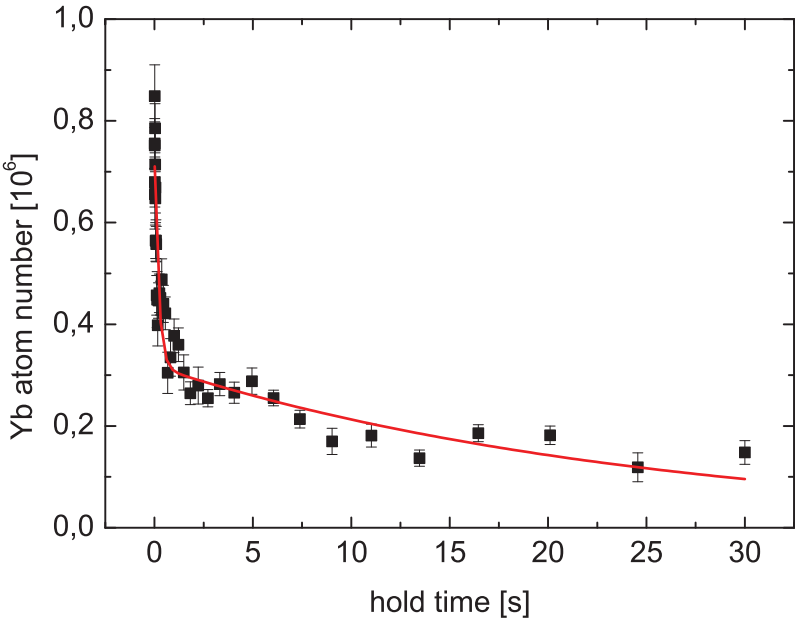

Figure 4.3: *Lifetime measurement of ytterbium in the ODT$_{1064}$. The red curve is an exponential decay fit composed of two different $1/e$-decay constants. It exhibits a small decay constant of $\tau_{\mathrm{short}} = 200\,\mathrm{ms}$ (due to plain evaporation) for the first 300 ms and a large decay constant of $\tau = 25\,\mathrm{s}$ for the rest of the experiment.*

which is then ready to store the Yb atoms. The compressed MOT is held for 100 ms on the focus of the ODT$_{1064}$ and subsequently the Yb MOT and slower lasers and magnetic fields are turned off. Typically, 10^6 Yb atoms are trapped in the ODT$_{1064}$ directly after transfer with a starting temperature of $\approx 50\,\mu\mathrm{K}$. The initial temperature of the Yb atomic sample is higher than the final MOT temperature due to adiabatic compression in the ODT$_{1064}$ [157]. Plain evaporation of the hottest atoms in the ODT leads to $3 \cdot 10^5$ atoms at 30 µK after 5 s and to $2 \cdot 10^5$ atoms after 17 s. This is the time that is needed to prepare an ultracold Rb sample (see sec. 4.1.2). The $1/e$-lifetime of 25 s (after the initial plain evaporation phase) for Yb in the ODT$_{1064}$, which is illustrated in fig. 4.3, and the low heating rate of $< 0.1\,\mu\mathrm{K/s}$ for Yb makes it useful for intermediate trapping. The calculated trap frequencies of this ODT following eq. 3.8 are $\omega_r = 2.5\,\mathrm{kHz}$ in radial direction and $\omega_z = 250\,\mathrm{Hz}$ in axial direction.

The same ODT at 1064 nm creates an approximately 4.6-times deeper potential for Rb as depicted in fig. 4.2 and hence Rb atoms at a higher temperature can easily be captured directly out of the MOT which would in turn heat the Yb atoms out of the trap. To avoid this undesired effect, the ODT$_{1064}$ containing the Yb sample is moved out of the vacuum chamber center by shifting the focussing lens by about 1.6 cm using a motorized translation stage (see fig. 3.19). Movement of the ODT does neither result in loss of atoms nor heating of the sample in this temperature regime. As a consequence, Rb can be prepared without disturbing the Yb sample.

4.1.2 Preparation of ultracold Rb atoms

As soon as Yb seeks shelter in the axially shifted ODT_{1064} the ultracold Rb sample can be prepared without further ado. Depending on the Rb isotope used, different spin projections m_F can be trapped by the (MT). For the experiments aiming at the production of excited molecules by means of photoassociation (chap. 5) ^{87}Rb was used, while ^{85}Rb was used for the search for magnetic Feshbach resonances (chap. 7). Since the magnetic trap acts similar on both isotopes, typical values are stated for ^{87}Rb and the parameters for ^{85}Rb are given in brackets (..).
The preparation of Rb starts by loading a Rb MOT operating on the $5^2\mathrm{S}_{1/2} \rightarrow 5^2\mathrm{P}_{3/2}$ transition at 780 nm (see sec. 3.2.1). This transition has a linewidth of $\gamma_{\mathrm{D2}} = 2\pi \times 6.06\,\mathrm{MHz}$ [140] and a Doppler limit of 146 µK [91]. The continuously loaded MOT typically contains 10^9 atoms at a temperature of 1.5 mK. Due to the spatially separated Yb sample no compromise for the Rb loading as in former experiments [5, 6] must be made and it can be optimized independently.
Similar to the transfer of Yb into the ODT_{1064}, the trapping parameters of the Rb MOT have to be modified and ramped in order to efficiently load the Rb MT. The transfer process begins by applying compensation magnetic offset fields after turning off the slower magnetic fields in order to move the Rb sample to the position of the magnetic trap. It follows a phase of optical molasses [158, 159] to decrease the temperature to $\approx 150\,\mu\mathrm{K}$. Here, contrary to Doppler-cooling the laser detuning is increased [160] and ramped to $-10\,\gamma_{\mathrm{D2}}$. In order to increase the population of the desired hyperfine state ($|F, m_F\rangle$), the Repumper is turned off shortly before transfer and if necessary the atoms are additionally exposed to the Depumper (see fig. 3.5). Subsequently, the magnetic fields required to magnetically trap Rb (see sec. 3.1 and fig. 3.2) are turned on. Initially, $5 \cdot 10^8$ Rb atoms are trapped in the MT with a temperature of 100 µK.
Before sympathetically cooling this atomic cloud by radio-frequency (RF) evaporation [161] (see sec. 2.2), unwanted magnetically trappable Rb atoms in the $|F = 2\rangle$ ($|F = 3\rangle$) state are removed by illuminating the cloud for 10 µs with imaging light resonant to the $|F = 2\rangle \rightarrow |F = 3\rangle$ ($|F = 3\rangle \rightarrow |F = 4\rangle$) transition. The previously optimized radio frequency ramping procedure [162] was adapted to get a shorter experimental cycle but still achieving low enough temperatures. The frequency is ramped from 27 MHz to 700 kHz within 17 s. It is important to know that the MT is loaded radially separated by 1.4 mm from the future interatomic contact position and moved later onto the Yb sample. Therefore, the ODT_{1064} containing the Yb atoms can be moved during the evaporative cooling of Rb back to the previous position in the center of the vacuum chamber. At the end of the cooling process, typically 10^7 spin polarized Rb atoms in the $|F = 1, m_F = -1\rangle$ ($|F = 2, m_F = -2\rangle$) state at a temperature of $T_{\mathrm{Rb}} = 1.7\,\mu\mathrm{K}$ reside in the MT.
As was shown in sec. 3.1 the trap frequencies of the MT in our experimental setup can be determined by measuring the trap bottom B_0 of the MT (see fig. 3.4). This measurement

yielded a magnetic field offset of $B_0 = 550\,\mathrm{mG}$ and hence trap frequencies of

$$\omega_x = \omega_y = \sqrt{\frac{\mu}{m}\left(\frac{B'^2}{B_0} - \frac{B''}{2}\right)} = 1.01\,\mathrm{kHz} \qquad \text{and} \tag{4.1a}$$

$$\omega_z = \sqrt{\frac{\mu}{m}B''} = 86\,\mathrm{Hz}\,. \tag{4.1b}$$

This leads with a temperature of $T_{\mathrm{Rb}} = 1.7\,\mu\mathrm{K}$ to cloud sizes of

$$\sigma_x = \sigma_y = \frac{1}{\omega_x}\sqrt{\frac{k_{\mathrm{B}}T}{m}} = 12.6\,\mu\mathrm{m} \qquad \text{and} \tag{4.2a}$$

$$\sigma_z = \frac{1}{\omega_z}\sqrt{\frac{k_{\mathrm{B}}T}{m}} = 148\,\mu\mathrm{m} \tag{4.2b}$$

which in turn yield peak densities of $\rho_{\mathrm{Rb}} \approx 2.7 \cdot 10^{13}\,\mathrm{cm}^{-3}$.

4.1.3 Rb and Yb in the combined hybrid conservative trap

The production of ultracold rovibronic RbYb ground state molecules requires both atomic species to be trapped in a combined conservative trap. This section deals with the newly implemented hybrid conservative trap used for the creation of excited molecules within this thesis. It consists of a magnetic trap for Rb and an optical dipole trap ODT_{556} at 555.95 nm for Yb which is based on the bichromatic optical dipole trap (BIODT) used in former experiments [5, 6]. This previous trapping method combined the same magnetic trap for Rb with a superposition of two optical dipole traps at 532 nm and 1064 nm for

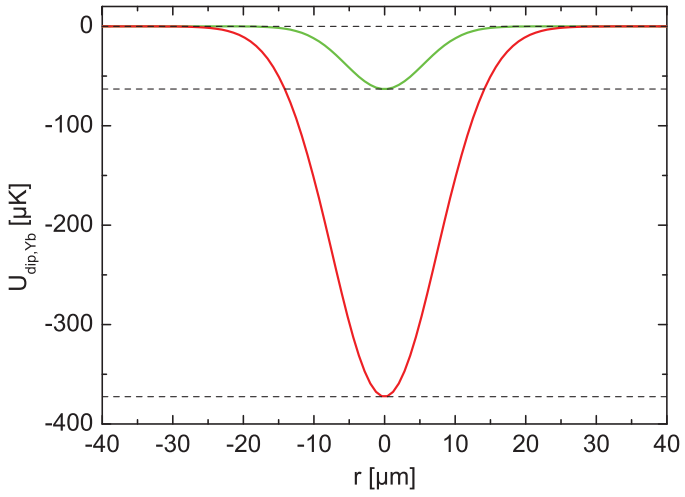

Figure 4.4: *Comparison of modeled potentials for the ODT_{1064} (red curve) and the ODT_{556} (green curve) for Yb in the process of transferring the atoms. The experimental parameters are beam waists of $w_{556} = 11\,\mu\mathrm{m}$ and $w_{1064} = 15\,\mu\mathrm{m}$ and powers of $P_{556} = 12\,\mathrm{mW}$ and $P_{1064} = 4\,\mathrm{W}$ producing potentials with depths of $U_{556} = -k_B \times 60\,\mu\mathrm{K}$ and $U_{1064,\mathrm{Yb}} = -k_B \times 370\,\mu\mathrm{K}$.*

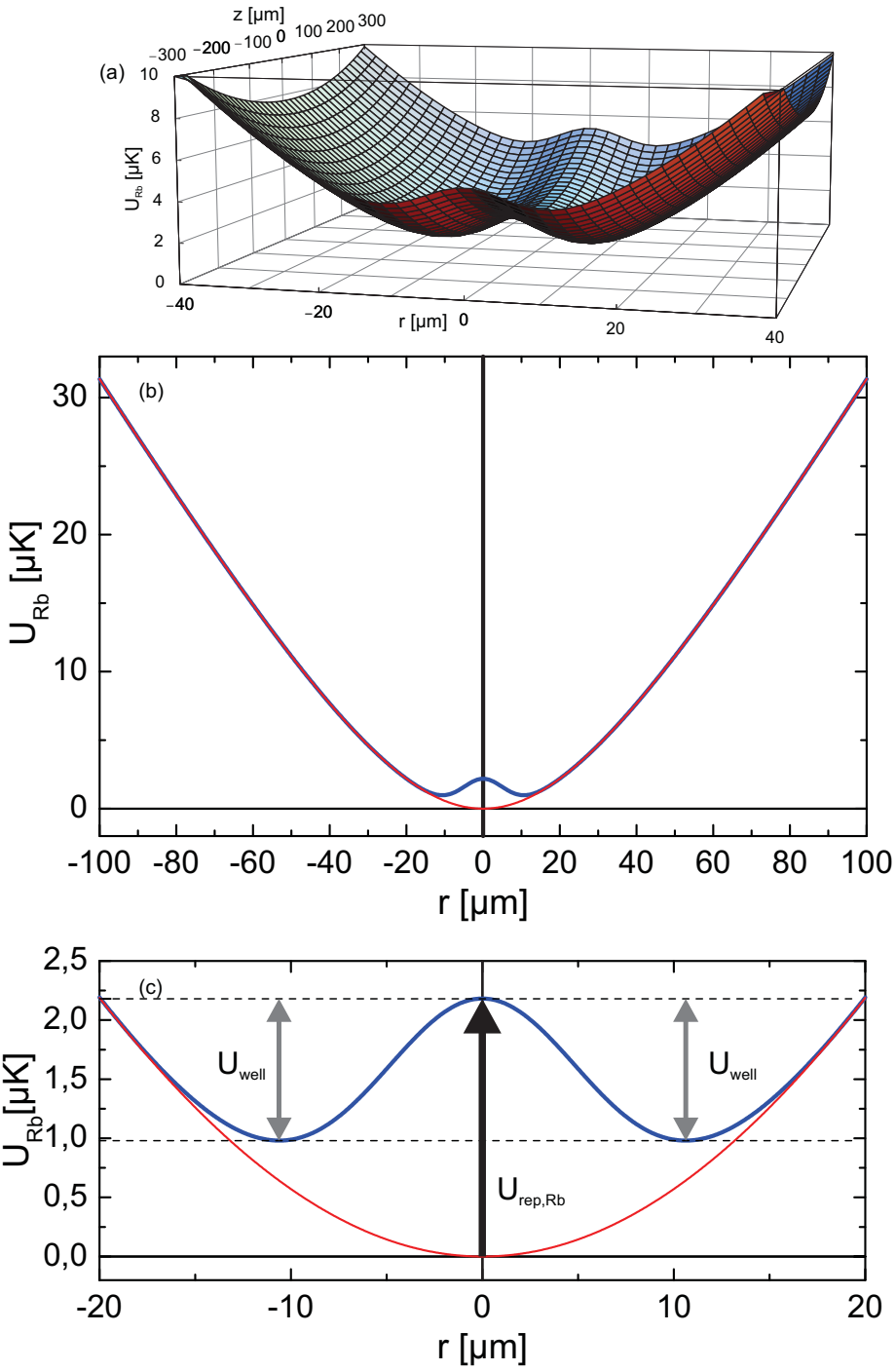

Figure 4.5: *Modeled potential for Rb in the hybrid conservative trap. (a) 3-dimensional plot showing the potential in radial (r) and axial (z) direction. (b)-(c) Combined potential in radial direction ($z = 0$) for Rb consisting of an attractive magnetic potential superimposed on a repulsive ODT potential (blue curve) compared to the single magnetic potential (red curve). The repulsive ODT potential lifts the bottom of the MT by $U_{\mathrm{rep,Rb}} = k_B \times 2.2\,\mu\mathrm{K}$ producing two potential wells with a depth of $U_{\mathrm{well}} = k_B \times 1.2\,\mu\mathrm{K}$. Thus good overlap of the atomic clouds is still assured. The ODT potential for Yb is not affected by the magnetic trapping field due to the lack of magnetic moment in the ground state of Yb.*

Yb which was designed to minimize the effect on Rb. However, this posed significant experimental challenges in overlapping the atomic clouds precisely. On the contrary, the new hybrid combined trap uses only one ODT beam at 555.95 nm for Yb which is red-detuned by only 140 GHz with respect to the $^1S_0 \rightarrow {}^3P_1$ intercombination line at 555.8 nm. After the initial separated preparation stage for Yb and Rb as described above, we have Rb in the magnetic trap and Yb in the ODT_{1064} laterally displaced by 1.4 mm after the Yb cloud has been moved back into the chamber. Since the ODT_{1064} creates an approximately 4.6-times deeper potential for Rb, simply moving the Rb MT onto the Yb sample would lead to high losses and short interrogation times. Instead, shortly before moving the MT, the Yb sample is transferred from the ODT_{1064} to the ODT_{556} by ramping the ODT_{1064} power down from 4...0 W and the ODT_{556} power up from 0..12 mW simultaneously. Figure 4.4 shows the difference between both ODT potentials for Yb which are $U_{1064,\mathrm{Yb}} = -k_B \times 370\,\mu\mathrm{K}$ and $U_{556} = -k_B \times 60\,\mu\mathrm{K}$. However, by adiabatic transformation of the trapping potential we obtain a transfer efficiency of $> 75\%$. The temperature of the Yb sample in the ODT_{556} at this point is $T_{\mathrm{Yb}} = 12\,\mu\mathrm{K}$. With an atom number of typically 10^5 this leads to calculated densities of $8 \cdot 10^{10}\,\mathrm{cm}^{-3}$. The temperature of the laterally displaced Rb sample with 10^7 atoms at this moment is $T_{\mathrm{Rb}} = 1.7\,\mu\mathrm{K}$.
As already stated, the Rb MT can be shifted by applying magnetic offset fields while care has to be taken to keep a constant offset field B_0 in the center of the MT over the whole range. The combined HT is then created by simply moving the Rb MT onto the ODT_{556}. Due to the diamagnetic ground state of Yb, the potential does not get any distortion by the present magnetic fields. On the contrary, an effect of the light field on the Rb atoms cannot be avoided. As was explained in sec. 2.1, the potential created by a focussed laser beam for a specific atomic species depends on the detuning δ to the atomic transitions and the intensity I of the laser: $U_{\mathrm{dip}} \propto I/\delta$ [68]. Here, the ODT_{556} creates a repulsive potential for Rb since the ODT light field at 556 nm is blue-detuned with respect to the dominant D-transitions of Rb at 780 and 795 nm. In order to minimize this effect on Rb, the ODT_{556} is operated at low laser power with 6 mW in the final performance which is ramped down from 12 mW before irradiating the photoassociation laser. Since a potential as deep as possible for Yb is desired, it is red-detuned by only $\delta = -140$ GHz to the $^1S_0 \rightarrow {}^3P_1$ intercombination line at 555.8 nm. The resulting combined potential for Rb (optical plus magnetic) compared to the potential created solely by the magnetic trap is depicted in fig. 4.5.
The repulsive ODT potential for Rb unfolds as an increased bottom of the nearly harmonic magnetic potential by $U_{\mathrm{rep,Rb}} = k_{\mathrm{B}} \times 2.2\,\mu\mathrm{K}$ producing two potential wells with a depth of $U_{\mathrm{well}} = k_{\mathrm{B}} \times 1.2\,\mu\mathrm{K}$ at a laser power of 6 mW. These are pronounced but obviously not large enough to prevent contact since the temperatures are on the order of a few μK. The first proof of a good overlap of the atomic clouds is the sympathetic cooling of Yb by Rb after the Rb cloud has been moved to the position of the Yb cloud. Since there are 10^7 Rb atoms at $T_{\mathrm{Rb}} = 1.7\,\mu\mathrm{K}$ and hence a factor of 100 more than Yb atoms at $T_{\mathrm{Yb}} = 12\,\mu\mathrm{K}$, the Yb sample can be cooled in the large cold reservoir formed by the Rb atoms as is illustrated in fig. 4.6. Here, the size of the Yb sample in radial σ_{y} and axial direction σ_{z}, which is a measure for the temperature, is plotted as a function of contact time between the atomic

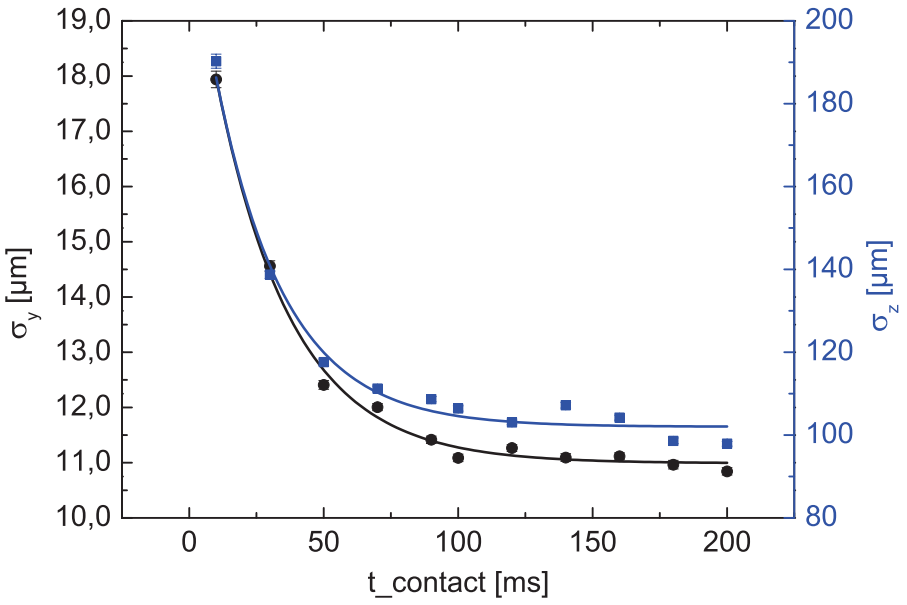

Figure 4.6: *Expansion of the Yb cloud after a TOF time of* $t_{\mathrm{TOF}} = 1\,\mathrm{ms}$ *in radial direction* σ_y *(black dots) and axial direction* σ_z *(blue dots) as a function of contact time between Rb and Yb. The final temperature is the one of the cold Rb reservoir of* $T_{\mathrm{Rb}} = 1.7\,\mu\mathrm{K}$. *The solid lines are simple exponential fits to the data meant to be a guide-to-the-eye.*

clouds. After 200 ms of sympathetic cooling in the case of the used isotopes ^{176}Yb and ^{87}Rb, a thermal equilibrium is reached with a common temperature of $T_{\mathrm{RbYb}} = 1.7\,\mu\mathrm{K}$, practically equal to the initial Rb temperature. Due to the much larger atom number no temperature change in the Rb sample can be detected.

The sympathetic cooling process can be exploited to achieve an optimum overlap of the atomic clouds. Figure 4.7 illustrates the size of the Yb cloud after a shortened contact time of $t = 10\,\mathrm{ms}$ as a function of final MT position in both axes. Here, *dx* and *dy* represent the two perpendicular axes, in which the Rb MT can be shifted by magnetic offset fields relative to an arbitrary origin. It shows clearly a sensitive dependence on the order of $< 5\,\mu\mathrm{m}$. This emphasizes that care has to be taken while overlapping both atomic clouds. For experimental investigations, the magnetic fields where set at the values yielding the minimum extensions of the Yb cloud. This procedure was typically performed each day during the experiments in order to guarantee the best overlap but the position turned out to be pretty stable. Additionally, a displacement of up to $4\,\mu\mathrm{m}$ in steps of $1\,\mu\mathrm{m}$ is modeled in fig. 4.8 revealing asymmetric wells of maximum $1.7\,\mu\mathrm{K}$ but still assuring good overlap. This shows that the overlap of both atomic clouds is not as sensitive as before in the BIODT [5, 6].

An approximation for the characteristic trapping parameters for Yb in this configuration of the ODT_{556} is obtained from the fitted temperatures (fig. 3.24). These yield a temperature of $T_{\mathrm{Yb}} = 1.75 \pm 0.06\,\mu\mathrm{K}$ and initial cloud sizes of $\sigma_r(0) = 7.7 \pm 0.3\,\mu\mathrm{m}$ in radial and $\sigma_z(0) = 100 \pm 2\,\mu\mathrm{m}$ in axial direction. With the typical atom number of $N_{\mathrm{Yb}} = 10^5$ this

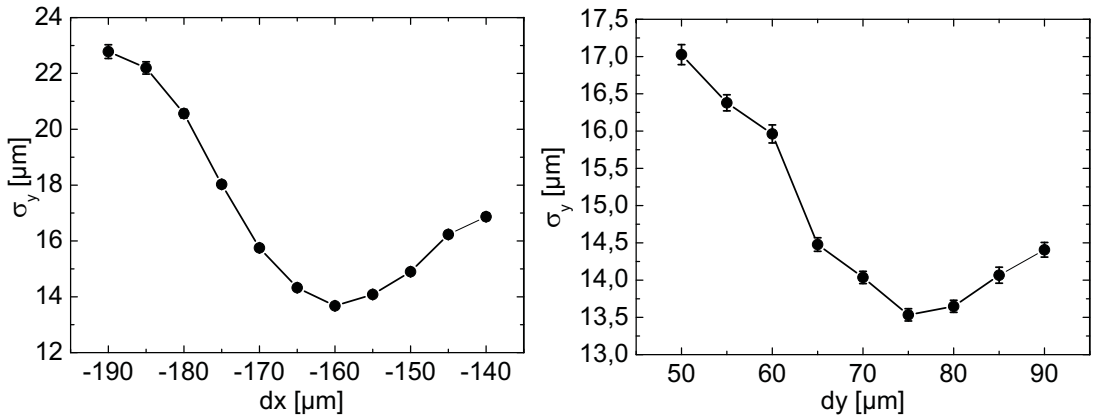

Figure 4.7: *Radial size σ_y of the Yb cloud after a short contact time of 10 ms with the colder Rb cloud and a TOF time of 1 ms as a function of final magnetic trap position. dx and dy denote the two radial axes in which the magnetic trap can be shifted (given in* µm *and relative to an arbitrary position). The lines are just guides-to-the-eye. The minima in both directions indicate the position of maximum overlap of the two atomic clouds.*

leads to final peak densities of $\rho_{\mathrm{Yb}} = 1.1 \pm 0.09 \cdot 10^{12}\,\mathrm{cm}^{-3}$. The present trap frequencies can be calculated with the help of the following harmonic approximation

$$\omega_i = \frac{1}{\sigma_i(0)}\sqrt{\frac{k_{\mathrm{B}}T}{m}} \qquad i = r, z \tag{4.3}$$

and constitute $\omega_r = 1.18 \pm 0.05\,\mathrm{kHz}$ and $\omega_z = 90 \pm 2\,\mathrm{Hz}$. However, since the fitting procedures may have larger uncertainties, these values are just approximations.
This HT is the experimental starting point for producing electronically excited molecules in the course of this work. With both atomic species at the same place at reasonably high densities, photoassociative production of molecules is in principal possible. An important property that determines the maximum possible interrogation time with the PA-laser is the lifetime of both atomic species in the combined trap. Figure 4.9 displays the lifetime of Yb in the ODT_{556} with (red dots) and without (black dots) the cold Rb reservoir. The corresponding curves are exponential fits with two decay constants. Without the cold Rb atoms the lifetime is composed of a fast decay with a $1/e$-decay constant of $\tau_{\mathrm{Yb},1} = 85\,\mathrm{ms}$ and a slow decay with $\tau_{\mathrm{Yb},2} = 4.7\,\mathrm{s}$. With Rb both constants get extended to $\tau_{\mathrm{YbRb},1} = 1.1\,\mathrm{s}$ and $\tau_{\mathrm{YbRb},2} = 10\,\mathrm{s}$, respectively. Both measurements emphasize a low heating rate of Yb in the ODT_{556} with a theoretical value of $0.5\,\mu\mathrm{K/s}$ (see eq. 2.19). The lifetime of Rb in the magnetic trap is significantly longer (several minutes) but gets limited due to heating by the PA-laser during exposure (see fig. 3.15).

4.2 Preparation in the crossed ODT

The experiments concerning the investigation of magnetic Feshbach resonances in RbYb (chap. 7) were performed chronologically before the photoassociation experiments. The

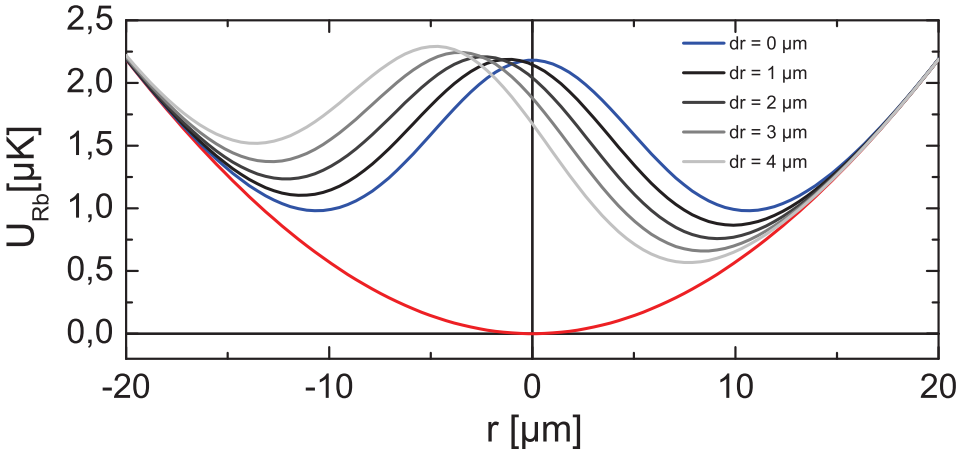

Figure 4.8: *Modelled effect of an imperfect overlap of the optical and magnetic potentials on the combined potential for Rb. With increasing deviation dr the potential wells become asymmetric while the potential depth increases. For the maximum modelled deviation of* $4\,\mu m$ *the deeper well has a depth of* $U_{well} = 1.7\,\mu K$.

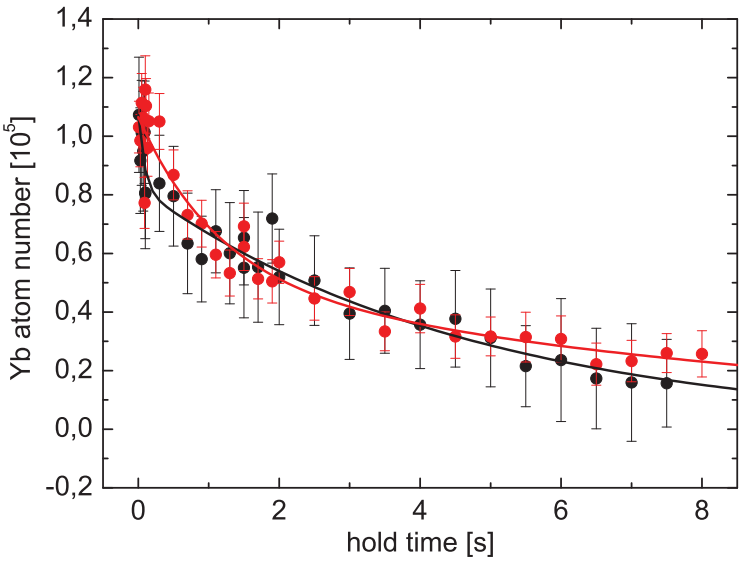

Figure 4.9: *Lifetime of Yb in the* ODT_{556} *with (red dots) and without (black dots) the cold Rb reservoir. The correlated solid lines are exponential fits to the data composed of two* $1/e$*-decay constants. Singly Yb in the ODT shows a fast decay with* $\tau_{Yb,1} = 85\,ms$ *(for the first 200 ms) and a slow decay with* $\tau_{Yb,2} = 4.7\,s$. *Due to the cold Rb reservoir both decay constants get extended to* $\tau_{YbRb,1} = 1.1\,s$ *and* $\tau_{YbRb,2} = 10\,s$. *During contact with Rb the RF was kept constant at the final value assuring a constant temperature.*

hybrid conservative trap presented in sec. 4.1.3 was not yet implemented and the single ODT_{1064} as well as the crossed ODT (CODT) were used for this purpose. In principle, it is easily possible to modify the novel combined conservative trap by transferring the Rb atoms from the magnetic trap into the single beam ODT_{1064} which would also allow to search for Feshbach resonances. In this case, further care has to be taken in order to overlap the atomic clouds accurately enough.
The experimental cycle for loading of the CODT is significantly different from the preparation process in the hybrid trap. This is partly due to the usage of ^{85}Rb and ^{171}Yb instead of ^{87}Rb and ^{176}Yb. One crucial drawback of ^{85}Rb is the negative scattering length of $a = -400\,a_0$ [127] which prevents the atomic cloud from an efficient evaporative cooling to temperatures on the order of a few µK. In general, cooling to $\approx 5...10\,\mu K$ is possible without any problem but further cooling comes along with huge losses in atom number. ^{171}Yb has a comparable natural relative abundance of 14.3% compared to ^{176}Yb with 12.7% [149]. Additionally, it has a slightly lower temperature in the MOT because the presence of more magnetic substates enables more cycling transitions.
Figure 4.10 summarizes graphically details for each single step of the experimental sequence (from [143]) while searching for Feshbach resonances. The setup for the CODT was already introduced in sec. 3.2.5. As a reminder, it is composed of two crossing ODT beams at 1064 nm, the ODT_{1064} with a waist of $w_{1064} = 15\,\mu m$ and the $ODT_{1064,2}$ with a waist of $w_{1064,2} = 25\,\mu m$. The power distribution for this purpose in the maximum configuration was $P_{1064} = 1.5\,W$ and $P_{1064,2} = 5.5\,W$, respectively.
In contrast to the loading of the hybrid trap, the experimental sequence starts with loading of a ^{85}Rb MOT and subsequently transferring the atoms into the MT. At this point the atoms have a temperature of 100 µK and are already spin polarized in the desired state $|F = 2, m_F = -2\rangle$. After an evaporative cooling phase of 17 s we have typically 10^7 Rb atoms in the MT and the atoms are transferred into the $ODT_{1064,2}$ with 50% of the maximum power (2.75 W). The atoms are stored in the ODT while loading the Yb MOT for 9 s. Shortly before transferring the Yb atoms into the $ODT_{1064,2}$, its power is increased to the maximum value (5.5 W). We see a heating of the Rb sample after ramping the $ODT_{1064,2}$ up and subsequently a sympathetic cooling of Rb by the colder Yb atoms. Directly after loading both atomic samples in the $ODT_{1064,2}$ we have $N_{Rb} = 1.5 \cdot 10^5$ at $T_{Rb} = 45\,\mu K$ and $N_{Yb} = 1 \cdot 10^6$ at $T_{Yb} = 30\,\mu K$. Thus, in this case we chose the number of Yb atoms to be larger than the number of Rb atoms. Due to the low density, the two clouds are not yet thermalized directly after ramping of the $ODT_{1064,2}$.
It follows a forced evaporative cooling sequence by decreasing the power of the $ODT_{1064,2}$ to 1.1 W and achieving $N_{Rb} = 8 \cdot 10^4$ at $T_{Rb} = 12\,\mu K$ and $N_{Yb} = 2 \cdot 10^5$ at $T_{Yb} = 10\,\mu K$. In a typical experimental cycle, the magnetic fields used for the Feshbach resonance are already applied during this evaporation sequence. Meanwhile, the ODT_{1064} power is ramped up to $\approx 300\,mW$ creating the crossed optical dipole potential.
Figure 4.12 shows models of the single beams and crossed optical dipole potentials for Rb with the final power used in Feshbach experiments ($P_{1064} = 300\,mW$ and $P_{1064,2} = 1.1\,W$) taken as basis. After the preparation process is completed, there are $N_{Rb} = 5 \cdot 10^4$ Rb atoms at a temperature of $T_{Rb} = 12\,\mu K$ and $N_{Yb} = 1.5 \cdot 10^5$ Yb atoms at a tempera-

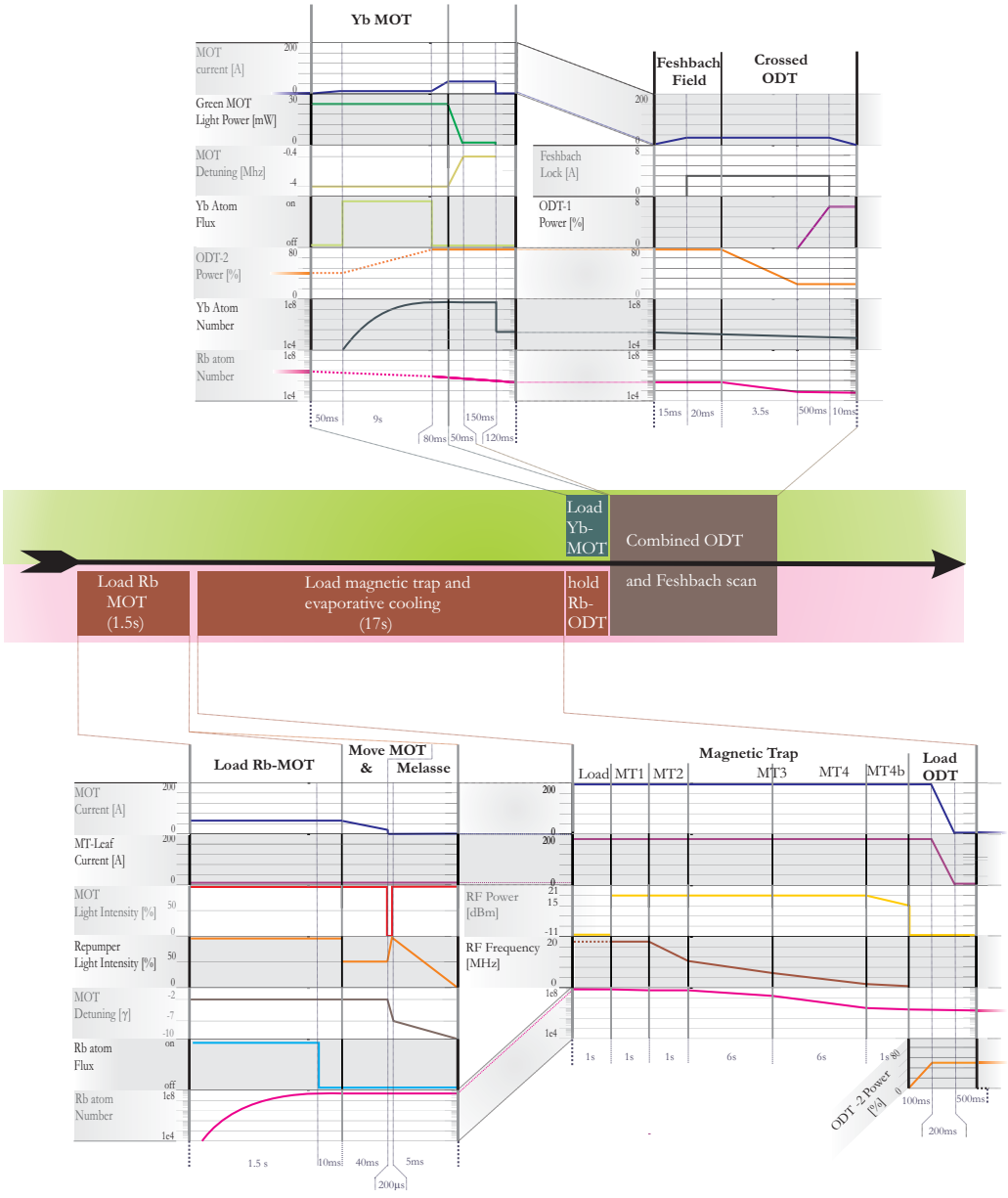

Figure 4.10: *Experimental cycle for the search for Feshbach resonances in RbYb from [143]. Shown are the single experimental steps including details of the experimental properties that are used to prepare Yb and Rb in the CODT and finally scan for Feshbach resonances.*

ture of $T_{\mathrm{Yb}} = 10\,\mu\mathrm{K}$. Due to cooling by the colder Yb sample, Rb is confined in the dimple produced in the crossing area. The resulting density for ^{85}Rb in this CODT is $\rho_{\mathrm{Rb}} = 3.8 \cdot 10^{11}\,\mathrm{cm}^{-3}$ calculated again using temperature measurements. These imply trap frequencies of $\omega_r = 2.6\,\mathrm{kHz}$ and $\omega_z = 670\,\mathrm{Hz}$. With these experimental conditions the Feshbach magnetic fields are either fixed to a specific value or ramped during the holding time of 500 ms (see chap. 7). Figure 4.11 illustrates some absorption images of Rb and Yb in these different kind of traps.

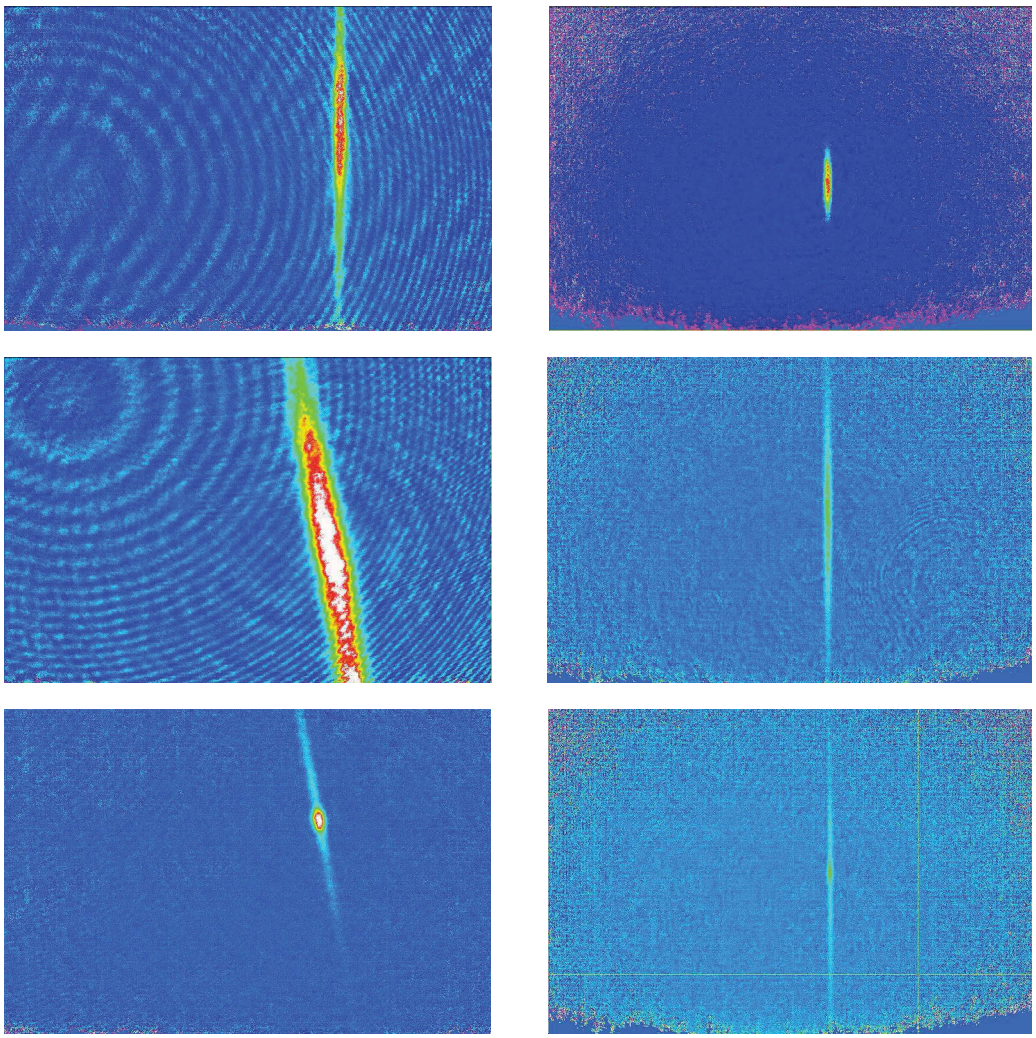

Figure 4.11: *Absorption images of Rb (left) and Yb (right) in three different trapping potentials provided by the laser at 1064 nm. The images for Rb and Yb were taken by CCD camera 3 and CCD camera 2, respectively (see fig. 3.23). The single beam ODT_{1064} (top) was initially used to trap both atomic species. It was replaced by a combination of $ODT_{1064,2}$ (middle) as intermediate storage and the crossed ODT (bottom) in order to increase the achievable final densities.*

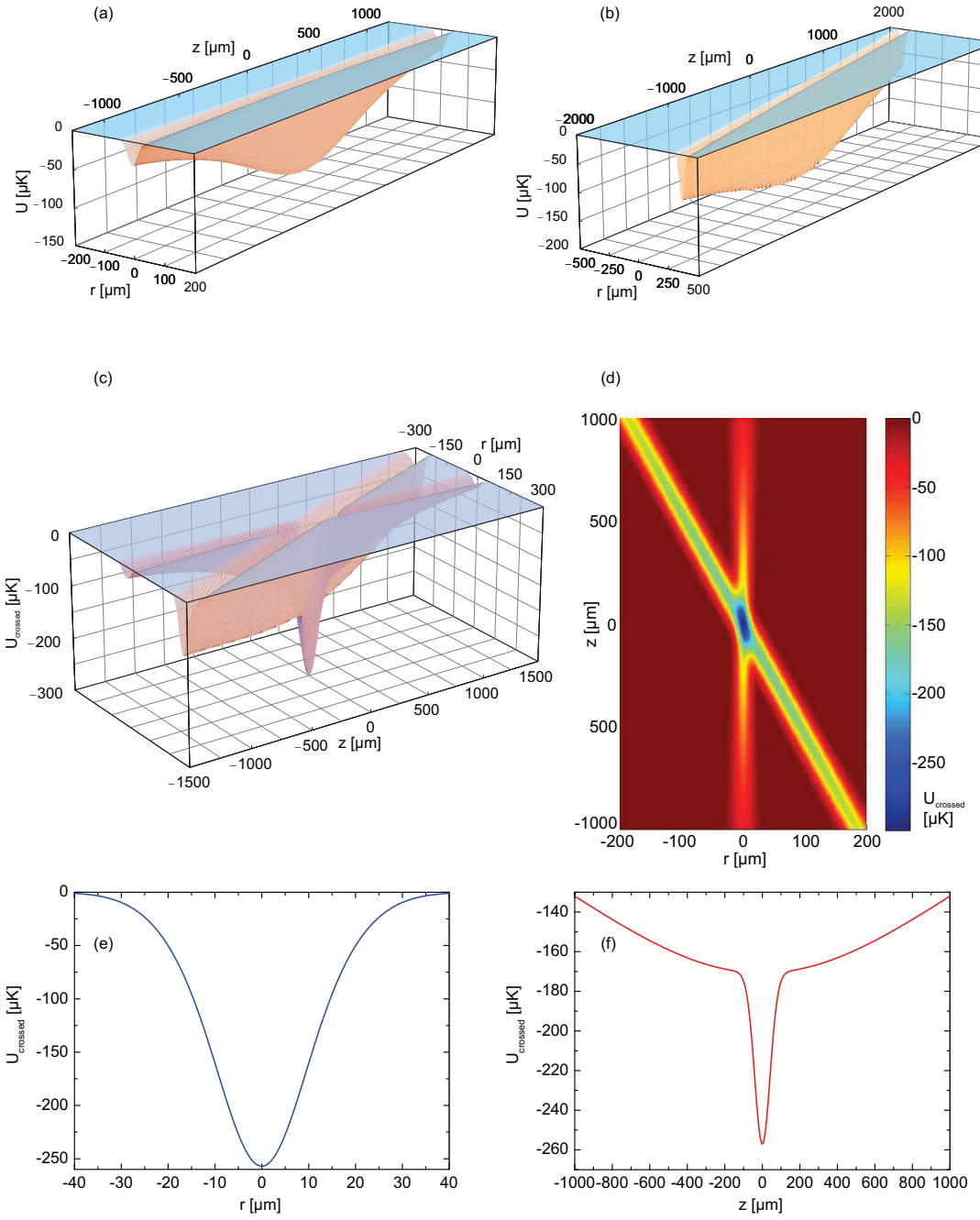

Figure 4.12: *Modeled potentials of the crossed optical dipole trap for Rb. (a)-(c) 2D cross sections in radial and axial direction of (a) the single beam ODT*$_{1064}$ *with* $P_{1064,1} = 300\,\mathrm{mW}$ *focussed to* $w_{1064} = 15\,\mu\mathrm{m}$ *and (b)* $ODT_{1064,2}$ *with* $P_{1064,2} = 1.1\,\mathrm{W}$ *focussed to* $w_{1064} = 25\,\mu\mathrm{m}$ *and with an angle of 10.5° (see fig. 3.22). (c) The resulting crossed optical dipole potential* U_{crossed} *exhibits a dimple in the overlap region in which the Rb and the Yb atoms are captured. (d) Horizontal cut of the crossed dipole potential. (e)-(f) Cuts through the axis of* $ODT_{1064,2}$ *around the dimple of* U_{crossed} *in radial (e) and axial (f) direction.*

5

Photoassociation spectroscopy

This chapter describes our experimental results achieved by means of 1-photon photoassociation (1-PA) experiments in an ultracold mixture of Rb and Yb close to the Rb D_1 line. First, I will give a short introduction with general information on the characteristics of PA experiments before I will briefly review the experiments performed in a combined double species MOT and the important extracted properties for the excited Rb*Yb molecular level. The main part of this chapter consists of the experimental results in the newly designed combined hybrid conservative trap (HT) described in detail in chapter 4. The results are composed of PA spectra of vibrational levels up to a binding energy of $E_b = -h \times 2.2\,\mathrm{THz}$ (sec. 5.3.2) and a reduction in the molecular hyperfine splitting by more than 30% (section 5.3.5) with increasing binding energy. The reduction of the splitting is related to a hyperfine coupling which depends on the separation of the two nuclei in the RbYb-molecule. It has been pointed out by Brue et al. [13] that a similar coupling if present in the electronic ground state might lead to observable Feshbach resonances.

5.1 Introduction

Photoassociation (PA) is an experimental technique to create ultracold molecules in an electronically excited state starting from ultracold atomic samples with the help of photons [46]. In a simple picture, two colliding atoms A and B can absorb the photon and create an excited molecule

$$A + B + \nu_L \rightarrow (AB)^* \,, \tag{5.1}$$

if the photon's frequency ν_L provided by the PA-laser matches the energy difference between the atomic threshold in the ground state and a vibrational level in the excited state. This process is schematically illustrated in fig. 5.1 using the example of RbYb. Within this thesis, the excited molecular $^2\Pi_{1/2}$ state dissociating to the $Rb_{5p1}(^2P_{1/2})$ + $Yb_{6s2}(^1S_0)$ atomic channel was analyzed further building on the work done in [1, 7]. The PA laser is thus red detuned to the Rb D_1 line at 795 nm.
After formation of the molecule it typically decays either into two free atoms with a high kinetic energy or into a ground state molecule that typically cannot be trapped or detected directly depending on the experimental conditions. Most presumably, the decay into a vibrational level of the RbYb molecular ground state is the dominant process which is

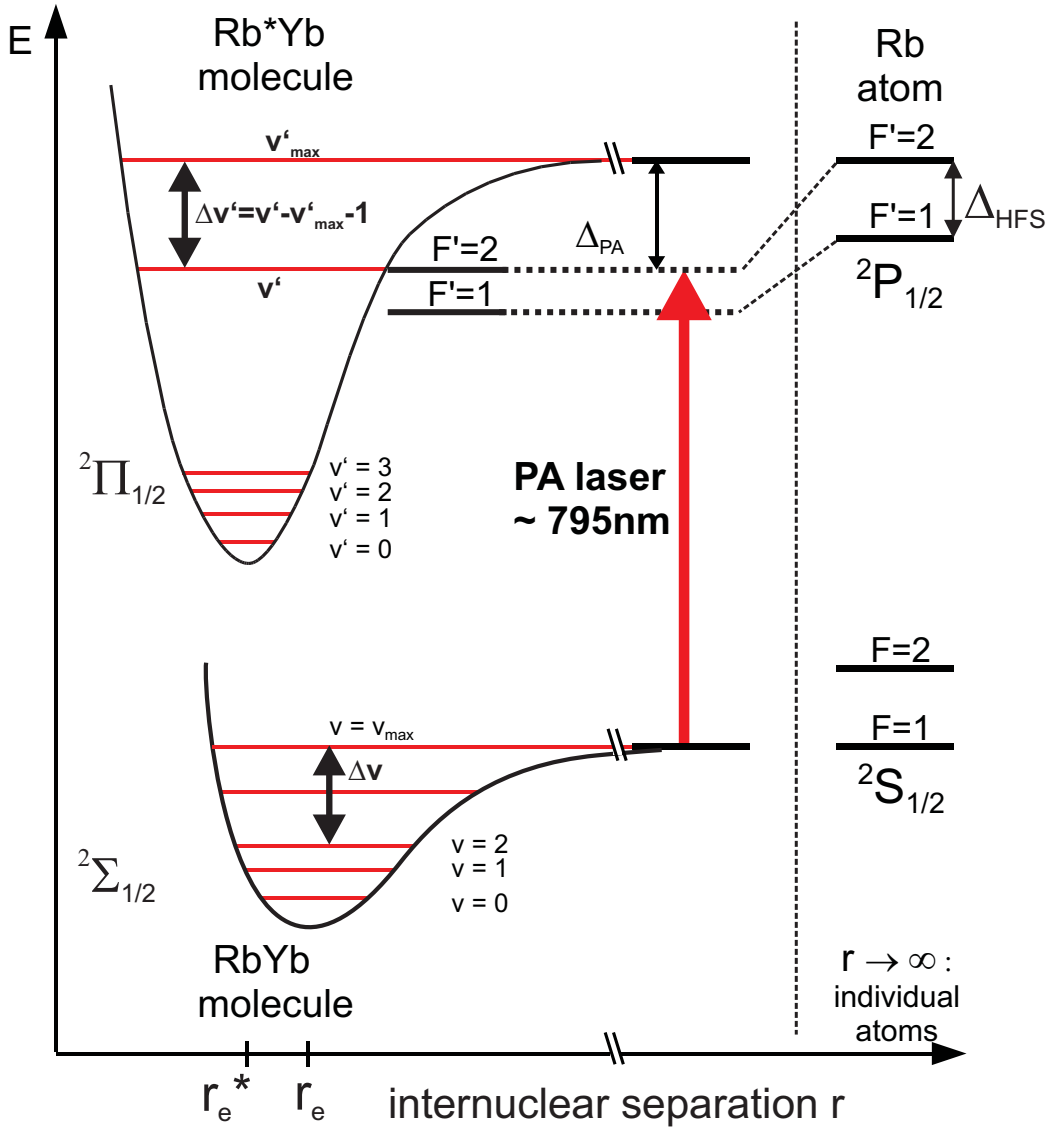

Figure 5.1: *Relevant RbYb levels (not to scale) (adapted from [8]). The PA-laser is red-detuned with respect to the Rb D_1 line whose frequency is given in relative wavenumbers Δ_{PA}.*

supported by the large Franck-Condon overlaps that are additionally measured in [3] and presented chap. 6. Either way, after the decay of the molecule the products are lost from the initial detection channel and therefore a common method to monitor the formation of molecules is the so called *trap-loss technique*. Consequently in our case, a PA spectrum consists of trap-loss as a function of PA-laser frequency. Due to the low temperatures in ultracold PA experiments, a high spectral resolution can be achieved giving the possibility to address single vibrational and even rotational levels. As was done in our previous work [1, 7], the relative wavenumber Δ_{PA} will be given relative to the $5^2\mathrm{S}_{1/2}$, $F = 1 \rightarrow 5^2\mathrm{P}_{1/2}$,

$F' = 2$ transition at $\tilde{\nu}_{\mathrm{D1}} = 12579.1037\,\mathrm{cm}^{-1}$

$$\Delta_{\mathrm{PA}} = \tilde{\nu}_L - \tilde{\nu}_{\mathrm{D1}}\,, \tag{5.2}$$

which on resonance gives directly the binding energy Δ_{bind} for a specific state with the wavenumber $\tilde{\nu}_L$ of the PA laser. Traditionally, this binding energy is specified in molecular spectroscopy in wavenumbers $\tilde{\nu}$ given in cm^{-1} that is proportional to an energy. The relation to frequency can be found by:

$$\tilde{\nu} = \frac{1}{\lambda^*} = \frac{\nu}{c^*}\,, \tag{5.3}$$

where the * superscript indicates that the quantity needs to be given in cm. The conversion yields therefore $1\,\mathrm{cm}^{-1} = 29979.24\,\mathrm{MHz}$.
Typically, the exact number of bound states supported by the interaction potential is not known and the vibrational levels are analyzed from top of the potential. Therefore, we label the observed vibrational states by the relative vibrational quantum number

$$\Delta \mathrm{v}' = \mathrm{v}' - N = \mathrm{v}' - \mathrm{v}'_{\mathrm{max}} - 1 \tag{5.4}$$

where v' denotes the vibrational quantum number counted from the bottom of the interaction potential (starting from 0), $\mathrm{v}'_{\mathrm{max}}$ the maximum vibrational quantum number and $N = \mathrm{v}'_{\mathrm{max}} + 1$ the number of bound states (see fig. 5.1). The least bound state is hence labelled by $\Delta\mathrm{v}' = -1$.
In general, molecules produced by 1-PA in the electronically excited molecular state are loosely bound molecules with a low binding energy. These so-called *physicists' molecules* are long-range molecules with a large internuclear separation that hence inherit the properties of their constituent atoms. As a consequence, each highly excited vibrational state assigned in our experiment is accompanied by an „echo“ which is approximately 817 MHz apart, corresponding to the hyperfine splitting of the ^{87}Rb atom in the excited state. On the contrary, when passing to the short range of the interatomic potential (see sec. 2.4), chemical bonding gains in importance and the atomic electron clouds get distorted. In the work reported here, we were able to measure a decrease in hyperfine splitting with increasing binding energy showing a gradual passage to more tightly bound molecules.

5.2 1-Photon Photoassociation in a combined MOT

This section will review the 1-photon photoassociation experiments performed in a combined MOT. This was studied in detail in the PhD-thesis of Nils Nemitz [1] where further details can be found. Thus, in this section the main results of [1, 7] are repeated as a reference. In addition, the most important consequences for the $^2\Pi_{1/2}$ excited potential for RbYb are summarized.

Experiment

The principle of the experiments performed in the thesis of N. Nemitz was to overlap continuously loaded MOTs for both species, Rb and Yb, at suitable trapping parameters and

additionally superimpose the PA-laser which was then continuously scanned. As already explained in sec. 5.1, the PA-spectrum was obtained by trap-loss spectroscopy. For that reason, both atomic numbers in the MOTs were monitored by their fluorescence. While a simple photodiode was used to observe the fluorescence of the Rb MOT, a photomultiplying tube was needed to collect the fluorescence of the Yb MOT, which has a much smaller intensity. These experiments were redone in the course of this work as a preparation step for the experiments in the conservative trap.
If the PA-laser is resonant with a rovibrational level in the electronically excited state, excited molecules are produced. This results in a reduction in atom numbers since the produced molecules leave the cycling transition of the MOT by either decaying into ground state molecules or into atoms with a high kinetic energy. Due to the large difference in atom numbers (10^8 Rb and 10^5 Yb atoms) this loss can only be observed in the Yb MOT fluorescence. Typical scans of vibrational levels that were recorded in the course of this work are shown in fig. 5.2. In order to obtain a better signal to noise ratio and cancel out effects resulting from loading rates of the MOTs, the PA-laser was typically swept two times back and forth over the line with a scan rate between 2...10 MHz/s and the extracted signal was smoothed afterwards. Several rotational components up to $R' = 2$ appear in the spectrum agreeing with the temperature of $T_{\mathrm{MOT}} \approx 300\,\mu\mathrm{K}$ in the MOT and thereby connected rotational barriers (see eq. 2.52 and fig. 2.9).
One drawback of 1-PA in the MOT is that due to repeated absorption and emission cycles each addressed electronic state as well as all hyperfine states and their magnetic substates are present (see fig. 3.5). These states might contribute to a transition induced by the PA-laser and thus the observed lines cannot necessarily be assigned unambiguously. In order to guarantee a good signal and a high molecule production rate, 1-PA was performed close to the Rb D_1 transition $|^2\mathrm{S}_{1/2}, F = 1\rangle \rightarrow |^2\mathrm{P}_{1/2}, F' = 2\rangle$. The MOT was therefore operated in the Dark Spot MOT configuration [163] in order to avoid the density limiting repulsion in the MOT [145] and increase the population in the $F = 1$ substate of the Rb ground state. This was achieved by selectively cutting out the center of the Repumper light [1], reducing the Repumper light power to $\approx 1\,\mathrm{mW}$ and irradiating an additional $\approx 20\,\mu\mathrm{W}$ of Depumper light (see again fig. 3.5 for affected states). The obtained population of the $F = 1$ state as well as the position of the PA-laser were tested and adjusted by measuring the absorption through the Rb cloud at an intensity less than the saturation intensity.

Rotational Structure

Figure 5.2 illustrates some example scans of the vibrational levels $\Delta\mathrm{v}' = -9, -11, -13$ in the combined MOT revealing rotational components up to $R' = 2$ and an additional substructure for rotations $R' \neq 0$. These spectra were recorded within this thesis as a preparation regarding 1-PA in the conservative trap. The number of substates for each rotational level leads to the conclusion that Hund's coupling case (e) is the predominating coupling scheme for the observed rovibrational levels in Rb*Yb. Since there is no angular momentum coming from the Yb atom, the number of rotational substates $2X + 1$ can be related to the quantum numbers F' and R', where X represents the smaller value of

both (see sec. 2.5). Another important information can be extracted from the fact that the energy spacing ΔE_{rot} between different rotational levels ($R' = 0$ and $R' = 1$) increases with increasing binding energy. Some examples are given in fig. 5.2.
Nils et al. analyzed this energy spacing in the rigid rotor approximation and were able to deduce the internuclear separation r_{eff} for the vibrational levels. In this case, the rotational energy of the molecule is given by (see eq. 2.51)

$$E'_{\mathrm{rot}} = B'_{\mathrm{rot}} R'(R'+1), \tag{5.5}$$

with the rotational constant $B'_{\mathrm{rot}} = \hbar^2/(2\mu {r_{\mathrm{eff}}}^2)$. Measuring the energy difference $\Delta E_{\mathrm{rot}}(\Delta_{\mathrm{bind}})$ between the rotational states $R' = 0$ and $R' = 1$ as a function of binding energy Δ_{bind} gives the relation $B'_{\mathrm{rot}}(\Delta_{\mathrm{bind}}) = \Delta E_{\mathrm{rot}}(\Delta_{\mathrm{bind}})/2$ and therefore

$$r_{\mathrm{eff}}(\Delta_{\mathrm{bind}}) = \hbar/\sqrt{\Delta E_{\mathrm{rot}}(\Delta_{\mathrm{bind}})\,\mu}\,. \tag{5.6}$$

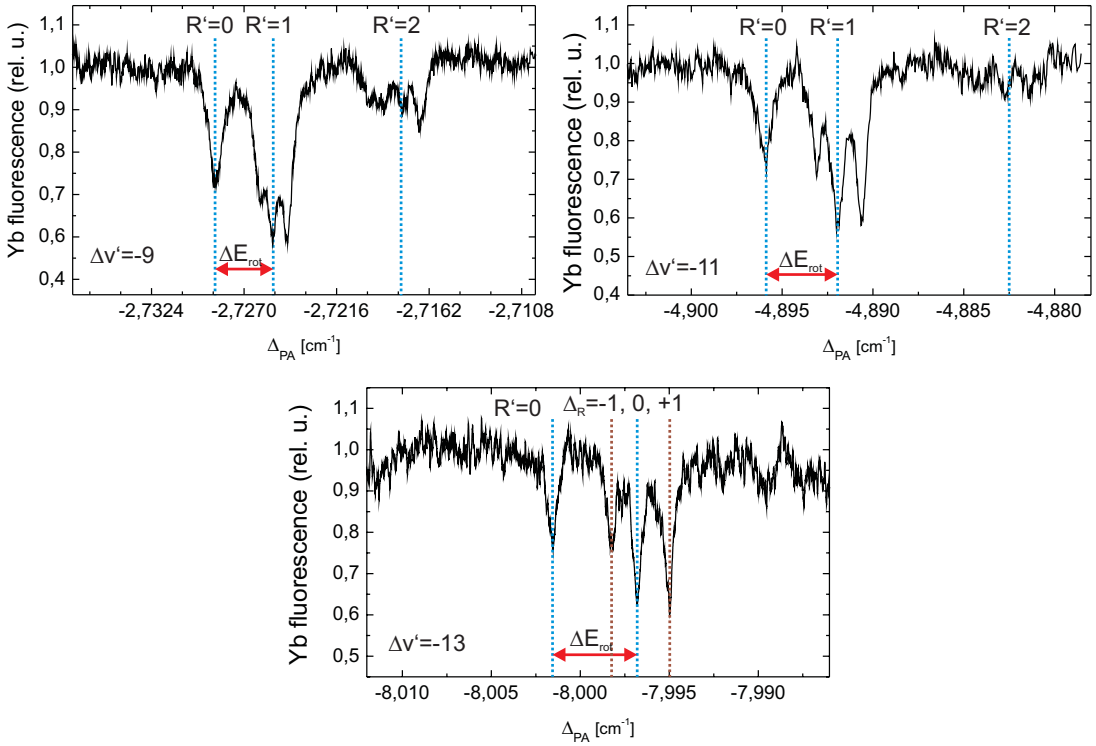

Figure 5.2: *Typical PA-spectra in a continuously loaded combined MOT recorded within this thesis as reference. Shown are the vibrational levels $\Delta v' = -9$, $\Delta v' = -11$ and $\Delta v' = -13$ in a mixture of ^{87}Rb and ^{176}Yb and at temperatures of $T_{\mathrm{MOT}} \approx 300\,\mu\mathrm{K}$. Shown is the Yb MOT fluorescence as a function of PA-laser frequency. A drop in fluorescence signifies a production of excited Rb*Yb molecules. Substantial is the appearance of rotational components up to $R' = 2$ including a substructure for each rotation. Note the Yb fluorescence dropping to only ≈70% of the maximum signal for $R' = 0$ of the strongest vibrational level $\Delta v' = -9$. An effective internuclear separation can be directly deduced out of the splitting ΔE_{rot} between the rotational components $R' = 0$ and $R' = 1$ which increases with increasing binding energy (fig. 5.12).*

Consequently, every observed vibrational level can be directly related to the internuclear separation r_{eff}. In sec. 5.3.5 we will use an extrapolation of r_{eff} to analyze the 1-PA spectra in the hybrid conservative trap.

5.3 Photoassociation in a combined conservative trap

Our previous experiments concerning 1- and 2-photon photoassociation spectroscopy for RbYb were performed in the continuously loaded combined MOT as described in sec. 5.2 at temperatures of a few 100 µK which is generally too high to occupy the absolute ground state, internal and external, sufficiently. Additionally, the produced molecules, either in the excited or ground molecular state, are simply lost from the trap. These are surely two undesired effects on the way to the production of rovibrational ground state molecules and their subsequent investigation and manipulation. The experiments have thus eventually to be performed in a conservative trap which is able to capture the produced molecules and lower temperatures and higher densities can be achieved. Since the RbYb molecules exhibit a magnetic as well as an electric dipole moment they can also be trapped by a magnetic trap as well as an optical dipole trap.
The experiments within this thesis were carried out in the newly designed hybrid conservative trap presented in sec. 4.1.3 at temperatures of a few µK. As already pointed out, the new trap is based on the BIODT used in [5, 6] but was refined to allow for a more efficient and stable molecule production (see sec. 4.1). The PA spectroscopy builds on the work done by [1] but was extended to reach binding energies down to $E_{\text{bind}} \approx -75\,\text{cm}^{-1}$ for the vibrational level $\Delta\text{v}' = -28$.
Figure 5.3 shows, as an example, the vibrational level $\Delta\text{v}' = -13$ observed within this thesis in the combined MOT as well as in the HT and emphasizes the differences. Due to the low temperature of $T_{\text{RbYb}} = 1.7\,\mu\text{K}$ in the conservative trap only a single rotational component $R' = 0$ appears while the rotational barrier of $E_c = k_B \times 66\,\mu\text{K}$ for p-wave resonances ($R' = 1$, see fig. 2.9) can be overcome in the MOT with temperatures of $T_{\text{MOT}} \approx 300\,\mu\text{K}$. This results in a more pronounced $R' = 1$ level with respect to $R' = 0$.
Another difference is the depletion depth of the Yb number on resonance. The Yb sample can be depleted completely in the conservative trap leading to a considerably improved signal-to-noise ratio, while the Yb number drops to only 70% of the maximum signal in the MOT for the $R' = 0$ rotational level of the strongest $\Delta\text{v}'$. This can be attributed to the higher densities of $\rho_{\text{Rb}} = 2.7 \cdot 10^{13}\,\text{cm}^{-3}$ and $\rho_{\text{Yb}} = 1.1 \cdot 10^{12}\,\text{cm}^{-3}$ in the HT compared to $\rho_{\text{Rb}} = 6.8 \cdot 10^{10}\,\text{cm}^{-3}$ and $\rho_{\text{Yb}} = 4.5 \cdot 10^{9}\,\text{cm}^{-3}$ [3] in the double-species MOT and the maximum achievable PA-rates of $r_{\text{PA}}^{\text{max}} \approx 7000\,\text{s}^{-1}$ per ytterbium ground state atom (eq. 2.63) which are strongly influenced by the Rb density. A further advantage of 1-PA in the conservative trap stems from the well defined states (F, m_F) of the Rb atoms present in the trap. This gives us the possibilty of a state selective addressing of (F', m'_F) in the excited molecular state by choosing the proper polarization of the PA-laser radiation as explained in sec. 5.3.4. On the other hand, as is presented in chap. 4, a complete experimental cycles takes $\approx 45\,\text{s}$ which limits the achievable scanning rate.

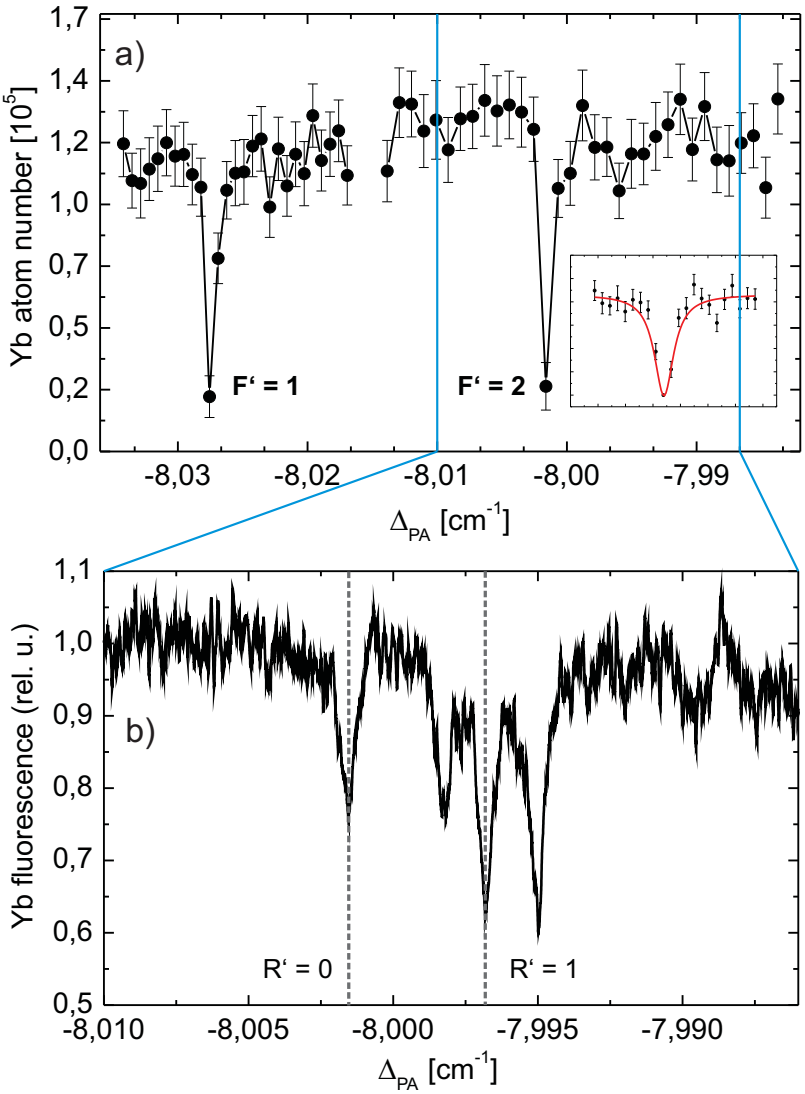

Figure 5.3: *Comparison of spectroscopy signals recorded in the course of this work corresponding to the vibrational level $\Delta v' = -13$ taken by 1-PA in a combined MOT (b) and the combined conservative trap (a). Due to the lower temperature of $T_{\mathrm{RbYb}} = 1.7\,\mu\mathrm{K}$ in the conservative trap only the $R' = 0$ rotational component can be observed. Note the improved signal-to-noise ratio.*

5.3.1 Preparation of Rb and Yb in the hybrid conservative trap

The experimental cycle was already presented in chap. 4 with detailed information of each single step. Here just a brief summary with focus on important physical aspects relevant for PA will be given.
As already mentioned, the 1-PA spectroscopy presented in this thesis was carried out in a newly designed combined hybrid conservative trap (HT) consisting of a near-resonant optical dipole trap at 555.95 nm (ODT_{556}) for Yb and a clover-leaf magnetic trap (MT) for Rb. The combined potential for Rb is modeled in fig. 4.5 which shows two potential wells created by the repulsive potential stemming from the ODT_{556}. Since the occurring potential depths are on the order of a few μK, both atomic species have to be pre-cooled to be trapped.
The Yb atoms are first loaded from a Zeeman-slower red-detuned to the $^1S_0 \rightarrow {}^1P_1$ transition at 399 nm into a MOT operating on the $^1S_0 \rightarrow {}^3P_1$ transition at 555.8 nm (sec. 3.2.2). Afterwards, they are transferred into the intermediate ODT_{1064} at 1064 nm with a potential depth of $- \approx k_B \times 370\,\mu K$ (sec. 4.1.1.2). This ODT is able to capture hotter Rb atoms directly out of the Rb MOT due to an approximately 4.6-times deeper potential for Rb. Therefore, before loading the Rb MOT, the ODT_{1064} containing the Yb atoms is moved out of the center of the vacuum chamber by translating the focussing lens for the ODT by about 1.6 cm using a motorized translation stage (fig. 3.19). As a result, the Rb MOT operating on the $^2S_{1/2} \rightarrow {}^2P_{3/2}$ transition can be loaded from a Zeeman slower (sec. 4.1.2) without disturbing the optically trapped Yb atoms. The Rb atoms are then transferred into the MT and cooled down to $T_{Rb} = 1.7\,\mu K$ by rf-evaporation.
At the end of the preparation of the ultracold Rb sample the Yb atoms in the ODT_{1064} can be moved back to their previous position which is laterally separated by 1.4 mm from the position of the MT. The Yb atomic sample is then transferred to the final ODT_{556} with a starting power of $P_{556} = 12\,mW$ generating a potential of $U_{556,Yb} = -k_B \times 60\ \mu K$ with a transfer efficiency of >75% (sec. 4.1.3). Typically, 10^5 Yb atoms at a temperature of $T_{Yb} = 12\,\mu K$ are confined in the ODT_{556} beam and 10^7 Rb atoms spin polarized in the $|F = 1, m_F = -1\rangle$ hyperfine state at a temperature of $T_{Rb} = 1.7\,\mu K$ in the MT. After bringing both atomic species into contact by applying magnetic offset fields to the clover leaf MT, the atomic samples thermalize to the combined temperature of $T_{RbYb} = 1.7\,\mu K$. Here, the Rb cloud acts as the cold reservoir whose temperature does not vary. With a final power of $P_{556} = 6\,mW$ the calculated peak densities are $\rho_{Rb} = 2.7 \cdot 10^{13}\,cm^{-3}$ and $\rho_{Yb} = 1.1 \cdot 10^{12}\,cm^{-3}$, respectively.
After preparation of both atomic species in this HT, 1-PA spectroscopy is performed by illuminating the atoms with the PA-laser radiation tuned close to the Rb D_1 transition at 795 nm. A complete experimental cycle takes ≈ 45 s (see chap. 4). The data was recorded using the same datalogger as in our previous work [1, 3] but the evaluation was slightly different (sec. 3.2.6). Identical to our previous work the wavelength of the PA-laser was measured by a self-built wavemeter with a Rb stabilized laser as reference. It has an absolute accuracy of $5 \cdot 10^{-3}\,cm^{-1}$ but an estimated relative accuracy of $1 \cdot 10^{-3}\,cm^{-1}$. The state selective addressing is performed by choosing the desired polarization with a

$\lambda/4$-waveplate.

5.3.2 Spectra

Close to the Rb D_1 line it is possible to scan over the whole frequency range without gap since the density of vibrational states close to threshold is relatively high [7]. However, since the density of states decreases with increasing potential depth, only a local scan for each vibrational level is feasible. Due to the much larger atom number in Rb ($\approx$ factor 100) the molecule production can only be detected by Yb losses.
Figure 5.4 and 5.5 show the resonances found in the HT down to a relative detuning of $\Delta_{\mathrm{PA}} \approx -75\,\mathrm{cm}^{-1}$ for the vibrational number $\Delta\mathrm{v}' = -28$ in a mixture of ^{87}Rb and ^{176}Yb. Illustrated is the number of remaining Yb atoms after illumination by the PA-laser as a function of relative wavenumber Δ_{PA} in cm^{-1}. The Rb atom number is not plotted since the RbYb PA resonance is not visible in the Rb atom number and only few Rb_2 resonances have been observed in our scans. The identified vibrational states are labelled by the relative vibrational quantum number $\Delta\mathrm{v}'$ typically containing two hyperfine components related to $F' = 2$ and $F' = 1$ of the excited $^2\Pi_{1/2}$ state of the Rb atom. Two exceptions are depicted in fig. 5.6 corresponding to the vibrational states $\Delta\mathrm{v}' = -19$ and $\Delta\mathrm{v}' = -24$. These lines are referred to as weak resonances since already the $F' = 2$ hyperfine component could not be saturated and no $F' = 1$ component could be observed. Nevertheless, they are assigned as mentioned because the resonances' positions fit perfectly to the predictions. Details on the line assignment can be found in sec. 5.3.3 and 5.3.5.
The $\Delta\mathrm{v}' = -29$ level was expected to be at $\Delta_{\mathrm{PA}} = -82.66\,\mathrm{cm}^{-1}$ but could unfortunately not be detected as evidenced by the futile scan in fig. 5.7 indicating that the corresponding PA transition is rather weak. Further scanning for yet unobserved vibrational states could not be performed with the present setup due to the implemented interference filter needed to eliminate the ASE background of the tapered amplifier (see sec. 3.2.3). The transmitted laser power at $\Delta_{\mathrm{PA}} = -90.75\,\mathrm{cm}^{-1}$ respectively 800.7 nm, the expected position of $\Delta\mathrm{v}' = -30$, equals $\approx 10\,\mathrm{mW}$ and is impractical for photoassociation spectroscopy. Without interference filter the lifetime of the Rb cloud was reduced too much to perform PA spectroscopy as shown in fig. 3.15.
It is worth noting that the data was initially taken with a commercial DL-Pro laser (see sec. 3.2.3) as master laser which was used during the two-photon experiments (see chap. 6). Unfortunately, this laser could only be used for wavelengths below $\approx 796\,\mathrm{nm}$ and hence below the vibrational level $\Delta\mathrm{v}' = -18$ due to the specific gain profile of the laser diode. Thus, another laser was built with a wavelength range of 770...810 nm described in detail in sec. 3.2.3. The home-built PA-laser can cover $\approx 3\,\mathrm{GHz}$ in a continuous scan without mode hopping by only changing the voltage of the piezo. In general, the center wavelength was manually set and ramped by the control program while the range was large enough to search for new resonances.
Generally, σ^--polarization was used while searching for unknown resonances in a coarse scan with frequency steps of 40...100 MHz, exposure times of 500...1500 ms and a laser power of 100 mW. The scans depicted in fig. 5.4, 5.5 and 5.6 are typically detailed scans

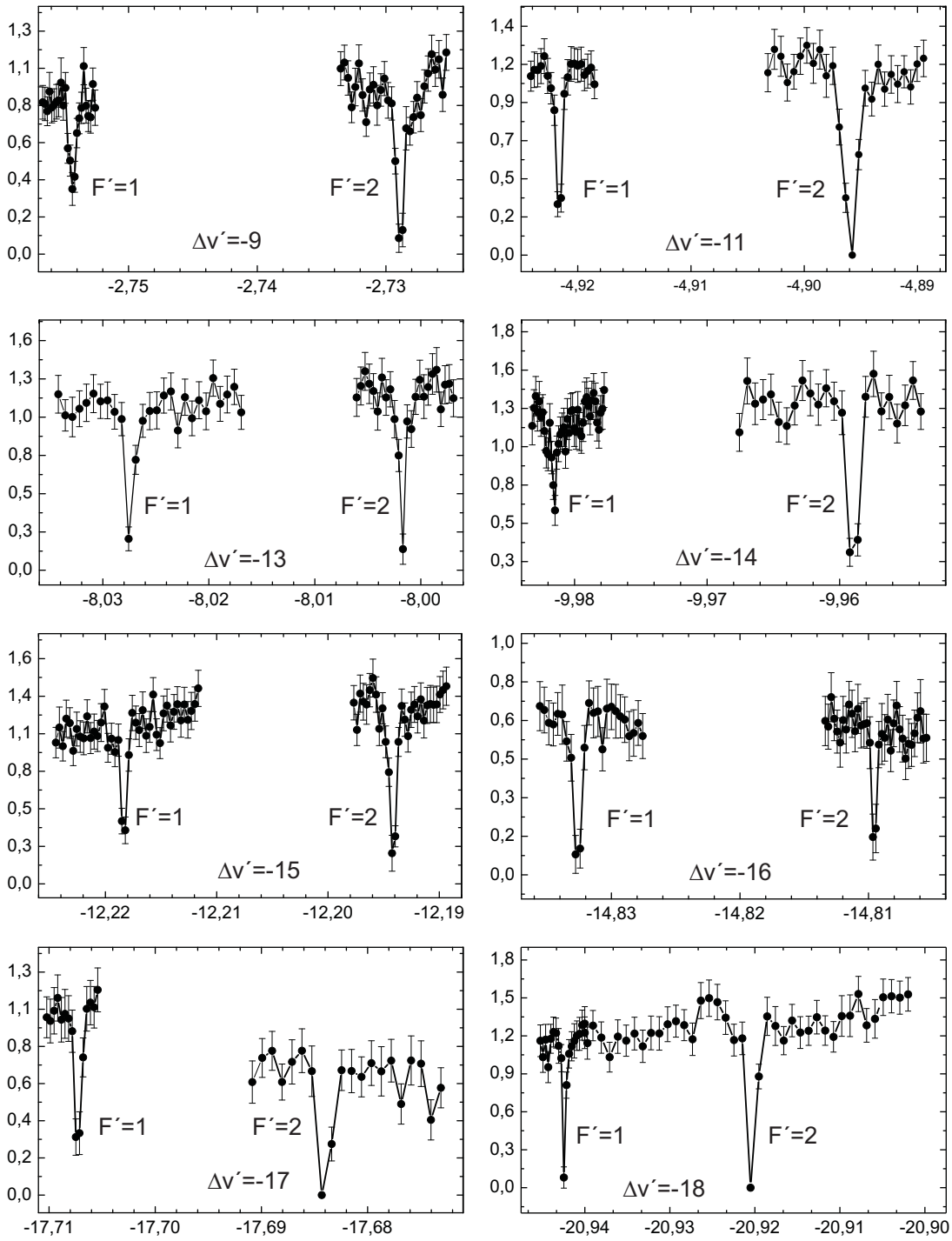

Figure 5.4: *Observed photoassociation lines of $^{87}Rb^{176}Yb$ up to -21 cm^{-1} in the newly designed HT. Plotted is the number of remaining Yb atoms in units of 10^5 after PA as a function relative wavenumber Δ_{PA} in units of cm^{-1}. The lines connecting adjacent points are just a guide-to-the-eye. Vibrational levels are marked by the relative vibrational quantum number $\Delta v'$. The lines corresponding to different F'-states are generally recorded with different circular polarizations (see sec. 5.3.4) in order to achieve highest possible molecule production. The background atom number for lines attributed to different hyperfine states of the same vibrational level may differ since the lines were not necessarily observed under the exact same experimental conditions.*

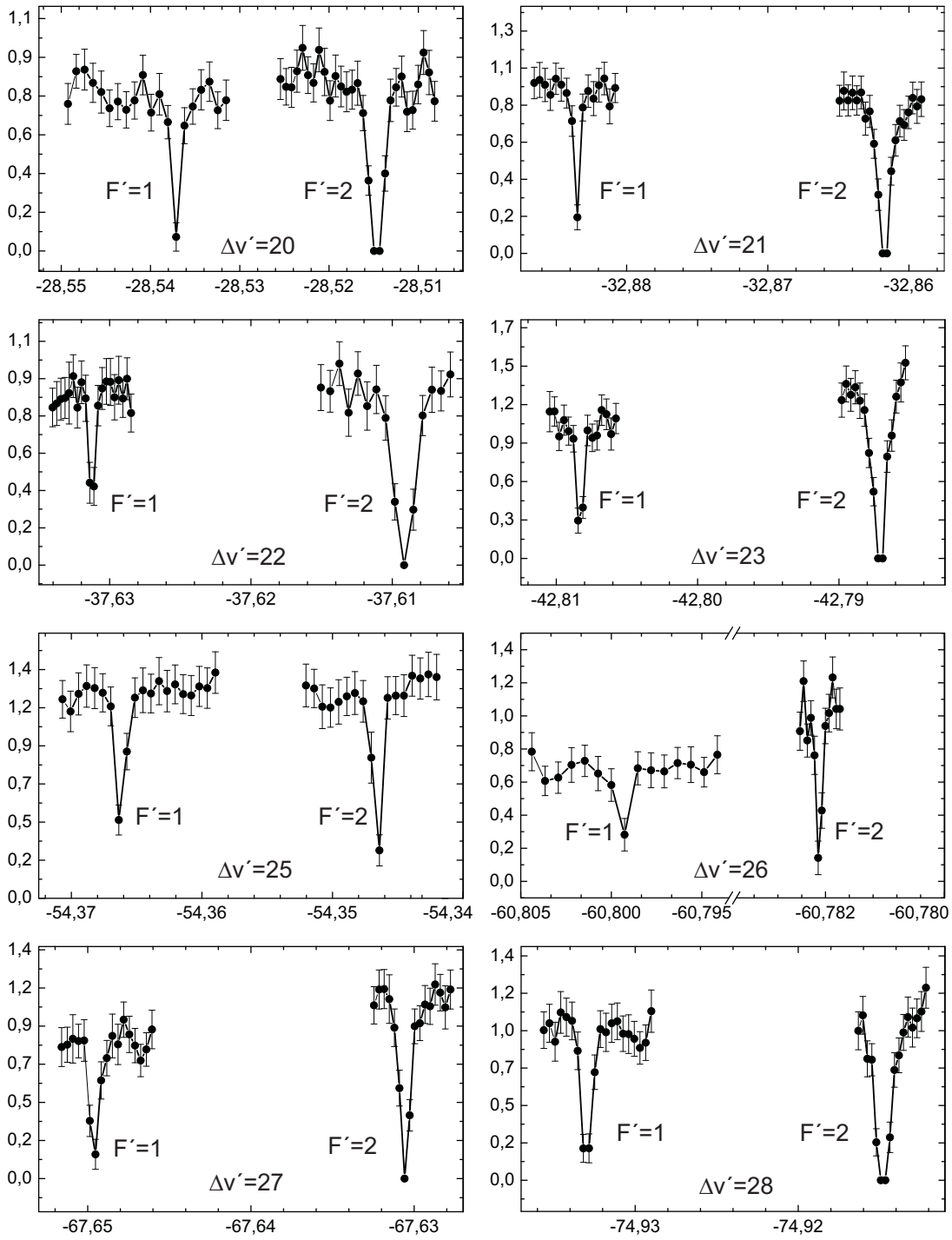

Figure 5.5: *Observed photoassociation lines of $^{87}Rb^{176}Yb$ for binding energies $\Delta_{\mathrm{bind}} = -21 ... -75\,\mathrm{cm}^{-1}$ in the newly designed HT. Shown is the number of remaining Yb atoms in units of 10^5 after PA as a function relative wavenumber Δ_{PA} in units of cm^{-1}. The lines connecting adjacent points are just a guide-to-the-eye. Vibrational levels are marked by the relative vibrational quantum number $\Delta v'$. The lines corresponding to different F'-states are generally recorded with different circular polarizations (see sec. 5.3.4) in order to achieve highest possible molecule production. The background atom number for lines attributed to different hyperfine states of the same vibrational level may differ since the lines were not necessarily observed under the exact same experimental conditions.*

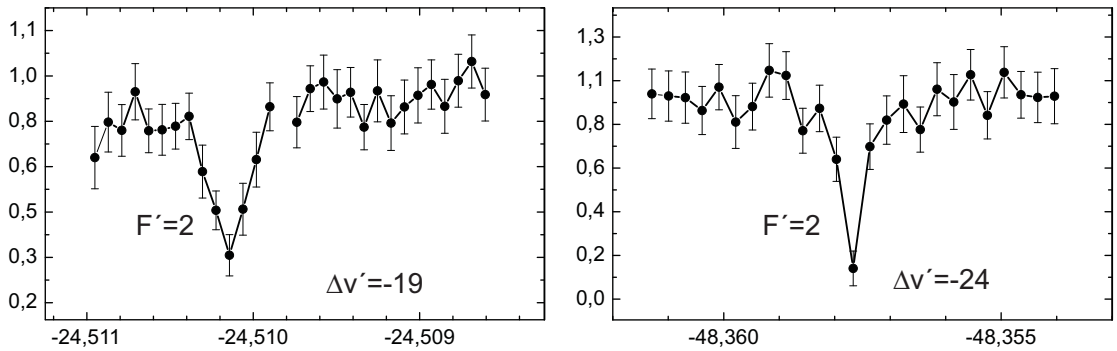

Figure 5.6: *Weak observed photoassociation lines of $^{87}Rb^{176}Yb$ in the newly designed combined conservative trap. Shown is again the number of remaining Yb atoms in units of 10^5 after photoassociation as a function of relative wavenumber Δ_{PA} in units of cm^{-1}. This data was recorded using σ^--polarized light and hence belongs to the $F' = 2$ hyperfine level (see again sec. 5.3.4). The lines are specified as weak since the signal could not be saturated and no component belonging to $F' = 1$ could be identified.*

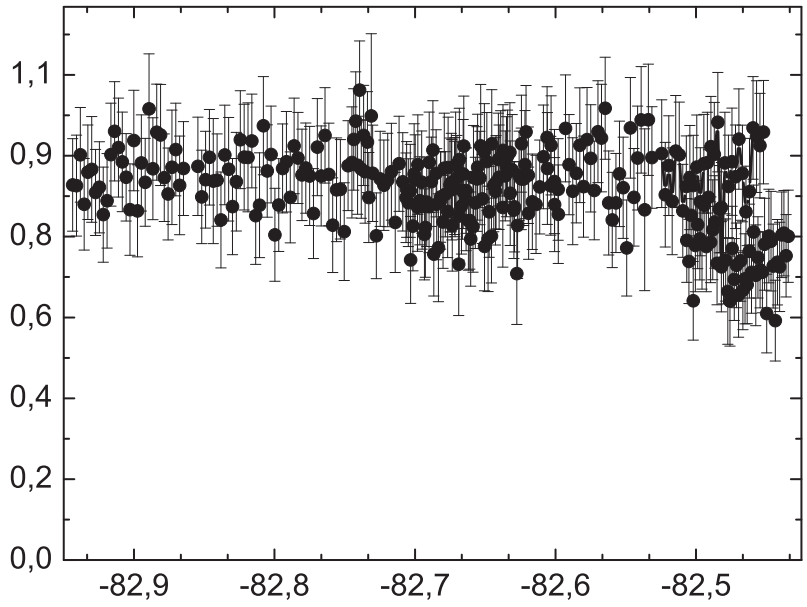

Figure 5.7: *Scans aiming for the detection of $\Delta v' = -29$ spanning more than 15 GHz in steps of $\approx 80\,\mathrm{MHz}$ with 100 mW of PA-laser power illuminating the atoms for 1500 ms. This vibrational level is expected to be located at $\Delta_{\mathrm{PA}} = -82.66\,\mathrm{cm}^{-1}$ according to the local fit utilized for the predictions of unobserved vibrational levels (see sec. 5.3.3). No clear resonance was observed indicating a rather weak line.*

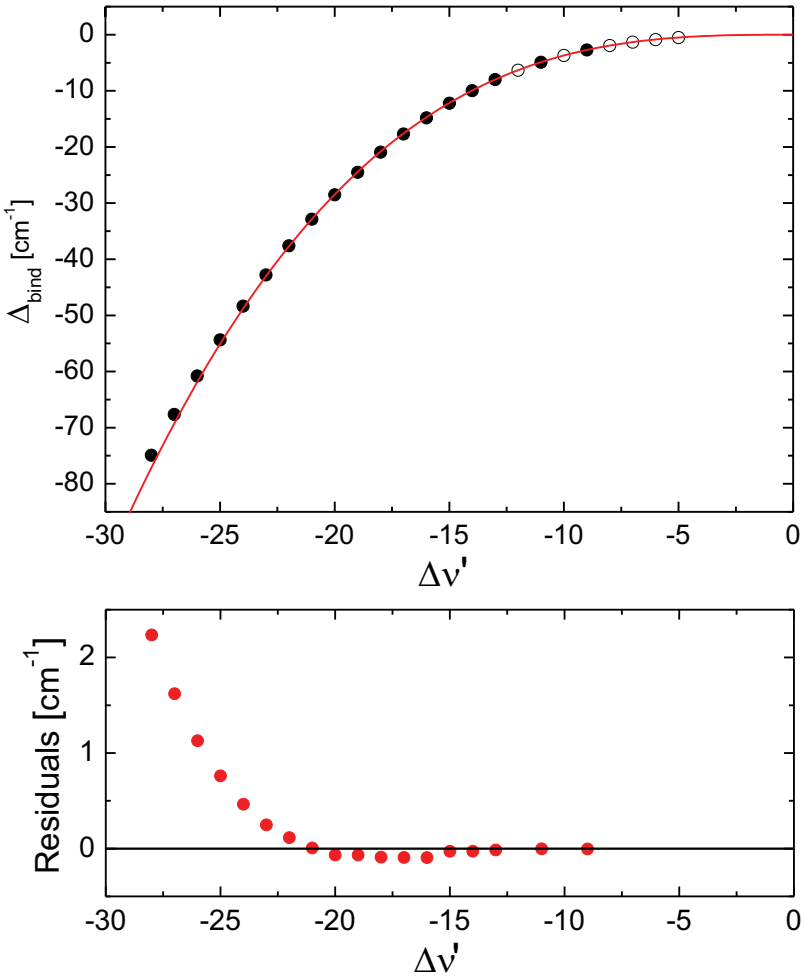

Figure 5.8: *Comparison of the binding energy of deeper bound molecules with the LeRoy-Bernstein model in eq. 2.50. (Top) Binding energy over relative vibrational quantum number $\Delta v'$. Solid circles represent the vibrational levels observed in the conservative trap while open circles are vibrational levels taken from [7]. The solid line is a LeRoy-Bernstein plot with values $C_6 = 5684 \cdot E_h a_0^6$ and $v_{frac} = 0.278$ assigned in [7]. (Bottom) Deviation of the vibrational levels observed in the HT from the LeRoy-Bernstein plot. A dramatic discrepancy is evident for vibrational states below $\Delta v' = -21$.*

with frequency steps of 2...10 MHz at exposure times of 10...500 ms and the same power of 100 mW. For these detailed scans, the polarization of the PA-laser was chosen according to the addressed F'-state (see again sec. 5.3.4) in order to achieve highest possible molecule production rate. The variation in absolute atom number can be attributed to experimental adjustments changing from day to day.

5.3.3 Line assignment

In contrast to the experiments performed in the combined MOT, the atoms prepared in the combined conservative trap are in well defined states prior to illuminating them with the

PA-laser. The Yb atoms are in their $^1S_0$ ground state and the Rb atoms are spin polarized in the $|F = 1, m_F = -1\rangle$ sublevel of the $^2S_{1/2}$ ground state. Thus line assignment is easier compared to PA in a MOT since only the excited state might be ambiguous. Additionally, excitation of Yb_2 could be ruled out for specific lines by performing the same experiment without the presence of Rb atoms.
In consideration of the fact that scanning over the whole frequency range is utterly impossible, one has to preset a restricted range to search for further vibrational levels. In order to do so, I initially used the LeRoy-Bernstein fit from eq. 2.50 with the values $C_6 = 5684 \cdot E_h a_0^6$ and $v_{\text{frac}} = 0.278$ from [7], which gives the binding energy as a function of vibrational number $\Delta v'$, and extrapolated it to the aspired vibrational level. This way, most of the levels could be reproduced and agree well with [1, 7] within error bars. However, the vibrational levels below $\Delta v' = -18$ are already so tightly bound that the deviation from the fit increases considerably, as depicted in fig. 5.8. As a consequence, I adapted and extrapolated the fit including only the last few lines and repeated it after each newly found resonance. These fits gave no meaningful physical information but predicted the positions of the vibrational levels astonishingly well.
As a result, the positions of the vibrational levels $\Delta v' = -19$ and $\Delta v' = -21$ were corrected by 1.5 GHz and 5.8 GHz, respectively, as compared to the values stated in [1, 7]. Here, a misinterpretation of artefacts as lines due to a low signal-to-noise ratio in the previous work has to be assumed. At the binding energies stated in [1, 7] no signatures of PA lines were found by the PA spectroscopy in the HT. The good agreement with the predictions is a confirmation for the attribution of the found levels to the excited Rb*Yb state $^2\Pi_{1/2}$. Table 5.1 lists all observed vibrational levels identified in the combined conservative trap and their corresponding hyperfine splitting.

5.3.4 Polarization effects

This subsection describes the magnetic sublevel selective excitation of Rb*Yb molecules due to the preparation of spin-polarized Rb atoms in the $|F = 1, m_F = -1\rangle$ ground state. This is an inevitable requirement for our general objective of producing and manipulating RbYb ground state molecules in well defined internal quantum states. The ability to experimentally control the excited m'_F-component is illustrated in fig. 5.9. It shows the dependence of the line strength for the transition $|F = 1, m_F = -1\rangle \rightarrow |F' = 1\rangle$ associated with $\Delta v' = -13$ on the polarization of the PA-laser.
The highest molecule production rate can be achieved by illuminating the atoms with σ^+-polarized light while no atom loss is observed with σ^--polarized light. Since the PA-laser beam propagates in parallel to the magnetic field used as quantization axis, no π-polarized light can be produced but the linear polarization is a superposition of both circular polarizations leading simply to a weaker signal. This result can be understood and is in good qualitative agreement with the dipole matrix elements of the involved transitions (see fig. 5.10).
Figure 5.10 displays the relevant magnetic sublevels of the Rb atom and the coupling using polarized light together with the relevant dipole matrix elements (Clebsch-Gordan-

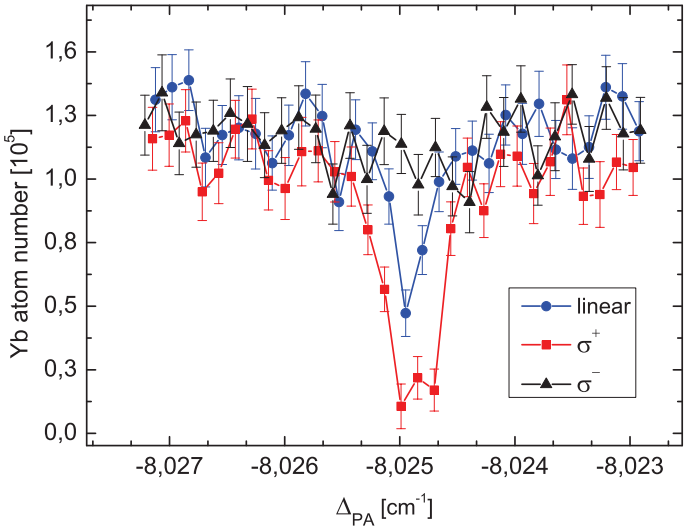

Figure 5.9: *Polarization effects of the PA-laser on the photoassociation transition to the $F' = 1$ hyperfine level of the $\Delta v' = -13$ vibrational level. The observed line strengths agree qualitatively with the dipole matrix elements for the $|F = 1, m_F = -1\rangle \rightarrow |F' = 1\rangle$ transition in Rb. The strongest observed transition has a dipole matrix element of $|F = 1, m_F = -1\rangle \rightarrow |F' = 1, m_F = 0\rangle = -1/\sqrt{12}$ as is also displayed in fig. 5.10. Most importantly, a vanishing of the line for σ^--polarized PA light is observed.*

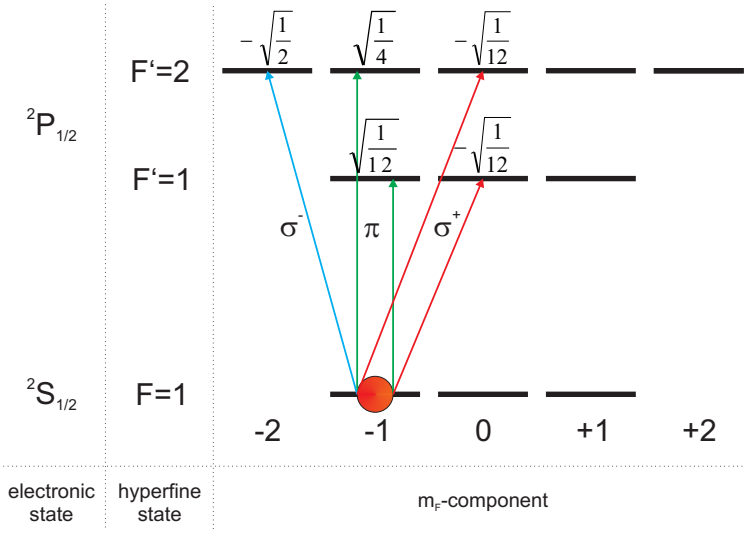

Figure 5.10: *Relevant Rb hyperfine levels and magnetic substates for photoassociation close to the Rb D_1 line together with possible transitions and connected dipole matrix elements. Starting from the $|F = 1, m_F = -1\rangle$ state, specific m'_F-components can be addressed by choosing an adequate polarization. The strongest excitation occurs to the $|F' = 2, m'_F = -2\rangle$ state by σ^--polarized light while no transition to the $|F' = 1\rangle$ hyperfine level with the same polarization is possible.*

coefficients). Starting from the $|F = 1, m_F = -1\rangle$ state, no m'_F-state of the $|F' = 1\rangle$ hyperfine level can be addressed by σ^--polarized light ($|F = 1, m_F = -1\rangle$ is a dark state for σ^--polarized light). This is the same polarization that drives the overall strongest transition to the excited $|F' = 2, m'_F = -2\rangle$-state which is a factor of six stronger than the strongest transition to the $F' = 1$ state. Therefore, σ^--polarization was chosen when searching for unobserved vibrational levels and σ^+-polarization when examining the $F' = 1$-component of a specific already identified vibrational level.

5.3.5 Hyperfine interaction

As a consequence of the fact that photoassociation spectroscopy addresses the so-called physicists' very long-range molecules, the detected vibrational levels appear in pairs that correspond to the molecular equivalent of the hyperfine structure of the $^2P_{1/2}$ excited state in Rb. According to [140] the splitting Δ_{HFS}, defined as the frequency difference between the hyperfine levels $F' = 2$ and $F' = 1$, has a value of 817 MHz for atomic Rb. Due to the lack of angular momentum of the Yb atom in its ground state, the coupling of the nuclear spin to the electronic angular momentum in Rb remains essentially unchanged for very weakly bound molecules. However, we observe a decreasing splitting with increasing binding energy of the vibrational level showing a gradual passage to tightly bound molecules as displayed in fig. 5.11 and indicating a hyperfine coupling which depends on the spatial separation between the Rb and Yb nuclei.
The measured splitting is plotted in fig. 5.11 against vibrational quantum number $\Delta v'$ on the one hand and binding energy on the other hand. Both show a monotonically decreasing hyperfine splitting Δ_{HFS} when approaching tightly bound molecules.

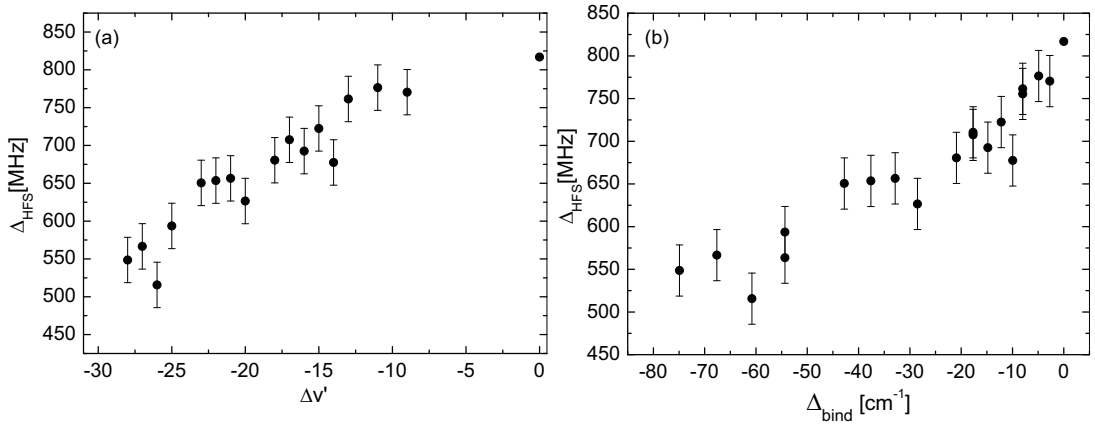

Figure 5.11: *Measured hyperfine splitting Δ_{HFS} defined as the frequency separation between the hyperfine levels $F' = 2$ and $F' = 1$ states of a specific vibrational level over relative vibrational quantum number $\Delta v'$ (a) and binding energy Δ_{bind} (b). As a reference also the hyperfine splitting of atomic Rb with a value of 817 MHz was added at $\Delta v' = 0$ and $\Delta_{\mathrm{bind}} = 0\,\mathrm{cm}^{-1}$, respectively. A monotonically decreasing hyperfine splitting is observed.*

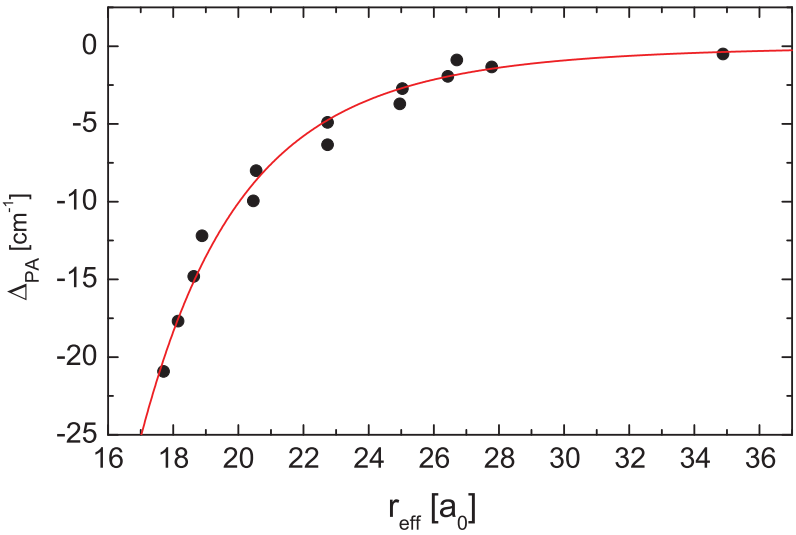

Figure 5.12: *Effective internuclear separation r_{eff} in units of bohr radius a_0 as a function of binding energy Δ_{bind} of the vibrational levels taken from [1, 7]. The values for r_{eff} were calculated from the measured rotational constants B'_{rot}. The solid line represents a fit according to $V(r) = -\alpha/r^6 - \beta/r^{12}$ which allows for an extrapolation of r_{eff} to the deeper bound vibrational levels. See more details in the text.*

The origin of the hyperfine structure, and specifically the hyperfine structure belonging to the $^2\mathrm{P}_{1/2}$ state of ^{87}Rb as detailed explained in sec. 2.11, lies in the coupling between the magnetic moments from the electronic total angular momentum $\vec{j}_{\mathrm{Rb}}$ and the nuclear spin $\vec{i}_{\mathrm{Rb}}$. The value of the hyperfine energy depends on the hyperfine coupling constant $A_{^2\mathrm{P}_{1/2}}$ which in turn depends on the electron density probability $|\Psi(r)|^2$ (see eq. 2.81). In the process of forming molecules this atomic electron cloud gets distorted as chemical bonding gains in importance. The closer the Rb and Yb nuclei approach each other the stronger will be the distortion of the electronic wavefunction of Rb. In turn this has an impact on $A_{^2\mathrm{P}_{1/2}}$ and hence on the hyperfine splitting in the electronically excited state of the molecule.

I therefore plotted the measured hyperfine splitting Δ_{HFS} as a function of internuclear separation r_{eff} in fig. 5.13. The separation r_{eff} correlated to the binding energy of the newly observed vibrational levels was extrapolated from the molecular rotation observed in previous experiments [1] since higher rotational components could not be detected in the hybrid conservative trap. Figure 5.12 illustrates the binding energy of the resonances as a function of r_{eff} from [1]. Assuming an interatomic potential of the form $V(r) = -\alpha/r^6 - \beta/r^{12}$ gives us the possibility to extrapolate r_{eff} to the additionally found vibrational levels by their binding energy Δ_{bind}. The red curve yields fitted values of $\alpha = 6.7 \cdot 10^8$(a.u.) and $\beta = -1.4 \cdot 10^{15}$(a.u.). The extrapolated values to the newly detected vibrational levels can be found in table 5.1.

It is evident that the molecular hyperfine splitting decreases with decreasing internuclear separation. The deepest bound vibrational state belongs to $\Delta \mathrm{v}' = -28$ and exhibits a

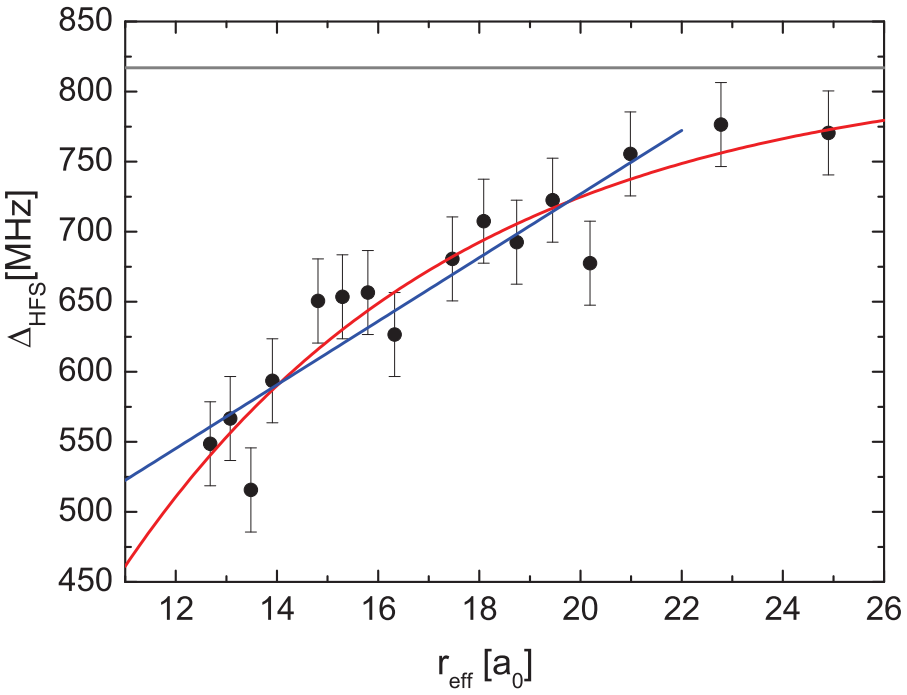

Figure 5.13: *Hyperfine splitting* Δ_{HFS} *in MHz as a function of internuclear separation* r_{eff} *in Bohr radius* a_0 *extrapolated from the molecular rotational structure. The blue line is a linear fit of the crucial region that yields a slope of* $22\,\mathrm{MHz}/a_0$*. The red curve is an exponential fit with a* $1/e$ *- „decay constant“ of* $\upsilon = 6.7\,a_0$ *that asymptotically reaches the atomic hyperfine splitting of* $\Delta_{\mathrm{HFS},0} = 817\,\mathrm{MHz}$ *indicated by the grey line.*

hyperfine splitting of 549(30) MHz which is already less than 70% of the atomic splitting. In the absence of further theoretical work I tried to fit simple functions in order to achieve quantitative results. Figure 5.13 displays a linear fit (blue line) which provides a slope of $22\,\mathrm{MHz}/a_0$ for the crucial range. The red curve in fig. 5.13 shows an exponential fit according to

$$\Delta_{\mathrm{HFS}} = C \cdot \exp\left(-r/\upsilon\right) + \Delta_{\mathrm{HFS},0} \tag{5.7}$$

with $\Delta_{\mathrm{HFS},0} = 817\,\mathrm{MHz}$. This yields a $1/e$ - „decay constant“ of $\upsilon = 6.7\,a_0$. Since the magnitude of the hyperfine splitting decreases with increasing binding energy the magnitude of the magnetic field created by the electron cloud at the position of the nucleus has to decrease, too. This emphasizes, that the production of tightly bound excited Rb*Yb molecules (in the examined region) comes along with an ejection of the valence electron of Rb from the nucleus (see sec. 2.11).

This effect found in the excited molecular state of Rb*Yb is closely related to the interaction that has been proposed to lead to observable Feshbach resonances in the RbYb ground state and alkali-alkaline earth molecules [11, 12, 13]. If a variation of the molecular equivalent of the hyperfine splitting and hence of the hyperfine coupling constant $A_{^2\mathrm{S}_{1/2}}$ in the RbYb ground state is observed, this will be an indication for an actually existing

Table 5.1: Measured vibrational levels $\Delta v'$ and corresponding hyperfine splitting Δ_{HFS} in a mixture of ^{87}Rb and ^{176}Yb. The binding energies are given relative to the Rb D_1 transition at Δ_{PA} =12579.1037 cm^{-1}. Absolute positions have an error of $5 \cdot 10^{-3}$ cm^{-1}, Δ_{HFS} has an estimated error of 30 MHz. No hyperfine splitting could be measured for the two weak lines $\Delta v' = -19$ and $\Delta v' = -24$. r_{eff} gives the internuclear separation calculated using the fitted values from fig. 5.12.

	$F' = 2$	$F' = 1$		
$\Delta v'$	Δ_{bind} [cm^{-1}]		Δ_{HFS} [MHz]	r_{eff} [a_0]
0	0	-0,02725	817	∞
-9	-2,7287	-2,7544	770	24,8998
-11	-4,8958	-4,9217	776	22,776
-13	-8,0016	-8,027	761	20,9875
-14	-9,9589	-9,9815	678	20,1892
-15	-12,1942	-12,2183	722	19,4493
-16	-14,8096	-14,8327	693	18,738
-17	-17,6897	-17,7134	711	18,086
-18	-20,9236	-20,9463	681	17,4685
-19	-24,5102	-	-	16,8849
-20	-28,5149	-28,5358	627	16,325
-21	-32,8616	-32,8835	657	15,7982
-22	-37,6097	-37,6315	654	15,2952
-23	-42,7869	-42,8086	651	14,8124
-24	-48,3581	-	-	14,3519
-25	-54,3464	-54,3662	594	13,9104
-26	-60,7821	-60,7993	516	13,4847
-27	-67,6306	-67,6495	567	13,076
-28	-74,9147	-74,933	549	12,6816

coupling permitting magnetically induced Feshbach resonances.

5.3.6 Line strengths

In general, precise theoretical knowledge of the wavefuntions of the involved states is difficult to obtain (see fig. 2.8 for model wavefunctions) since the wavefunctions depend sensitively on the interaction potential [1]. The Franck-Condon principle [113] (see sec. 2.8) states that the strength of a transition is proportional to the overlap integral of the correlated wavefunctions. Hence, by measuring the amplitude of the line strength as a function of vibrational quantum number it is possible to gain a (qualitative) understanding of this overlap [1]. In fact, in favourable systems, it is possible to map the ground state wavefunction by the amplitude of the photoassociation rates [114]. This *reflection approximation*

can only be applied for systems with a large density of states which is especially valid for homonuclear systems (dominating C_3 coefficient) but unfortunately not for heteronuclear systems (dominating C_6 coefficient) [164].
The laser system used to produce excited Rb*Yb molecules by photoassociation was introduced in sec. 3.2.3. The PA-laser was not frequency-stabilized for experimental convenience and the frequency was changed in each experimental run by simply applying a corresponding voltage to the piezo. Unfortunately, this prevents us from extracting precise quantitative results such as an exact linewidth (see sec. 3.2.3). Additionally, the PA-laser setup suffers from a ASE background which excites the Rb atoms out of the magnetic trap on a timescale depending on the detuning from the Rb D_1 line and hence the examined vibrational level. This changes the Rb density with time during exposure. Therefore, it is also difficult to have identical experimental conditions for each vibrational state in order to get exact line strengths. This section tries nonetheless to deduce some quantitative knowledge on the excited molecular potential which will require further analyzation in the future.
Figure 5.14 illustrates the depletion of the Yb cloud as a function of PA-laser power for an illumination time of 50 ms. The PA-laser was fixed in frequency on the vibrational state $\Delta v' = -17$ using our resonator-transfer lock [152]. It exhibits a non-linear saturation behaviour. A similar effect is achieved by varying the pulse length for a fixed intensity as displayed in fig. 5.15(a). Here, the laser was not stabilized in frequency but scanned over the line in steps of ≈ 5 MHz. While the Yb atoms can be completely converted into molecules for a pulse length of $t = 50$ ms, the signal strength decreases with decreasing pulse length. The smallest exposure time that still can clearly produce molecules is $t = 2$ ms. In fig. 5.15(b) the line depth corresponding to atom loss is plotted as a function of pulse length. It shows that the signal gets saturated. A linear fit including only the first 5 ms, in

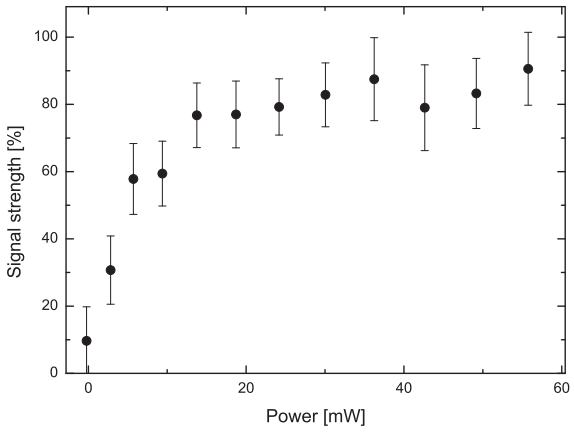

Figure 5.14: *Depletion of the Yb cloud as a function of PA-laser power for the vibrational level $\Delta v' = -17$. The PA-laser was frequency stabilized using our resonator-transfer lock [152]. A saturation of the signal strength is obvious. The pulse length for this measurement was 50 ms.*

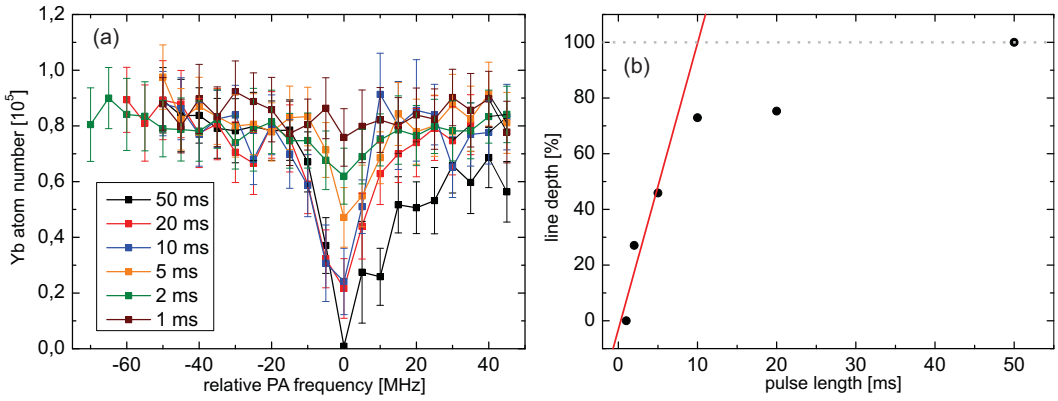

Figure 5.15: *(a) Line shape of the strong transition to $\Delta v' = -13$ for different PA-laser pulses with $P = 50\,\mathrm{mW}$. For pulses with $t > 2\,\mathrm{ms}$ a loss in Yb atom number becomes visible. (b) Atom loss as a function of pulse length. The red line is a linear fit including only the firt three values.*

which saturation is not yet achieved gives an indication of the timescales needed to drive molecular transitions. It shows a duration of 10 ms needed to convert all the Yb atoms into excited Rb*Yb molecules and hence a photoassociation rate of $100\,\mathrm{s}^{-1}$ and a molecule production rate of $8.5 \cdot 10^6\,\mathrm{s}^{-1}$. However, this measurement represents just a lower limit since only $P = 50\,\mathrm{mW}$ were used, saturation occurred at an early stage and the Rb density decreased quickly with the exposure time. According to eq. 2.70 the maximum achievable photoassociation rates are $r_{\mathrm{PA}}^{\mathrm{max}} \approx 7000\,\mathrm{s}^{-1}$ per ytterbium ground state atom, assuming a temperature of $T_{\mathrm{RbYb}} = 1.7\,\mu\mathrm{K}$ and a rubidium density of $\rho_{\mathrm{Rb}} = 2.7 \cdot 10^{13}\,\mathrm{cm}^{-3}$ (see sec. 4.1) and hence still way above the rates estimated here.

In principle, if every applied parameter is known accurately enough, one can deduce the Rabi-frequency of the transition (see sec. 2.8) and hence the Franck-Condon factor. If this is done for every vibrational level, one can map the overlap of the wavefunctions at these discrete positions. Figure 5.16 trys to evaluate the recorded data in order to get a line strength as a function of vibrational level and internuclear separation. Plotted is the depth of every resonance normalized by the applied intensity and interrogation time. Unfortunately, in a usual scan for the $F' = 2$ state, the Yb atom number was completely depleted which hinders a comparison for the lines. Thus, I evaluated the levels for the $F' = 1$ state measured with σ^+-polarized light. The strength is a factor of six smaller than the strength for $F' = 2$ and therefore saturation in not reached. Although the Franck-Condon factors can vary independently for the different F' states, this gives a first idea of the wavefunction's overlap.

However, the large fluctuations in line strength noticed in fig. 5.16 (a) emphasize a sensitive dependence on the experimental properties. If several values for one vibrational state were recorded, I averaged the line strength as illustrated in fig. 5.16 (b) which is then plotted against internuclear separation r_{eff}. The two strong transitions $\Delta \mathrm{v}' = -9$ and $\Delta \mathrm{v}' = -11$ are striking and also the nodes (blue dots) at $\Delta \mathrm{v}' = -19$, $\Delta \mathrm{v}' = -24$ and $\Delta \mathrm{v}' = -29$

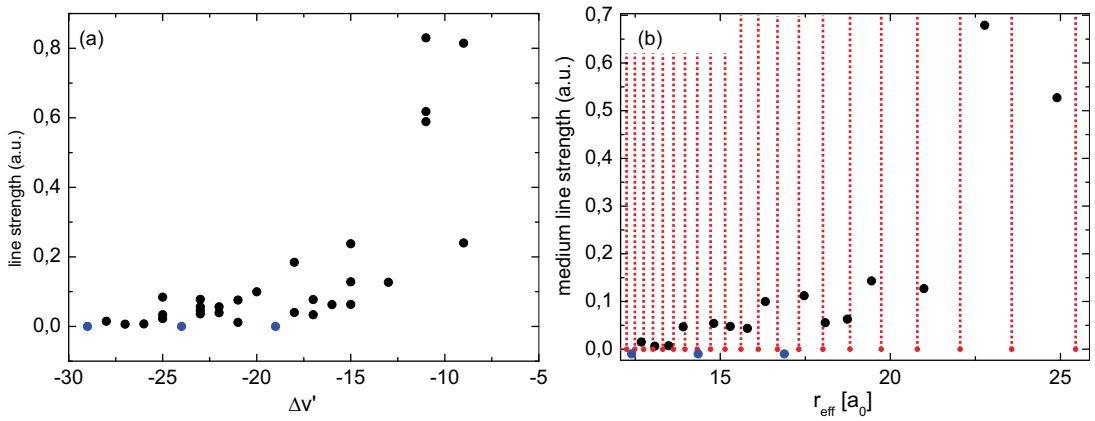

Figure 5.16: *(a) Recorded data showing the line strength normalized by the applied intensity and PA-laser exposure time as a function of vibrational quantum number $\Delta v'$. (b) If more data is present for one vibrational state, the value for the strength is averaged and plotted as a function of internuclear separation r_{eff}. The blue dots correspond to weak vibrational states whose line strength was manually set to zero. The red dots and dashed lines in (b) denote the position of nodes in the overlap of the wavefunctions following eq. 2.56 (fig. 2.10) with a van-der-Waals coefficient of $C_6 = -2837.2\, E_h a_0^6$ and a scattering length of $a = +216.8\, a_0$ [2].*

which were set to 0 since they were not observed. Most importantly, a decrease in transition probability while approaching the inner part of the potential is demonstrated.
According to eq. 2.56 the position of nodes in the wavefunction overlap and hence the Franck-Condon factor is connected to the C_6-dispersion coefficient and the s-wave scattering length of the considered system. Figure 2.10 displays the scattering length as a function of the position of nodes for a van-der-Waals coefficient of $C_6 = -2837.2\, E_h a_0^6$ of the molecular ground state in RbYb [2]. The dashed line corresponds to a scattering length of $a = +216.8\, a_0$ for $^{87}\mathrm{Rb}^{176}\mathrm{Yb}$ [2] and the nodes are marked by the red dots and lines in fig. 5.16 (b). The density of nodes in the overlap integral of the wavefunctions increases considerably for small internuclear separations. This is the reason for the decreasing line strength (fig. 5.16 (b)) while approaching the inner part of the interaction potential. Therefore, a direct transition from atom pairs to tightly bound molecules is unlikely and the best choice for production of rovibronic ground state molecules is using multiple transition steps.

6

2-Photon Photoassociation

This chapter summarizes the most important experimental results that we achieved by means of 2-photon photoassociation (2-PA) spectroscopy in an ultracold mixture of ^{87}Rb and various Yb isotopes [8, 3]. It is not meant to give detailed information but rather emphasize the basic experimental procedure and conclusions for the RbYb molecule. The main results are already discussed extensively in the PhD thesis of F. Münchow [3].
The experiments were performed in a continuously loaded combined MOT based on the work in [1] but extended in order to gain information about the molecular electronic ground state $^2\Sigma_{1/2}$ of RbYb. We were able to detect seven vibrational levels with a binding energy reaching up to $E_b = -h \times 58.5\,\mathrm{GHz}$ for the vibrational level $\Delta \mathrm{v} = -8$ in ^{87}Rb^{176}Yb using a *loss-from-loss-spectroscopy* as detection.
In a collaboration with a theory group we were able to map out the interaction potential by combining the experimental results for ^{87}Rb^{176}Yb and three isotopic combinations with a theoretical model [2]. We were able to deduce the most probable number N of bound states supported by the potential, the potential depth D_e together with C_6-coefficients and also to give an accurate prediction of the interspecies s-wave scattering lengths of all Rb-Yb isotopic combinations. A summary of the theory part of this work can be found in sec. 6.3. A similar analysis was done independently by Brue et al. [13] based on the experimental data published in [3]. Brue et al. analyzed the interaction potential with regard to magnetic Feshbach resonances in RbYb and determined possible positions (see chap. 7).
In addition to the determination of the binding energies, we were able to determine approximate values for several molecular transition probabilities by means of Autler-Townes spectroscopy [3].

6.1 Principle and experiment

Experiment

In a usual two-color photoassociation experiment, three atomic or molecular states are coupled by two laser frequencies which allows to determine the binding energies of weakly bound vibrational levels in the electronic ground state. The principle of the 2-photon photoassociation (2-PA) experiment in our case of RbYb is illustrated in fig. 6.1. The first step is the 1-PA process described in chapter 5 which uses a PA-laser with frequency ν_1 (ν_L in chap. 5) to create excited Rb*Yb molecules in the $^2\Pi_{1/2}$ state starting from

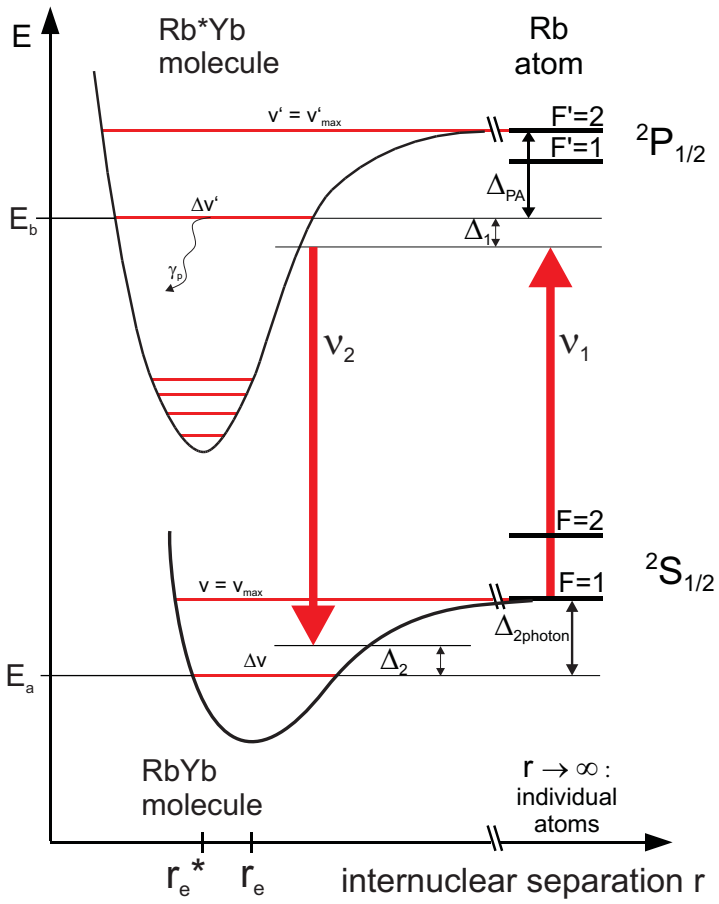

Figure 6.1: *Principle of 2-photon photoassociation (adapted from [8]). The PA-laser with frequency ν_1 can have a detuning Δ_1 from the vibrational level $\Delta v'$. The probe laser with frequency ν_2 acts on the same excited vibrational level $\Delta v'$ and probes a vibrational level Δv of the ground molecular state. For resonant probe laser ($\Delta_2 = 0$) the binding energy of Δv is given by the frequency difference $\Delta_{2\text{photon}}$ of the two lasers.*

unbound atom pairs. Contrary to the 1-PA experiment, this laser is not scanned in frequency but fixed on a free-bound resonance ($\Delta_1 = 0$) in order to continuously create excited molecules in a specific vibrational state $\Delta v'$. Since the experiment was performed in the combined MOT [3], the produced excited molecules were detected as before by trap-loss spectroscopy by observing the Yb-MOT fluorescence. As described in chap. 5 the Yb MOT fluorescence is reduced if the PA-laser is on resonance with a transition from an unbound atom pair to a molecular state.

For 2-PA, the region of molecule production is superimposed with a second laser, the probe laser, with frequency ν_2 and continuously scanned. If this laser has to address a bound vibrational state Δv of the RbYb ground state $^2\Sigma_{1/2}$ ($F = 1$), ν_2 needs to be greater than ν_1. Whenever ν_2 is resonant with a bound-bound molecular transition, the excited level is perturbed by lightshift effects which causes the PA-laser to be slightly off-resonant.

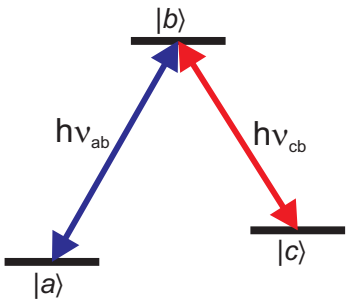

Figure 6.2: *Schematic illustration of a three level system. For details see text.*

This in turn leads to a lower excited molecule production rate by the PA-laser and an increased atom number in the MOT. For the detection channel it means that less losses are recorded resulting in an increased Yb MOT fluorescence. Therefore, this detection scheme is referred to as *loss-from-loss spectroscopy*. A typical spectrum obtained from such a measurement is depicted in fig. 6.3. The first 2-PA spectroscopy was performed with ^{7}Li in 1995 [165].

Principle of two-photon photoassociation spectroscopy

Before giving details on the experimental results, I will outline the basic physical processes responsible for the 2-photon photoassociation spectrum. I will not derive the complete formalism but instead just emphasize the essential formulas. A more detailed description can be found in [3, 91, 70].
Consider a three level system with levels $|a\rangle$, $|b\rangle$ and $|c\rangle$ with energies $h\nu_i = \hbar\omega_i$ $(i = a, b, c)$ as depicted in fig. 6.2. In our system, $|a\rangle$ corresponds to the vibrational level Δv of the ground molecular state, $|b\rangle$ to the vibrational level Δv$'$ of the excited molecular state and $|c\rangle$ to the situation of two unbound atom pairs. If the transition $|a\rangle \leftrightarrow |b\rangle$ with resonance frequency $\omega_{ab} = 2\pi\nu_{ab}$ is driven by a strong laser field $\vec{E}_L = E_0\vec{\epsilon}\cos\left(\omega_L t - \vec{k}_L \cdot \vec{r}\right)$ with polarization vector $\vec{\epsilon}$, frequency ω_L and detuning $2\pi\delta = \omega_L - \omega_{ab}$, Rabi oscillations are induced [91]. The corresponding resonant Rabi frequency

$$\Omega_0 = \frac{\vec{\epsilon}E_0}{\hbar} \cdot \langle a|\vec{d}|b\rangle \tag{6.1}$$

with the dipole operator $\vec{d}$ and the transition dipole moment $\langle a|\vec{d}|b\rangle$ is connected to eq. 2.59. The Rabi frequency is the oscillation frequency of the population probability of the involved states in the presence of the laser field $\vec{E}_L$. After introducing spontaneous emission with a rate γ, the resonant Rabi frequency can be rewritten as

$$\Omega_0 = \gamma\sqrt{\frac{I}{I_{\text{sat}}}} \tag{6.2}$$

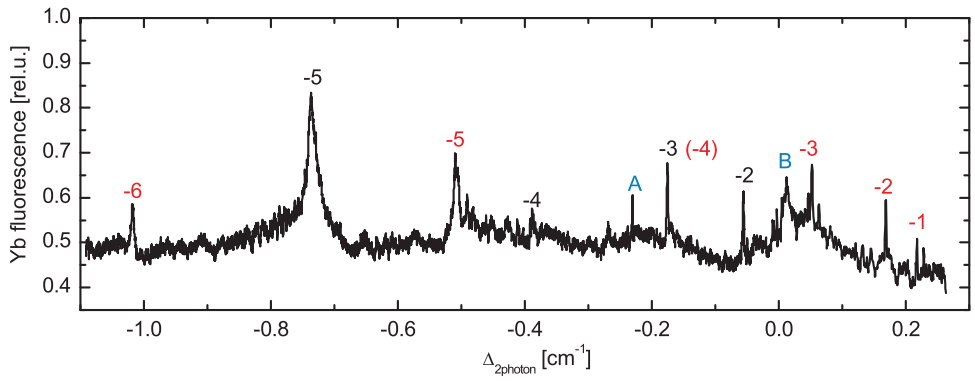

Figure 6.3: *2-Photon-Photoassociation spectrum with the PA-laser frequency stabilized on the 1-Photon-PA resonance $|\Delta v' = -9,\ F' = 2\rangle$ (from [8]). Resonances are assigned by their relative quantum number Δv of the molecular ground state. Both hyperfine levels, $F = 1$ (black) and $F = 2$ (red), could be identified. Blue capital letters indicate an increase in the Yb atom number due to losses in the Rb MOT induced by the PA-laser.*

with the intensity $I = 1/2\, c\varepsilon_0 E_0^2$ and the saturation intensity

$$I_{\mathrm{sat}} = \frac{\hbar\omega_{ab}^3\gamma}{12\pi c^2} \tag{6.3}$$

of the driving laser field. If the laser field is not resonant with the (atomic) transition but has a small detuning δ, the oscillations between the two states can be described by the generalized Rabi frequency

$$\Omega = \sqrt{(2\pi\delta)^2 + \Omega_0^2}\,. \tag{6.4}$$

Experimental results and conclusions

In order to probe the ground state (state $|a\rangle$ in fig. 6.1) by two-color photoassociation, the frequency of the PA-laser was first set to a free-bound transition continuously producing excited molecules in a specific vibrational level (e.g. $\Delta \mathrm{v}' = -9$ with a binding energy of $\Delta_{\mathrm{bind}} = -2.7287\,\mathrm{cm}^{-1}$) [8]. For details regarding the stabilization of the PA-laser one may refer to [152, 109, 3]. The additional loss channel reduced the fluorescence signal to a new steady state of roughly 50% of the maximum signal in the case of $\Delta \mathrm{v}' = -9$.
The probe laser with frequency ν_2 was continuously scanned and whenever it was resonant with a bound-bound transition, the resonance was detected by an increased Yb MOT fluorescence as illustrated in fig. 6.3.
The frequency of the probe laser was recorded by the same wavemeter and same datalogging system as for 1-PA experiments (see chap. 5 and sec. 3.2.6) with an accuracy of $5{\cdot}10^{-3}\,\mathrm{cm}^{-1}$. While in 1-photon PA experiments the binding energy Δ_{bind} of an excited vibrational level is given by the difference of the PA-laser with respect to the atomic threshold, $\Delta_{\mathrm{bind}} =$

$\tilde{\nu}_1 - \tilde{\nu}_{\mathrm{D1}}$ (eq. 5.2), in 2-PA experiments the binding energy of the ground state

$$\Delta_{\mathrm{2photon}} = \tilde{\nu}_1 - \tilde{\nu}_2 \tag{6.5}$$

can be inferred from the frequency difference between the irradiated lasers. Thus, for states with $\Delta_{\mathrm{2photon}} < 0.07\,\mathrm{cm}^{-1} \mathrel{\widehat{=}} 2\,\mathrm{GHz}$ we could achieve a better accuracy of $5 \cdot 10^{-4}\,\mathrm{cm}^{-1}$ by taking directly the beat-note of the PA-laser and the probe laser.
Analogous to the 1-PA experiment, the 2-PA experiment resolves the molecular equivalent of the hyperfine structure in Rb, but in this case for the Rb ground state with a splitting of $\Delta_{\mathrm{HFS}} = 0.227\,\mathrm{cm}^{-1}$ between the hyperfine states $F = 1$ and $F = 2$. This knowledge could be used as a guide for line assignment and it is therefore evident that the detected lines on the blue side of the spectrum ($\Delta_{\mathrm{2photon}} > 0$) belong to the $F = 2$ hyperfine level. Furthermore, the frequency of the lines assigned to the $F = 2$ hyperfine state have to be corrected for the hyperfine splitting in order to extract correct binding energies. Also, similar to the 1-PA, the line strengths are an indication for the transition probability between the involved molecular states and hence for the overlap of the molecular wave functions, according to the Franck-Condon principle [113]. In principle, it is possible to determine the transition probabilities by measuring the intensity dependence of the transition strength as was done in [3]. I will not show this procedure but shortly demonstrate a rather elegant way to quantify those values by means of Autler-Townes spectroscopy [166, 167] in sec. 6.2.
In order to verify our experimental results we repeated the measurement with the PA-laser stabilized on the vibrational level $\Delta \mathrm{v}' = -11$ with a binding energy of $\Delta_{\mathrm{bind}} = -4.8958\,\mathrm{cm}^{-1}$. For precise modeling of the ground state potential which was done in collaboration with a theory group [2], our 2-PA data was reanalyzed, absolute positions were stated more precisely and error bars estimated for each data point individually. The reevaluated detected vibrational levels for $^{87}\mathrm{Rb}^{176}\mathrm{Yb}$ can be found in table 6.1 and the ones for the other isotopes $^{87}\mathrm{Rb}^{x}\mathrm{Yb}$ in table 6.2. Additionally, the values from the modeled potential were included [2].
It is worth noting that even each rotational component R' in the excited state can be addressed separately. In the case of the bound-bound molecular transition ($|a\rangle \rightarrow |b\rangle$) only states with equal rotational quantum numbers ($R = R'$) are coupled. This allows us in principle to determine the rotational energy for the vibrational states in the molecular ground state and to deduce an effective internuclear separation r_{eff} as was done in sec. 5.2 for the excited state.

6.2 Autler-Townes spectroscopy

As was already mentioned, the strength of a bound-bound transition is connected to the Rabi frequency from eq. 6.4. By measuring the intensity dependence of the linewidth of a transition it is possible to deduce the transition probability and hence the corresponding Franck-Condon factors (see sec. 2.8). But this experimental method might give inaccurate values since the width itself can be also effected by other factors like the temperature of

the atomic sample or the stimulated width [46]. An elegant experimental technique for determining the Rabi frequency can be achieved by probing the coupled states through an auxiliary state. In this Autler-Townes spectroscopy [166, 70] the two coupled states exhibit a splitting which directly corresponds to the Rabi frequency. This was also explained in [3] and is only briefly summarized here.
In 1955, Autler and Townes observed a splitting of a microwave transition of the OCS molecule [166]. The experimental situation in our case of RbYb is a simple variation of the 2-photon photoassociation spectroscopy explained in sec. 6.1. Instead of stabilizing the PA-laser to a free-bound transition, in this case the probe laser is fixed onto the bound-bound transition. The Autler-Townes splitting becomes consequently visible by scanning the PA-laser over the well-known 1-PA resonance as illustrated in fig 6.4. Here, the probe laser was held fixed in frequency on the $R' = 1, \Delta_R = +1$ line (see also fig. 5.2) which hence shows a striking splitting. This splitting depends, considering eq. 6.4, on the intensity as well as the detuning of the probe-laser. Figure 6.5 shows our examination of the splitting as a function of both parameters.
The most promising method to extract Franck-Condon factors f_{FC} is to measure the splitting for resonant ($\delta = 0$) lasers for a specific irradiated power as displayed in fig. 6.5 (a) by the black dots. With the $1/e^2$-radii of $r_{\mathrm{x,probe}} = 952\,\mu\mathrm{m}$ and $r_{\mathrm{y,probe}} = 245\,\mu\mathrm{m}$ [3] of the probe laser the power can be transformed to the needed intensity I in order to obtain the Franck-Condon factor out of the relation

$$f_{\mathrm{FC}} = |\langle a|b\rangle|^2 = \frac{\Omega^2}{\gamma_1^2}\frac{4I_{sat}}{I}\,. \tag{6.6}$$

The Franck-Condon factor for example for the transition $|F' = 2, \Delta\mathrm{v}' = -11, \Delta R = +1\rangle \leftrightarrow |F = 1, \Delta\mathrm{v} = -6\rangle$ can be calculated with the saturation intensity $I_{\mathrm{sat}} = 1.496\,\mathrm{mW/cm^2}$ and $\gamma_1/2\pi = \gamma_{\mathrm{Rb,D1}}/2\pi = 5.75\,\mathrm{MHz}$ [140]. The value obtained for this specific transition is

$$f_{\mathrm{FC}} = 0.20 \pm 0.02\,. \tag{6.7}$$

The stated error only gives the statistical error and does not account for possibly much larger effects due to a large uncertainty of the laser intensity at the location of the atoms (possibly up to a factor of 2). Further Franck-Condon factors for some transitions that we measured can be found in [3] but no value exceeds a factor of $f_{\mathrm{FC}} = 0.4$. Even though the absolute values of the f_{FC} could not be determined precisely, they reveal a high spontaneous decay rate to specific rovibrational level $\Delta\mathrm{v}$ of the molecular electronic ground state after production of excited molecules.

6.3 RbYb isotopologues and modeling of ground state potential

The experiments described until now were usually performed using the isotopic combination $^{87}\mathrm{Rb}^{176}\mathrm{Yb}$. However, by comparing binding energies for different isotopologues, a more precise understanding of the molecular ground state potential can be obtained. Thus, we have measured the binding energies of several isotopologues of RbYb and together with a

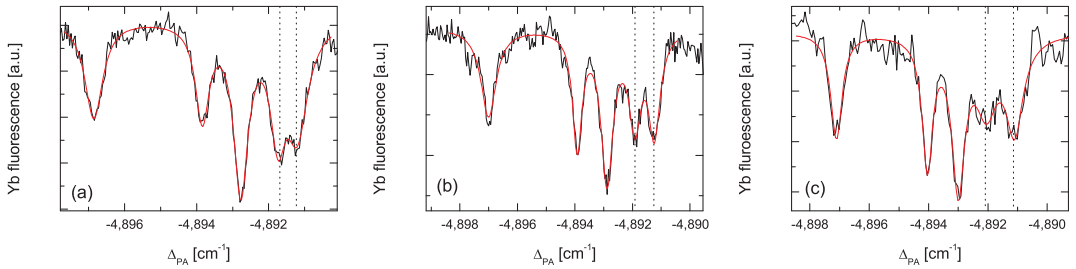

Figure 6.4: *Autler-Townes spectra of $\Delta v' = -9$ with increasing intensity of the probe laser (from [3]). The probe laser is fixed in frequency on the $R' = 1, \Delta_R = +1$ line (see also fig. 5.2 (bottom)) which consequently shows a characteristic splitting. This Autler-Townes splitting is marked by dotted lines and increases with increasing intensity: (a) 1.4 mW, (b) 4 mW, (c) 9.3 mW.*

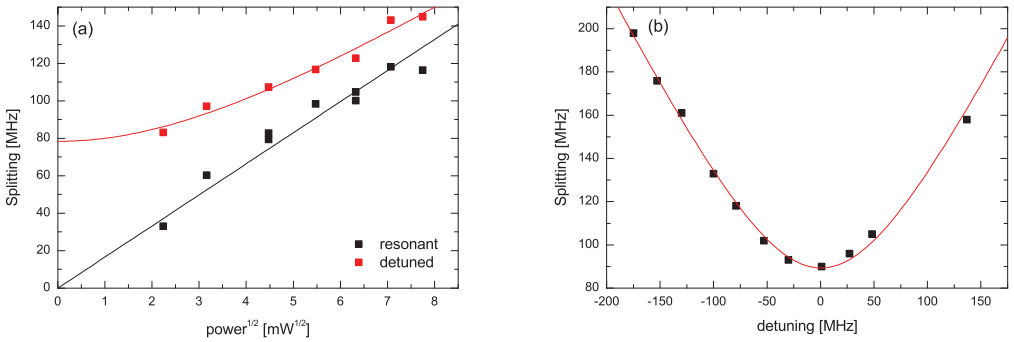

Figure 6.5: *Dependence of the Autler-Townes splitting on the experimental parameters according to eq. 6.4 (from [3]). (a) Splitting plotted against the square-root of the intensity of the probe laser for a resonant (black) and detuned (red) probe laser. The solid lines are linear (black) or parabolic (red) fits to our data. (b) Autler-Townes splitting as a function of detuning from resonance of the probe laser for a fixed intensity. The stabilization and the evaluation of the exact frequency was carried out with our resonator-transfer lock from [152].*

theoretical group used this to obtain a more precise ground state potential [2]. This also allowed us to infer the s-wave scattering lengths for all isotopic combinations of Rb and Yb.

The usefulness of combining data for different isotopologues can be seen from the equations (see sec. 2.4)

$$a = \bar{a}\left(1 - \tan\left(\Phi - \frac{\pi}{8}\right)\right) \tag{2.43}$$

and

$$\Phi = \frac{\sqrt{2\mu}}{\hbar}\int_{r_{\mathrm{in}}}^{\infty}\sqrt{-V(r)}dr\,. \tag{2.45}$$

These connect the interparticle s-wave scattering length a with the phase integral ϕ for the interaction potential and the reduced mass μ of the system. Therefore, by already knowing the position of one bound state for another isotopic combination one can fix the ratio $\phi/\sqrt{\mu}$ and obtain precise knowledge of the interaction potential. The most important quantities related to the ground state potential are the number of bound states N, the potential depth D_e and the position of the least bound state E_{-1}. Using eq. 2.47 these quantities can be used to calculate the scattering lengths a for each isotopic combination.

In [2] our theory colleagues used our experimental data for the ^{87}Rb^{176}Yb molecular ground state (see table 6.1) together with the following data for several Yb isotopes. In order to gain information with high accuracy we measured the binding energy of rovibrational states close to threshold ($E_b < 2\,\mathrm{GHz}$) with the technique of the beat frequency for three other isotopes as listed in table 6.2. The measured binding energies of the vibrational levels are listed in the column *Expt.* with the experimental uncertainty in the column *Error*, which was assigned according to the actual data quality. The vibrational levels are labelled by the vibrational, rotational and total angular momentum quantum numbers $\Delta\mathrm{v}$, R and F, respectively. The value for $\Delta\mathrm{v}$ differs from previous publications by labelling the least bound state by $\Delta\mathrm{v}_{-1} = -1$ instead of $\Delta\mathrm{v}_{-1} = 0$. The column E_{th} gives the theoretical line position from the best fit potential.

Typically, interaction potentials calculated by ab-initio methods are not precise enough in the long-range part to extract the scattering lengths accurately. Figure 6.6 shows possible interaction potentials for the RbYb ground state modeled by Borkowski et al. [2]. The dashed lines represent interaction potentials that differ from the best fit potential in the number of bound states by ± 1.

The theoretical approach was to combine ab-initio potentials employed by coupled-cluster theory (CCSD(T)) for the short-range part and smoothly connect them by means of a switching function in the range of $r \approx 20\,a_0$ to the analytic potential $V(r) = -C_6/r^6 - C_8/r^8$ for the long-range region. This long-range part could be well approximated using the data for ^{176}Yb whereas the data for the other isotopologues was used to choose the best fitting potential by mass scaling.

Table 6.3 features the three potentials with the smallest χ^2-deviation. The potentials are characterized by the number of bound states N, the potential depth D_e and the van der Waals coefficients C_6 and C_8. The most probable potential is the one supporting $N = 66$

$\Delta v'$	Δv	R	F	Expt. [MHz]	Error [MHz]	E_{th} [MHz]
-9	-2	0	1	-304.2	7.7	-300.7
-11	-2	0	1	-304.9	7.1	-300.7
-9	-2	1	1	-283.4	7.2	-276.3
-11	-2	1	1	-291.6	14.9	-276.3
-9	-2	1	2	-304.2	134.2	-275.8
-9	-3	0	1	-1748.6	10.0	-1743.9
-11	-3	0	1	-1748.5	7.3	-1743.9
-9	-3	1	1	-1700.2	10.0	-1700.5
-11	-3	1	1	-1712.1	14.9	-1700.5
-9	-3	1	2	-1748.5	134.2	-1699.0
-11	-3	1	2	-1754.1	200.0	-1699.0
-9	-4	0	1	-5235.0	155.7	-5250.2
-11	-4	0	1	-5277.5	150.0	-5250.2
-11	-4	0	2	-5249.7	20.0	-5247.0
-9	-4	1	1	-5203.7	143.7	-5188.2
-11	-4	1	1	-5190.9	100.0	-5188.2
-9	-4	1	2	-5196.3	14.9	-5185.0
-11	-4	1	2	-5190.2	19.8	-5185.0
-11	-5	0	1	-11760.3	220.5	-11750.9
-11	-5	0	2	-11765.5	150.0	-11745.5
-9	-5	1	1	-11697.3	257.2	-11670.6
-11	-5	1	1	-11673.7	212.1	-11670.6
-11	-5	1	2	-11642.2	100.0	-11665.2
-9	-6	0	1	-22174.8	116.7	-22181.7
-9	-6	0	2	-22207.4	94.5	-22173.4
-9	-6	1	1	-22082.9	143.7	-22083.4
-9	-6	1	2	-22132.0	73.1	-22075.1
-9	-7	0	1	-37487.4	120.0	-37476.0
-11	-7	0	1	-37292.7	212.1	-37476.0
-9	-7	0	2	-37446.2	155.7	-37464.3
-11	-7	0	2	-37431.7	220.5	-37464.3
-9	-7	1	1	-37395.9	120.0	-37359.8
-11	-7	1	1	-37288.0	212.1	-37359.8
-9	-7	1	2	-37381.0	143.7	-37348.1
-11	-7	1	2	-37315.1	212.1	-37348.1
-11	-8	0	1	-58557.4	84.9	-58559.7
-11	-8	0	2	-58430.3	212.1	-58543.9
-11	-8	1	1	-58452.4	93.7	-58425.9
-11	-8	1	2	-58455.4	134.2	-58410.0

Table 6.1: *Reanalyzed binding energies (column Expt.) with experimental uncertainty (column Error) for $^{87}Rb^{176}Yb$ measured by 2-PA [2]. $\Delta v'$ denotes the vibrational level addressed in the excited state. The ground vibrational state is assigned by Δv, R and F. Theoretical values for the binding energies from the fit are included under E_{th}.*

bound states with a potential depth of $D_e = 787.4\,\mathrm{cm}^{-1}$ and a value of $C_6 = -2837.2\,E_h a_0^6$. But since the χ^2-value differs by only 13% ($N = 65$) and 40% ($N = 67$), respectively, the result has to be taken with a pinch of salt.
However, this model allows for accurate predictions of the interspecies scattering lengths for every possible isotopic combination of the ^{x}Rb-^{x}Yb system as specified in table 6.4. According to eq. 2.43 the scattering length varies with the reduced mass μ following a tangent relation which is in turn outlined in fig. 6.7. This shows one of the great benefits of this special molecular system consisting of the atomic species Rb and Yb. Due to the large mass of the involved atoms and the large number of stable Yb isotopes a variety of s-wave scattering lengths can be selected (see table 6.4). For example, ^{87}Rb provides a large and negative scattering length in combination with ^{173}Yb and a large and positive one with ^{174}Yb. The latter one manifests itself experimentally in a spatial separation observed in [6, 10]. An experimental evidence for the scattering length of ^{87}Rb^{170}Yb close to zero is the low thermalization rate measured in previous experiments [6, 9]. The results of these experiments deduce relative scattering lengths compared by the relative thermalization rates and agree qualitatively with the analysis presented here. On the other hand, each scattering length belonging to ^{85}Rb^{x}Yb is small and positive. Brue et al. [13] also modeled the interaction potential and extracted scattering lengths but with a focus on magnetic tunable Feshbach resonances. The extracted values agree to a large extend with the values

Yb	Δ_{PA} [GHz]	Δv	R	F	Expt. [MHz]	Error [MHz]	E_{th} [MHz]
170	-24	-1	0	1	-113.3	15.0	-102.9
170	-24	-1	1	1	-97.4	15.0	-85.6
170	-24	-2	0	1	-1028.8	15.8	-1018.6
170	-24	-2	1	1	-990.8	9.5	-981.7
172	-29	-1	0	1	-166.0	10.0	-155.1
172	-64	-1	0	1	-153.8	20.0	-155.1
172	-29	-1	1	1	-146.1	10.0	-135.3
172	-29	-2	0	1	-1237.1	15.0	-1236.6
172	-29	-2	1	1	-1210.7	15.0	-1197.4
174	-34	-2	0	1	-227.9	10.0	-220.8
174	-34	-2	1	1	-206.7	9.8	-198.6
174	-34	-3	0	1	-1477.6	10.0	-1478.3
174	-34	-3	1	1	-1443.7	18.6	-1437.0

Table 6.2: *Reevaluated binding energies for ^{87}Rb with different Yb isotopes close to threshold and measured by 2-PA [2]. The binding energy, i.e. the frequency difference $\Delta_{2\mathrm{photon}}$ of probe laser and PA-laser, was measured using a fast photodiode and a spectrum analyzer with an accuracy on the order of 15 MHz. The column labelling is almost the same as in table 6.1 except from the intermediate state. Instead of the vibrational quantum number $\Delta v'$ it is labelled by the binding energy Δ_{PA}.*

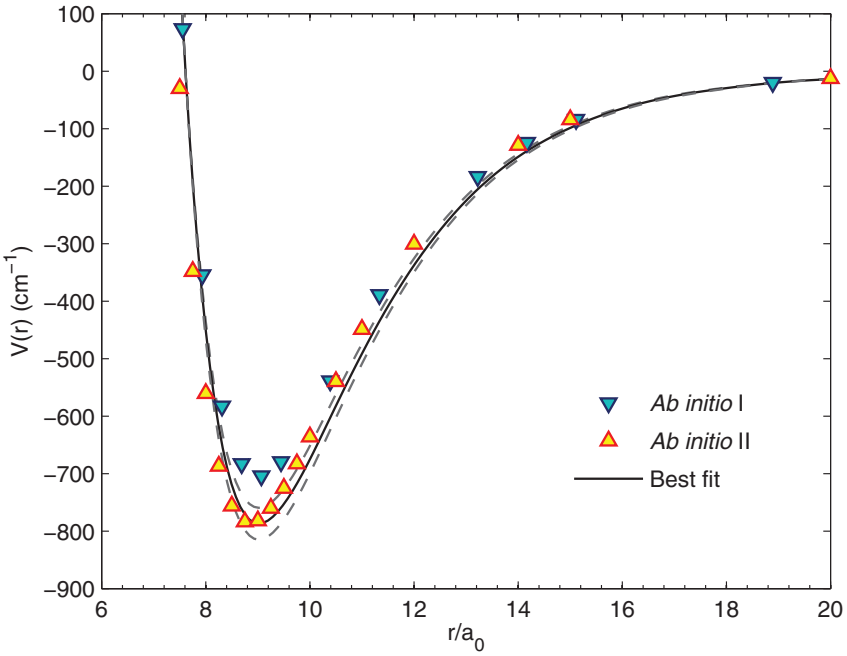

Figure 6.6: *Modeled RbYb ground state interaction potentials (from [2]). Borkowski et al. used two different ab-initio potentials whose calculated points are depicted by blue and orange triangles. The three black lines represent the final potentials matching best to our experimental data (see table 6.3). The solid line is the best fitting potential and the dashed lines are the potentials supporting ± 1 bound vibrational states.*

N	D_e $\left[\mathrm{cm}^{-1}\right]$	C_6 $\left[E_h a_0^6\right]$	C_8 $\left[E_h a_0^8\right]$	χ^2
65	759.9	-2820.0	-4.47	6.0
66	787.4	-2837.2	-4.62	5.3
67	815.4	-2854.0	-4.75	7.5

Table 6.3: *Parameters for the modelled ground state potentials of $^{87}Rb^{176}Yb$ agreeing best with the experimental data [2]. The potentials are characterized by the number of bound states N and the potential depth D_e. The dispersion coefficients C_6 and C_8 describe the long-range behaviour of the interaction potential. The quality of the theoretical fit to our experimental data is evaluated by the χ^2-deviation.*

from Borkowski et al. and are presented in chapter 7.

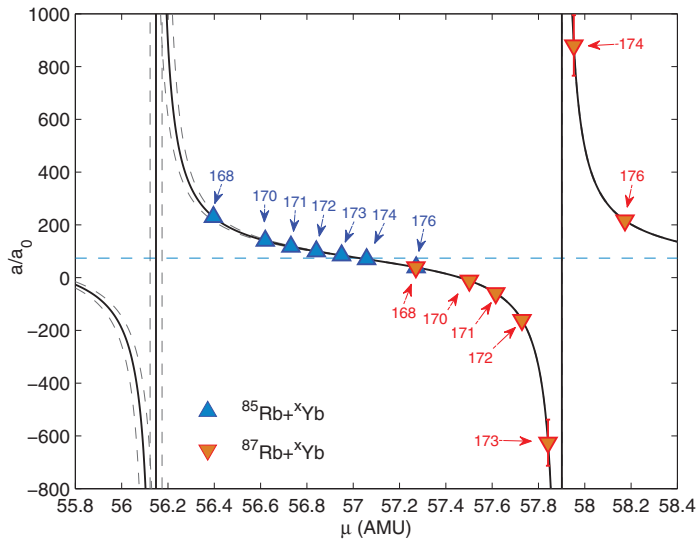

Figure 6.7: *Scattering length a as function of reduced mass μ in RbYb [2]. The black line corresponds to numerical calculations following eq. 2.43. By choosing a proper isotopic combination it is possible to select a variety of absolute values for a. The dashed blue line is the mean scattering length $\bar{a}$ from eq. 2.44 for this system ($\bar{a} = 74.9\,a_0$ for $^{87}Rb^{176}Yb$). The black dashed lines correspond to the same relation belonging to interaction potentials with ± 1 bound states.*

Rb	Yb	a [a_0]
85	168	+230(12)
85	170	+139.9(3.3)
85	171	+117.3(2.3)
85	172	+99.7(1.9)
85	173	+84.3(1.6)
85	174	+69.9(1.5)
85	176	+39.0(1.6)
87	168	39.2(1.6)
87	170	-11.5(2.5)
87	171	-58.9(4.4)
87	172	-161(11)
87	173	-626(88)
87	174	+880(120)
87	176	+216.8(4.7)

Table 6.4: *Scattering lengths of each isotopic combination in ^{x}Rb-^{x}Yb [2] obtained from the theoretically modeled interaction potential (see text). The values agree qualitatively well with the scattering lengths estimated from thermalization experiments [6, 9].*

7

Magnetic Feshbach Resonances in ultracold mixtures of Rb and Yb

This chapter deals with the experiments that we performed searching for magnetically induced Feshbach resonances in mixtures of ^{85}Rb and ^{171}Yb, ^{172}Yb and ^{174}Yb, respectively. These resonances were predicted by theoretical groups [13, 168] but unfortunately not yet detected. During this work, bachelor's and master's theses of A. Obert [169], A. Al-Masoudi [170] and F. Wolf [143] were completed which are partly summarized in this chapter. The chapter begins with the predictions of the positions for the interspecies Feshbach resonances based on our two-photon experiments and continues with a detailed description of the preparation of both atomic species in a crossed optical dipole trap (CODT, see sec. 4.2). Furthermore, the experimental tools to scan for and detect Feshbach resonances are presented. Finally, the experimental results are shown including the observation of intraspecies Feshbach resonances in $^{87}Rb_2$ and $^{85}Rb_2$.

7.1 Predictions

Magnetically tunable Feshbach resonances can occur if the continuum scattering state of the involved atom pair crosses a bound molecular state as a function of external magnetic field (see also sec. 2.10) [45, 44]. With our results obtained from two-photon photoassociation spectroscopy (chap. 6) the long range part of the ground state molecular potential was well determined. This knowledge gives the possibility to predict the positions of possible magnetic Feshbach resonances. The first prediction in the case of Rb-Yb was given by Münchow et al. [3] using the simplest approach of shifting the Rb potential in an external magnetic field by the measured molecular binding energy. An example is illustrated in fig. 7.1 using the isotopic combination of ^{85}Rb and ^{171}Yb.
Due to the absence of a magnetic moment in the Yb ground state, the molecular energy lies almost parallel to the energy of the Rb atom as a function of magnetic field. Feshbach resonances can occur if the molecular energy (dashed curves), which is shifted by the molecular binding energy, crosses the atomic Rb dissociation energy (solid curves) as a function of this external magnetic field B following the relation of the Breit-Rabi formula [171]:

$$E_{|J=1/2,m_J,I,m_I\rangle} = -\frac{\Delta E_{hfs}}{2\,(2I+1)} + g_I\,\mu_B\,m\,B \pm \frac{\Delta E_{hfs}}{2}\left(1+\frac{4mx}{2I+1}+x^2\right)^{1/2}, \quad (7.1)$$

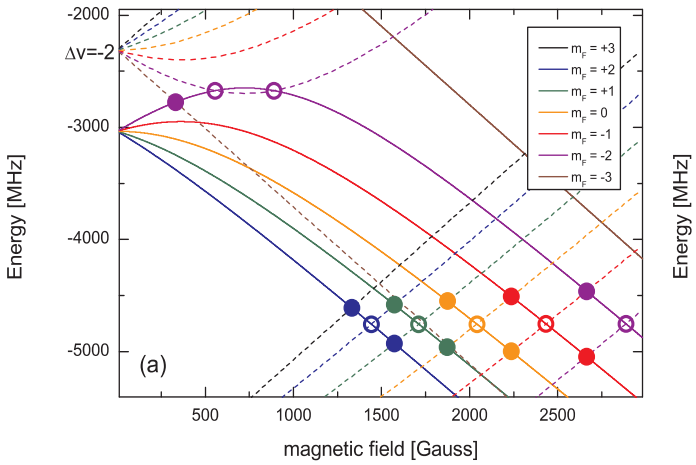

Figure 7.1: *Graphical demonstration for predicting magnetic Feshbach resonances, here using the example of* $^{85}Rb^{171}Yb$ *by Münchow [3]. Shown is the molecular energy (dashed curves), which is shifted by its binding energy, as well as the atomic Rb energy (solid curves) in an external magnetic field B following the Breit-Rabi formula from eq. 7.1 [171]. Feshbach resonances can occur if these two potentials cross as a function of magnetic field for states with* $\Delta m_F = 0$ *(open circles), and additionally in the case of fermionic Yb isotopes with* $\Delta m_F = \pm 1$ *(closed circles).*

with the hyperfine splitting $\Delta E_{\mathrm{hfs}} = A_{\mathrm{hfs}}(I + 1/2)$, the magnetic dipole constant A_{hfs} (see sec. 2.11) and the magnetic quantum number $m = m_I \pm m_J$. The value x is defined as

$$x = \frac{(g_J - g_I)\,\mu_B B}{\Delta E_{\mathrm{hfs}}}\,, \tag{7.2}$$

with the Landé- g-factors g_J and g_I.

The Breit-Rabi formula consists of a linear behaviour for small magnetic fields, known as the anomalous Zeeman effect, which is proportional to the m_F quantum number. It passes into the Paschen-Back effect of the hyperfine structure for strong external magnetic fields that break the coupling between m_I and m_J and is therefore specified by the quantum numbers $|J, m_J, I, m_I\rangle$. Selection rules dictate that only a coupling between states with $\Delta m_F = 0$ (bosonic isotopes of Yb) or $\Delta m_F = \pm 1$ (fermionic isotopes of Yb) can occur. Possible Feshbach resonances are thus characterized by crossings of these states and are marked by open circles for $\Delta m_F = 0$ and solid circles for $\Delta m_F = \pm 1$, respectively.

However, this method only yields the position and does not provide any width for the predicted Feshbach resonances. Theoretical values for the widths together with improved predictions for the positions were calculated by Brue et al. [13] using coupled-channel quantum scattering calculations. Their approach was similar to the one which was used in the context of the analysis of our 2-PA experiments ([2]) (see sec. 6.3). The interaction potential was modeled using CCSD(T) calculations for the short and medium range and connected to the long-range part characterized by the usual dispersion coefficients that could be precisely determined by means of our two-photon PA experiments. Additionally, they calculated the R-dependent hyperfine coupling constant $\zeta_a(R)$ for the molecular

ground state in RbYb (see sec. 2.11) using density-functional theory. Table 7.1 lists several promising resonances and their widths calculated by Brue for every isotopic combination and compares them to the predictions of Münchow. It is worth noting that wide resonances are expected when a „double crossing“ occurs in which a bound state crosses the atomic state just before the turning point [11, 13]. One such crossing is shown in fig. 7.1 for the $m_F = -2$ state (open violet circles), but the actual existence of these crossings is very sensitive to the details of the potential.
In the experiment, we have focussed on the on the magnetic field range up to $\approx 800\,\mathrm{G}$ achievable in our present setup as was described in sec. 3.1. Nearly every resonance for an isotopic combination including ^{87}Rb resides at magnetic fields lying above 1000 G and occasionally reaching almost 5000 G. The only exception is the mixture ^{87}Rb^{168}Yb which exhibits a resonance at 877 G but is experimentally challenging due to the low natural abundance of only 0.13% for ^{168}Yb [149]. On the contrary, ^{85}Rb features multiple resonances with magnetic fields below 1000 G. As was explained in sec. 2.10 the linewidth of a Feshbach resonance is proportional to B^2. Thus, we chose the mixture ^{85}Rb^{171}Yb which shows a resonance at one of the highest reachable fields of 526 G. The resonance occurs in the $m_F = -2$ state that is directly captured by the magnetic trap and is thus easy to prepare in our experiment. To detect such narrow Feshbach resonances (expected linewidth of $\Delta < 1\,\mathrm{mG}$) is experimentally challenging since it requires a very high level of control of the magnetic field. Nevertheless, we had hopes to detect this particular RbYb resonance, since resonances in Na with a calculated width of $0.2\,\mu\mathrm{G}$ had been observed [172].
At the time that we were scanning for magnetic Feshbach resonances, we had preliminary predictions from P. Żuchowski [168] who expected the resonance to be at $\approx 606\,\mathrm{G}$ or $\approx 540\,\mathrm{G}$, depending on the assumed potential depth. We therefore restricted our investigation in the magnetic field range of $\approx 495\,\mathrm{G} \ldots \approx 640\,\mathrm{G}$.

7.2 Searching for magnetic Feshbach resonances

7.2.1 Summary of preparation of Rb and Yb in the CODT

A detailed description of the preparation of an ultracold mixture in ^{85}Rb and ^{171}Yb in the CODT can be found in sec. 4.2. Here, only the most relevant steps will be described.
The experiment attempting to induce magnetic Feshbach resonances in RbYb starts by loading a ^{85}Rb MOT and transferring the atoms into the MT. Similar to the PA experiments (sec. 5.3), this trap is used to spin polarize the atomic sample in the $|F = 2, m_F = -2\rangle$ state and to evaporatively cool it to $\approx 5\,\mu\mathrm{K}$. The atoms are then transferred to the $\mathrm{ODT}_{1064,2}$ with 50% of the maximum power where 100% corresponds to 5.5 W.
Subsequently, an Yb MOT is loaded analogue to the PA experiments. Shortly before transferring the Yb atoms into the $\mathrm{ODT}_{1064,2}$ the trap power is increased to 100%. Here, the Yb atomic sample serves as cold reservoir for the following forced evaporative cooling by reducing the $\mathrm{ODT}_{1064,2}$ power to 20 %. Therefore, the atom numbers have to be adapted in order to not lose too much Yb which can be heated by Rb. Typically, the magnetic Feshbach fields are already applied during the forced evaporative cooling stage. Simulta-

Rb-Yb	m_F	$B_0[G]$ from [13]	$\Delta[mG]$	B_0 [G] from [3]
85-168	2	1100	0.066	1067
85-170	-2	526	-0.10	-
	-2	918	0.30	-
85-171	-2	526	-0.10	555
85-172	-2	340	-0.019	354
	-2	1104	0.21	1091
85-173	-2	206	-0.0055	216
	-2	1238	0.21	1228
85-174	-2	90	-0.0009	99
	-2	1354	0.24	1346
	-1	270	-0.11	-
	-1	452	0.30	-
85-176	-1	925	0.43	917
	0	434	0.14	422
	1	203	0.021	194
	2	120	0.0033	114
87-168	1	877	0.3	834
	1	4466	2.4	-
87-170	1	1287	-3.8	1246
	1	4965	-17.9	-
87-171	-1	3923	-10.9	3886
	1	1487	-1.6	1447
87-172	-1	4122	-10.4	4085
	1	1686	-1.7	1646
87-173	-1	4320	-20.7	4283
	1	1883	-3.9	1845
87-174	-1	4517	23.9	4481
	1	2081	5.2	2043
87-176	-1	4912	3.5	4878
	1	2476	0.9	2439

Table 7.1: *Predictions for the positions B_0 and elastic widths Δ of interspecies Feshbach resonances with $\Delta m_F = 0$ in ytterbium-rubidium mixtures from [13] compared to [3]. All resonances with $B_0 \lesssim 1000\,\mathrm{G}$ and additionally resonances with experimentally simple accessible entrance channels m_F are listed. For further predictions see [13].*

neously, the ODT_{1064} power is increased to 300 mW producing the crossed optical dipole trap. This results in atom numbers of $N_{\mathrm{Rb}} = 5 \cdot 10^4$ and $N_{\mathrm{Yb}} = 1.5 \cdot 10^5$ at temperatures of $T_{\mathrm{Rb}} = 12\,\mu\mathrm{K}$ and $T_{\mathrm{Yb}} = 10\,\mu\mathrm{K}$. Finally, the magnetic fields are either fixed or ramped while holding the atomic species together in the CODT for 500 ms.

One drawback of this preparation cycle is the population of Rb atoms in undesired spin states. Since the MOT magnetic fields for Yb are applied during storage of Rb in the $ODT_{1064,2}$, the magnetic field defining the orientation axis for the m_F projections of Rb is missing. Therefore, a small percentage of Rb atoms resides in a wrong spin state due to Majorana spin flips [80]. This leads occasionally to losses due to Rb_2 Feshbach resonances (see for example fig. 7.12) and to a reduction in the experimental signal strength. The spin polarization is not lost while ramping the Feshbach magnetic field up or down since it is parallel to the orienting magnetic field that preserves the spin polarization for the rest of the experiment.

7.2.2 Stern-Gerlach separation of spins

The Stern-Gerlach separation is an experimental tool to identify the magnetic spin state of an atomic sample [173]. In our case, the atom of interest is the optically trapped Rb atom. Due to the different properties of the Rb isotopes, we used two somewhat different methods. Both are based upon the spin dependent force F in an inhomogeneous magnetic field B

$$F = \nabla(\mu \cdot B) = \mu \cdot (\nabla B)\,. \tag{7.3}$$

The magnetic moment μ of an atom along the quantization axis for small magnetic fields is given by

$$\mu = -m_F\, g_L\, \mu_B\,, \tag{7.4}$$

and is therefore dependent on the Landé-factor g_L, the Bohr magneton μ_B and the specific spin state m_F.

Method 1: Stern-Gerlach separation in ^{87}Rb

If an atomic sample evolves ballistically in such an inhomogeneous magnetic field, it experiences a spin dependent displacement along the external magnetic field axis. This technique was used for ^{87}Rb where low temperatures of 1 µK at high atomic densities can be reached. This allows for a sufficiently long TOF-time (≈ 12 ms) to spatially separate the atomic spins in the inhomogeneous magnetic field created by the MOT coils (see sec. 3.1). Absorption images indicating the preparation in different m_F-states are depicted in fig. 7.2 (a).

Method 2: Stern-Gerlach separation in ^{85}Rb

^{85}Rb cannot reach this temperature with the same atom number and after the required expansion times of more than 10 ms the atomic sample cannot be imaged unambiguously. Thus, the Stern-Gerlach experiment was modified in such a way that the atomic sample does not experience a TOF phase. Instead of turning the ODT completely off, its intensity is ramped down to values that produce a shallow potential depth. The inhomogeneous magnetic field is then kept on for ≈ 10 ms displacing the atomic sample inside the trap according to the magnetic moment. Some absorption images demonstrating the spin dependent displacement are shown in fig. 7.2 (b).

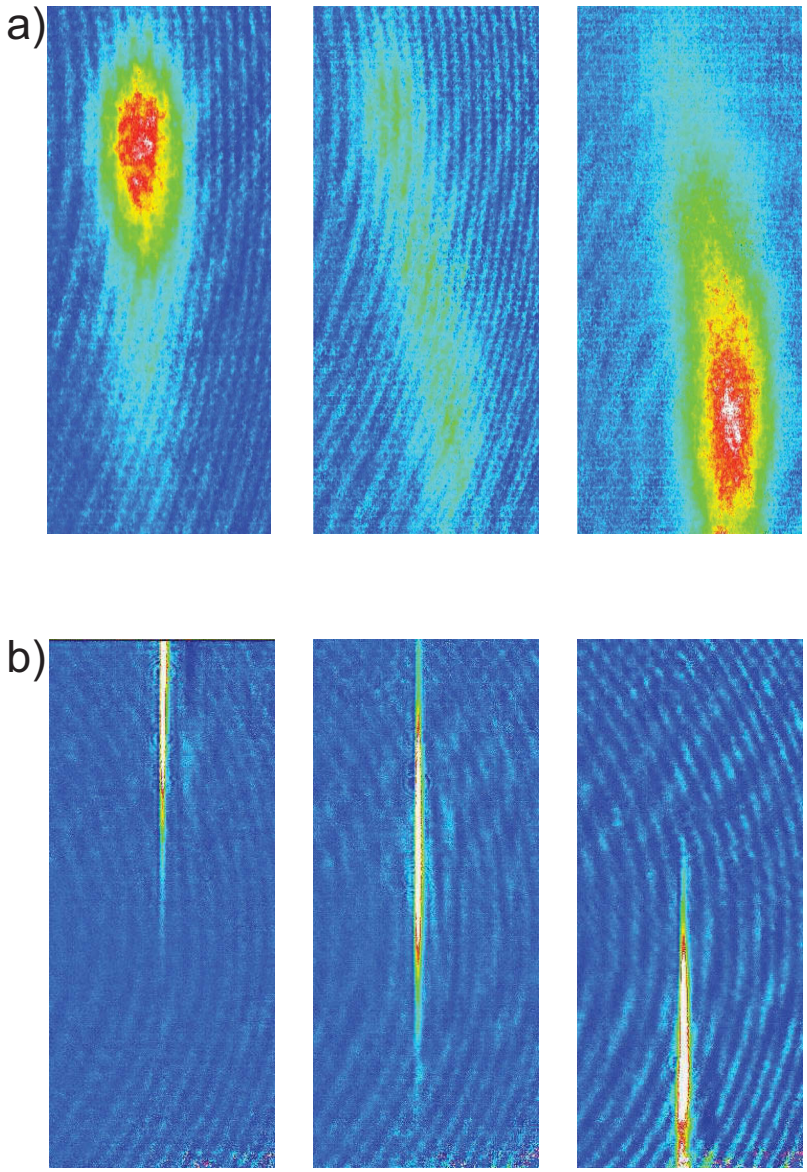

Figure 7.2: *Stern-Gerlach separation in (a) ^{87}Rb and (b) ^{85}Rb (adapted from [170, 169]). (a) Method 1: The sample temperature of ^{87}Rb is sufficiently low to be imaged after a ballistic expansion of 12 ms. A clear spin dependent displacement can be observed for $m_F = -1$ (left) and $m_F = 1$ (right). A distribution over all magnetic substates is shown in the middle picture.*
(b) Method 2: The spin dependent displacement for ^{85}Rb evolves in the shallow ODT. The Zeeman sublevel is encoded in the position of the cloud after a fixed hold time ($\approx$10 ms) $m_F = -2$ (left), $m_F = 0$ (middle) and $m_F = +2$ (right). The external magnetic fields defining the orientation axis as well as the magnetic field gradient are aligned along the axial axis.

7.2.3 Magnetic field calibration

Magnetically induced Feshbach resonances require a homogenous magnetic field applied to the atomic samples. The production of such a magnetic field using the coils already available in the present setup was presented in sec. 3.1. An accurate calibration of the magnetic field as a function of applied current can be achieved by analyzing a magnetic-field dependent radio-frequency transition between Zeeman-m_F substates.
Experimentally, the magnetic field calibration was obtained as follows. A ^{85}Rb sample was prepared in the optical dipole trap after spin-polarizing the sample in the $|F = 2, m_F = -2\rangle$ state in the magnetic trap similar to the usual experimental sequence (sec. 4.2). After applying and stabilizing a specific value for the current a well-defined radio-frequency was irradiated onto the atoms and transfer into the $m_F = -1$ state observed as a function of the frequency. The detection of this population transfer was realized by means of Stern-Gerlach separation as described in sec. 7.2.2.
The energy and thus frequency difference between two Zeeman sublevels of ^{85}Rb atom in an external magnetic field is again described by the Breit-Rabi relation from eq. 7.1 and illustrated in fig. 7.3(a). Here we have used the $m_F = -2$ and $m_F = -1$ states, with an energy difference as a function of magnetic field as displayed in fig. 7.3(b). Performing this for several values of the current through the magnetic field coils allows for a calibration of the present magnetic field as a function of current which is plotted in fig. 7.4. This leads to the following linear relation between the applied current I in ampere and the magnetic field:

$$B(I) = 2.72924\,\mathrm{G/A} \cdot I + 2.05729\,\mathrm{G}\,. \tag{7.5}$$

7.3 Scanning for magnetic Feshbach resonances

After preparing Yb and Rb in the desired spins in the combined optical dipole trap, either a single beam ODT or the CODT, a well defined magnetic field can be applied in order to try to induce magnetic Feshbach resonances. For this purpose, the magnetic field was stabilized by measuring the current flowing through the coils as described in sec. 3.1. The method that was implemented to search for Feshbach resonances is to observe 3-body losses [48] due to the accompanied variation in the inelastic scattering cross section as a function of the applied magnetic field (see sec. 2.10 for a detailed description). In our typical experimental sequence, the magnetic field was already turned on during evaporative cooling of Rb and Yb in the $\mathrm{ODT}_{1064,2}$ and ramped while keeping them in the CODT. In order to test whether the implemented experimental procedure was is in principle working, we studied well-known Feshbach resonances in Rb_2 [174, 175]. These were also observed while scanning for RbYb resonances and additionally, so far undetected Rb_2 Feshbach resonances in other m_F-substates could be observed.

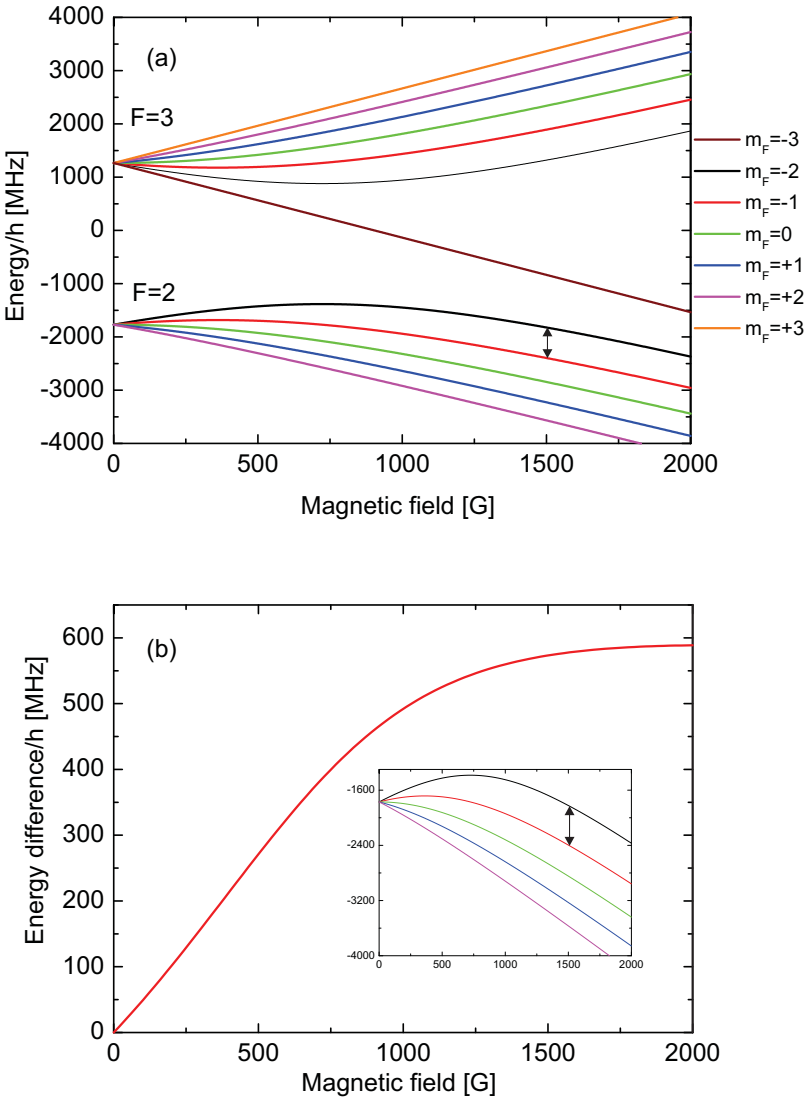

Figure 7.3: *Relevant energies used to calibrate the magnetic field in our vacuum chamber. (a) Breit-Rabi spectrum of the ^{85}Rb ground state atom. Transitions between adjacent spin states can be induced by irradiating a radio-frequency matching their energy difference. (b) Energy difference between the $m_F = -2$ and $m_F = -1$ states. By measuring the frequency needed to drive the transitions as a function of applied current I it is possible to deduce the corresponding magnetic field (see also fig. 7.4).*

7.3.1 Rb_2 Feshbach resonances

Feshbach resonances in Rb were analyzed very thoroughly in many experiments. More than 40 intraspecies magnetic Feshbach resonances have been observed in ^{87}Rb by Marte et al. in 2002 [174]. One of the first Feshbach resonances ever observed in ultracold atoms was seen by Courteille et al. in 1998 in ^{85}Rb [47] which was predicted in 1997 [176]. This is a very broad resonance with an elastic width of $\Delta = 10.9\,\mathrm{G}$ at 156 G that was also used

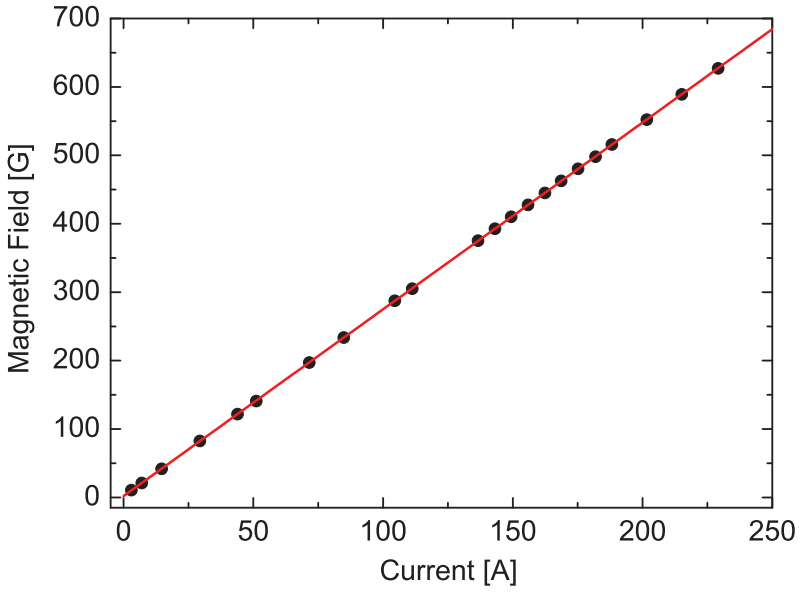

Figure 7.4: *Magnetic field as a function of applied current in our experimental setup. The magnetic field was calculated by measuring the radio-frequency needed for the population transfer between $m_F = -2$ and $m_F = -1$ in the ^{85}Rb $F = 2$ hyperfine ground state detected by Stern-Gerlach experiments (see also fig. 7.3). The linear fit yields a conversion of $B(I) = 2.72924\,\mathrm{G/A} \cdot I + 2.05729\,\mathrm{G}$.*

to produce Bose-Einstein condensates by tuning the intrinsic negative scattering length to a suitable positive value [127]. Table 7.2 lists the positions of experimentally detected Feshbach resonances in ^{85}Rb and ^{87}Rb from [174, 175] including their elastic width Δ that were used to test the capability of our experimental methods to observe Feshbach resonances.

Figure 7.5 depicts our experimental examination of the two broadest resonances in ^{85}Rb at 156 G and 532.3 G revealing general characteristics of Feshbach resonances. Plotted are the numbers of remaining Rb atoms (black dots) as well as the size σ_y of the Rb cloud in radial direction (blue dots), which is a measure for the temperature, after the hold time in the magnetic field. First of all, huge losses as a function of magnetic field are monitored. As already mentioned, these result from three-body losses and therefore the position of maximum losses corresponds to large values of the scattering length a close to the pole of the Feshbach resonance (see also fig. 2.15). It is evident, that this experimentally measured „width“ for atomic losses does not agree with the theoretical elastic width of $\Delta = 2.3\,\mathrm{G}$ respective $\Delta = 10.5\,\mathrm{G}$ (see table 7.2) but appears to be much larger. As will be shown in fig. 7.10 the magnetic field range in which atom loss can be observed dramatically depends on the temperature of the atomic sample. Furthermore, saturation effects complicate the determination of this width.

Nevertheless, measurements of the temperature of the atomic cloud as a function of the applied magnetic field can be used to obtain information on the elastic width of a Feshbach

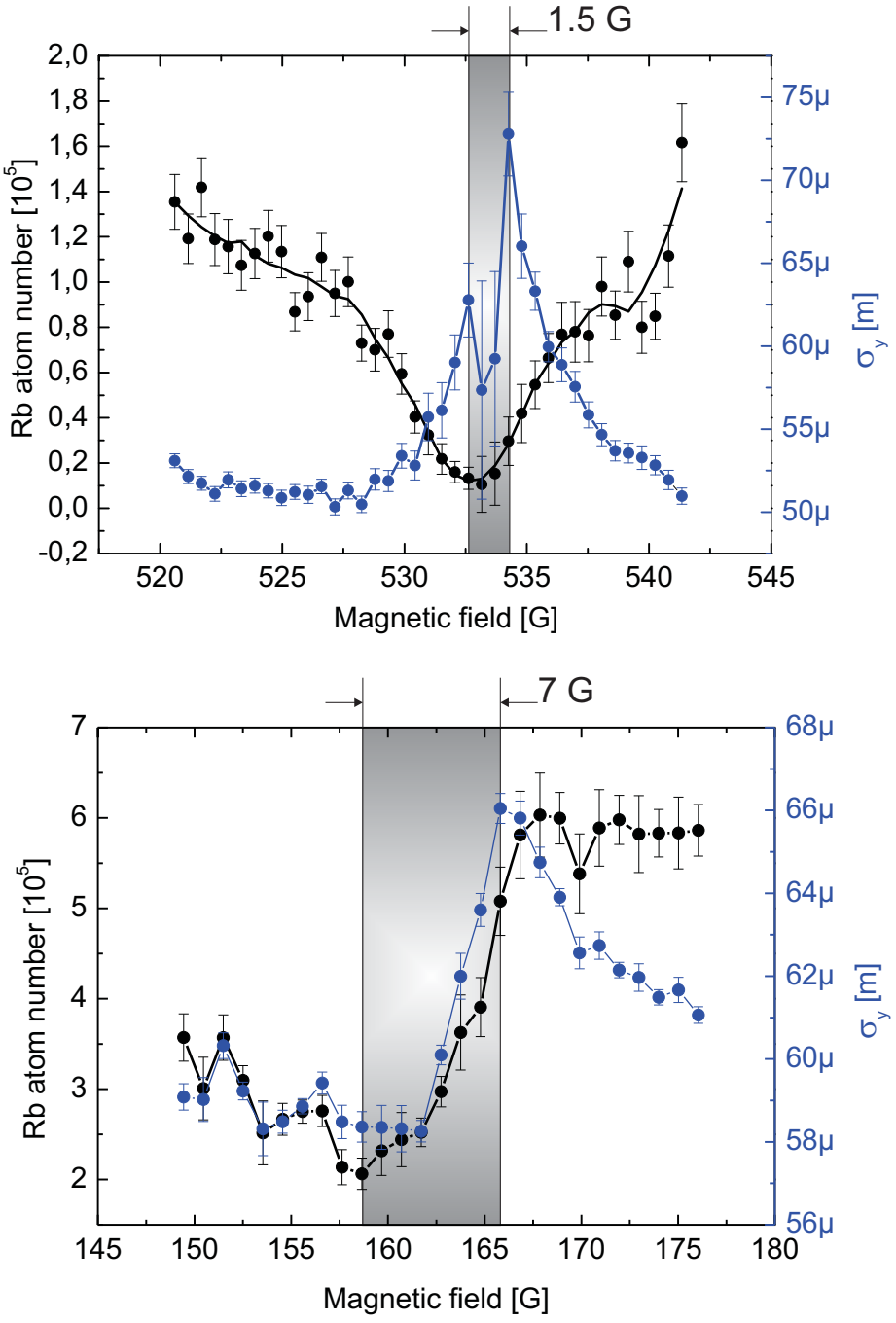

Figure 7.5: *The two broadest $^{85}Rb_2$ Feshbach resonances at 156 G and 532.3 G. Shown are the numbers of remaining Rb atoms (black dots) and the radial width of the atomic cloud σ_y (blue dots) as a function of applied Feshbach magnetic fields where the spacing between adjacent points is 0.5 G (top) and 1 G (bottom), respectively. The lines connecting adjacent points are just a guide-to-the-eye. The „linewidth" in atom number corresponding to the range in which atom loss can be observed is much larger than the elastic width Δ. The latter one is marked in the figures and yields values of 1.5 G and 7 G, respectively, agreeing much better with the experimentally determined values from the literature (see table 7.2).*

Rb	$B_0[G]$	Δ_{exp} [G]	Δ_{th} [mG]
85	156(1)	10.5(5)	10900
85	219.58(1)	0.22(9)	9.1
85	232.25(1)	0.23(1)	2.0
85	248.64(1)	0.12(2)	2.9
85	297.42(1)	0.09(1)	1.8
85	382.36(2)	0.19 (1)	-
85	532.3(3)	3.2(1)	2300
85	604.1(1)	604.1(1)	0.03
85	924.52(4)	2.8(1)	-
87	551.47	-	0.2
87	632.45	-	1.5
87	685.43	-	0.5
87	719.48	-	17

Table 7.2: *Position B_0 and experimentally as well as theoretically determined elastic width Δ_{exp} and Δ_{th}, respectively, of intraspecies Feshbach resonances in ^{85}Rb and ^{87}Rb from the literature [174, 175] that were observed in our experiment. The Feshbach resonances in ^{85}Rb belong to the $|F = 2, m_F = -2\rangle$ entrance channel while the Feshbach resonances in ^{87}Rb belong to the $|F = 1, m_F = -1\rangle$ entrance channel.*

resonance. The elastic width Δ (see again fig. 2.15 and eq. 2.71) is defined as the difference between the position of the pole to the position of the zero crossing of the resonance. Since the magnetic field was turned on directly after transferring the Rb atoms into the ODT which was followed by a phase of forced evaporation, the thermalization depends on the scattering cross section (proportional to the square of the scattering length, eq. 2.41) at the applied magnetic field. The zero-crossing of a is marked in fig. 7.5 by the maximum in temperature of the atomic sample indicating a decreased thermalization efficiency by means of forced evaporation in the ODT. The positions of the minimum in atom number (corresponding to the maximum of a) and the maximum in temperature (corresponding to $a \approx 0$) yields $\approx 1.5\,\mathrm{G}$ and $\approx 7\,\mathrm{G}$ for the two resonances, respectively, which coincides much better with the elastic widths from the literature [175] (table 7.2). The observation of the zero crossing could also be used to detect Feshbach resonances [177].
Figures 7.6 and 7.7 summarize detected intraspecies Feshbach resonances in ^{85}Rb and ^{87}Rb, respectively. Due to experimental simplicity, most of theses lines were recorded with the Rb atoms in the narrow single ODT beam ODT_{1064}. The resonances were mainly detected by monitoring the atom loss as a function of magnetic field. Small deviations of the positions from the literature can be attributed to a deviation of our calibration from the linear behaviour according to eq. 7.5, but are in general less than 0.5%. Typically, the entrance channels for the resonances are $|F = 2, m_F = -2\rangle$ for ^{85}Rb and $|F = 1, m_F = -1\rangle$ for ^{87}Rb, where the m_F state was mainly chosen to simplify the experiment. Saturation and broadening effects are visible for several lines.

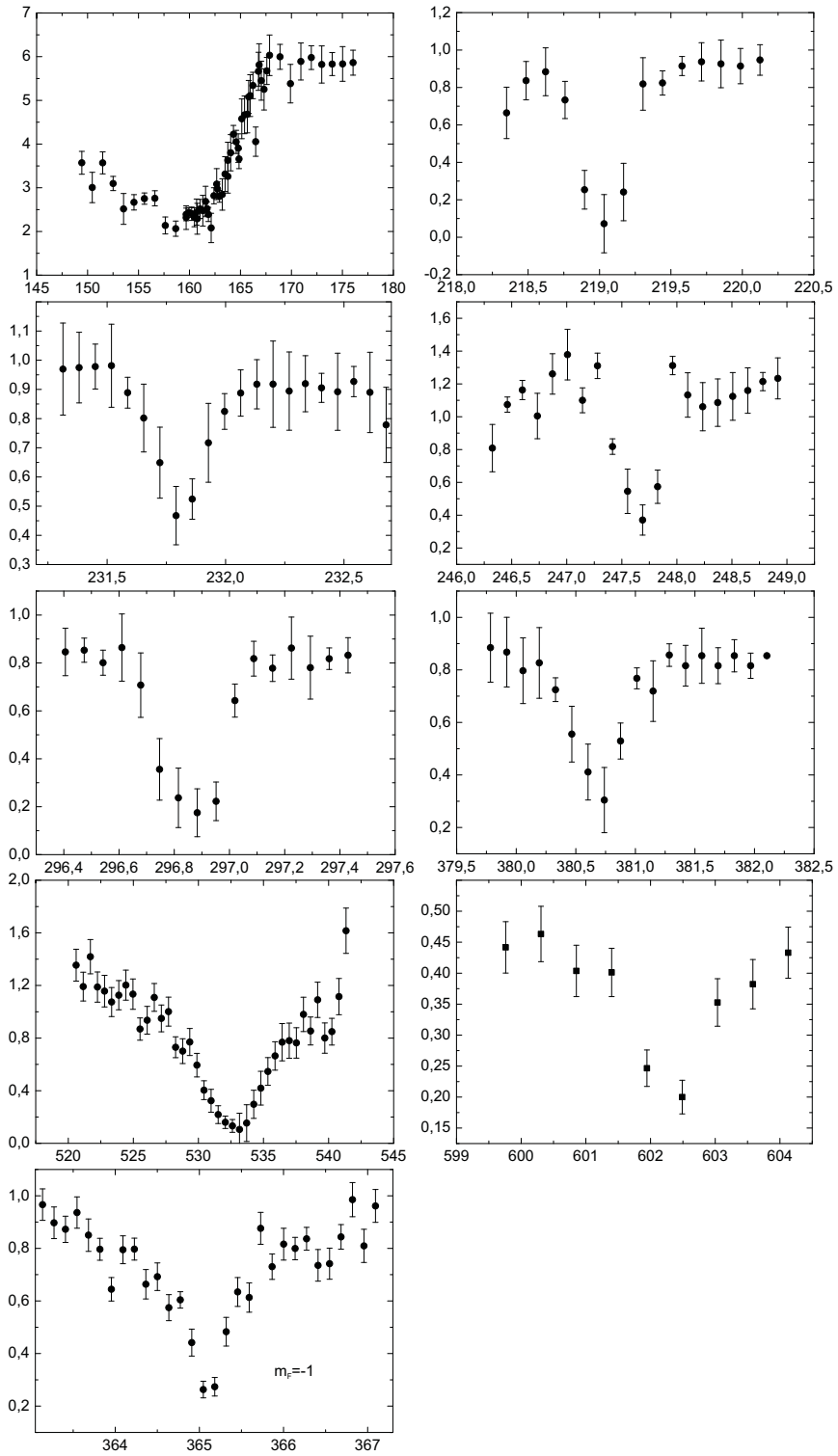

Figure 7.6: *Detected Feshbach resonances in $^{85}Rb_2$ in our experiment. Displayed are the numbers of remaining Rb atoms in units of 10^5 as a function of magnetic field in Gauss. The error bars are simply fitting errors to the atomic cloud. The entrance channel is the $|^2S_{1/2}, F = 2, m_F = -2\rangle$ state except for the bottom Feshbach resonance which belongs to the $|^2S_{1/2}, F = 2, m_F = -1\rangle$ entrance channel.*

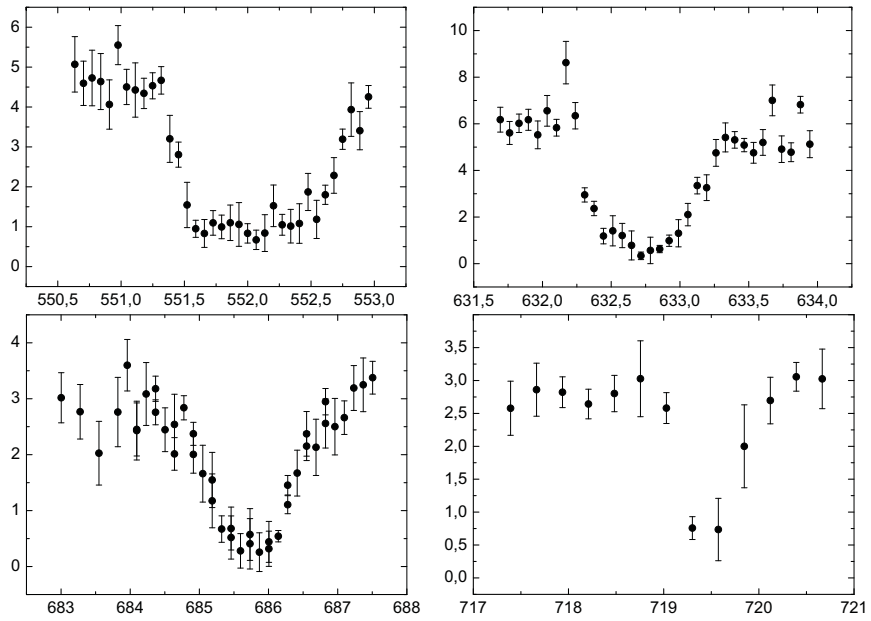

Figure 7.7: *Detected Feshbach resonances in $^{87}Rb_2$ in our experiment. Displayed are the numbers of remaining Rb atoms in units of 10^5 as a function of magnetic field in Gauss. The error bars are simply fitting errors to the atomic cloud. The entrance channel is the $|^2S_{1/2}, F = 1, m_F = -1\rangle$ state.*

Dependence on density and holding times

In general, in ultracold experiments high atomic densities are desired as already underlined by the photoassociation experiments (see sec. 5.3). Similarly, the shape of Feshbach resonances depends on the atomic density which in turn is determined by the potential used to trap the atoms. In order to show to which extend the density has an influence, we investigated the depth of the $^{85}Rb_2$ resonance at $\approx 604.1\,G$, defined as the magnitude of atom number loss on resonance, for the three different trapping geometries (and hence atomic densities) accessible in our experiment as depicted in fig. 7.8. Care was taken to prepare the atomic samples with the same atom number and temperature. From left to right the density of the sample decreases which has a distinct impact on the depth of the observed resonance. The best signal and hence highest loss in Rb atom number is achieved in the crossed ODT (left). The resonance gets less pronounced in the single beam ODT_{1064} (middle) and can only be assumed to be present in the $ODT_{1064,2}$ (right). Typically, it is not possible to completely deplete the atomic sample presumably due to the fact that at a certain point the critical density is undercut and no further losses can be induced.
A similar effect is observed if the interrogation time of the magnetic field is varied as is shown in fig. 7.9 in the ODT_{1064}. While a holding time of $t = 50\,ms$ produces small losses, the line becomes more visible for $t = 150\,ms$ and gets even more pronounced and broadened for $t = 300\,ms$. We therefore typically chose a holding time of 150 ms for Rb_2 resonances and 500 ms while searching for RbYb resonances.

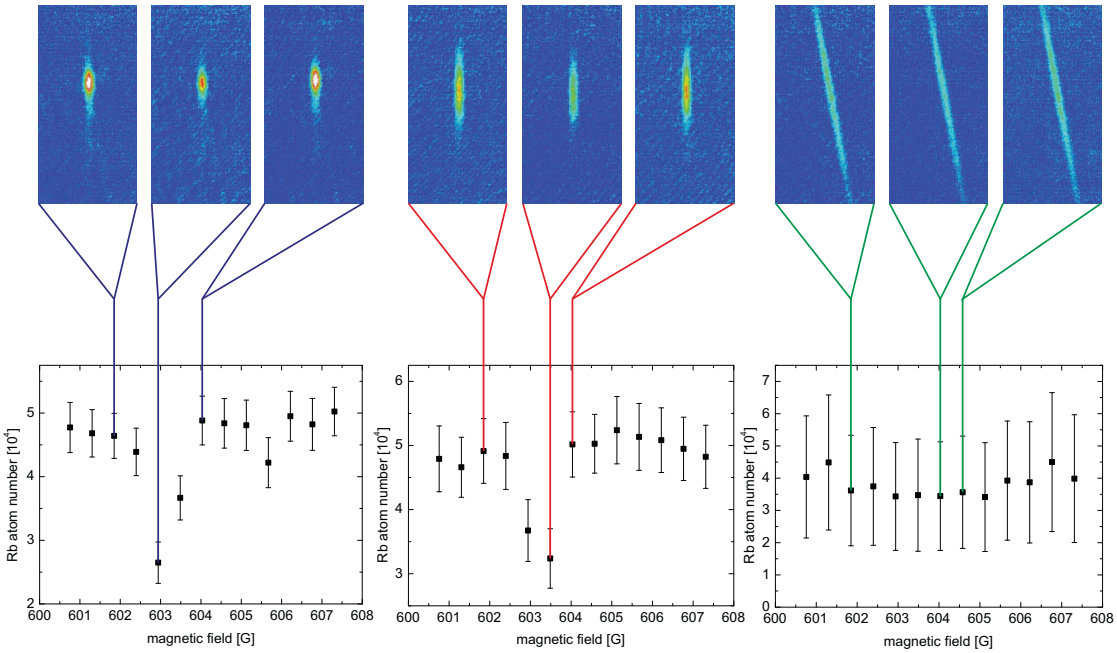

Figure 7.8: *Density dependence of the Rb_2 Feshbach resonance at 604.1 G observed by loss-spectroscopy in a pure ^{85}Rb sample (adapted from [143]). The resonance is observed in the three different trapping potentials CODT (left), ODT_{1064} (middle) and $ODT_{1064,2}$ (right). Each dataset is an average of two scans. The density decreases from left to right and hence the resonance becomes less pronounced while it (nearly) vanishes in the $ODT_{1064,2}$.*

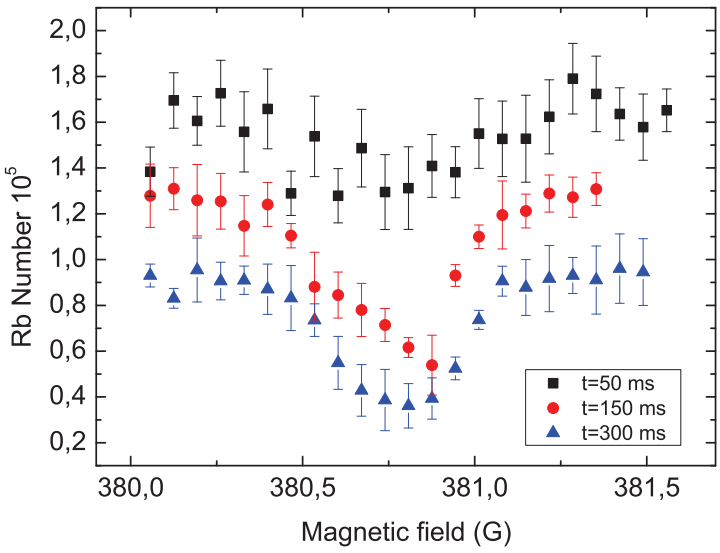

Figure 7.9: *Effect of duration of interrogation by Feshbach magnetic fields on the $^{85}Rb_2$ Feshbach resonance at 382.36 G. While the line is not really clear for $t = 50$ ms it becomes distinct for $t = 150$ ms and gets even saturated for $t = 300$ ms. Adapted from [170].*

Temperature effects

In order to determine the effect of temperature on the observability of RbYb Feshbach resonances, we additionally tested the influence of the temperature on the visibility of a well known Rb_2 resonance. For this measurement we used the $^{85}Rb_2$ Feshbach resonance in the $|F = 2, m_F = -1\rangle$ state at $\approx 365\,\mathrm{G}$ (which has not been reported yet) that we found while calibrating the magnetic field. Starting from the $m_F = -2$ state, the atoms had to be transferred by means of radio-frequency induced spin flips into the final $|F = 2, m_F = -1\rangle$-state. The atomic sample was prepared as usual in the ODT_{1064} at $\approx 4\,\mu\mathrm{K}$. Subsequently, the intensity of the ODT was systematically increased in order to heat the atomic sample. The results can be found in fig. 7.10.
At $T = 4\,\mu\mathrm{K}$ the narrowest line can be achieved that gets broader with increasing temperature. Unfortunately, by increasing the intensity of the ODT in order to heat the atomic sample additionally the density is increased and both effects contribute to the broadening simultaneously. It is worth noting that a thermal broadening appears only to the left of the narrow line since a higher temperature lifts the continuum energy of the ultracold system. This is comparable to the temperature effect on photoassociation resonances depicted in fig. 2.12 that shifts the resonance to the red side of the frequency. At $30\,\mu\mathrm{K}$ a second line appears. Both lines become broader with increasing temperature and density until they merge together and cannot be distinguished anymore. The existence of a second line can be attributed to the rotational barrier (fig. 2.9) for ^{85}Rb atoms and a rotational quantum number $R = 1$ according to eq. 2.52 of

$$T_{\mathrm{c,Rb}} = 53.1\,\mu\mathrm{K}\,, \tag{7.6}$$

which can be overcome when the temperature of the atomic sample reaches suitable values. Again, this effect can be compared to the rotational components appearing in the photoassociation spectrum at higher temperatures (see fig. 5.3). The fact that the p-wave scattering event (not to mistake with a p-wave resonance) occurs already at smaller temperatures than $53.1\,\mu\mathrm{K}$ can be explained by tunneling through the rotational barrier. It is observed that the maximum losses reach always the same value regardless of temperature. We therefore decided that the temperature of $\approx 10\,\mu\mathrm{K}$ in the combined CODT could be enough to detect losses resulting from RbYb Feshbach resonances.

7.4 Scanning for magnetic Feshbach resonances in RbYb

This section presents our data related to the (unfortunately unsuccessful) search for magnetic Feshbach resonances in an ultracold mixture of Rb and Yb. As explained in sec. 7.1 based on theoretical predictions, we mainly focussed our attention on the isotopic combination of $^{85}Rb^{171}Yb$ and the magnetic field range of $\approx 495\,\mathrm{G}\,... \approx 640\,\mathrm{G}$. Figure 7.11 displays the combined results of multiple scans taken over a period of more than 60 days. Plotted is the remaining atom number for Rb and Yb as a function of magnetic field for the complete investigated range. Our data was evaluated by F. Wolf [143] who normalized the atomic numbers to the average number of a single scan in order to eliminate daily

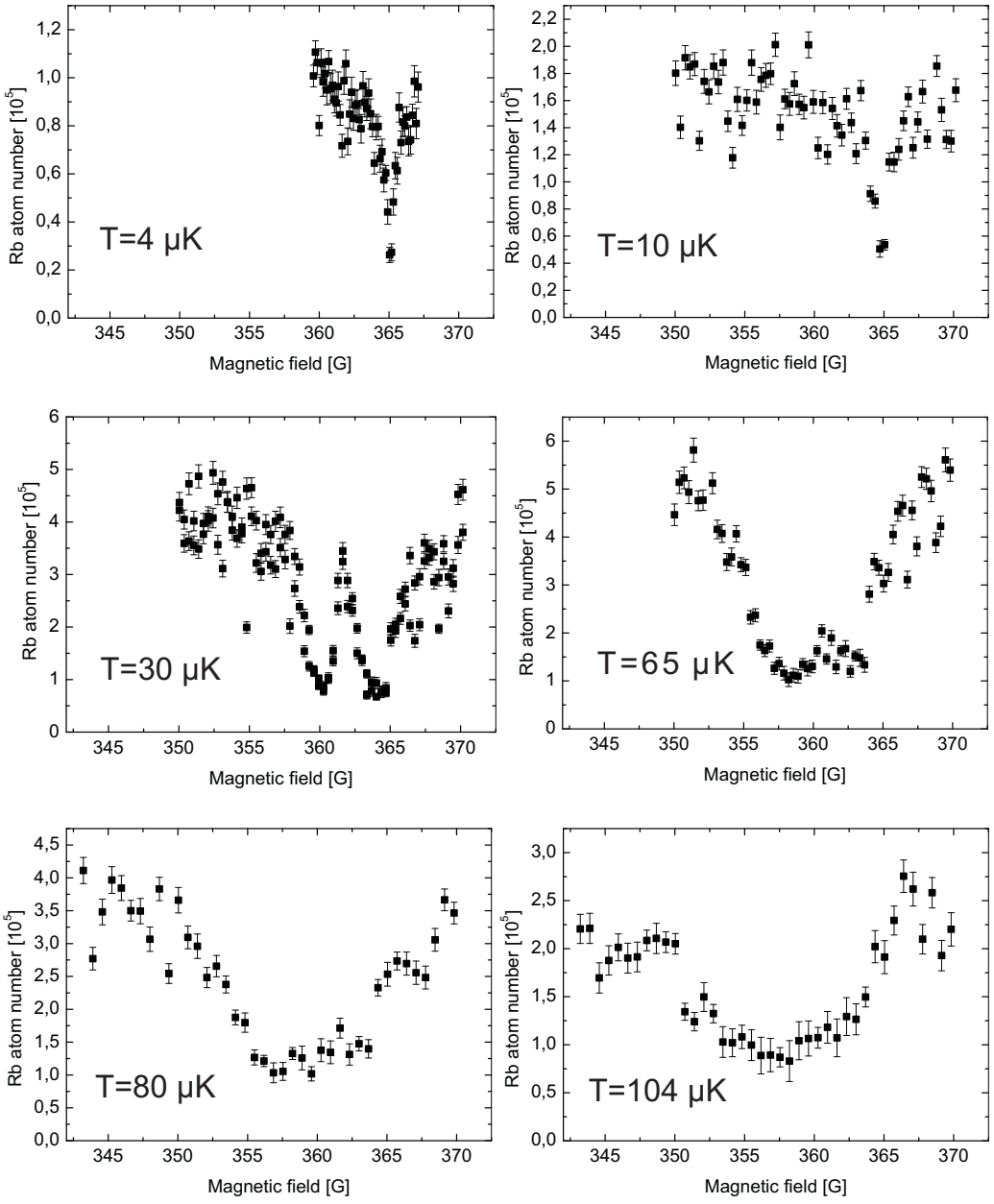

Figure 7.10: *Temperature dependence of a $^{85}Rb_2$ Feshbach resonance at $\approx 365\,\mathrm{G}$ (not yet reported) after preparing the atoms in the $|F = 2, m_F = -1\rangle$ state. With increasing temperature the lines gets broader and a second line appears that can be attributed to a p-wave scattering event connected to the rotational barrier of* $53.1\,\mu\mathrm{K}$.

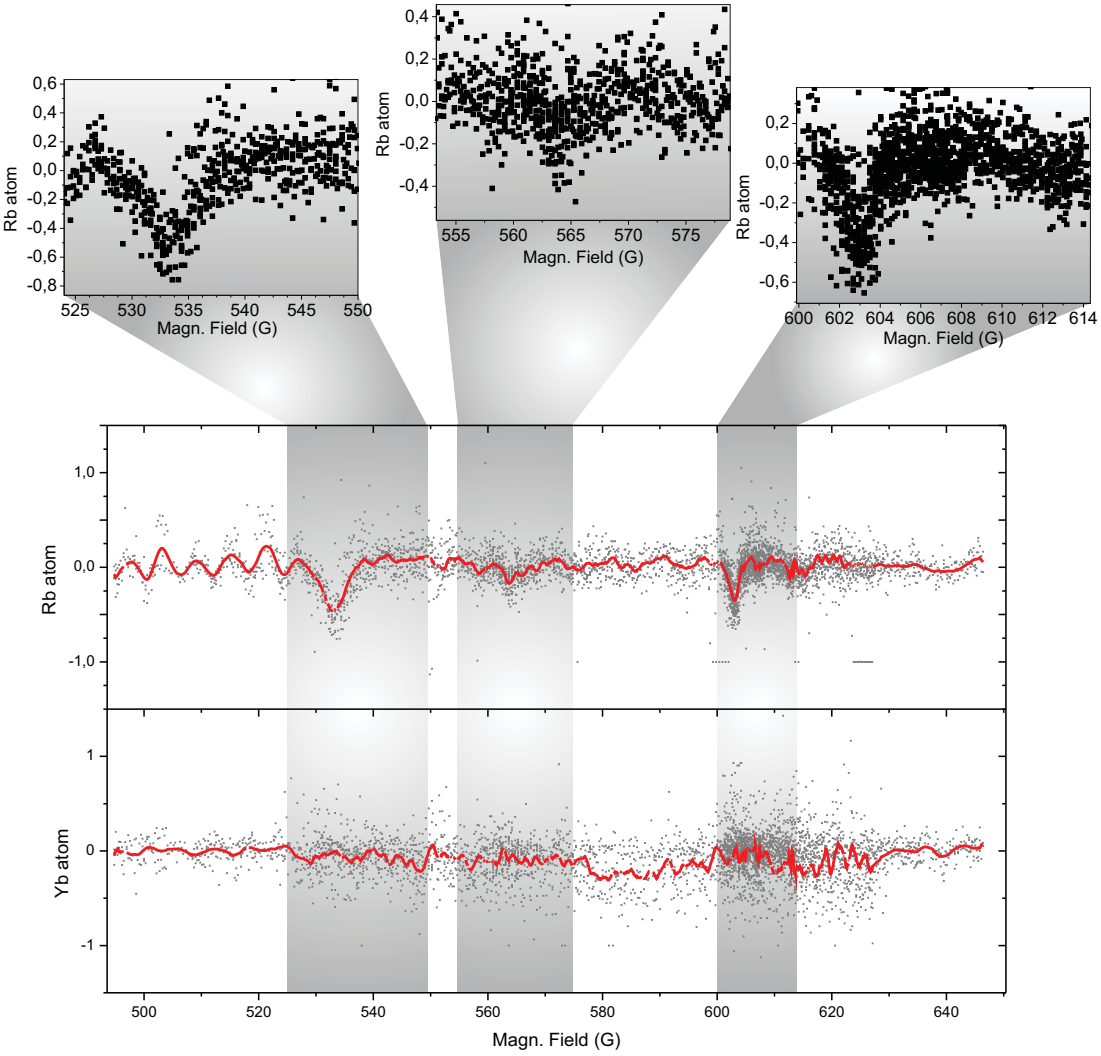

Figure 7.11: *Compilation of all data recorded during the search for $^{85}Rb^{171}Yb$ Feshbach resonances in the CODT. The data was already evaluated in the scope of the Master's thesis of F. Wolf [143]. It combines multiple single scans that were normalized to the mean atom number in a scan and shifted by this average. In the upper graphs Rb_2 resonances are highlighted. Unfortunately, no interspecies Feshbach resonance in RbYb could be observed. For more details see text.*

fluctuations.

As already mentioned, the typical atom number was $1.5 \cdot 10^5$ for Yb and $5 \cdot 10^4$ for Rb in the CODT. Since the loss in atom number close to a Feshbach resonance is expected to be of the same order of magnitude for both atomic species, a resonance should rather be observable in the Rb atom number than in the Yb atom number. The complete spectrum features also losses induced by Rb_2 Feshbach resonances, which are scaled up in the zoomed graphs on top in fig. 7.11. The two resonances at 532 G and 604.1 G have already

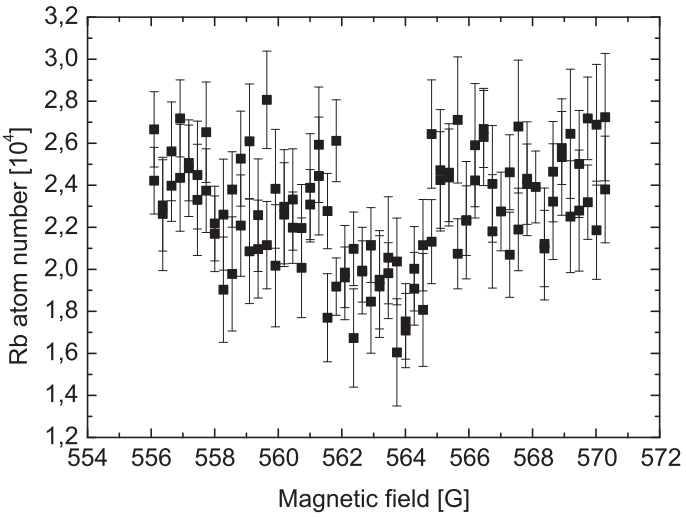

Figure 7.12: *$^{85}Rb_2$ Feshbach resonance at $\approx 563\,G$ (not yet reported) attributed to another spin state than the desired $m_F = -2$ state populated by imperfections in the preparation of the atomic samples. The shape of the resonance leads to the conclusion that this spin state is completely depleted on resonance while the atom number is only reduced by a maximum of 20%.*

been shown in fig. 7.6.

On the contrary, the resonance at $\approx 563\,\mathrm{G}$ was not yet identified. It is displayed again in fig. 7.12 and a maximum reduction of the total atom number by $\approx 20\%$ could be observed. This resonance appeared also in experiments that followed the same preparation cycle only without loading Yb. They did not occur in Rb atomic samples with pure $m_F = -2$-states which was checked by separate experiments with solely Rb in the ODT_{1064}. We therefore attribute this resonance to another spin state. The population of other Zeeman states might occur due to spin flips while storing Rb in the ODT and loading the Yb MOT. The origin of the oscillations in the range from 500 G...520 G were not identified.

Unfortunately, no reproducible losses were observed that could unambiguously be assigned to RbYb Feshbach resonances. This may lead to the conclusion, that the coupling responsible for the predicted Feshbach resonances is not strong enough to be observed under our experimental conditions at that time. Another explanation might be an overlap between a RbYb resonance and one of the Rb_2 resonances. It is rather unlikely that there is no RbYb Feshbach resonance within the investigated range since the molecular ground state potential is known relative precisely [2, 13] as a consequence of our two-photon photoassociation spectroscopy [3] (see chap. 6).

Apart from the comprehensive scan for Feshbach resonances in ^{85}Rb–^{171}Yb in the CODT, we also searched for Feshbach resonances in ^{85}Rb–^{172}Yb and ^{85}Rb–^{174}Yb in the single beam ODT_{1064} in the scope of the Master's thesis of A. Al-Masoudi [170]. The resulting data is plotted in fig. 7.13 and fig. 7.14, respectively. There are few resonance features detected by losses in the Rb atom number, which could not be confirmed by the Yb atom number.

These are obviously Rb_2 Feshbach resonances belonging to different m_F states in the open channel that were unintentionally rather strongly populated.
As a consequence, the theoretical proposal [2, 13] that magnetic Feshbach resonances might exist in a mixture of an alkali metal (such as Rb) and an alkaline-earth metal (such as Yb) could not be verified by the experiments performed within this thesis. This might be attributed to a too weak coupling between the relevant states that induce the Feshbach resonances. Another unfavourable effect might be resulting from the present temperatures of $\approx 10\,\mu\mathrm{K}$ and thereby connected densities that might reduce the signal strength. Before searching further for Feshbach resonances with improved experimental conditions it would be advantageous to first confirm the presence of the relevant coupling. This coupling has the same origin as the hyperfine interaction observed by means of photoassociation in the excited molecular state (see sec. 5.3.5). Therefore, if a variation in hyperfine splitting of the Rb ground state ($\Delta E_{\mathrm{hfs}} = h \times 6.85\,\mathrm{GHz}$) can be measured this would indicate an existing coupling. Additionally, due to the increasing elastic width of the resonance with B^2, a better choice would be an ultracold mixture combining an Yb isotope with ^{87}Rb whose resonances are located generally at higher magnetic fields up to $\approx 5000\,\mathrm{G}$ (see table 7.1). This would implicitly come along with lower temperatures and higher densities due to the favourable intraspecies scattering length of ^{87}Rb compared to ^{85}Rb which might result in an increased signal strength.

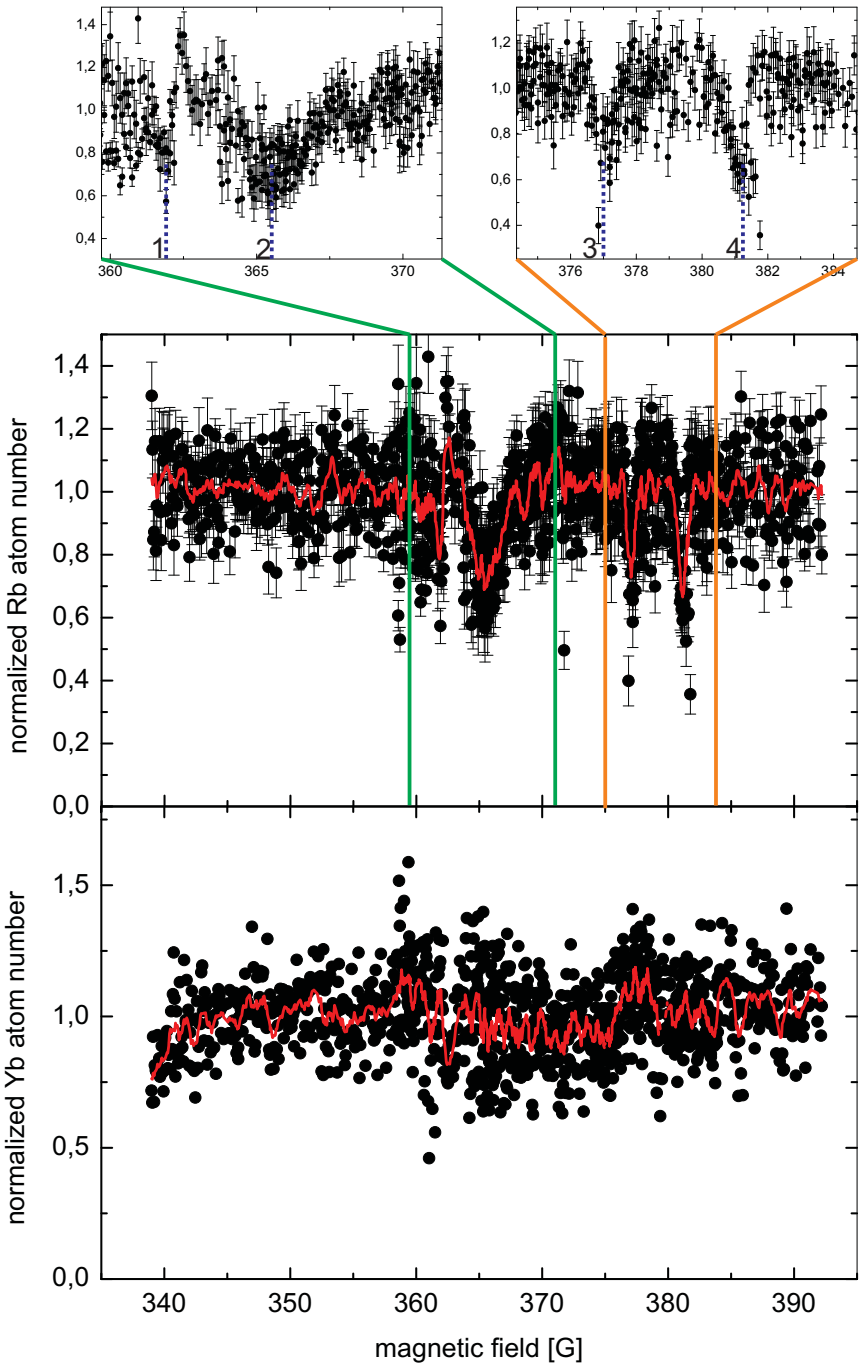

Figure 7.13: *Search for magnetic Feshbach resonances in ^{85}Rb–^{172}Yb in the single beam ODT_{1064}. Shown are the numbers of remaining Rb and Yb atoms normalized by the median value as a function of magnetic field. The red lines are 10-point averages of the recorded data. Four resonance features in Rb were observed that are highlighted in the upper zoomed graphs. The resonance marked by „4“ belongs to a Rb_2 resonance in the $|F = 2, m_F = -2\rangle$ state (see table 7.2). Resonance „2“ could be attributed to the $|F = 2, m_F = -1\rangle$ entrance channel (see fig. 7.6). The other positions determined by losses in the Rb atom number could not be related to changes in the Yb atom number. They are thus attributed to Rb_2 resonances originating from other m_F states than $m_F = -2$ in the open channel.*

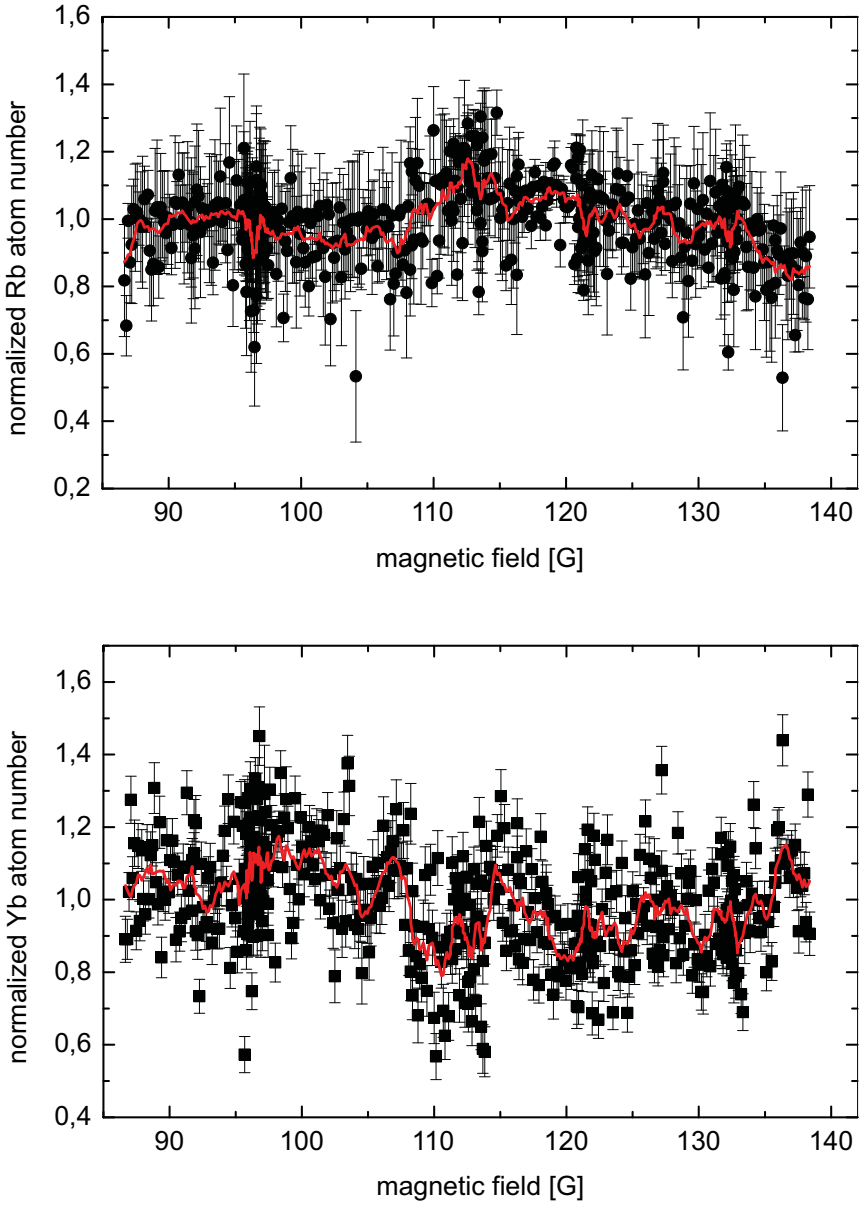

Figure 7.14: *Search for magnetic Feshbach resonances in ^{85}Rb–^{174}Yb in the single beam ODT_{1064}. Shown are the numbers of remaining Rb and Yb atoms normalized by the median value as a function of magnetic field. The red lines are 10-point averages of the recorded data. No clear resonance was observed and rather large fluctuations in atom numbers do not allow for any interpretation of weak resonances.*

8

Outlook and future experiments

This chapter presents possible routes to the long term goal of creating ultracold RbYb molecules in the rotational and vibrational ground state of the electronic molecular ground state. Thus it is an extension of ideas that were presented in [1, 6, 3]. Within this thesis, RbYb molecules in highly excited vibrational states in the excited molecular state $^2\Pi_{1/2}$ have been produced in a novel hybrid conservative trap. In a next step, RbYb molecules in the electronic ground state $^2\Sigma_{1/2}$ have to be created and detected, most likely first in highly excited vibrational states. Finally, the molecules have to be transferred to the rotational, vibrational and electronic (short *rovibronic*) molecular ground state. To achieve this goal, a novel experimental apparatus is being built and set up in the group of Prof. A. Görlitz. While the experiments within this thesis were carried out in a single vacuum chamber that forced us to make compromises when preparing ultracold Yb and Rb atoms successively, the novel apparatus separates the preparation of Yb and Rb in optical dipole traps by using independent vacuum chambers. RbYb molecules will subsequently be produced in an additional vacuum chamber to which the atoms will be transferred by shifting and overlapping the optical dipole traps containing the ultracold atoms. Within this thesis, first steps showing the experimental feasibility of moving ultracold Yb samples in an optical dipole trap by using a motorized translation stage have been carried out.

8.1 Vibrationally excited ground state molecules

The final goal of producing ultracold rovibronic ground state molecules with subsequent manipulation requires the experiments to be performed in a conservative trap that is able to confine the molecules for a sufficiently long time. The first step is the transfer of ultracold unbound atom pairs to weakly bound molecules in the electronic ground state. Some possible techniques for this purpose will be presented in this section. While in general during these processes (for coherent processes) the phase-space density of the initial atomic sample is preserved, the produced weakly bound molecules suffer from dissociation after a collision. In [178] molecule production of KRb has been performed in a single beam ODT that led to lifetimes of only 850 µs. Therefore for the following schemes, 3D optical lattices are beneficial and ideally with lattice sites occupied by only two atoms, one of each species. This way, long lived molecules with a lifetime of up to 25 s have been produced [66].

8.1.1 Magnetic Feshbach resonances

A common technique to coherently transfer pairs of atoms into electronic ground state molecules is to use magnetic Feshbach resonances [44]. This has been successfully performed for various bialkali homo- and heteronuclear mixtures [45]. Recently, theoretical predictions have been made [11, 13] that these type of resonances might also exist in a mixture of an alkali and an alkaline earth(-like) metal such as the system Rb-Yb. Although it is not clear whether these Feshbach resonances might eventually be useful for the production of molecules, their experimental investigation would be a useful test of sophisticated atomic theories.
In order to convert pairs of atoms into molecules close to a Feshbach resonance, the application of magnetic field ramps or oscillatory fields [45] can be used which is schematically depicted in fig. 8.1. The resonant coupling between the scattering state (grey line) and the bound molecular state ($|m\rangle$, solid line) leads to a mixing of these states that can be exploited to produce molecules by adiabatically sweeping over the resonance. In the example of fig. 8.1, starting from a magnetic field value above the resonance position ($B > B_0$) the Feshbach resonance level has to be swept downward until $B < B_0$. The first observation of magnetically induced Feshbach molecules has been reported in 2002 [179] in a ^{87}Rb BEC. Here, a suddenly changed magnetic field led to oscillations in the Rb BEC atom number. In 2003 Feshbach molecules have also been produced in $^{40}K_2$ [180]. After a magnetic field ramp as described above that led to atom loss, molecule production could be demonstrated by reversing the magnetic field ramp and dissociation the molecules back into pairs of atoms. In that, a molecule production efficiency of 50% could be measured and meanwhile higher efficiencies up to 100% have been reported [66].
Within this thesis work, extensive experimental attempts have been made to detect Feshbach resonances in mixtures of ^{85}Rb and various Yb isotopes (see chap. 7) by atom loss spectroscopy. Unfortunately, no interspecies Feshbach resonance could be detected. The

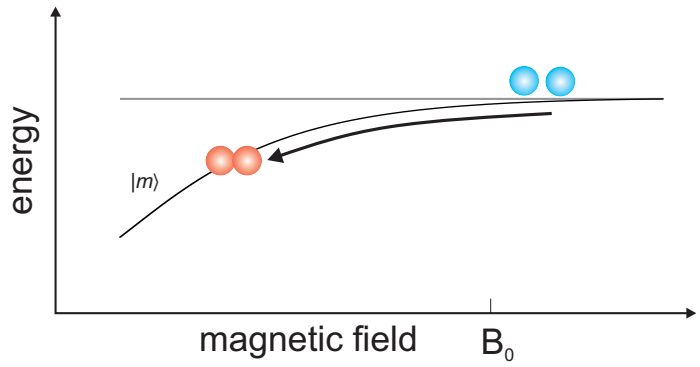

Figure 8.1: *Schematic illustration of the formation of ultracold molecules by using a Feshbach resonance. Atom pairs (blue dots) are transferred from the continuum energy (grey line) into a weakly bound molecular state $|m\rangle$ (solid curve) by adiabatically ramping the magnetic field across the resonance at B_0.*

predicted widths Δ for the examined Feshbach resonances are on the order of or below 100 µG (table 7.1) and hence comparably shallow. The absence of experimental detection is assumed to be caused by a too weak coupling between the scattering state and the molecular state which determines also the width Δ. Equation 2.73 points out, that Δ is proportional to B^2. Due to experimental considerations, our investigations were limited by magnetic field values up to 800 G. Generally, Feshbach resonances combining ^{87}Rb with different Yb isotopes (see table 7.1) reside at magnetic fields up to 5000 G yielding predicted widths up to 24 mG which would facilitate experimental detection. So an option would be to repeat the search for magnetic Feshbach resonances with a setup that allows for the stable generation of higher magnetic fields, which could be implemented in the new experimental apparatus.
Another approach was proposed by Tomza et al. [181] that treated an artificial broadening of the Feshbach resonance by irradiation of non-resonant light. They found that using intensities of the order of 10^9 W/cm^2 the width could be increased by 3 orders of magnitude. This resonant light can be provided by our optical dipole trap beam at 1064 nm. With our beam waist of 15 µm and power of 5 W we can achieve an intensity of $\approx 10^6$ W/cm^2. By reducing the beam waist and increasing the power as will be available in the experiment that is under construction (50 W), it is easily possible to increase the intensity by a factor of 50. This might already be enough to increase the width of the Feshbach resonance making the detection easier.
Besides investigating Feshbach resonances in an ultracold mixture of Rb and Yb with larger predicted elastic widths, it might be beneficial to test whether the coupling responsible for observable Feshbach resonances is actually present. As was in detail described in sec. 2.11, this theoretically predicted coupling [11, 13] is provoked by a variation of the hyperfine coupling constant of Rb due to the presence of the Yb nucleus. The presence of this effect in the electronically excited state $^2\Pi_{1/2}$ of RbYb could be demonstrated within this thesis by the observed variation of hyperfine splitting with increasing binding energy of the vibrational levels (sec. 5.3.5). To prove the existence of a similar effect in the electronic ground state $^2\Sigma_{1/2}$, the measurement of the binding energies of the vibrational levels in the electronic ground state [8, 3, 2] would have to be extended to more deeply bound levels. However, although a coupling might be present and Feshbach resonances might be detected by inelastic losses, it is not clear whether these type of resonances can be efficiently used to create ground state molecules. Therefore in the following, techniques are presented for systems lacking of magnetic Feshbach resonances.

8.1.2 Accumulation by spontaneous decay

An alternative approach for reaching the electronic molecular ground state is by spontaneous decay from an electronically excited state. The excitation in the case of the mixture Rb-Yb can be performed by 1-photon photoassociation (1-PA) close to the Rb D_1 line at 795 nm into the $^2\Pi_{1/2}$ state that was already achieved in previous works in a combined MOT [1, 7] and extended within this thesis in the novel hybrid conservative trap (chap. 5). As was already outlined, the produced excited molecules decay either back into pairs of atoms

or more likely in vibrational levels of the electronic ground state. In [3] the transition probabilities (Franck-Condon factors) between highly excited vibrational levels of the $^2\Pi_{1/2}$ and the $^2\Sigma_{1/2}$ states were measured by means of Autler-Townes spectroscopy and the results are also summarized in sec. 6.2. These measurements yielded Franck-Condon factors of up to 0.4 for the strongest studied bound-bound transition $\Delta v' = -9 \leftrightarrow \Delta v = -6\,(F = 1)$ which is presumably a lower limit due to underestimation of the acting laser intensities.
This means that the transfer of free atoms into weakly bound excited molecules by 1-PA is followed by spontaneous emission processes that most likely populate specific vibrational levels of the molecular ground state according to the Franck-Condon factors. Consequently, depending on the addressed excited vibrational state $\Delta v'$, molecule production predominantly into a single specific vibrational state Δv of the ground state may be efficiently carried out although not coherently. This kind of molecule production with subsequent detection has been performed for the first time in Cs_2 [52].
Furthermore, the downward process can be guided by stimulated emission with the help of 2-photon photoassociation as was for example already done in RbCs [56] or Cs_2 [55].

8.1.3 STIRAP: from atoms to molecules

A further technique to create ground state molecules starting from atom pairs has been recently demonstrated experimentally in Sr_2 [14] and uses a so-called *stimulated Raman adiabatic passage* (STIRAP) [57, 58] process. In [14] a transfer efficiency of 30% is reported with a subsequent photoassociation spectroscopy of the vibrational levels. This is a major step towards ground state molecules for systems without accessible magnetic Feshbach resonances. Since this technique is rather commonly employed to convert weakly bound molecules already in the electronic ground state to deeply bound ground state molecules, the basic idea will be further described in the following section 8.2.

8.2 Rovibronic ground state molecules

After producing ground state molecules in excited vibrational states, these have to be converted into the rotational and vibrational ground state. This can be achieved by a STIRAP process [57] which has first been employed in $^{87}Rb_2$ [182] yet not populating the lowest state. Since then, this technique has been adopted in various ultracold mixtures to reach the rovibronic ground state such as Rb_2 [59], KRb [60], Cs_2 [61], RbCs [62, 63] and very recently NaK [64].
Basically, in a STIRAP process (fig. 8.2(a)) two molecular states of the electronic ground state (states $|1\rangle$ and $|3\rangle$) are coupled by two laser fields ($S \mathrel{\widehat{=}}$ Stokes-laser and $P \mathrel{\widehat{=}}$ Pump-laser) to a common vibrational level of the electronically excited state ($|2\rangle$). By using a counter-intuitive pulse sequence (fig. 8.2(b)) the molecules are coherently transferred from the initial state $|1\rangle$ to the final state $|3\rangle$ (fig. 8.2(c)) without populating state $|2\rangle$ that would lead to losses due to spontaneous decay. This requires the maximum magnitude of the Rabi frequencies Ω_S and Ω_P of the two laser fields S and P, respectively, to be identical (fig. 8.2(b)). With this technique transfer efficiencies reaching even 100% have

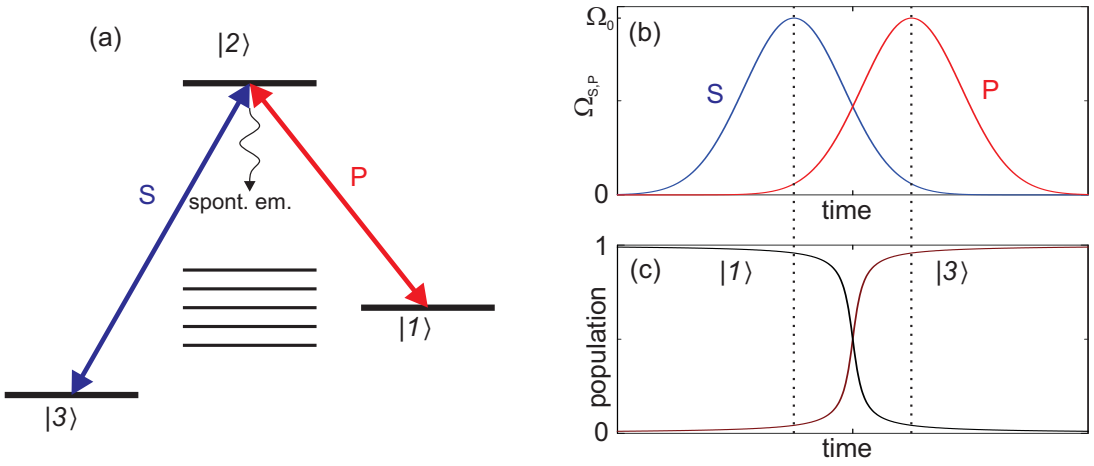

Figure 8.2: *Schematic illustration of STIRAP (taken from [58]). (a) The molecules are transferred from the initial molecular state* $|1\rangle$ *to the final state* $|3\rangle$ *by coupling to the auxiliary state* $|2\rangle$*. (b) Counter-intuitive pulse sequence in a STIRAP process. The Stokes-laser with Rabi frequency* Ω_S *preceding the Pump laser with* Ω_P *leaves state* $|2\rangle$ *in a dark state. (c) Population of the states* $|1\rangle$ *and* $|3\rangle$ *as a function of time during STIRAP.*

been reported [66]. Since the molecule production proceeds coherently, it is possible to reverse the STIRAP sequence and dissociate the molecules back into unbound atom pairs without heating the mixture. This way, the created molecules can be indirectly detected by the usual atomic imaging.

The possibility of forming ground state molecules from unbound atoms as mentioned in sec. 8.1.3 in our case of Rb-Yb is experimentally challenging. The order of magnitude for possible Rabi frequencies Ω_S and Ω_P have already been measured in previous experiments [1, 3] in a combined MOT. While Ω_P is on the order of several Hz [1] and could be increased to 100...1000 Hz in the hybrid conservative trap, Ω_S is on the order of tens of MHz and is hence more than a factor of 10^7 higher. This imbalance can be corrected by the applied laser intensities but the conversion from atoms to molecules remains challenging.

In order to reach the rovibronic ground state also in RbYb, precise knowledge on the positions of deeply bound vibrational levels not only of the electronic ground state but also of the excited state is crucial. Within this thesis work, characterization of the electronically excited state $^2\Pi_{1/2}$ has been carried out up to the vibrational level $\Delta v' = -28$ which has already a binding energy of $E_b = -h \times 2.2\,\mathrm{THz}$ (sec. 5.3.2). According to ab-initio calculations [94] (see also fig. 2.5) this state has a potential depth of $D'_e \approx 7700\,\mathrm{cm}^{-1}$. Thus up to now, only 1% of this excited state has been investigated experimentally. The ground state $^2\Sigma_{1/2}$ has only been studied up to a binding energy of $E_b = -h \times 58.5\,\mathrm{GHz}$ [3] and with the modeled potential depth of $D_e = 787.4\,\mathrm{cm}^{-1}$ [2] (sec. 6.3) this corresponds to only 0.3% of the potential.

Comprehensive spectral data on molecular potentials can be obtained from Fourier-transform spectroscopy as was for example performed with Ca_2 [183], NaRb [184] or LiCs

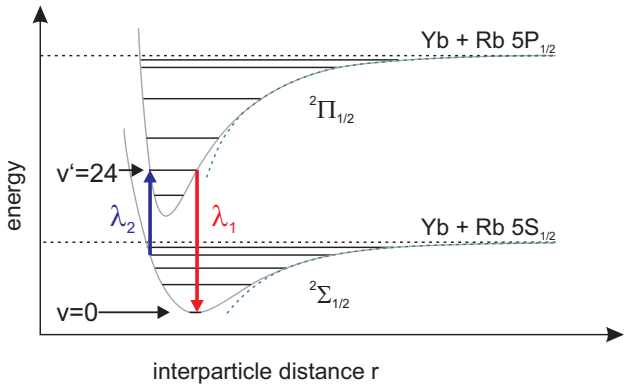

Figure 8.3: *Possible route to rovibronic RbYb ground state molecules. The weakly bound molecules in the electronic ground state are transferred to the absolute ground state* $v = 0$ *by coupling to an auxiliary vibrational level (e.g.* $v' = 24$*) in the electronic excited state with* λ_1 *and* λ_2*. Adapted from [1, 6].*

[185]. Here, the atomic species are heated inside a heat pipe until molecules are produced. A following laserinduced fluorescence provides a huge amount of spectroscopic data that subsequently requires fitting procedures based on coupled channels models to be evaluated and explain the observations. By choosing suitable excitation schemes it is possible to selectively collect information about desired potentials. If such an experiment can be applied for the system Rb-Yb, information on deeply bound vibrational states can be obtained. As a first approximation for the needed wavelengths for the STIRAP process, one can use the results from the ab-initio calculations for the involved potentials [94, 2]. In [94] additionally transitions to the rovibronic ground state with large Franck-Condon factors to vibrational states of the electronically excited level were stated. The largest one belongs to the $v' = 24$ state with calculated transition wavelengths of

$$\lambda_1 \approx 1345\,\text{nm} \qquad \text{and} \qquad \lambda_2 \approx 1520\,\text{nm}\,, \tag{8.1}$$

where λ_1 denotes the transition wavelength for $v = 0 \leftrightarrow v' = 24$ and λ_2 for weakly bound ground state molecules to $v' = 24$ (see fig. 8.3). Assuming a ground state potential as was modeled in [2], λ_1 changes its value to

$$\lambda_1 \approx 1357\,\text{nm}\,. \tag{8.2}$$

However, these wavelengths are based on ab-initio calculations and sensitively depend on the exact interaction potentials which can vary from the modeled ones and hence need to be investigated further. Most likely the next steps will be the investigation of more deeply bound states in the electronically excited state as well as in the ground state by photoassociation and the subsequent theoretical refinement of the molecular potentials. The most suitable environment for this will be an optical lattice. For a Rb-Yb atom pair trapped at a single site of a 3D optical lattice the pair density may reach $10^{15}\,\text{cm}^{-3}$ and thus the photoassociation rate is further increased as compared to the hybrid trap presented in this thesis. This will allow observing weak transitions from free atom pairs to more deeply bound vibrational levels in the excited molecular state.

Bibliography

[1] N. Nemitz, *Production and spectroscopy of ultracold YbRb* molecules*, Ph.D. thesis, Heinrich-Heine-Universität Düsseldorf (2008).

[2] M. Borkowski, P. S. Zuchowski, R. Ciurylo, P. S. Julienne, D. Kedziera, L. Mentel, P. Tecmer, F. Muenchow, C. Bruni, and A. Goerlitz, *Scattering lengths in isotopologues of the RbYb system*, Physical Review A **88**, 052708 (2013).

[3] F. Münchow, *2-Photon-Photoassociation spectroscopy in a mixture of Ytterbium and Rubidium*, Ph.D. thesis, Heinrich-Heine-Universität Düsseldorf (2012).

[4] A. Batär, *Erzeugung und Charakterisierung ultrakalter Rubidium- und Ytterbiumatome – auf dem Weg zu einem gemischten Quantengas*, Ph.D. thesis, Universität Düsseldorf (2005), URL `http://deposit.ddb.de/cgi-bin/dokserv?idn=975498614`.

[5] S. Tassy, *Sympathetische Kühlung von Ytterbium mit Rubidium*, Ph.D. thesis, Institut für Experimentalphysik, Heinrich-Heine-Universität Düsseldorf (2007), URL `http://deposit.ddb.de/cgi-bin/dokserv?idn=986914169`.

[6] F. Baumer, *Isotope dependent interactions in a mixture of ultracold atoms*, Ph.D. thesis, Heinrich-Heine-Universität Düsseldorf (2010), URL `http://deposit.ddb.de/cgi-bin/dokserv?idn=100670289X`.

[7] N. Nemitz, F. Baumer, F. Münchow, S. Tassy, and A. Görlitz, *Production of heteronuclear molecules in an electronically excited state by photoassociation in a mixture of ultracold Yb and Rb*, Phys. Rev. A **79**, R061403 (2009).

[8] F. Muenchow, C. Bruni, M. Madalinski, and A. Goerlitz, *Two-photon photoassociation spectroscopy of heteronuclear YbRb*, Physical Chemistry Chemical Physics **13**, 18734–18737 (2011).

[9] S. Tassy, N. Nemitz, F. Baumer, C. Hoehl, A. Batär, and A. Görlitz, *Sympathetic cooling in a mixture of diamagnetic and paramagnetic atoms*, J. Phys. B **43**, 205309 (2010).

[10] F. Baumer, F. Münchow, A. Görlitz, S. E. Maxwell, P. Julienne, and E. Tiesinga, *Spatial separation in a thermal mixture of ultracold ^{174}Yb and ^{87}Rb atoms*, Phys. Rev. A **83**, 040702 (2011).

[11] P. S. Zuchowski, J. Aldegunde, and J. M. Hutson, *Ultracold RbSr Molecules Can Be Formed by Magnetoassociation*, Phys. Rev. Lett. **105**, 153201 (2010).

[12] D. A. Brue and J. M. Hutson, *Magnetically Tunable Feshbach Resonances in Ultracold Li-Yb Mixtures*, Phys. Rev. Lett. **108**, 043201 (2012).

[13] D. A. Brue and J. M. Hutson, *Prospects of forming ultracold molecules in (2)Sigma states by magnetoassociation of alkali-metal atoms with Yb*, Physical Review A **87**, 052709 (2013).

[14] S. Stellmer, B. Pasquiou, R. Grimm, and F. Schreck, *Creation of Ultracold Sr-2 Molecules in the Electronic Ground State*, Physical Review Letters **109**, 115302 (2012).

[15] J. Prodan, W. Phillips, and H. Metcalf, *Laser Production of a Very Slow Monoenergetic Atomic Beam*, Phys. Rev. Lett. **49**, 1149 (1982).

[16] W. Phillips and H. Metcalf, *Laser deceleration of an atomic beam*, Phys. Rev. Lett. **48**, 596 (1982).

[17] W. Phillips, *Laser cooling and trapping of neutral atoms*, Rev. Mod. Phys. **70**, 721 (1998).

[18] K. Davis, *Evaporative cooling of sodium atoms*, Ph.D. thesis, Massachusetts Institute of Technology (1995).

[19] M. H. Anderson, J. R. Ensher, M. R. Matthews, C. E. Wieman, and E. A. Cornell, *Observation of Bose-Einstein Condensation in a Dilute Atomic Vapor*, Science **269**, 198 (1995).

[20] C. Bradley, C. Sackett, J. Tollet, and R. Hulet, *Evidence of Bose-Einstein Condensation in an Atomic Gas with Attractive Interactions*, Phys. Rev. Lett. **75**, 1687 (1995).

[21] K. B. Davis, M.-O. Mewes, M. R. Andrews, N. J. van Druten, D. S. Durfee, D. M. Kurn, and W. Ketterle, *Bose-Einstein Condensation in a Gas of Sodium Atoms*, Phys. Rev. Lett. **75**, 3969–3973 (1995).

[22] A. Einstein, *Quantentheorie des einatomigen idealen Gases*, Sitzungsber. Preuss. Akad. Wiss. **Bericht 22**, 261–267 (1924).

[23] S. Bose, *Plancks Gesetz und Lichtquantenhypothese*, Z. Phys. **26**, 178 (1924).

[24] J. Bardeen, L. N. Cooper, and J. R. Schrieffer, *Theory of Superconductivity*, Phys. Rev. **108**, 1175–1204 (1957), URL `http://link.aps.org/doi/10.1103/PhysRev.108.1175`.

[25] M. Greiner, O. Mandel, T. Esslinger, T. W. Hänsch, and I. Bloch, *Quantum phase transition from a superfluid to a Mott insulator in a gas of ultracold atoms*, Nature **415**, 44 (2002).

[26] O. Mandel, M. Greiner, A. Widera, T. Rom, T. W. Hänsch, and I. Bloch, *Controlled collisions for multi-particle entanglement of optically trapped atoms*, Nature **415**, 44 (2003).

[27] R. V. Krems, *Molecules near absolute zero and external field control of atomic and molecular dynamics*, International Reviews in Physical Chemistry **24**, 99–118 (2005), URL `http://dx.doi.org/10.1080/01442350500167161`.

[28] S. Y. T. van de Meerakker, N. Vanhaecke, M. P. J. van der Loo, G. C. Groenenboom, and G. Meijer, *Direct Measurement of the Radiative Lifetime of Vibrationally Excited OH Radicals*, Phys. Rev. Lett. **95**, 013003 (2005), URL `http://link.aps.org/doi/10.1103/PhysRevLett.95.013003`.

[29] S. Ospelkaus, K. K. Ni, D. Wang, M. H. G. de Miranda, B. Neyenhuis, G. Quemener, P. S. Julienne, J. L. Bohn, D. S. Jin, and J. Ye, *Quantum-State Controlled Chemical Reactions of Ultracold Potassium-Rubidium Molecules*, Science **327**, 853–857 (2010).

[30] D. DeMille, S. B. Cahn, D. Murphree, D. A. Rahmlow, and M. G. Kozlov, *Using molecules to measure nuclear spin-dependent parity violation*, Physical Review Letters **1**, 023003 (2008).

[31] T. Zelevinsky, S. Kotochigova, and J. Ye, *Precision test of mass-ratio variations with lattice-confined ultracold molecules*, Phys. Rev. Lett. **1**, 043201 (2008).

[32] E. R. Hudson, H. J. Lewandowski, B. C. Sawyer, and J. Ye, *Cold molecule spectroscopy for constraining the evolution of the fine structure constant*, Physical Review Letters **96**, 143004 (2006).

[33] E. A. Hinds, *Testing Time Reversal Symmetry Using Molecules*, Physica Scripta **T70**, 34 (1997).

[34] J. J. Hudson, B. E. Sauer, M. R. Tarbutt, and E. A. Hinds, *Measurement of the Electron Electric Dipole Moment Using YbF Molecules*, Phys. Rev. Lett. **89**, 023003 (2002).

[35] E. R. Meyer and J. L. Bohn, *Electron electric-dipole-moment searches based on alkali-metal- or alkaline-earth-metal-bearing molecules*, Phys. Rev. A **80**, 042508 (2009).

[36] D. DeMille, *Quantum Computation with Trapped Polar Molecules*, Phys. Rev. Lett. **88**, 067901 (2002).

[37] G. Pupillo, A. Griessner, A. Micheli, M. Ortner, D.-W. Wang, and P. Zoller, *Cold Atoms and Molecules in Self-Assembled Dipolar Lattices*, Phys. Rev. Lett. **100**, 050402 (2008), URL `http://link.aps.org/doi/10.1103/PhysRevLett.100.050402`.

[38] L. D. Carr, D. DeMille, R. V. Krems, and J. Ye, *Cold and ultracold molecules: science, technology and applications*, New Journal of Physics **11**, 055049 (2009).

[39] A. Micheli, G. K. Brennen, and P. Zoller, *A toolbox for lattice-spin models with polar molecules*, Nature Physics **2**, 341 (2006).

[40] G. K. Brennen, A. Micheli, and P. Zoller, *Designing spin-1 lattice models using polar molecules*, New Journal Of Physics **9**, 138 (2007).

[41] J. F. Barry, E. S. Shuman, E. B. Norrgard, and D. DeMille, *Laser Radiation Pressure Slowing of a Molecular Beam*, Physical Review Letters **108**, 103002 (2012).

[42] J. F. Barry, D. J. McCarron, E. B. Norrgard, M. H. Steinecker, and D. DeMille, *Magneto-optical trapping of a diatomic molecule*, Nature **512**, 286–+ (2014).

[43] J. Doyle, B. Friedrich, R. Krems, and F. Masnou-Seeuws, *Quo vadis, cold molecules?*, EUROPEAN PHYSICAL JOURNAL D **31**, 149–164 (2004).

[44] T. Köhler, K. Goral, and P. S. Julienne, *Production of cold molecules via magnetically tunable Feshbach resonances*, Reviews Of Modern Physics **78**, 1311–1361 (2006).

[45] C. Chin, R. Grimm, P. Julienne, and E. Tiesinga, *Feshbach resonances in ultracold gases*, Rev. Mod. Phys. **82**, 1225 (2010).

[46] K. M. Jones, E. Tiesinga, P. D. Lett, and P. S. Julienne, *Ultracold photoassociation spectroscopy: Long-range molecules and atomic scattering*, Reviews Of Modern Physics **78**, 483–535 (2006).

[47] P. Courteille, R. Freeland, D. Heinzen, F. van Abeelen, and B. Verhaar, *Observation of a Feshbach resonance in cold atom scattering*, Phys. Rev. Lett. **81**, 69 (1998).

[48] S. Inouye, M. Andrews, J. Stenger, H.-J. Miesner, D. Stamper-Kurn, and W. Ketterle, *Observation of Feshbach resonances in a Bose-Einstein condensate*, Nature **392**, 151–154 (1998).

[49] S. Inouye, J. Goldwin, M. L. Olsen, C. Ticknor, J. L. Bohn, and D. S. Jin, *Observation of Heteronuclear Feshbach Resonances in a Mixture of Bosons and Fermions*, Phys. Rev. Lett. **93**, 183201 (2004).

[50] C. A. Stan, M. W. Zwierlein, C. H. Schunck, S. M. F. Raupach, and W. Ketterle, *Observation of Feshbach Resonances between Two Different Atomic Species*, Phys. Rev. Lett. **93**, 143001 (2004).

[51] K. M. Jones, S. Maleki, L. P. Ratliff, and P. D. Lett, *Two-colour photoassociation spectroscopy of ultracold sodium*, Journal of Physics B **30**, 289–308 (1997), URL `http://stacks.iop.org/0953-4075/30/289`.

[52] A. Fioretti, D. Comparat, A. Crubellier, O. Dulieu, F. Masnou-Seeuws, and P. Pillet, *Formation of Cold* Cs_2 *Molecules through Photoassociation*, Phys. Rev. Lett. **80**, 4402–4405 (1998), URL `http://link.aps.org/doi/10.1103/PhysRevLett.80.4402`.

[53] T. Rom, T. Best, O. Mandel, A. Widera, M. Greiner, T. W. Hänsch, and I. Bloch, *State Selective Production of Molecules in Optical Lattices*, Phys. Rev. Lett. **93**, 073002 (2004).

[54] J. Deiglmayr, A. Grochola, M. Repp, K. Moertlbauer, C. Glueck, J. Lange, O. Dulieu, R. Wester, and M. Weidemueller, *Formation of Ultracold Polar Molecules in the Rovibrational Ground State*, Phys. Rev. Lett. **101**, 133004 (2008).

[55] M. Viteau, A. Chotia, M. Allegrini, N. Bouloufa, O. Dulieu, D. Comparat, and P. Pillet, *Optical Pumping and Vibrational Cooling of Molecules*, Science **321**, 232–234 (2008), URL `http://www.sciencemag.org/content/321/5886/232.abstract`.

[56] J. M. Sage, S. Sainis, T. Bergeman, and D. DeMille, *Optical Production of Ultracold Polar Molecules*, Phys. Rev. Lett. **94**, 203001 (2005).

[57] U. Gaubatz, P. Rudecki, S. Schiemann, and K. Bergmann, *Population transfer between molecular vibrational levels by stimulated Raman scattering with partially overlapping laser fields. A new concept and experimental results*, Journal of Chemical Physics **92**, 5363–5376 (1990), URL `http://link.aip.org/link/?JCP/92/5363/1`.

[58] K. Bergmann, H. Theuer, and B. Shore, *Coherent population transfer among quantum states of atoms and molecules*, Reviews of Modern Physics **70**, 1003–1025 (1998).

[59] F. Lang, K. Winkler, C. Strauss, R. Grimm, and J. H. Denschlag, *Ultracold Triplet Molecules in the Rovibrational Ground State*, Phys. Rev. Lett. **101**, 133005 (2008), URL `http://link.aps.org/doi/10.1103/PhysRevLett.101.133005`.

[60] K. K. Ni, S. Ospelkaus, M. H. G. de Miranda, A. Pe'er, B. Neyenhuis, J. J. Zirbel, S. Kotochigova, P. S. Julienne, D. S. Jin, and J. Ye, *A High Phase-Space-Density Gas of Polar Molecules*, Science **322**, 231 (2008).

[61] J. G. Danzl, M. J. Mark, E. Haller, M. Gustavsson, R. Hart, J. Aldegunde, J. M. Hutson, and H.-C. Naegerl, *An ultracold high-density sample of rovibronic ground-state molecules in an optical lattice*, Nature Physics **6**, 265 (2010).

[62] T. Takekoshi, L. Reichsöllner, A. Schindewolf, J. M. Hutson, C. R. Le Sueur, O. Dulieu, F. Ferlaino, R. Grimm, and H.-C. Nägerl, *Ultracold Dense Samples of Dipolar RbCs Molecules in the Rovibrational and Hyperfine Ground State*, Phys. Rev. Lett. **113**, 205301 (2014), URL `http://link.aps.org/doi/10.1103/PhysRevLett.113.205301`.

[63] P. K. Molony, P. D. Gregory, Z. Ji, B. Lu, M. P. Köppinger, C. R. Le Sueur, C. L. Blackley, J. M. Hutson, and S. L. Cornish, *Creation of Ultracold* $^{87}Rb^{133}Cs$ *Molecules in the Rovibrational Ground State*, Phys. Rev. Lett. **113**, 255301 (2014), URL `http://link.aps.org/doi/10.1103/PhysRevLett.113.255301`.

[64] J. W. Park, S. A. Will, and M. W. Zwierlein, *Ultracold Dipolar Gas of Fermionic* $^{23}Na^{40}K$ *Molecules in Their Absolute Ground State*, Phys. Rev. Lett. **114**, 205302 (2015), URL `http://link.aps.org/doi/10.1103/PhysRevLett.114.205302`.

[65] S. Ospelkaus, K. . K. Ni, D. Wang, M. H. G. de Miranda, B. Neyenhuis, G. Quemener, P. S. Julienne, J. L. Bohn, D. S. Jin, and J. Ye, *Quantum-State Controlled Chemical Reactions of Ultracold Potassium-Rubidium Molecules*, Science **327**, 853–857 (2010).

[66] A. Chotia, B. Neyenhuis, S. A. Moses, B. Yan, J. P. Covey, M. Foss-Feig, A. M. Rey, D. S. Jin, and J. Ye, *Long-Lived Dipolar Molecules and Feshbach Molecules in a 3D Optical Lattice*, Phys. Rev. Lett. **108**, 080405 (2012), URL `http://link.aps.org/doi/10.1103/PhysRevLett.108.080405`.

[67] S. E. Maxwell, E. Tiesinga, P. Julienne, F. Baumer, F. Münchow, C. Bruni, and A. Görlitz, *Ultracold Rb + Yb collisions and near-threshold bound states*, (unpublished) (2011).

[68] R. Grimm, M. Weidemüller, and Y. B. Ovchinnikov, *Optical Dipole Traps for Neutral Atoms*, Advances in Atomic, Molecular and Optical Physics **42**, 95–170 (2000).

[69] S. Chu, J. E. Bjorkholm, A. Ashkin, and A. Cable, *Experimental Observation of Optically Trapped Atoms*, Physical Review Letters **57**, 314 (1986).

[70] C. Cohen-Tannoudji, J. Dupont-Roc, and G. Grynberg, *Atom-Photon Interactions* (Wiley, New York, 1992).

[71] H. Metcalf and P. van der Straten, *Cooling and trapping of neutral atoms*, Phys. Rep. **244**, 203 (1994).

[72] P. Meystre, *Atom Optics* (Springer-Verlag, 2001).

[73] E. Hecht, *Optics* (Addison-Wesley, Reading, 1989).

[74] A. Migdall, J. Prodan, W. Phillips, T. Bergeman, and H. Metcalf, *First Observation of Magnetically Trapped Neutral Atoms*, Phys. Rev. Lett. **54**, 2596 (1985).

[75] T. Bergeman, G. Erez, and H. Metcalf, *Magnetostatic trapping fields for neutral atoms*, Phys. Rev. A **35**, 1535 (1987).

[76] D. Pritchard, *Cooling Neutral Atoms in a Magnetic Trap for Precision Spectroscopy*, Phys. Rev. Lett. **51**, 1336 (1983).

[77] M. Mewes, M. Andrews, N. V. Druten, D. Kurn, D. Durfee, and W. Ketterle, *Bose-Einstein Condensation in a Tightly Confining DC Magnetic Trap*, Phys. Rev. Lett. **77**, 416 (1996).

[78] W. Wing, *On neutral particle trapping in quasistatic electromagnetic fields*, Prog. Quant. Electr. **8**, 181–199 (1984).

[79] W. Paul, *Electromagnetic traps for charged and neutral particles*, Rev. Mod. Phys. **62**, 531–540 (1990), URL `http://link.aps.org/doi/10.1103/RevModPhys.62.531`.

[80] W. Petrich, M. Anderson, J. Ensher, and E. Cornell, *Behavior of atoms in a compressed magneto-optical trap*, J. Opt. Soc. Am. B **11**, 1332 (1994).

[81] K. Huang, *Statistical Mechanics* (Wiley, New York, 1987).

[82] F. Schwabl, *Quantenmechanik QMI* (5. Auflage, Springer–Verlag, Berlin, 1998).

[83] J. Dalibard, *Collisional dynamics of ultra-cold atomic gases*, in *Bose-Einstein Condensation of Atomic Gases. Proceedings of The International School of Physics Enrico Fermi - Course CXL*, edited by M. Inguscio, S. Stringari, and C. E. Wieman, p. 321 (IOS Press, Amsterdam, 1999).

[84] L. Landau and E. Lifshitz, *Quantum Mechanics: Non-Relativistic Theory* (Pergamon Press, New York, 1977).

[85] N. F. Mott and H. S. W. Massey, *The Theory of Atomic Collisions* (Oxford University Press, Oxford, UK, 1965).

[86] P. O. Schmidt, *Scattering properties of ultra-cold chromium atoms*, Ph.D. thesis, Universität Stuttgart (2003).

[87] H. Haken and H. C. Wolf, *Molekülphysik und Quantenchemie* (Springer Verlag, 1998), 3 edn.

[88] J. Brown and A. Carrington, *Rotational spectroscopy of diatomic molecules* (Cambridge University Press, 2003).

[89] J. Taylor, *Scattering Theory: The Quantum Theory on Nonrelativistic Collisions* (John Wiley & Sons, Inc., 1972).

[90] B. DeMarco, J. L. Bohn, J. P. Burke, M. Holland, and D. S. Jin, *Measurement of p-Wave Threshold Law Using Evaporatively Cooled Fermionic Atoms*, Phys. Rev. Lett. **82**, 4208 (1999).

[91] H. J. Metcalf and P. van der Straten, *Laser Cooling and Trapping* (Springer-Verlag, 1999).

[92] C. J. Pethick and H. Smith, *Bose-Einstein Condensation in Dilute Gases* (Cambridge University Press, 2002), 1st edition edn.

[93] W. Demtröder, *Molekülphysik, Theoretische Grundlagen und experimentelle Methoden* (De Gruyter, Berlin, Boston, 2013).

[94] L. K. Sorensen, S. Knecht, T. Fleig, and C. M. Marian, *Four-Component Relativistic Coupled Cluster and Configuration Interaction Calculations on the Ground and Excited States of the RbYb Molecule*, J. Phys. Chem. A **113**, 12607 (2009).

[95] J. Burke, *Theoretical Investigation of Cold Alkali Atom Collisions*, Ph.D. thesis, University of Colorado, Boulder (1999).

[96] R. J. LeRoy and R. B. Bernstein, *Dissociation Energy and Long-Range Potential of Diatomic Molecules from Vibrational Spacings of Higher Levels*, Journal of Chemical Physics **52**, 3869–3879 (1970), URL `http://link.aip.org/link/?JCP/52/3869/1`.

[97] P. D. Lett, K. Helmerson, W. D. Phillips, L. P. Ratliff, S. L. Rolston, and M. E. Wagshul, *Spectroscopy of* Na_2 *by photoassociation of laser-cooled Na*, Phys. Rev. Lett. **71**, 2200–2203 (1993), URL `http://link.aps.org/doi/10.1103/PhysRevLett.71.2200`.

[98] R. A. Cline, J. D. Miller, and D. J. Heinzen, *Study of Rb2 Long-Range States by High-Resolution Photoassociation Spectroscopy*, Physical Review Letters **73**, 632–635 (1994).

[99] M. Marinescu and H. R. Sadeghpour, *Long-range potentials for two-species alkali-metal atoms*, Physical Review A **59**, 390–404 (1999).

[100] G. F. Gribakin and V. V. Flambaum, *Calculation of the scattering length in atomic collisions using the semiclassical approximation*, Physical Review A **48**, 546–553 (1993).

[101] J. Trost, C. Eltschka, and H. Friedrich, *Quantization in molecular potentials*, Journal of Physics B: Atomic, Molecular and Optical Physics **31**, 361 (1998), URL `http://stacks.iop.org/0953-4075/31/i=3/a=006`.

[102] V. V. Flambaum, G. F. Gribakin, and C. Harabati, *Analytical calculation of cold-atom scattering*, Phys. Rev. A **59**, 1998–2005 (1999), URL http://link.aps.org/doi/10.1103/PhysRevA.59.1998.

[103] J. Weiner, V. S. Bagnato, S. Zilio, and P. S. Julienne, *Experiments and theory in cold and ultracold collisions*, Reviews of Modern Physics **71**, 1–85 (1999).

[104] C. Samuelis, E. Tiesinga, T. Laue, M. Elbs, H. Knöckel, and E. Tiemann, *Cold atomic collisions studied by molecular spectroscopy*, Phys. Rev. A **63**, 012710 (2000), URL http://link.aps.org/doi/10.1103/PhysRevA.63.012710.

[105] M. Kitagawa, K. Enomoto, K. Kasa, Y. Takahashi, R. Ciuryło, P. Naidon, and P. S. Julienne, *Two-color photoassociation spectroscopy of ytterbium atoms and the precise determinations of s -wave scattering lengths*, Phys. Rev. A **77**, 012719 (2008).

[106] J. P. Burke, C. H. Greene, J. L. Bohn, H. Wang, P. L. Gould, and W. C. Stwalley, *Determination of K-39 scattering lengths using photoassociation spectroscopy of the 0(g)(-) state*, Physical Review A **60**, 4417–4426 (1999).

[107] F. Hund, *Concerning the importance of some appearances in the molecular spectra*, Zeitschrift für Physik **36**, 658 (1926).

[108] G. Herzberg, *Molecular Spectra and Molecular Structure*, vol. I. Spectra of Diatomic Molecules (Van Nostrand Reinhold, 1950).

[109] M. Madalinski, *Zweiphotonen-Photoassoziationsspektroskopie in einem Gemisch aus Ytterbium und Rubidium*, Master's thesis, Universität Düsseldorf (2011).

[110] A. Derevianko, J. F. Babb, and A. Dalgarno, *High-precision calculations of van der Waals coefficients for heteronuclear alkali-metal dimers*, Physical Review A **63**, 052704 (2001).

[111] D. Comparat, *Improved LeRoy-Bernstein near-dissociation expansion formula, and prospect for photoassociation spectroscopy*, Journal of Chemical Physics **120**, 1318–1329 (2004), URL http://link.aip.org/link/?JCP/120/1318/1.

[112] H. Jelassi, B. Viaris de Lesegno, and L. Pruvost, *Reexamination of the LeRoy-Bernstein formula for weakly bound molecules*, Phys. Rev. A **77**, 062515 (2008), URL http://link.aps.org/doi/10.1103/PhysRevA.77.062515.

[113] E. Condon, *A Theory of Intensity Distribution in Band Systems*, Physical Review **28**, 1182–1201 (1926).

[114] C. Boisseau, E. Audouard, J. Vigue, and P. S. Julienne, *Reflection approximation in photoassociation spectroscopy*, Physical Review A **62**, art. no.–052705 (2000).

[115] E. Tiesinga, C. Williams, P. Julienne, K. Jones, P. Lett, and W. Phillips, *A spectroscopic determination of scattering lengths for sodium atom collisions*, J. Res. Natl. Inst. Stand. Technol. **101**, 505 (1996).

[116] H. R. Thorsheim, J. WEINER, and P. S. JULIENNE, *Laser-induced Photoassociation of ultracold sodium atoms*, Physical Review Letters **58**, 2420–2423 (1987).

[117] R. Napolitano, J. Weiner, C. J. Williams, and P. S. Julienne, *Line Shapes of High Resolution Photoassociation Spectra of Optically Cooled Atoms*, Physical Review Letters **73**, 1352–1355 (1994).

[118] J. Bohn and P. Julienne, *Prospects for influencing scattering lengths with far-off-resonant light*, Phys. Rev. A **56**, 1486 (1997).

[119] H. Feshbach, *Unified theory of nuclear reactions*, Annals of Physics **5**, 357 – 390 (1958), URL http://www.sciencedirect.com/science/article/pii/0003491658900071.

[120] H. Feshbach, *'Feshbach resonance'*, Annals of Physics **19**, 287 (1962).

[121] U. Fano, *Effects of Configuration Interaction on Intensities and Phase Shifts*, Phys. Rev. **124**, 1866–1878 (1961), URL http://link.aps.org/doi/10.1103/PhysRev.124.1866.

[122] F. K. Fatemi, K. M. Jones, and P. D. Lett, *Observation of Optically Induced Feshbach Resonances in Collisions of Cold Atoms*, Phys. Rev. Lett. **85**, 4462–4465 (2000), URL http://link.aps.org/doi/10.1103/PhysRevLett.85.4462.

[123] M. Theis, G. Thalhammer, K. Winkler, M. Hellwig, G. Ruff, R. Grimm, and J. H. Denschlag, *Tuning the Scattering Length with an Optically Induced Feshbach Resonance*, Phys. Rev. Lett. **93**, 123001 (2004), URL http://link.aps.org/doi/10.1103/PhysRevLett.93.123001.

[124] A. Moerdijk, B. Verhaar, and T. Nagtegaal, *Collisions of dressed ground-state atoms*, Phys. Rev. A **53**, 4343 (1996).

[125] M. Marinescu and L. You, *Controlling atom-atom interaction at ultralow temperatures by dc electric fields*, Phys. Rev. Lett. **81**, 4596 (1998).

[126] A. Moerdijk, B. Verhaar, and A. Axelsson, *Resonances in ultra-cold collisions of ^{6}Li, ^{7}Li and ^{23}Na*, Phys. Rev. A **51**, 4852–4861 (1995).

[127] S. L. Cornish, N. R. Claussen, J. L. Roberts, E. A. Cornell, and C. E. Wieman, *Stable ^{85}Rb Bose-Einstein Condensates with Widely Tunable Interactions*, Phys. Rev. Lett. **85**, 1795 (2000).

[128] T. Weber, J. Herbig, M. Mark, H.-C. Nägerl, and R. Grimm, *Bose-Einstein Condensation of Cesium*, Science **299**, 232 (2003).

[129] K. M. O'Hara, S. L. Hemmer, S. R. Granade, M. E. Gehm, J. E. Thomas, V. Venturi, E. Tiesinga, and C. J. Williams, *Measurement of the zero crossing in a Feshbach resonance of fermionic ^{6}*Li, Phys. Rev. A **66**, 041401 (2002), URL http://link.aps.org/doi/10.1103/PhysRevA.66.041401.

[130] T. Volz, S. Dürr, S. Ernst, A. Marte, and G. Rempe, *Characterization of elastic scattering near a Feshbach resonance in* ^{87}Rb, Phys. Rev. A **68**, 010702 (2003), URL http://link.aps.org/doi/10.1103/PhysRevA.68.010702.

[131] J. Stenger, S. Inouye, M. Andrews, H.-J. Miesner, D. Stamper-Kurn, and W. Ketterle, *Strongly enhanced inelastic collisions in a Bose-Einstein condensate near Feshbach resonances*, Phys. Rev. Lett. **82**, 2422–2425 (1999).

[132] P. O. Fedichev, M. W. Reynolds, and G. V. Shlyapnikov, *Three-body recombination of ultracold atoms to a weakly bound s level*, Phys. Rev. Lett. **77**, 2921–2924 (1996).

[133] B. D. Esry, C. H. Greene, and H. Suno, *Threshold laws for three-body recombination*, Phys. Rev. A **65**, 010705 (2001), URL http://link.aps.org/doi/10.1103/PhysRevA.65.010705.

[134] T. Weber, J. Herbig, M. Mark, H.-C. Nägerl, and R. Grimm, *Three-Body Recombination at Large Scattering Lengths in an Ultracold Atomic Gas*, Phys. Rev. Lett. **91**, 123201 (2003), URL http://link.aps.org/doi/10.1103/PhysRevLett.91.123201.

[135] P. F. Bedaque, E. Braaten, and H.-W. Hammer, *Three-body Recombination in Bose Gases with Large Scattering Length*, Phys. Rev. Lett. **85**, 908–911 (2000), URL http://link.aps.org/doi/10.1103/PhysRevLett.85.908.

[136] V. Vuletic, A. Kerman, C. Chin, and S. Chu, *Observation of Low-Field Feshbach Resonances in Collisions of Cesium Atoms*, Phys. Rev. Lett. **82**, 1406 (1999).

[137] T. Loftus, C. A. Regal, C. Ticknor, J. L. Bohn, and D. S. Jin, *Resonant Control of Elastic Collisions in an Optically Trapped Fermi Gas of Atoms*, Phys. Rev. Lett. **88**, 173201 (2002), URL http://link.aps.org/doi/10.1103/PhysRevLett.88.173201.

[138] W. Demtröder, *Experimentalphysik 3 - Atome, Moleküle und Festkörper* (Springer Berlin Heidelberg, Berlin, Heidelberg, 2010).

[139] H. Haken and H. C. Wolf, *Atom- und Quantenphysik* (Springer Verlag, 1996), 6 edn.

[140] D. A. Steck, *Rubidium 87 D Line Data* (last revised 23 December 2010), URL http://steck.us/alkalidata/, accessed 30.05.2015.

[141] S. Friebel, C. D'Andrea, J. Walz, M. Weitz, and T. W. Hänsch, *CO_2 optical lattice with cold rubidium atoms*, Phys. Rev. A **57**, R20 (1998).

[142] R. Jáuregui, *Nonperturbative and perturbative treatments of parametric heating in atom traps*, Phys. Rev. A **64**, 053408 (2001), URL http://link.aps.org/doi/10.1103/PhysRevA.64.053408.

[143] F. Wolf, *Interactions of Yb and Rb in a crossed dipole trap*, Master's thesis, Heinrich-Heine-Universität Düsseldorf (2013).

[144] D. A. Steck, *Rubidium 85 D Line Data* (last revised 20 September 2013), URL `http://steck.us/alkalidata/`, accessed 30.05.2015.

[145] W. Ketterle, K. Davis, M. Joffe, A. Martin, and D. Pritchard, *High-Densities of Cold Atoms in a Dark Spontaneous-Force Optical Trap*, Phys. Rev. Lett. **70**, 2253–2256 (1993).

[146] L. Ricci, M. Weidemüller, T. Esslinger, A. Hemmerich, C. Zimmermann, V. Vuletic, W. König, and T. W. Hänsch, *A compact grating-stabilized diode laser system for atomic physics*, Optics Communications **117**, 541 (1995).

[147] M. Gilowski, C. Schubert, M. Zaiser, W. Herr, T. Wübbena, T. Wendrich, T. Müller, E. Rasel, and W. Ertmer, *Narrow bandwidth interference filter-stabilized diode laser systems for the manipulation of neutral atoms*, Optics Communications **280**, 443 – 447 (2007), URL `http://www.sciencedirect.com/science/article/pii/S0030401807008577`.

[148] W. Demtröder, *Laserspektroskopie* (Springer Verlag, Berlin, 1993).

[149] D. R. Lide, *Handbook of Chemistry and Physics* (CRC Press, 2001), 82nd edn. edn.

[150] *NIST Atomic Spectra Database*, URL `http://www.nist.gov/pml/data/asd.cfm`, accessed 30.05.2015.

[151] Barber, *Ytterbium Optical lattice Clock*, Ph.D. thesis, University of Colorado (2007).

[152] M. Madalinski, *Aufbau eines Lasersystems für die Photoassoziationsspektroskopie an YbRb*, Bachelor's Thesis, Universität Düsseldorf (2009).

[153] W. Ketterle, D. Durfee, and D. Stamper-Kurn, *Making, probing and understanding Bose-Einstein condensates*, in *Proceedings of the International School of Physics - Enrico Fermi*, edited by M. Inguscio, S. Stringari, and C. Wieman, p. 67 (IOS Press, 1999).

[154] K. Borkowski, *Speicherung von Ytterbium in einer infraroten optischen Falle*, Bachelor's Thesis, Universität Düsseldorf (2012).

[155] T. Kuwamoto, K. Honda, Y. Takahashi, and T. Yabuzaki, *Magneto-optical trapping of Yb atoms using an intercombination transition*, Phys. Rev. A **60**, R745 (1999).

[156] R. Maruyama, R. H. Wynar, M. V. Romalis, A. Andalkar, M. D. Swallows, C. E. Pearson, and E. N. Fortson, *Investigation of sub-Doppler cooling in an ytterbium magneto-optical trap*, Physical Review A **68**, 011403 (2003).

[157] P. Pinkse, A. Mosk, M. Weidemüller, M. Reynolds, T. Hijmans, and J. Walraven, *Adiabatically changing the phase-space density of a trapped Bose gas*, Phys. Rev. Lett. **78**, 990–993 (1997).

[158] S. Chu, L. Hollberg, J. Bjorkholm, A. Cable, and A. Ashkin, *Three-Dimensional Viscous Confinement and Cooling of Atoms by Resonance Radiation Pressure*, Phys. Rev. Lett. **55**, 48 (1985).

[159] P. Lett, W. Phillips, S. Rolston, C. Tanner, R. Watts, and C. Westbrook, *Optical Molasses*, J. Opt. Soc. Am. B **6**, 2084 (1989).

[160] J. Dalibard and C. Cohen-Tannoudji, *Laser cooling below the Doppler limit by polarization gradients: simple theoretical models*, Journal of the Optical Society of America B **6**, 2023 (1989).

[161] N. Masuhara, J. Doyle, J. Sandberg, D. Kleppner, T. Greytak, H. Hess, and G. Kochanski, *Evaporative Cooling of Spin-Polarized Atomic Hydrogen*, Phys. Rev. Lett. **61**, 935 (1988).

[162] L. Zimmermann, *Charakterisierung eines ultrakalten Quantengases aus Rubidiumatomen*, Bachelor's Thesis, Universität Düsseldorf (2008).

[163] M. Anderson, W. Petrich, J. Ensher, and E. Cornell, *Reduction of light-assisted collisional loss rate from a low-pressure vapor-cell trap*, Phys. Rev. A **50**, R3597 (1994).

[164] S. Azizi, M. Aymar, and O. Dulieu, *Prospects for the formation of ultracold ground state polar molecules from mixed alkali atom pairs*, European Physical Journal D **31**, 195–203 (2004).

[165] E. Abraham, W. McALexander, C. Sackett, and R. Hulet, *Spectroscopic Determination of the s-Wave Scattering Length of Lithium*, Phys. Rev. Lett. **74**, 1315 (1995).

[166] S. H. Autler and C. H. Townes, *Stark Effect in Rapidly Varying Fields*, Physical Review **100**, 703–722 (1955).

[167] U. Schloder, T. Deuschle, C. Silber, and C. Zimmermann, *Autler-Townes splitting in two-color photoassociation of ^{6}Li*, Physical Review A **68**, 051403 (2003).

[168] P. S. Zuchowski, private communication (2013).

[169] A. Obert, *Feshbachresonanzen in einem ultrakalten Gemisch aus Yb und Rb*, Bachelor's Thesis, Universität Düsseldorf (2013).

[170] A. Al-Masoudi, *Investigation of optically trapped mixtures of ultracold Yb and Rb*, Master's thesis, Heinrich-Heine-Universität Düsseldorf (2012).

[171] G. Breit and I. I. Rabi, *Measurement of Nuclear Spin*, Phys. Rev. **38**, 2082–2083 (1931), URL `http://link.aps.org/doi/10.1103/PhysRev.38.2082.2`.

[172] S. Knoop, T. Schuster, R. Scelle, A. Trautmann, J. Appmeier, M. K. Oberthaler, E. Tiesinga, and E. Tiemann, *Feshbach spectroscopy and analysis of the interaction potentials of ultracold sodium*, Phys. Rev. A **83**, 042704 (2011), URL `http://link.aps.org/doi/10.1103/PhysRevA.83.042704`.

[173] W. Gerlach and O. Stern, *Der experimentelle Nachweis der Richtungsquantelung im Magnetfeld*, Zeitschrift fÃ¼r Physik **9**, 349–352 (1922), URL `http://dx.doi.org/10.1007/BF01326983`.

[174] A. Marte, T. Volz, J. Schuster, S. Dürr, G. Rempe, E. G. M. van Kempen, and B. J. Verhaar, *Feshbach Resonances in Rubidium 87: Precision Measurement and Analysis*, Phys. Rev. Lett. **89**, 283202 (2002), URL `http://link.aps.org/doi/10.1103/PhysRevLett.89.283202`.

[175] C. L. Blackley, C. R. Le Sueur, J. M. Hutson, D. J. McCarron, M. P. Köppinger, H.-W. Cho, D. L. Jenkin, and S. L. Cornish, *Feshbach resonances in ultracold ^{85}Rb*, Phys. Rev. A **87**, 033611 (2013), URL `http://link.aps.org/doi/10.1103/PhysRevA.87.033611`.

[176] J. Vogels, C. Tsai, R. Freeland, S. Kokkelmans, B. Verhaar, and D. Heinzen, *Prediction of Feshbach resonances in collisions of ultracold rubidium atoms*, Phys. Rev. A **56**, R1067 (1997).

[177] J. Roberts, N. Claussen, J. Jr., C. Greene, E. Cornell, and C. Wieman, *Resonant magnetic field control of elastic scattering in cold ^{87}Rb*, Phys. Rev. Lett. **81**, 5109 (1998).

[178] S. Ospelkaus, A. Pe'er, K. . K. Ni, J. J. Zirbel, B. Neyenhuis, S. Kotochigova, P. S. Julienne, J. Ye, and D. S. Jin, *Efficient state transfer in an ultracold dense gas of heteronuclear molecules*, Nature Physics **4**, 622–626 (2008).

[179] E. A. Donley, N. R. Claussen, S. T. Thompson, and C. E. Wieman, *Atom-molecule coherence in a Bose-Einstein condensate*, Nature **417**, 529–533 (2002), URL `http://dx.doi.org/10.1038/417529a`.

[180] C. A. Regal, C. Ticknor, J. L. Bohn, and D. S. Jin, *Creation of ultracold molecules from a Fermi gas of atoms*, Nature **424**, 47–50 (2003).

[181] M. Tomza, R. Gonzalez-Ferez, C. P. Koch, and R. Moszynski, *Controlling Magnetic Feshbach Resonances in Polar Open-Shell Molecules with Nonresonant Light*, Physical Review Letters **112**, 113201 (2014).

[182] K. Winkler, F. Lang, G. Thalhammer, P. v. d. Straten, R. Grimm, and J. H. Denschlag, *Coherent Optical Transfer of Feshbach Molecules to a Lower Vibrational State*, Phys. Rev. Lett. **98**, 043201 (2007), URL `http://link.aps.org/doi/10.1103/PhysRevLett.98.043201`.

[183] O. Allard, A. Pashov, H. Knöckel, and E. Tiemann, *Ground-state potential of the Ca dimer from Fourier-transform spectroscopy*, Phys. Rev. A **66**, 042503 (2002), URL `http://link.aps.org/doi/10.1103/PhysRevA.66.042503`.

[184] A. Pashov, O. Docenko, M. Tamanis, R. Ferber, H. Knöckel, and E. Tiemann, *Potentials for modeling cold collisions between Na (3S) and Rb (5S) atoms*, Phys. Rev. A **72**, 062505 (2005), URL `http://link.aps.org/doi/10.1103/PhysRevA.72.062505`.

[185] P. Staanum, A. Pashov, H. Knöckel, and E. Tiemann, *$X\Sigma+1$ and $a\Sigma+3$ states of LiCs studied by Fourier-transform spectroscopy*, Phys. Rev. A **75**, 042513 (2007), URL http://link.aps.org/doi/10.1103/PhysRevA.75.042513.

Danksagung

Zum Schluss möchte ich mich bei allen herzlich bedanken, die zum Gelingen dieser Arbeit, sei es direkt oder indirekt, beigetragen haben und die mich während meiner Promotionszeit unterstützt und motiviert haben.

- Mein Dank gilt in erster Linie Prof. Axel Görlitz, in dessen Arbeitsgruppe ich diese Doktorarbeit und auch schon meine Diplomarbeit angefertigt habe. Zusätzlich zu einem ausgeprägten, intuitiven Verständnis für Physik besitzt er eine offene, menschliche Art. Beides hat in Zeiten, in denen es im Labor mal nicht so lief, wie man es wollte, geholfen, die entstandenen Probleme zu lösen. Seiner beachtenswerten Begeisterung selbst im Labor mitzuwirken verdanke ich unter anderem den Aufbau eines Lasers. Zudem bedanke ich mich für das sorgfältige Korrekturlesen dieser Arbeit mit guter, konstruktiver Kritik vor der Abgabe und für die Übernahme und schnelle Fertigstellung des Hauptberichtes.
- Ich danke Prof. Georg Pretzler für die freundliche Übernahme des Koreferates und ganz besonders für die zügige Fertigstellung des Gutachtens. Wie auch während meiner Diplomarbeit und meiner Studienzeit habe ich ihn als kompetenten Physiker und verständnisvollen Menschen kennengelernt.
- Für die Zusammenarbeit am selben Projekt mit einer Menge an Leuten während dieser langjährigen Erfahrung würde ich mich auch gerne bedanken. Besonders wichtig sind mir da Maximilian Madalinski und Arnd Obert, mit denen die Arbeit am Projekt sowohl vorantreibend und lehrreich war als auch Spaß gemacht hat. Beiden wünsche ich auf ihren Wegen, die im Augenblick weniger physikalisch sind, viel Erfolg. Danke auch an Frank Münchow, mit dem ich den längsten Teil meiner Arbeit zusammen gearbeitet habe. Seine Grill- und Bierbegeisterung ist unvergleichbar. Desweiteren gilt es die Leute zu erwähnen, die in meiner Obhut Master- und Bachelorarbeiten angefertigt haben. Danke an Kira Borkowski, Ali Al-Masoudi und Fabian Wolf. Ihr habt einen entscheidenden Beitrag zur Arbeit geleistet und meine vertiefte Auswertung damit erleichtert.
- Erweiternd möchte ich mich bei all jenen bedanken, mit denen ich zwar nicht direkt an meinem Projekt gearbeitet, aber dennoch sehr viel Zeit im Labor verbracht habe. Danke an Charbel Abou Jaoudeh, für seine nette Gesellschaft und hilfreiche Art. Ein Dank geht außerdem an Gregor Mura, der vieles auch außerhalb des Labors organisiert hat. So manche Partie in der Zeit zwischen der Arbeit wird wohl unvergesslich bleiben. Danke an Tobias Franzen, der bereits seine Bachelor- und Masterarbeiten in unserer Arbeitsgruppe hervorgebracht hat und sich nun an ein komplett neues Experiment zur Molekülherstellung herantraut. Seinem physikalisch-technischen Talent

habe ich so einige Problemlösungen zu verdanken. Außerdem zu erwähnen ist Simone Kipp, meine Büronachbarin, die zum Ende meiner Arbeit hinzugekommen ist und mir viel unterhaltsame Zeit gegeben hat.

- Ralf Stephan kann man nicht genug danken. Der Techniker unserer Gruppe und die Konstante im Labor. Wenn man mal nicht weiter weiß, und nicht nur bei Problemen elektro-technischer Art, findet man bei ihm wertvolle Hilfe mit guten Ideen und Ratschlägen zusammen mit einer zuvorkommenden Art. Eine (nicht endende) Auflistung aller hilfreichen Schritte ist gar nicht möglich. Vielen Dank für alles über diese lange Zeit.
- Natürlich möchte ich mich noch bei allen Menschen bedanken, die mir außerhalb des Labors wichtig sind und die mir Kraft und Ausdauer für diese Arbeit gegeben haben:
- Es gilt zunächst einmal meiner Familie zu danken, bestehend aus meinen Eltern, meiner Schwester und meinem Neffen. Ihr habt mich stets unterstützt und zu euch kann ich mich immer begeben, um neue Kraft zu schöpfen.
- Tiefe Dankbarkeit verdienst auch Du, Sara, weil Du mein Auffangbecken für schwierige Zeiten warst und bist. Dein tiefes Verständnis und dein Rückhalt sind ein Fundament für mein Fortschreiten. Zusätzlich hatte unsere parallel verlaufende Promotionszeit schöne und abwechslungsreiche Momente, die entspannend und stärkend wirkten.
- Zu guter Letzt geht ein tiefer Dank an meinen Freundeskreis, der ein weiteres essenzielles Fundament für mich darstellt. Danke für wundervolle, fröhliche Momente die unvergessen bleiben werden. Auf dass es ewig so sein wird!

Bei allen möchte ich mich auch nochmal für die abwechslungsreiche und unterhaltsame Zeit außerhalb des Labors bedanken, die mitunter auch mal nötig war! Es hat mir sehr viel Spaß gemacht!